

Pushing the Limits of Resonance Ionization Mass Spectrometry

–

Ionization Efficiency in Palladium and Spectral Resolution in Technetium

Dissertation

zur Erlangung des Grades

„Doktor der Naturwissenschaften“

am Fachbereich Physik, Mathematik und Informatik

der Johannes Gutenberg-Universität in Mainz

Tobias Kron

geb. in Worms



JOHANNES GUTENBERG
UNIVERSITÄT MAINZ

Mainz, den 19. Dezember 2016

1. Berichtersteller: -
2. Berichtersteller: -

Datum der mündlichen Prüfung: 22.08.2017

ABSTRACT

Resonance ionization mass spectrometry (RIMS) is a versatile technique for highly selective ionization and optical spectroscopy. It is based on the stepwise, resonant excitation and subsequent ionization of atoms via powerful, precisely tuned laser radiation, followed by conventional mass spectrometry. As the resonant ionization process addresses sequences of unique optical transitions, it offers extremely high element selectivity and can even achieve isotope and isomer selectivity depending on the spectral resolution of the setup. In this way, RIMS enables the production of highly pure ion beams, which is widely used at on-line facilities worldwide in order to investigate atomic and nuclear properties of the most exotic nuclei. Furthermore, as ions can be very efficiently detected, the technique features a high sensitivity making it also ideally suited for spectroscopy on smallest samples and ultra trace analysis experiments.

This thesis presents advancements on two important key aspects of RIMS: ionization efficiency and spectral resolution. New highly efficient excitation ladders and new instruments for high-resolution spectroscopy are developed and their performance is demonstrated in specific experiments on the elements Pd and Tc.

A highly efficient ionization scheme was requested for Pd in order to enable high-precision measurements on neutron-rich isotopes far off stability, yielding valuable data for nuclear physics. In the first part of this thesis, various 2-, 3-, and 4-step RIMS excitation ladders suitable for Ti:sapphire laser systems are developed and compared with regard to maximum ionization efficiency. The ionization potential of Pd is precisely determined using an advanced graphical analysis method to derive the limit of Rydberg series observed in the energetically high-lying region in the atomic spectrum. The result agrees with literature but increases the precision by more than a factor of five. Using the most efficient ionization scheme identified, excellent efficiencies well above 50 % are demonstrated at two independent mass separator setups yielding the highest efficiencies presently reported for laser ion sources.

The second part of this thesis presents the development of a new laser prototype and an upgrade for the laser ion source, which enable precise spectroscopy with highest spectral resolution. Both instruments are used for high-resolution measurements on the HFS in $^{97,98,99}\text{Tc}$. Outstanding experimental linewidths of less than 100 MHz FWHM and excellent signal-to-noise ratios are demonstrated on smallest radioactive samples of down to 10^{11} atoms. The HFS coupling constants and isotope shifts are precisely derived via a detailed analysis of the highly resolved spectra. The here presented measurements pose the very first HFS spectroscopy in the isotopes $^{97,98}\text{Tc}$ and allow the first determination of the respective nuclear magnetic dipole moments and the nuclear electric quadrupole moments. In addition, the experimental data verifies the formerly unconfirmed nuclear spin of ^{98}Tc .

ZUSAMMENFASSUNG

Resonanzionisations-Massenspektrometrie (RIMS) ist eine vielseitige Technik für die hochselektive Ionisation und die optische Spektroskopie. Sie basiert auf der schrittweisen, resonanten Anregung und anschließenden Ionisation von Atomen mittels leistungsstarker und präzise abgestimmter Laserstrahlung, gefolgt von konventioneller Massenspektrometrie. Durch die Nutzung von Sequenzen einzigartiger optischer Übergänge besitzt der resonante Ionisationsprozess eine extrem hohe Elementselektivität und kann, abhängig von der spektralen Auflösung des Experiments, sogar Isotopen- und Isomeraselektivität ermöglichen. Auf diese Weise erlaubt RIMS die Produktion von hochreinen Ionenstrahlen, was weltweit an On-line-Einrichtungen Anwendung findet, um die atomaren Eigenschaften und die Eigenschaften des Kerns von exotischen Nukliden zu untersuchen. Aufgrund des effizienten Nachweises von Ionen besitzt die Methode eine hohe Sensitivität, womit sie auch bestens für die Spektroskopie an kleinsten Proben und für die Ultrapurenanalyse geeignet ist.

Die vorliegende Arbeit präsentiert die Verbesserung von zwei wichtigen Kernaspekten der RIMS: Ionisationseffizienz und spektrale Auflösung. Neue, hocheffiziente Anregungsleitern und neue Instrumente für die hochaufgelöste Spektroskopie werden entwickelt und ihre Leistungsfähigkeit in konkreten Experimenten an den Elementen Pd und Tc demonstriert.

Ein hocheffizientes Ionisationsschema wurde für Pd benötigt um Hochpräzisionsexperimente an neutronenreichen Isotopen fernab der Stabilität zu ermöglichen, welche wertvolle Information für die Kernphysik beinhalten. Im ersten Teil dieser Arbeit werden verschiedene 2-, 3- und 4-Schritt RIMS-Anregungsleitern, welche sich für Ti:Saphir Lasersysteme eignen, entwickelt und bezüglich ihrer maximalen Ionisationseffizienz verglichen. Hierbei wird das Ionisationspotenzial von Pd präzise ermittelt, wobei eine fortschrittliche graphische Analyseverfahren zur Bestimmung des Konvergenzlimits der beobachteten Rydbergserien im energetisch hochliegenden Bereich des atomaren Spektrums zur Anwendung kommt. Das Ergebnis bestätigt den Literaturwert, wobei die Genauigkeit allerdings um mehr als einen Faktor fünf gesteigert wird. Unter Nutzung des effizientesten Ionisationsschemas werden exzellente Effizienzen von weit über 50% an zwei unabhängigen Massenseparatoren demonstriert, was die zurzeit höchsten Effizienzwerte für Laserionenquellen darstellt.

Der zweite Teil dieser Arbeit präsentiert die Entwicklung eines neuen Laserprototyps und einer Erweiterung für die Laserionenquelle, welche präzise Spektroskopie mit höchster spektraler Auflösung ermöglichen. Diese Instrumente werden für hochaufgelöste Messungen der HFS in $^{97,98,99}\text{Tc}$ genutzt. An kleinsten radioaktiven Proben von bis hinunter zu 10^{11} Atomen werden herausragende experimentelle Linienbreiten von weniger als 100 MHz Halbwertsbreite und ein exzellentes Signal-Rausch-Verhältnis demonstriert. Die HFS-Kopplungskonstanten und Isotopieverschiebungen werden mittels detaillierter Analyse der hochaufgelösten Spektren bestimmt. Die Messungen stellen die allererste HFS-Spektroskopie an den Isotopen $^{97,98}\text{Tc}$ dar und erlauben die erste Bestimmung der entsprechenden magnetischen Dipolmomente und der elektrischen Quadrupolmomente des Kerns. Darüber hinaus verifizieren die experimentellen Daten den vorher unbestätigten Kernspin von ^{98}Tc .

CONTENTS

1	Introduction	1
2	Theoretical Background	5
2.1	Atomic Level Structure	5
2.1.1	Atomic Energy Levels	5
2.1.2	Optical Transitions	6
2.1.3	Splittings and Shifts	7
2.1.4	Multi Electron Systems and Electronic Configurations	10
2.1.5	Rydberg States	12
2.2	Basic Principles of Tunable Lasers	13
2.2.1	The Titanium:Sapphire Laser medium	13
2.2.2	Frequency Selection	14
2.3	Experimental Method - RIMS	17
2.3.1	The Basic Concept of RIMS	17
2.3.2	Ionization Processes	20
2.3.3	Line Shapes and Broadening Effects	22
3	Experimental Setup	27
3.1	Laser System	27
3.1.1	Standard Titanium:Sapphire Laser	27
3.1.2	Grating-Assisted Ti:Sapphire Laser	29
3.1.3	Injection-Locked Ti:Sapphire Laser	31
3.1.4	Frequency Conversion	34
3.2	Mass Spectrometer	36
3.2.1	RISIKO	36
3.2.2	MABU	42
4	Ionization Efficiency: Ionization Scheme Development in Palladium	47
4.1	Ionization Scheme Development	48
4.1.1	Resonant 2-Step Scheme	50
4.1.2	Resonant 4-Step Scheme	53
4.1.3	Resonant 3-Step Scheme	55
4.2	Analysis of the Rydberg Series	58
4.2.1	Even Parity Series	58
4.2.2	Odd Parity Series	61
4.2.3	Graphical Analysis of the Rydberg Series Limits	62
4.3	Investigation of the Efficiency	68
4.3.1	Sample Preparation Process	68
4.3.2	Measurement Analysis	69
4.3.3	Measurements at the RISIKO Separator	71

4.3.4	Efficiency Measurements at the IRIS2 Separator at ORNL	80
4.3.5	Influence of the Temperature Distribution	84
4.3.6	Summary	86
5	Spectral Resolution: HFS Spectroscopy in Technetium	89
5.1	Development of a High-Repetition Rate Single Mode Laser	89
5.1.1	Laser Resonator Design	90
5.1.2	Ray Transfer Matrix Analysis	92
5.1.3	Characterization and First Spectroscopic Application	95
5.2	Spectroscopy in Tc at the MABU	99
5.2.1	Experimental Setup	99
5.2.2	Study of the Ionization Scheme	100
5.2.3	High-Resolution HFS Study of the First and Second Excitation Steps .	105
5.3	The PI-LIST: A New Tool for High-Resolution Spectroscopy	116
5.3.1	Development of the PI-LIST	116
5.3.2	First Test Run with Pd	121
5.3.3	Investigation of the Isotope Shift in Pd	124
5.4	High-Resolution HFS Spectroscopy in Tc	126
5.4.1	Experimental Setup	126
5.4.2	Characterization of the Spectroscopic Performance of the Setup	130
5.4.3	High-Resolution HFS Study of the First Excitation Steps	139
5.4.4	Determination of Nuclear Moments	153
6	Conclusion and Outlook	157
	Appendix	160
A	Ionization Scheme Development in Pd	161
B	HFS Spectroscopy in Tc at the MABU Spectrometer	171
C	Additional Information on the PI-LIST Development	173
D	HFS Spectroscopy in Tc Using the PI-LIST	175
	Abbreviations and Symbols	179
	Bibliography	180
	Curriculum Vitae	191

LIST OF FIGURES

1.1	Periodic table	3
2.1	Absorption and Emission	7
2.2	Level scheme of 4-level laser and Ti:sapphire laser	14
2.3	Function of a birefringent Lyot filter.	15
2.4	Light transmission through an etalon	16
2.5	Reflective diffraction grating	17
2.6	Basic RIS excitation schemes	18
2.7	Elemental and isobaric selection	19
2.8	Superposition of Coulomb potential and an external electric field	21
3.1	Cavity of the standard Ti:sapphire laser	28
3.2	Schematic layout of the grating laser cavity	30
3.3	Tuning range of the grating-assisted Ti:sapphire laser	30
3.4	Spatial hole burning	32
3.5	Cavity of the injection locked Ti:sapphire laser	33
3.6	Accessible wavelength regions	35
3.7	Intracavity cavity SHG layout	35
3.8	Sketch of the RISIKO mass separator	37
3.9	Technical drawing of ion source	38
3.10	Technical drawing of the LIST	40
3.11	LIST repeller scans	41
3.12	Schematic layout of the MABU spectrometer	42
3.13	Sectional view of the MABU oven region	43
3.14	Perpendicular Ionization Geometry	44
3.15	Rod arrangement of a QMS	44
3.16	Stability diagrams of an ideal quadrupole mass filter	45
3.17	Sketch of Channeltron detector	46
4.1	Pd region in the charts of nuclides	48
4.2	Mass spectrum in the Pd region	49
4.3	Non-resonant Pd ionization schemes	50
4.4	Overview about the Pd excitation schemes investigated	51
4.5	Frequency scans and saturation curves of the 2-step ionization scheme in Pd	53
4.6	Frequency scans and saturation curves of the 4-step ionization scheme in Pd	54
4.7	Different second excitation steps for the 3-step ionization scheme in Pd	56
4.8	Frequency scans and saturation curves of the 3-step ionization scheme in Pd	57
4.9	Quantum defect and phase shift as a function of atomic number	59
4.10	Rydberg spectrum of even parity in Pd	60
4.11	Low-energy section of the even parity Rydberg spectra in Pd	60

4.12 Rydberg spectra of odd parity in Pd	61
4.13 Low-energy section of the odd parity Rydberg spectra in Pd	62
4.14 Rydberg spectrum in Pd plotted against the effective principal quantum number	63
4.15 2D-plot of the Rydberg spectra in Pd	64
4.16 2D-plot of the Rydberg spectra in Pd	65
4.17 Projection plots of the Rydberg spectra in Pd	66
4.18 Photographs of the sample preparation process	69
4.19 Typical overshoots of the ion current after blocking of the laser beams	71
4.20 Example Pd efficiency measurement using the 3-step scheme on the RISIKO mass separator	72
4.21 Visualization of the repeller charging	74
4.22 Influence of grounded and floating repeller electrode	74
4.23 Mass spectrum of the Pd region with strong ZrO background	76
4.24 Overall Pd efficiency values for the 3-step scheme	78
4.25 Sketch of efficiency correction procedure	79
4.26 Schematic view of the ORNL ion source	80
4.27 Schematic view of the ORNL ion source geometry	81
4.28 Saturation curves of the 3-step scheme used at the ORNL separator	82
4.29 Pd efficiency measurement using the 3-step scheme at the IRIS2 mass separator	83
4.30 Computer simulated temperature distribution of the RISIKO ion source	85
4.31 Comparison of the temperature along the ionizer tube	86
4.32 Graphical comparison of the efficiencies in Pd	87
5.1 Cavity layout of the unseeded single mode Ti:sapphire laser	90
5.2 Selection of a single cavity mode using thin and air-spaced etalon	91
5.3 Evolution of the beam radius in the ring cavity	93
5.4 3D model of the PI-LIST	94
5.5 Influence of curved mirror distance and folding angle on beam shape parameters	94
5.6 Evolution of the beam radius in the ring cavity with optimized parameters	95
5.7 Spatial beam profile of the output of the ring laser cavity	95
5.8 Scanning FPI spectrum of the stand-alone single mode Ti:sapphire laser	96
5.9 Excitation scheme in Cu	97
5.10 High-resolution frequency scans of the second excitation step in Cu	97
5.11 Basic layout of the experimental setup for Tc spectroscopy in the MABU	99
5.12 Tc mass spectrum obtained at the MABU spectrometer	101
5.13 Ionization schemes for Tc	102
5.14 Study of HFS in Tc with standard and narrowband laser configuration	103
5.15 Narrowband frequency scan of the ultra trace analysis ionization scheme	104
5.16 Comparison of frequency scans with dual etalon laser and single mode laser	106
5.17 Schematic hyperfine splitting of the first step transition for Tc	106
5.18 HFS structure in the first step transition in Tc	107
5.19 Incorrect frequency readout of the wavemeter	109
5.20 Schematic hyperfine splitting of the second step transition for Tc	111
5.21 HFS structure in the second step transition in Tc	112
5.22 2D map of first and second excitation step in Tc	115
5.23 3D CAD model of the PI-LIST	118
5.24 PI-LIST installed at the RISIKO frontend	119
5.25 Photograph of the PI-LIST setup installed at the RISIKO ion source	120
5.26 Mass spectra obtained with the PI-LIST	121
5.27 Comparison of frequency scans of the first excitation step in Pd	122

5.28	Spectrum of the Ti:sapphire laser in dual etalon configuration	123
5.29	Frequency scan of the first excitation step in Pd with higher resolution	125
5.30	Basic structure of the experimental setup for spectroscopy in Tc	126
5.31	Spectroscopy laser beam after horizontal expansion for perpendicular alignment	127
5.32	Mass scans with and without second repeller	128
5.33	3D computer model of the PI-LIST with double repeller	129
5.34	Scans of repeller voltages in dual repeller configuration	129
5.35	Influence of the laser power on the spectral linewidth	131
5.36	Influence of temporal laser pulse separation on the spectral linewidth	132
5.37	Influence of temporal pulse separation on the spectral linewidth and ioniza- tion rate	133
5.38	Influence of the laser beam halo on the spectral structure	134
5.39	Influence of the laser beam spot size of the second excitation step laser	134
5.40	Re-evaluation of power broadening in the first step transition	135
5.41	Influence of the LIST settings on the spectral structure	136
5.42	Spatial dependence of the ion count rate in the extraction field	137
5.43	Spatial dependence of the ion count rate inside the PI-LIST	137
5.44	Mass spectrum of the Tc region at the RISIKO separator using the PI-LIST . . .	139
5.45	Schematic illustration of the HFS splitting of ground state and first excited state Tc	140
5.46	HFS structure of the $J = 5/2 - J' = 7/2$ transition in Tc	141
5.47	Fit to the experimental data of the $J = 5/2 - J' = 7/2$ transition in ^{99}Tc	142
5.48	Comparison of different fitting models	144
5.49	Schematic illustration of the different excitation phases	145
5.50	Fit to the experimental data of the ${}^6S_{5/2} - {}^6P_{7/2}^o$ transition in Tc	146
5.51	HFS structure of the $J = 5/2 - J' = 5/2$ transition for Tc	147
5.52	HFS structure of the $J = 5/2 - J' = 3/2$ transition for Tc	148
5.53	Evolution of the nuclear magnetic moment and the nuclear g-factor in the isotopic chain of Tc	154
5.54	King plots for the investigated ground state transitions in Tc	156
5.55	Evolution of the change in nuclear mean square charge radius in the Tc region	156
A.1	Mass spectrum of the Pd region with strong ZrO background	161
A.2	Spatial profiles of the laser beams for the 3-step scheme	161
A.3	2D-plot of the Rydberg spectra in Pd	162
A.4	Projection plots of the Rydberg spectra in Pd	163
A.5	2D-plot of the Rydberg spectra in Pd	164
A.6	Projection plots of the Rydberg spectra in Pd	165
A.7	2D-plot of the Rydberg spectra in Pd	166
A.8	Projection plots of the Rydberg spectra in Pd	167
A.9	Pd Efficiency measurement 7 using the 3-step scheme at RISIKO	168
A.10	Pd efficiency measurement 14 using the 3-step scheme at RISIKO	168
A.11	Pd efficiency measurement 15 using the 3-step scheme at RISIKO	169
A.12	Pd efficiency measurement 16 using the 3-step scheme at RISIKO	169
A.13	Pd efficiency measurement 17 using the 3-step scheme at RISIKO	170
A.14	Pd efficiency measurement 4 using the 3-step scheme at IRIS2	170
B.1	Narrowband frequency scan of the ultra trace analysis ionization scheme . . .	171
B.2	Narrowband frequency scan of the ultra trace analysis ionization scheme . . .	172
B.3	Narrowband frequency scan of the ultra trace analysis ionization scheme . . .	172

C.1	3D-model of the PI-LIST with internal reflection	174
D.1	Fit to the experimental data of the $J = 5/2 - J' = 7/2$ transition in Tc	175
D.2	Fit to the experimental data of the $J=5/2$ to $J'=5/2$ transition in Tc	176
D.3	Fit to the experimental data of the $J=5/2$ to $J'=3/2$ transition in Tc	176

LIST OF TABLES

4.1	Compilation of upper Rydberg states of even parity in Pd	59
4.2	Compilation of upper Rydberg states of odd parity in Pd	62
4.3	Results of the graphical evaluation of the autoionizing Rydberg series in Pd .	64
4.4	Results of the efficiency measurement using the 4-step scheme in Pd at the RISIKO mass separator	75
4.5	Results of the efficiency measurements at the RISIKO separator	77
4.6	Correction of the final overall efficiency values for the 3-step scheme	79
4.7	Results of the efficiency measurements at the IRIS2 separator	83
4.8	Compilation of the efficiencies in Pd	86
5.1	List of Tc sample used at the MABU spectrometer	100
5.2	Contributions to the FWHM of in the first excitation step spectra	108
5.3	Compilation of the results from the fit for the first step spectra	110
5.4	Contributions to the FWHM of in the second excitation step spectra	113
5.5	Compilation of the results from the fit for the second step spectra	114
5.6	List of the Tc samples used for the PI-LIST experiment	128
5.7	Estimated efficiency values for the PI-LIST operation modes	138
5.8	Contributions to the FWHM of the $J = 5/2 - J' = 7/2$ spectrum	143
5.9	Contributions to the FWHM of the $J = 5/2 - J' = 5/2$ spectrum	148
5.10	Contributions to the FWHM of the $J = 5/2 - J' = 3/2$ spectrum	149
5.11	Compilation of the HFS coupling constants of the first excitation step	150
5.12	Compilation of the final HFS coupling constants	152
5.13	Compilation of the isotope shifts	152
5.14	Nuclear magnetic dipole moments of Tc	153
5.15	Spectroscopic nuclear electric quadrupole moments	155
D.1	Results of the Voigt based fit of the Tc HFS spectra	177

INTRODUCTION

Physics is part of humanity's everlasting quest for comprehensive knowledge. The resulting discoveries, theories, and predictions changed our life and perception radically over the millennia, but they also raised new, more complex questions. In the last 100 years, atomic, nuclear, and particle physics became some of the most important research fields in the physics community. Even though, these fields are devoted to objects and effects on microscopic scales, the discoveries and progress in these areas had far-reaching consequences.

Modern atomic physics emerged at the beginning of the 20th century, when radioactivity was just discovered. Ernest Rutherford conducted scattering experiments, which led him to the development of the first atom model predicting a small, positively charged nucleus in the center of the atom, surrounded by negatively charged electrons on planetary orbits. Eventually, this model became the basis for the Bohr model, which included first quantum mechanical interpretations. As a consequence, Niels Bohr was awarded the Nobel Prize in Physics in 1922 "for his services in the investigation of the structure of atoms and of the radiation emanating from them" [1].

Since then, the research field evolved rapidly, leading to important achievements, like the development of the laser, the use of nuclear fission, the understanding of fusion processes inside stars, the emergence of nuclear medicine, and the development of a vast number of scientific and technical instruments which enable the precise study of matter, particles, radiation, time, and outer space. As already mentioned, such great achievements led to many new open questions. One fundamental, yet unsolved example is the comprehensive understanding of the formation of the universe as we know it and the creation of all the matter which we observe today. Especially the origin of heavy elements is not yet well understood, as stellar nucleosynthesis by nuclear fusion within stars primarily creates elements up to iron with $Z = 26$. To identify the origin of the many heavier elements known, additional nucleosynthesis processes in the most extreme environments of the universe must be considered, investigated and interpreted. Currently, 118 different chemical elements with a total of 243 stable and about 3000 unstable isotopes have been discovered [2]. To understand the formation of these elements via the different types of nucleosynthesis processes, a detailed study of the nuclear properties like mass, charge distribution, shape, spin, and electromagnetic moments, is essential. This requires multifarious experiments on stable and radioactive nuclides up to the most short-lived exotic species at the borderline of the nuclear chart far-off stability. The latter can only be accessed at *Radioactive Ion Beam* (RIB) facilities, where they are produced in nuclear reactions induced by highly energetic projectiles. A number of such RIB facilities are established worldwide, such as: ISOLDE at CERN (Switzerland), ISAC at TRIUMF (Canada), and SPIRAL2/S3 at GANIL (France) [3].

In the study of atomic and nuclear structure, *Resonance Ionization Mass Spectrometry*

(RIMS) plays an important role. Its basic principle is the stepwise, resonant excitation and subsequent ionization of atoms via powerful laser radiation, followed by conventional mass selection. The technique of resonance ionization offers highest element selectivity, as it addresses a sequence of optical transitions in the excitation spectrum of the respective atom which are unique for each chemical element. Together with mass selection, an isotopically pure ion beam can be provided without the need of extensive chemical preparation of the initial sample. Depending on the chosen set of optical transitions, high ionization efficiencies of up to 50 % and even beyond can be achieved [4]. A detailed description of the concept of resonance ionization is given in chapter 2.

RIMS contributes in several ways to the investigation of atomic and nuclear properties. First, it is used to investigate atomic transitions with high spectral resolution to obtain nuclear information via the analysis of the hyperfine structure and the isotope shift in optical transitions. Second, RIMS is used to selectively ionize and extract the isotope of interest at RIB facilities. There, the desired isotope is produced in nuclear reactions most often together with a multitude of interfering radioisotopes which might have several orders of magnitude higher production rates. To ensure highly efficient excitation and ionization of the element of choice, high laser intensities are required, which is why pulsed laser systems are typically used at laser ion sources [5]. A prominent example, which is found at nearly all RIB facilities worldwide, is the high repetition rate Ti:sapphire laser system which originated from Mainz university. Depending on the spectral resolution of the setup, the resonant ionization process can also be used to achieve isotope and even isomer selectivity by making use of the hyperfine splittings and respective shifts in the addressed transitions. The performance of such on-line laser ion sources is vital for the success of subsequent on-line experiments like high-precision mass measurements, decay spectroscopy, or collinear optical high-resolution spectroscopy setups [6, 5, 7, 8]. As RIMS offers a wide variety of benefits compared to other ionization methods, it is mandatory to steadily improve individual aspects to enable new measurements on rarest isotopes with highest precision and maximum efficiency.

The present thesis focuses on advancements of the two perhaps most important aspects: ionization efficiency and spectral resolution. This includes the development of new, highly efficient excitation ladders as well as the development of new instruments and techniques for high-resolution spectroscopy. Both aspects are demonstrated in specific experiments on selected elements.

The elements of interest in the present thesis belong to the group of transition metals within the periodic table, as highlighted in blue in figure 1.1. Together with lutetium and lawrencium they form the *d*-block, which comprises the elements with partially or completely filled *d* sub-shells and includes groups 3 to 12 in period 4 to 7. Transition metals share similar chemical properties, like the formation of many oxidation states, and physical properties, such as high melting and boiling points. The included sub-group of the refractory metals and their neighboring elements feature some of the highest melting points across the periodic table. A prerequisite for RIMS is the evaporation of the atoms of interest, which is achieved by heating the ion source to temperatures comparable or even higher than the melting point of the sample atoms to enable efficient and fast evaporation. Consequently, elements with high melting pose challenging demands on the operation and the material of the laser ion source. This causes heavy thermal stress, which can result in mechanical deformation or even critical damage. Furthermore, the construction materials of the hot ion source set additional limits to the achievable temperature. Typically used materials are tantalum, molybdenum, tungsten or graphite, but also rhenium or special ceramics. In addition, colder parts inside the ion source are very critical when using a sample with high melting point as they can hinder the proper evaporation significantly. As a result, the production of ion beams made from high-melting elements suffers from relatively low efficiency and difficult long-term

H 1																	He 2
Li 3	Be 4											B 5	C 6	N 7	O 8	F 9	Ne 10
Na 11	Mg 12											Al 13	Si 14	P 15	S 16	Cl 17	Ar 18
K 19	Ca 20	Sc 21	Ti 22	V 23	Cr 24	Mn 25	Fe 26	Co 27	Ni 28	Cu 29	Zn 30	Ga 31	Ge 32	As 33	Se 34	Br 35	Kr 36
Rb 37	Sr 38	Y 39	Zr 40	Nb 41	Mo 42	Tc 43	Ru 44	Rh 45	Pd 46	Ag 47	Cd 48	In 49	Sn 50	Sb 51	Te 52	I 53	Xe 54
Cs 55	Ba 56		Hf 72	Ta 73	W 74	Re 75	Os 76	Ir 77	Pt 78	Au 79	Hg 80	Tl 81	Pb 82	Bi 83	Po 84	At 85	Rn 86
Fr 87	Ra 88		Rf 104	Db 105	Sg 106	Bh 107	Hs 108	Mt 109	Ds 110	Rg 111	Cn 112	Nh 113	Fl 114	Mc 115	Lv 116	Ts 117	Og 118
		La 57	Ce 58	Pr 59	Nd 60	Pm 61	Sm 62	Eu 63	Gd 64	Tb 65	Dy 66	Ho 67	Er 68	Tm 69	Yb 70	Lu 71	
		Ac 89	Th 90	Pa 91	U 92	Np 93	Pu 94	Am 95	Cm 96	Bk 97	Cf 98	Es 99	Fm 100	Md 101	No 102	Lr 103	

Figure 1.1: Periodic table. The transition metals are colored in blue. The orange colored symbols indicate exclusively radioactive elements.

operation of the experiment at optimum settings.

Under these tough conditions, the efficiency of the resonant laser ionization process must be maximized in order to enable measurements on rarest isotopes of these elements at RIB facilities. In the first experimental part of this thesis, chapter 4, the development and characterization of a highly efficient excitation ladder for the resonance ionization of palladium ($Z = 46$) is presented. Palladium features a high melting point of 1555 °C, causing challenges as discussed above. Few excitation schemes for Pd were previously available, but ionization efficiencies were by far not sufficient for the use on exotic isotopes at on-line ion sources. A highly efficient and selective excitation ladder was required as Pd has an increasing relevance in nuclear astrophysics. Its neutron-rich isotopes along the isotopic chain towards the neutron shell closure at $N = 82$ play an important role in the *r*-process, a nucleosynthesis process involving rapid neutron capture [9, 10]. The isotope ^{128}Pd is expected to be a waiting-point, a key point in the *r*-process pathway across the chart of nuclides. Although the sites of this mechanism are not clearly identified, most probably core-collapse supernovae or neutron stars, it is assumed to be the origin of about half of the heavy elements in the universe. Future high-precision mass measurements along the isotopic chain of neutron-rich Pd isotopes aim to improve nuclear mass models and to provide valuable input for a conclusive description and understanding of the *r*-process [11, 12]. In addition, a precise investigation of the atomic level structure of palladium is also of interest as its $4d^{10}1S_0$ ground state features a fully occupied *d*-shell acting as the valence shell without any outer *s*- or *p*-shell being populated, which is an exceptional property, unique along the periodic table.

Further feasible applications also rely on the highly efficient and selective ionization of palladium, for example the production and purification of the radioisotope ^{103}Pd for nuclear medicine. With its half-life of 17 days and decay via electron capture, emitting hard X-ray photons and Auger electrons, it is well suited for dedicated treatment of cancer via internal radiotherapy (brachytherapy). It is often used to treat prostate cancer as well as choroidal melanoma (eye cancer) [13, 14]. Another important radioisotope is ^{107}Pd , which is a long-lived (half-life 6.5 million years) fission product of $^{235,238}\text{U}$ and $^{239,241}\text{Pu}$. As a consequence, it constitutes a long-term contamination in nuclear waste and could also be used as indicator of nuclear activities and depositions. Therefore it is of high interest

to monitor its environmental distribution and migration, which could be implemented by sensitive ultra trace analysis based on RIMS, as currently performed at the institute of nuclear chemistry at Mainz university [15, 16, 17].

The second part of this thesis is devoted to advancements in high-resolution *Resonance Ionization Spectroscopy* (RIS) to enable the direct study of nuclear properties via the precise investigation of hyperfine structure and isotope shifts of atomic transitions. Here, two specific points must be addressed to achieve highest resolution. First, the spectral linewidth of the probing laser radiation must be sufficiently narrow, typically in the order of only a few MHz. Second, the atomic ensemble of interest must offer a correspondingly narrow absorption linewidth, which is typically hampered by different broadening mechanisms in the experiment. Some examples are Doppler broadening, power broadening, and in some experimental setups pressure broadening. This defines special requirements on the laser interaction region. Two important developments in this direction are presented in chapter 5. The first one is the design of a new pulsed laser prototype which provides narrowband single longitudinal mode operation with a linewidth well below 100 MHz while being operated at a high repetition rate of 10 kHz. The second development is a new upgrade for the laser ion source which reduces the Doppler broadening significantly in order to enable access to atomic transitions with smallest absorption linewidths. Both instruments were developed with regard to future implementation at on-line ion sources like ISOLDE.

Subsequent to the technical development, the two devices have been successfully used to investigate the hyperfine structure and the isotope shift in long-lived technetium isotopes in two different experiments, which are described in chapter 5. These measurements focused on multiple objectives. One was the provision of essential input for an ongoing RIMS-based ultra trace analysis project, which aims for monitoring the environmental contamination of the radioactive ^{99}Tc , which is a major fission product of ^{235}U [18, 17]. Here, a known amount of ^{97}Tc is added as tracer to the initial sample during the chemical preparation process, which allows the quantification the initial amount of ^{99}Tc in the sample via the experimentally determined isotope ratio of $^{97}\text{Tc}/^{99}\text{Tc}$. Therefore, it is crucial to precisely characterize the hyperfine structure and the isotope shifts of the optical transitions used to ensure equal ionization rate in the simultaneous resonant ionization of both isotopes using a single laser system. Aside from that, technetium is an element of special interest for fundamental research, as only very limited experimental data is available due to the fact that it is very rare and has no stable isotopes. In the course of this work, high-resolution spectroscopy on the long-lived radioisotopes $^{97,98,99}\text{Tc}$ was performed, yielding the first experimental determination of hyperfine structure parameters, nuclear moments, and isotope shifts for $^{97,98}\text{Tc}$, as well as the clear assignment of the nuclear spin I of ^{98}Tc .

Before presenting the experiments and their results, a brief summary of the theoretical background is provided in chapter 2, followed by a description of the components of the experimental setup in chapter 3. Chapter 6 will close the thesis with a conclusion and an outlook on next steps and future applications of the newly developed experimental instruments and techniques.

THEORETICAL BACKGROUND

2.1 Atomic Level Structure

The experimental techniques in the present work rely on the knowledge of the atomic energy level structure and its interaction with radiation. Therefore, the following sections provide a brief, basic description. The aim is to recap relevant information and to clarify the notation used in the present work. Comprehensive descriptions of the topic are available in a large number of modern physics books like [19, 20, 21, 22].

2.1.1 Atomic Energy Levels

The correct description of the orbit of the electrons around the positively charged nucleus, can not be achieved with a purely classical approach. Quantization is required, which gives rise to several so-called quantum numbers, which characterize the state of an atom. The hydrogen atom or hydrogen-like atoms with only one electron are the most simple atomic systems and therefore the best models to start with. In its simplest form, the Hamiltonian expresses the sum of the operators of the kinetic energy and the potential energy and can be written as:

$$H = \frac{-\hbar^2}{2m_n} \Delta_n + \frac{-\hbar^2}{2m_e} \Delta_e - \frac{Z e^2}{4\pi\epsilon_0 r}, \quad (2.1)$$

where m_n and m_e are the masses of nucleus and electron, while Δ_n and Δ_e represent the Laplace operators acting on the coordinates of nucleus and electron, respectively. Due to the symmetry of the electric field, the potential energy depends only on the distance r between nucleus and electron. The atomic spherical system is described by the wave function Ψ which solves the Schrödinger equation

$$H |\Psi(\mathbf{r}, t)\rangle = i\hbar \frac{\partial}{\partial t} |\Psi(\mathbf{r}, t)\rangle \quad . \quad (2.2)$$

The coordinates can be transferred to relative coordinates of the center of mass and the reduced mass

$$\mu = \frac{m_e \cdot m_n}{m_e + m_n} \quad . \quad (2.3)$$

For most atoms, it can be approximated by $\mu \approx m_e$, as $m_n \gg m_e$. The kinetic energy of the motion of the center of mass does not contribute to the internal energy of the atom and can be neglected. The Schrödinger equation can be simplified to the stationary form, because

the Coulomb field is time-independent, resulting in

$$H |\Psi(\mathbf{r})\rangle = -\frac{\hbar^2}{2\mu} \Delta |\Psi(\mathbf{r})\rangle - \frac{Ze^2}{4\pi\epsilon_0 r} |\Psi(\mathbf{r})\rangle = E |\Psi(\mathbf{r})\rangle \quad . \quad (2.4)$$

This equation can be solved with the use of spherical coordinates and a separation of radial and angular contribution

$$\Psi(\mathbf{r}) = R_{nl}(r) \cdot Y_{lm}(\theta, \phi) \quad , \quad (2.5)$$

with the spherical harmonics $Y_{lm}(\theta, \phi)$ and the quantum numbers

principal quantum number	$n = 1, 2, 3, \dots$,
angular momentum quantum number	$l = 0, 1, 2, \dots, n-1$, and
magnetic quantum number	$m = -l, -l+1, \dots, l-1, l$.

The energy of the individual atomic levels is only depending on n and therefore degenerated corresponding to l and m :

$$E_n = -\frac{\mu}{2} \frac{Z^2 e^4}{4\epsilon_0^2 \hbar^2 n^2} = -R_y \frac{\mu}{m_e} \frac{Z^2}{n^2} \xrightarrow{\mu \approx m_e} -R_y \frac{Z^2}{n^2} \quad . \quad (2.6)$$

The constant $R_y = 13.61$ eV is the Rydberg unit of energy and can also be derived from the Bohr model.

In addition, the electron itself has an intrinsic angular momentum which is called spin \mathbf{s} . As the electron is a fermion it has a half-integer spin, which is $s = 1/2$ and has two projections along the z -axis $m_s = \pm 1/2$, which are usually called “up” and “down”. The Pauli exclusion principle prohibits two fermions to occupy the same quantum state, which is described by its full set of quantum numbers. Correspondingly, with the spin projection m_s taken into account, the total degree of degeneracy of the atomic energy level E_n is given by

$$\sum_{l=0}^{n-1} 2(2l+1) = 2n^2 \quad . \quad (2.7)$$

Additional interactions in the atomic system, like the fine structure as described in the following sections, remove this degeneracy.

2.1.2 Optical Transitions

An atom can transition between its discrete electronic states by the absorption or emission of a photon, as sketched figure 2.1. The photon’s frequency ν is proportional to the corresponding change in energy

$$E_{\text{phot}} = \Delta E = h\nu = h \frac{c}{\lambda} \quad . \quad (2.8)$$

The absorption process is stimulated by the interaction with a photon, which must have an energy matching the energetic difference between the current state and an accessible excited state of the atom. As shown in 2.1, the emission process can be either spontaneous or stimulated by a suitable photon. During spontaneous emission, the atom transitions from an energetically higher state to a lower state, emitting a photon of corresponding energy having random phase and random propagation direction. If the decay process is triggered by the interaction of the atom with another photon of correct energy, matching the energy difference of the upper and lower state, the emitted photon has the same frequency, phase, and propagation direction as the initial photon.

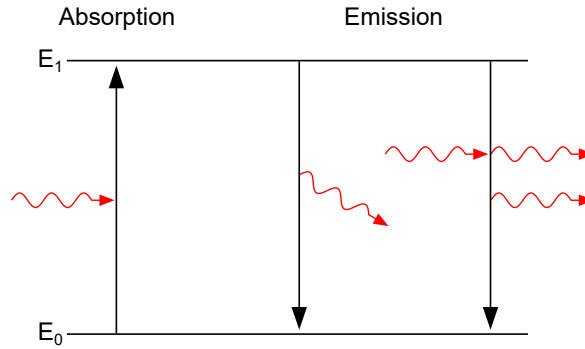


Figure 2.1: Absorption and Emission of photons (red) in a simplified two-state system. The emission process can be classified into spontaneous emission (center) and stimulated emission by an incident photon (right). In the first case, the photon is emitted in a random direction. In the second case, the emitted photon has the same properties as the initial photon.

Each chemical element possesses a specific atomic level structure and consequently characteristic transition frequencies. As a result, the corresponding emission or absorption spectrum shows characteristic spectral lines, which represent the unique spectral "fingerprint" of the element.

2.1.3 Splittings and Shifts

Additionally to the description in the first section, atomic states experience several types of shifts and splittings, which remove some degrees of degeneracy. Correspondingly, these effects introduce shifts and splittings in the observable spectral lines. This section will cover the basic principles of those mechanisms and the resulting consequences.

Fine Structure

The fine structure accounts for three effects, which remove the degeneracy of the energy levels, resulting in a splitting of the spectral lines. These effects are:

- The **spin-orbit coupling**, which describes the interaction between the magnetic field generated by the motion of the electron and its own magnetic moment,
- The consideration of the **relativistic kinetic energy** of the electron which introduces a shift on all atomic levels, and
- The **Darwin term** which considers the influence of the not exactly localized electron on its interaction with the Coulomb field of the nucleus.

Due to its fundamental importance, the caused removal of degeneracy, and its similarity to the hyperfine structure as discussed below, the spin-orbit coupling will be explained in more detail. The basis of this interaction is the spin of the electron \mathbf{s} , which can be interpreted as an intrinsic angular momentum of the charged electron. This causes a magnetic momentum:

$$\boldsymbol{\mu}_s = -g_s \frac{e}{2m_e} \mathbf{s} = -g_s \frac{\mu_B}{\hbar} \mathbf{s} \quad (2.9)$$

with the Landé g -factor of the electron $g_s \approx 2$ and the Bohr magneton μ_B . The electron's magnetic moment $\boldsymbol{\mu}_s$ interacts with the magnetic field generated by the angular motion of

the electron itself, $\mathbf{B}_e \propto \mathbf{l}$. A new quantum number can be introduced, the total angular momentum $\mathbf{j} = \mathbf{l} + \mathbf{s}$. The resulting energy shift can then be written as

$$\Delta E_{\text{SO}} = - \langle \boldsymbol{\mu}_s \cdot \mathbf{B}_e \rangle = a \langle \mathbf{l} \cdot \mathbf{s} \rangle = a \frac{\hbar^2}{2} [j(j+1) - l(l+1) - s(s+1)] \quad . \quad (2.10)$$

As described in section 2.1.4, the strength of the spin-orbit interaction is of special relevance for the coupling mechanisms which define the total angular momentum \mathbf{J} in multi-electron systems.

Lamb Shift

The Lamb shift is a small energy shift, which can be explained by *quantum electrodynamics* (QED). The interaction between the electron and virtual particles from the quantum vacuum fluctuation causes a small perturbation of the electron's position in the electrostatic field of the nucleus. The resulting shift in energy is depending on n and l and leads to the removal of the j -degeneracy, which is expected from the spin-orbit coupling.

Hyperfine Structure

The *hyperfine structure* (HFS) comprises several effects caused by the interaction between the electrons and the magnetic and electric moments of the nucleus. Correspondingly, it appears somewhat similar to the fine structure (section 2.1.3), but typically results in a factor 10^3 smaller energy perturbations. The following paragraphs will cover the two strongest coupling mechanisms. Effects due to moments of higher order, like the splitting due to the nucleus' magnetic octupole momentum, were already observed in few spectroscopy experiments with very high resolution (e.g. [23]), but are not of relevance for the present work.

The nucleus of the atom is composed of neutrons and protons, which are both baryons and therefore also fermions with half-integer spin, $|\mathbf{s}_{n,p}| = 1/2$. Like in an atomic system, the nucleus exhibit discrete energy levels which can be occupied by the nucleons. Their spins couple via *jj-coupling* to a total nuclear angular momentum \mathbf{I} , which is integer for an even total number of nucleons and half-integer otherwise. Similar to the electron, the spins $\mathbf{s}_{n,p}$ have two possible projections, corresponding to $m_{s_{n,p}} = \pm 1/2$, which allows two protons or neutrons to be in the same corresponding energy level or orbital. As a result of the coupling, $\mathbf{I} = 0$ is valid for all atoms with even proton and neutron numbers.

If $\mathbf{I} \neq 0$, the nucleus exhibits a magnetic dipole moment

$$\boldsymbol{\mu}_I = g_I \frac{e}{2m_p} \mathbf{I} = g_I \frac{\mu_N}{\hbar} \mathbf{I} \quad ,$$

analog to the electron's magnetic moment $\boldsymbol{\mu}_s$ in equation (2.9). Here, μ_N is the nuclear magneton and g_I is the Landé g -factor. The magnetic field at the position of the nucleus introduced by the electrons depends on the total angular momentum \mathbf{J} and can be described as

$$\mathbf{B}_J = -B_J \frac{\mathbf{J}}{|\mathbf{J}|} \quad (2.11)$$

and the energy shift can be calculated as

$$\Delta E_{\text{HFS,MD}} = -\boldsymbol{\mu}_I \cdot \mathbf{B}_J = g_I \mu_N B_J \frac{\mathbf{I} \cdot \mathbf{J}}{\hbar |\mathbf{J}|} \quad . \quad (2.12)$$

Similar to the spin-orbit coupling, a new quantum number is introduced, the total angular momentum of the atom $\mathbf{F} = \mathbf{J} + \mathbf{I}$. The shift can be written as

$$\Delta E_{\text{HFS,MD}} = \frac{A}{2} \cdot \underbrace{[F(F+1) - I(I+1) - J(J+1)]}_{C : \text{Casimir factor}} . \quad (2.13)$$

with the hyperfine coupling constant

$$A = \frac{\mu_I B_J(0)}{IJ} , \quad (2.14)$$

which is characteristic for each atomic level.

A nuclear moment of higher order is the electric quadrupole moment Q , which is present in all nuclei with $I > 1/2$. It is linked to a non-spherical distribution of the electric charge in the nucleus, which can either be oblate or prolate. The electric interaction between the electrons and the nuclear electric quadrupole moment lead to a perturbation of the energy levels, which can be written as

$$\Delta E_{\text{HFS,EQ}} = \frac{B}{2} \cdot \frac{3C(C+1) - 2I(I+1)2J(J+1)}{2I(2I-1)2J(2J-1)} \quad (2.15)$$

with the hyperfine coupling constant

$$B = eQ_s \left\langle \frac{\partial^2 V_e(0)}{\partial z^2} \right\rangle . \quad (2.16)$$

The last term of the equation describes the electric field gradient in z-direction produced by the electrons. The factor Q_s is the spectroscopic nuclear electric quadrupole moment. The nucleus shows a prolate shape for $Q_s > 0$ and an oblate shape for $Q_s < 0$. The intrinsic electric quadrupole moment of the nucleus Q can not be observed experimentally, as its interaction with the electrons is influenced by the nuclear spin I and its projection K on the symmetry axis of the nucleus. Their relation is given by the projection formula

$$Q_s = Q \frac{3K^2 - I(I+1)}{(I+1)(2I+3)} . \quad (2.17)$$

The total shift in energy of both HFS components discussed above is given by [24]

$$\Delta E_{\text{HFS}} = \frac{A}{2} C + \frac{B}{2} \frac{3C(C+1) - 2I(I+1)2J(J+1)}{2I(2I-1)2J(2J-1)} , \quad (2.18)$$

It is obvious that the resulting level structure is influenced significantly by I and the shape of the nucleus, as for example when regarding different isotopes or isomeric states in which the nucleus is not in its ground states.

A different approach to introduce the HFS interactions, is a multipole expansion using tensor operators in the space of the electron and the nucleus. This is well described in [25, 21]. This method offers an elegant way to derive contributions of higher order moments, like the interaction with the magnetic octupole moment, but it is slightly more intricate to introduce the relationship to the nuclear properties like shown in equation (2.14) and (2.16).

Isotope Shift

Isotopes are nuclei which possess the same number of protons Z but differ in their neutron number N . As a result, these nuclei have different masses and charge distributions, which also affects the atomic energy levels. The resulting perturbation can be divided into a mass dependent part and a volume, or rather a charge density dependent part. The observed shift in an optical transition between two atomic energy levels can be written as

$$\delta \nu_{IS}^{A,A'} = \nu^A - \nu^{A'} = \delta \nu_{MS}^{A,A'} + \delta \nu_{FS}^{A,A'} \quad (2.19)$$

The mass shift $\delta \nu_{MS}^{A,A'}$ is caused by the change in mass and the resulting change of the moments in the atomic system. If we consider the same transition in two isotopes with a different number of nucleons A and A' with corresponding masses m_A and $m_{A'}$, the shift can be expressed as

$$\delta \nu_{MS}^{A,A'} = \underbrace{(K_{NMS} + K_{SMS})}_{K_{MS}} \frac{m_A - m_{A'}}{m_A m_{A'}} \quad (2.20)$$

The *normal mass shift* K_{NMS} accounts for the change in the motion of the center of mass in the framework of the individual uncorrelated electrons. The second term, the *specific mass shift* K_{SMS} , describes the change of the correlated motion for multi-electron systems. The normal mass shift can be calculated, resulting in $K_{NMS} = m_e \nu^A$. In contrast, the theoretical determination of K_{SMS} relies on the solution of a complex many body problem. This requires extensive numerical calculation, which strongly depend on the atomic state. For this reason, useful results are only available for few cases. Formula (2.20) shows clearly, that the mass effect loses importance for heavy atoms.

The volume effect of the isotopic shift is caused by the altered finite size of the nucleus and its charge distribution. As the general probability of the electron to be found in the nucleus is non-zero, this alters the interaction with the electrostatic field of the nucleus, which is why this shift is referred to as the *field shift*. A simple nuclear model of a homogeneously charged sphere leads to

$$\delta \nu_{FS}^{A,A'} = F_{FS} \delta \langle r^2 \rangle_{A,A'} \quad (2.21)$$

It is proportional to the change in the mean-square charge radius $\delta \langle r^2 \rangle_{A,A'}$ between the two isotopes A and A' . The impact of the volume effect is depending on the electron's orbital and it's probability to be found inside the nucleus. Correspondingly, the effect is strongest for electrons in s -orbitals.

The total isotope shift can be written as

$$\delta \nu_{IS}^{A,A'} = \nu_A - \nu_{A'} = \underbrace{(K_{NMS} + K_{SMS})}_{K_{MS}} \frac{m_A - m_{A'}}{m_A m_{A'}} + F_{FS} \delta \langle r^2 \rangle_{A,A'} \quad (2.22)$$

The normal and specific mass shift, K_{NMS} and K_{SMS} , and the field shift F_{FS} are a characteristic for a specific atomic transition.

2.1.4 Multi Electron Systems and Electronic Configurations

This section aims to give a quick overview on the relevant coupling mechanisms and their notation. The present work follows the conventional form of notation, which is described in detail in chapter 10 of [21].

In the ground state of an multi-electron atom, the electrons occupy the available orbitals according to the *Pauli exclusion principle* and *Hund's rule*. Independent of the atomic state,

the Hamiltonian can be separated into a central field part H_c and a second part H_{ee} , a contribution accounting for the electron-electron interaction. The spin-orbit interaction (see section 2.1.3) adds an additional term

$$H_{SO} = \sum_i c_i \mathbf{l}_i \cdot \mathbf{s}_i \quad , \quad (2.23)$$

which results from the spin-orbit interaction of the individual electrons. The resulting Hamiltonian is

$$H_{tot} = H_c + H_{ee} + H_{so} \quad . \quad (2.24)$$

The state of each electron can be described with its quantum numbers n, l, m_l, m_s . The relative strength of the individual contributions determine the coupling of the orbital and spin angular moments. However, most atoms show a mixture of coupling mechanisms, or different couplings for sub-groups of electrons.

LS coupling

If the electron-electron interaction is stronger than the individual spin-orbit interaction of each electron, the individual moments couple to the total moments

$$\mathbf{L} = \sum_{i=1} \mathbf{l}_i \quad \text{and} \quad \mathbf{S} = \sum_{i=1} \mathbf{s}_i \quad . \quad (2.25)$$

The total angular momentum is

$$\mathbf{J} = \mathbf{L} + \mathbf{S} \quad \text{with} \quad |L - S| < J < |L + S| \quad . \quad (2.26)$$

This is called LS coupling or Russell–Saunders coupling [26] and is the dominant coupling mechanism in light atoms, with $Z < 30$. Energy levels are described by the total quantum numbers L, S, J and are denoted using the term symbol

$${}^{2S+1}L_J^{(o)} \quad , \quad (2.27)$$

where the o may indicate an odd parity of the atomic state. For historical reasons $L = 0, 1, 2, \dots$ is denoted in spectroscopic notation, using the letters S, P, D, \dots . The term $2S + 1$ is referred to as spin multiplicity. As the fine structure splitting is small compared to the separation of states with different L or S , the individual fine structure components lie closely together within the energy spectrum. These groups of fine structure components belonging to a specific L and S are called fine structure multiplets or, correspondingly to their number of components, singlets, doublet, triplets and so on.

jj coupling

This type of coupling occurs when H_{so} is bigger than the electron-electron interaction. This is usually the case for heavy atoms, with $Z > 60$, as well as for higher excited atomic levels. The individual momenta \mathbf{l}_i and \mathbf{s}_i of the electrons couple to

$$\mathbf{j}_i = \mathbf{l}_i + \mathbf{s}_i \quad (2.28)$$

and a resulting total angular momentum of

$$\mathbf{J} = \sum_i \mathbf{j}_i = \sum_i \mathbf{l}_i + \mathbf{s}_i \quad . \quad (2.29)$$

The total orbital angular momentum \mathbf{L} and the total spin \mathbf{S} are not defined. These atoms tend to exhibit quite complex spectra, because the strong individual spin-orbit coupling causes the energy levels for a specific l_i to distribute across a larger energy region. As a result, the typical formation of a multiplet structure, like in the LS coupling, is missing.

J_1K Coupling

Also referred to as J_1l or J_1L_2 coupling. Here, a sub-group of electrons couple to form \mathbf{J}_1 , which couples with the orbital angular momentum \mathbf{l} of an outer electron or with the total angular orbital momentum \mathbf{L}_2 of another group of outer electrons to form \mathbf{K} ,

$$\mathbf{K} = \mathbf{J}_1 + \mathbf{L}_2 \quad \text{with} \quad |J_1 - L_2| < K < |J_1 + L_2| \quad . \quad (2.30)$$

The total angular momentum \mathbf{J} results from the coupling of \mathbf{K} and the outer spin momentum \mathbf{s}_2 or \mathbf{S}_2 to

$$\mathbf{J} = \mathbf{K} + \mathbf{S}_2 \quad \text{with} \quad |K - S_2| < J < |K + S_2| \quad . \quad (2.31)$$

The electronic configuration and final term is noted as

$$n_1 l_1^{N_1} (\text{Term}_1) n_2 l_2^{N_2} (\text{Term}_2) {}^{(2S_2+1)} [K]_J^{(o)} \quad . \quad (2.32)$$

The J_1K coupling occurs when the Spin-Orbit interaction of the inner sub-group is stronger than the electrostatic interaction of the sub-group with the outer electron(s). Accordingly, J_1K coupling is often found in excited states where some electron(s) is in an orbital with higher principal quantum number n and therefore in average at a large distance to the electrons of the inner sub-group. One example for J_1K coupling is palladium, which was subject of the investigation presented in chapter 4.

2.1.5 Rydberg States

Atomic states with a highly excited electron given by a high principal quantum number n are called *Rydberg states* or sometimes *hydrogen-like configurations*¹. These *Rydberg atoms*, show unique features, which play a special role in optical spectroscopy.

The approximated radius of an atom is about $\langle r \rangle \approx a_0 n^2$, with the Bohr radius $a_0 \approx 0.5 \cdot 10^{-10}$ m. Due to its quadratic dependence on n , the size of the atom can increase by several orders of magnitude for higher n . For example, a diameter of $\langle d \rangle \approx 1 \mu\text{m}$ can be reached for $n = 100$. This huge size results in some particular properties. Rydberg atoms show a high sensitivity to external electric fields. Consequently, the Stark-effect is significantly stronger and field ionization is possible with electric field strength in the order of 1 kV/cm. Another consequence is the significantly increased cross-section, as it is proportional to n^4 . The enhanced probability of collisions or photon absorption plays an important role for ionization processes, which is discussed in more detail in section 2.3.2. Apart from the increased sensitivity to many kind of ionization processes, the Rydberg states show rather long lifetimes of $\sim 10 \mu\text{s}$ and longer, as the wavefunction of the remote electron has little overlap with the wavefunctions of inner states. As a result of the large geometrical size and the weakly bound excited electron, the polarizability of Rydberg atoms is also strongly enhanced.

The inner electrons shield the distant excited electron from the Coulomb potential of the nucleus. As a result, the excited electron experiences a Coulomb potential similar to that of a singly positively-charged nucleus, just like in the hydrogen atom. As a consequence,

¹This must not be confused with highly charged ions with only one electron, which are also referred to as hydrogen-like atoms.

the energy of the excited electron can be described by formula (2.6) with $Z = 1$. But due to the non-vanishing probability to find the excited electron inside the inner core of the atom, where the nucleus' Coulomb potential is not entirely shielded, a small correction, the *quantum defect* δn_l , must be applied to the principal quantum number n . As the quantum defect is linked to the probability to find the excited electron inside the inner core, it depends on n and on the orbital angular momentum l of the excited electron [27]. Consequently, the highest quantum defects are observed for excited electrons in S-orbitals with $l = 0$ which have the highest probability of finding the electron close to the nucleus, while decreasing quantum defects are observed for larger l . The resulting *effective principal quantum number* $n' = n - \delta_{n,l}$ is used to write the binding energy of the excited electron,

$$E_n = -\frac{R_y}{(n - \delta_{n,l})^2} = -\frac{R_y}{n'^2} \quad (2.33)$$

It is clear that the atomic states converge towards the ionization limit, resulting in series of states with shrinking energy spacing, so-called *Rydberg series*. The resulting binding energy of the electron is very weak, in the order of only 0.01 eV. This lies in the region of thermal energies, which is why Rydberg atoms are easily ionized by collisions, external electric fields, or even photons from blackbody radiation. This ionization will be discussed further in section 2.3.2.

2.2 Basic Principles of Tunable Lasers

This section will briefly summarize the basic principles of tunable lasers as used in the laser system in the LARISSA working group at Mainz university. The aim is to provide a concise overview of the relevant aspects as basis for a good understanding of the concept and operation of the experimental setup presented in chapter 3. More extensive descriptions can be found in [28, 29] as well as in a variety of textbooks, e.g. [22].

2.2.1 The Titanium:Sapphire Laser medium

Laser radiation relies on the amplification of a light field by stimulated emission, which gives laser light its characteristic coherence. In order to enable an amplification of the initial photons, the upper state of the laser transition must have a higher population n_{up} than the lower state n_{low} , a situation called *population inversion*. Due to the fact that for an atomic transition stimulated emission is always competing with absorption, the population in the upper state of a simple two-level system is limited to $n_{\text{up}}/n_{\text{low}} = 1/2$, preventing the formation of population inversion. To overcome this problem, the active medium, or gain medium, of a laser must feature a specific set of energy levels. A distinction can be made between three-level and four-level laser. As sketched in figure 2.2a, in a four-level laser, the system is excited into a high-lying state $|2\rangle$ by a pump process which can be an optical excitation, as well as other excitation processes like e.g. electric discharge or an electric current. The short-lived state $|2\rangle$ quickly decays into a long-lived state $|3\rangle$, which poses the upper state of the laser transition. The stimulated emission process along the lasing transition leads to state $|4\rangle$, which is quickly depopulated by a fast decay into the initial state $|1\rangle$, where the process starts again. In contrast, in a three-level laser, the laser transition directly leads to the low-lying state $|1\rangle$, which leads to the need of a very efficient pump process to achieve a sufficient inversion between state $|1\rangle$ and $|3\rangle$. For a more efficient laser amplification process, the gain medium is usually placed inside an optical cavity, also called optical resonator, providing an enhanced feedback of the laser light.

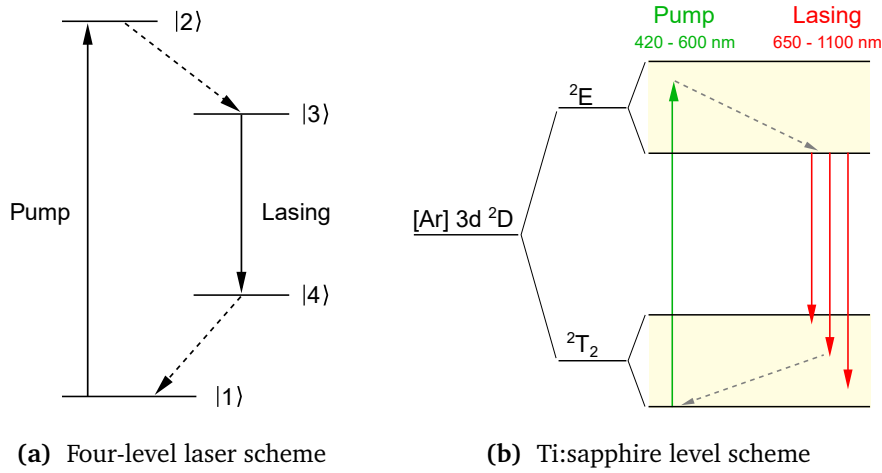


Figure 2.2: Level scheme of a classical 4-level laser and a the Ti:sapphire gain medium. Dashed lines indicate a fast decay. See text for description.

Titanium-doped sapphire crystal ($\text{Ti}^{3+}:\text{Al}_2\text{O}_3$) is a very prominent active laser medium as it allows the construction of widely tunable solid-state lasers. The characteristics of the Ti:sapphire medium are described in detail in literature [30, 31, 32]. Due to the coupling to the field and vibration of the sapphire crystal lattice, the Ti^{3+} ground state $[\text{Ar}] 3d^2D$ is split into two vibrational bands, as shown in figure 2.2b. The 2E -band and the 2T_2 -band form a four-level laser scheme with fast, non-radiative relaxation within the vibrational bands (gray). The energetic width of the lower band leads to the characteristic, broad emission bandwidth, spanning across 650 - 1100 nm with a peak gain at 800 nm. The lifetime of the upper level of the laser transition at room temperature is 3.2 μs . The pump transition ${}^2T_2 - {}^2E$ covers 420 - 600 nm and can be efficiently excited using for example frequency-doubled Nd:YAG lasers (532 nm) or frequency-doubled Nd:YLF lasers (527 nm). In both transitions, ${}^2T_2 - {}^2E$ as well as ${}^2E - {}^2T_2$, the cross-sections are significantly higher for p-polarized light compared to s-polarized light, which has to be considered in the laser design.

2.2.2 Frequency Selection

In order to select and control a specific laser frequency from the broad gain bandwidth of the Ti:sapphire laser medium, frequency selective elements are integrated in the laser resonator. The following paragraphs briefly describes the most important frequency selective elements in the LARISSA laser system.

Lyot Filter

A lyot filter or birefringent filter uses the polarization-dependent phase shift in a birefringent material. As illustrated in figure 2.3, inside the birefringent crystal, an incident linear polarized beam of light (red) with wavelength λ is split up into an ordinary and extraordinary beam (orange). The polarization of both beams is perpendicular to each other. Due to the different refractive indices n_o and n_e of the axes of the crystal with thickness L , the transmitted beams feature a relative phase shift of

$$\delta(\lambda) = \frac{2\pi}{\lambda} (n_o - n_e) L \quad , \quad (2.34)$$

resulting in elliptical polarization of the final beam (green).

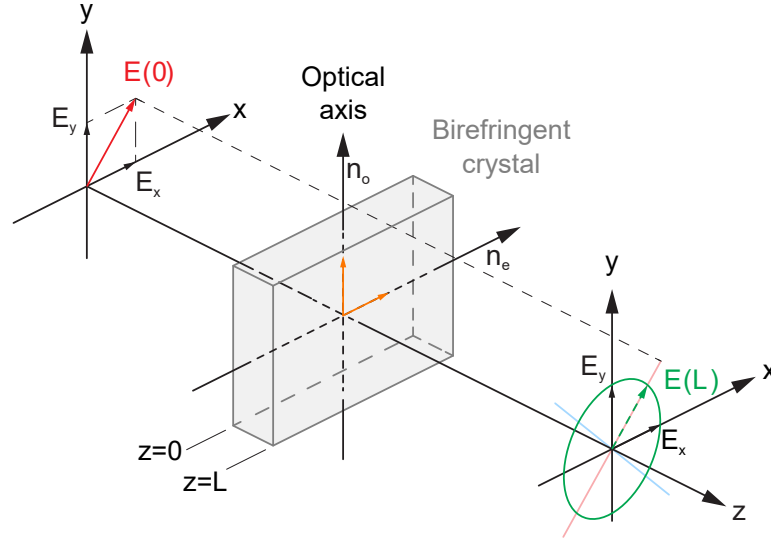


Figure 2.3: Function of a birefringent Lyot filter. See text for description. Graphic adapted from [22].

Inside the laser resonator, the polarization-dependent amplification in the gain medium as well as multiple Brewster surfaces cause strong losses of the s-polarized component (light blue). Considering only the component of the transmitted beam which is polarized parallel to the initial p-polarized beam (light red), the transmission function is given by

$$I(\lambda) = I_0 \cos^2 \left(\frac{(n_o - n_e)\pi L}{\lambda} \right) . \quad (2.35)$$

The free spectral range is given by $FSR = c/(L(n_o - n_e))$. In order to increase the spectral selectivity, a Lyot filter often consists of a set of birefringent plates with integer thickness ratio, like 1:4:16 as used in the Mainz Ti:sapphire laser setup. The transmission maximum of the filter can be continuously tuned by rotating the crystal in such a way that the angle between the optical axis of the crystal and the propagation axis of the beam is changed, thus altering the extraordinary refractive index n_e .

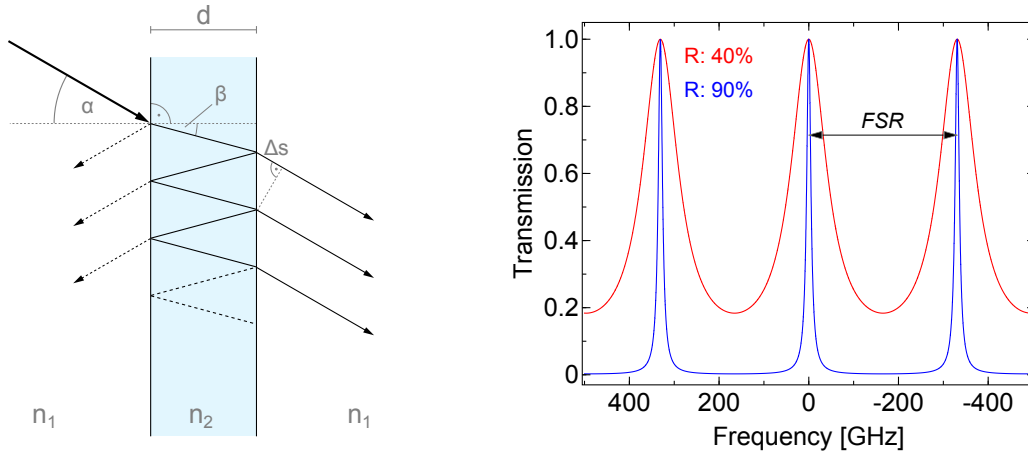
Fabry-Pérot Etalon

A Fabry-Pérot etalon or *Fabry-Pérot interferometer* (FPI) consists of two plan-parallel, partially reflective surfaces spaced by the distance d . This can be easily achieved by using a plan-parallel substrate with refractive index n_2 and a coating with reflectivity R on both sides, as visualized in figure 2.4a. The propagating beam is split up by multiple reflections inside the etalon, featuring a phase shift of

$$\delta(\beta) = \frac{2\pi}{\lambda} 2n_2 d \cos(\beta) \quad (2.36)$$

between the successively transmitted components. Based on the principle of superposition, the amplitude of all transmitted components can be summarized and one obtains the transmission function for the intensity I , which is given by an Airy function

$$I(\delta) = I_0 \frac{(1-R)^2}{(1-R)^2 + 4R \sin^2(\delta/2)} = I_0 \frac{1}{1 + q \sin^2(\delta/2)} , \quad (2.37)$$



(a) Light passing a Fabry-Pérot etalon. Internal multiple reflections cause phase shift leading to interference in the outgoing beam. (b) Transmission function of an etalon for two different reflectivities R . The substrate is assumed to be glass with a thickness of 0.3 mm, resulting in an FSR of 330 GHz.

Figure 2.4: Light transmission through a Fabry-Pérot etalon.

with the coefficient of finesse $q = 4R/(1-R)^2$. As an example, figure 2.4b illustrates the reduction of the width of the transmission peak for higher reflectivities R . When assuming small incident angles β , the spectral interval between the individual transmission peaks, the *free spectral range*, is given by $FSR = c/2n_2d$. Another characteristic property is the finesse F , the ratio between the width of the transmission peaks and the FSR ,

$$F = \frac{FSR}{\delta \nu_{FWHM}} = \frac{\pi}{2 \arcsin(1/\sqrt{q})} \approx \frac{\pi\sqrt{q}}{2} = \frac{\pi\sqrt{R}}{1-R} , \quad (2.38)$$

which is obviously increasing for higher reflectivities, as shown in figure 2.4b.

Reflective Diffraction Grating

Another method of frequency selection, widely used in tunable lasers, is the use of reflective diffraction gratings. An incident beam of light is diffracted on each groove of a periodically structured grating surface. The optical path difference Δs of the individually reflected components lead to interference in the corresponding superposition. For a wavelength λ , maximum constructive interference is reached when the optical path difference equals $m\lambda$ with the diffraction order $m \in \mathbb{N}$. So-called *blazed gratings* are often used, in order to improve the power percentage diffracted in the direction of a specific angle, respectively wavelength range. They feature a saw-tooth profiled surface with a characteristic *blaze angle* θ , as illustrated in figure 2.5.

In laser resonators, diffraction gratings are often installed in the so-called *Littrow* configuration, where the chosen maximum is reflected back into the cavity, following the path of the incoming beam. Consequently, the incident angle α equals the angle of the first diffraction order β of the chosen wavelength λ . The reflection angles for the interference maximum of the order m is defined by

$$m\lambda = 2g \sin(\alpha) , \quad (2.39)$$

where g is the groove spacing $\text{mm}/\text{grooves}$. For simplicity, most laser designs use the first diffraction order $m = 1$. It is clear that the resolving power of the grating is higher when

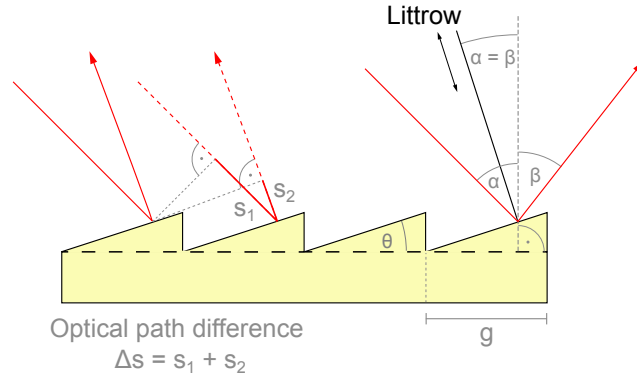


Figure 2.5: Diffraction on a reflective blazed grating.

involving a larger number of grooves n_{groove} . The relation is given by

$$\frac{\lambda}{\Delta\lambda} = m n_{\text{groove}} \quad (2.40)$$

2.3 Experimental Method - RIMS

The method of *resonance ionization* or *resonant laser ionization* relies on the step-wise successive excitation and final ionization of the atoms of choice via precisely tuned laser radiation. The development of the first widely tunable dye lasers at the end of the sixties allowed resonant excitation of a wide range of atomic transitions and paved the way for the development of the method of *resonance ionization spectroscopy* (RIS), which was proposed and demonstrated a few years later [33, 34]. Due to its high efficiency and high selectivity, the technique quickly became a successful tool specifically to provide isotopically pure ion beams at on-line facilities worldwide [5]. This section will briefly present its basic concepts and highlight its characteristic advantages. In addition typically observed broadening effects and the resulting line shapes will be discussed.

2.3.1 The Basic Concept of RIMS

Resonance ionization uses efficient stepwise excitation through strong atomic transitions and successive ionization, induced as final excitation step. It is mandatory to use laser light as intense and spatially controlled radiation with narrow spectral linewidth is required. Figure 2.6 illustrates the basic principle of a resonance *ionization scheme* with 2-step (left) or 3-step excitation (right).

The frequency of the lasers used is precisely tuned, to resonantly excite strong transitions of the atoms of interest. The usual starting point is the ground state of neutral atoms. Alternatively, energetically low-lying states with reasonable thermal population can be used as well. The statistical thermal population of the atomic levels follows the Maxwell-Boltzmann statistic and depends on the temperature of the atomic ensemble. For a suitable population of the higher state, its energy has to be in the order of $k_B T$. Typically, temperatures up to 2000 °C are used, which corresponds to energies up to about 0.2 eV or 1600 cm^{-1} . By absorption of the resonantly tuned laser photons, the atoms of interest are selectively excited into higher lying excited states. The final excitation step is used for the ionization of the atoms. It can be based non-resonant ionization, a transition to an autoionizing state, or ionization via population of Rydberg states close to the *ionization potential* (IP). The

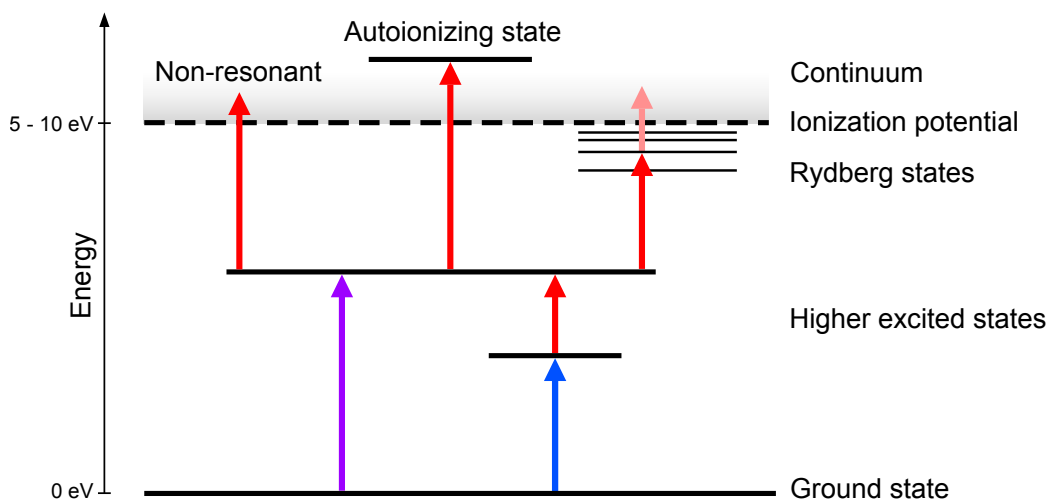


Figure 2.6: Basic excitation schemes for resonance ionization using a total number of two (left) or three (right) excitation steps. All optical transitions are addressed by precisely tuned laser radiation with frequencies ranging from ultraviolet to near infrared. The final ionization can be achieved by three different processes which are discussed in the text.

individual processes and their characteristics are discussed in the following section 2.3.2 in detail.

The energetic spacing of the atomic states in the lower region of an atomic spectrum is larger than in the higher regions of the spectrum, as the level density increases towards the ionization energy. This is reflected in the $E_n \propto n^{-2}$ relation in formula 2.6. As a result, first step transitions imply wavelengths in the ultraviolet or blue frequency range, whereas wavelengths of higher excitation steps are usually in the red to infrared region. To allow efficient saturation of these optical transitions, high intensity laser radiation is required. It also enables the generation of blue to ultraviolet radiation by efficient generation of higher harmonics using non-linear optical crystals. Therefore, the use of powerful pulsed lasers with high repetition rates of 100 – 10,000 Hz and pulse length in the nanosecond regime, has been established as standard tool within the RIS community.

Multi-step resonance ionization specifically addresses a set of individual atomic levels, which are unique for each element in the periodic table. Correspondingly, the excitation and ionization are highly element selective. *Resonance ionization mass spectrometry* (RIMS) combines the resonant ionization process with a subsequent mass selection process. This can be achieved by using, for example, a magnetic mass separator or a quadrupole mass filter. As illustrated in figure 2.7, the combination of the mass resolution with the element selectivity of the resonance ionization provides access to an isotopically pure ion beam.

Due to its high selectivity in combination with high ionization efficiency, RIMS is perfectly suited for the use at on-line ion sources, where the efficient ionization of rare species and a good suppression of surface ionized contaminations are of highest priority. Today, resonance ionization is used as predominant ion source at all leading *radioactive ion beam* (RIB) facilities worldwide, i.e. RILIS at ISOLDE (CERN), TRILIS at ISAC (TRIUMF), GISELE at SPIRAL2/S3 (GANIL) and FURIOS at IGISOL (JYFL) [5, 35]. In addition, RIMS is also used in a large variety of further applications due to its outstanding versatility. Some examples are ultra trace analysis [36, 37, 15, 38], atomic spectroscopy [39, 40], or isotope separation for ultra-pure sample preparation in fundamental research projects [41].

As discussed in the previous section 2.1.3, the optical transitions of different isotopes and isomers may exhibit different shifts and hyperfine splittings of the optical transition.

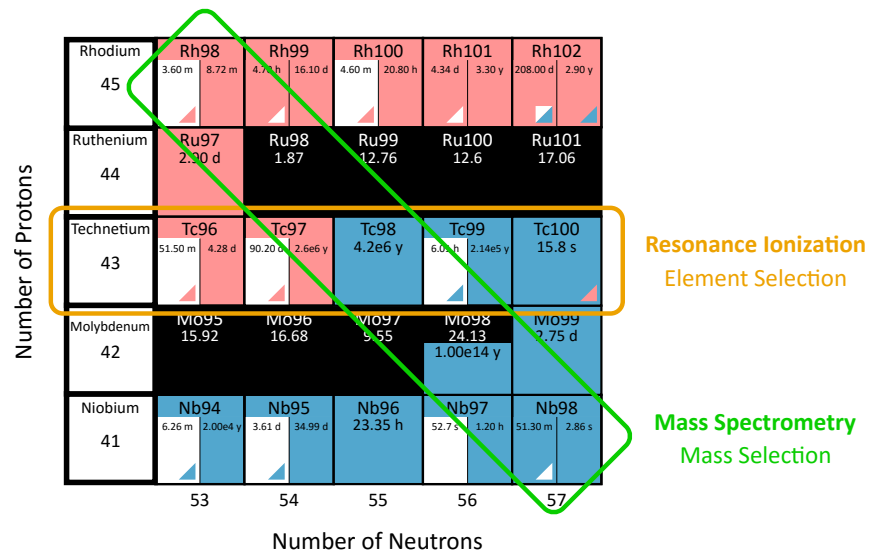


Figure 2.7: Illustration of the element and isobar selection along the chart of nuclei. In this scenario, the isotope ^{98}Tc is being selected by resonant ionization of Tc and successive mass selection.

Accordingly, if the experimental setup provides a sufficient spectral resolving power, individual isotopes and isomers can be selectively ionized. Isotope selectivities up to $5 \cdot 10^{12}$ were successfully demonstrated in the past by using narrowband cw laser radiation and a quadrupole mass filter [42, 43]. Independent of the kind of selectivity regarding element, isotope, or isomer, the effect is enhanced by the number of resonant steps used, which means that a fully resonant 3-step scheme usually exhibits significantly higher selectivity than a 2-step scheme or a 3-step scheme involving a non-resonant ionization step. In addition, resonant 3-step schemes usually outperform 2-step schemes in terms of ionization efficiency as the resulting lower frequencies for each excitation step can be accessed with significantly higher laser powers, avoiding the power losses in the higher harmonic generation process.

The performance of the experiment is crucially linked to stability, selectivity, and efficiency of the resonance ionization process. Four essential parameters of the laser radiation are of relevance for ensuring best conditions. These are the following:

I	ntensity
S	patial overlap
S	pectral control
T	emporal overlap

This set of experimental parameters will be referred to as the *ISST parameters*. It is evident that they have to be well controlled and adjusted to achieve the desired conditions for the experiment. The long-term stability of the parameters gains in relevance, when conducting measurements over the course of several hours up to several days, which was the case for many measurements in the present work.

2.3.2 Ionization Processes

This section presents the three commonly used ionization processes used in resonance ionization schemes. The ionization mechanism will be discussed and substantial differences will be highlighted.

Non-Resonant Photoionization

If the energy $E_{phot} = h\nu$ of an absorbed photon exceeds the energy gap E_{gap} between the highest populated excited state and the IP, the excited electron escapes into the continuum and the atom is ionized. This process is non-resonant, as no upper bound state is involved. Usually, it is the most inefficient of the possible ionization mechanisms. The ionization rate of non-resonant ionization is typically several orders smaller in magnitude than those involving a resonant excitation into a bound atomic state.

The probability of the ionization rate P is linearly depending on the photon flux density n_{phot} and can be written as

$$P_{nr} = \sigma_{nr} n_{phot} \quad , \quad (2.41)$$

where σ_{nr} is the corresponding cross-section for non-resonant ionization, which is typically in the order of 10^{-17} cm^2 . Consequently, the dependence between laser power and the number of generated ions per second can be estimated to be also linear. For an unstructured continuum without any states above the IP, this process is insensitive to the laser frequency except for the constraint $E_{phot} \geq E_{gap}$ and it does not exhibit any form of power broadening.

Despite its low cross-section, this ionization type offers benefits, which can be advantageous depending on the aim of the experiments. For example, due to the practically non-existent frequency-dependence within spectral ranges of several tens of cm^{-1} , this ionization step is often used when performing wide frequency scans in the previous excitation steps in order to probe different intermediate excited states. Also, HFS intensities of previous transitions are significantly better reproduced when deploying a spectrally insensitive ionization process.

Ionization via Rydberg States

As described in section 2.1.5, Rydberg states are excited atomic states with one electron exhibiting a specifically high principal quantum number n , located closely below the IP. After efficient, resonant excitation into one of these Rydberg states, the energetic gap to the IP is so small that subsequent ionization can occur via a variety of processes.

Already, an effective principal quantum number of $n^* = 20$ corresponds to a very weak binding energy of the valence electron of less than 0.04 eV, which is easily exceeded by thermal energies. For this reason, Rydberg atoms are easily ionized by collisions with other particles inside the heated ion source. The probability of this process is enhanced by the significantly increased size of the Rydberg atom of up to about $1 \mu\text{m}$, which correspondingly increases the geometrical cross-section.

Another possible way of ionization involves absorption of any additional photon, either from the laser radiation or from blackbody radiation of the hot ion source. The majority of the photons from the blackbody radiation at $T \approx 2000 \text{ }^\circ\text{C}$ are low-energy infrared photons, but their energy of about 0.01 – 1.0 eV is still enough to exceed the gap to the IP.

In addition, strong electric fields can ionize the atom efficiently, by lowering the electric field barrier of the atom's Coulomb potential, as sketched in figure 2.8. Due to the large diameter of the Rydberg atoms of up to $r = 1 \mu\text{m}$ and the required energy in the order of only 0.1 eV, electric field strength in the order of 1 kV/cm will lead to field ionization. Typically used magnetic mass separators are operated at several ten keV, which leads to

field strength of about 4 kV/cm in the extraction region at the exit of the ion source. In comparison, spectrometer with low extraction fields show a significantly weaker ionization of Rydberg states.

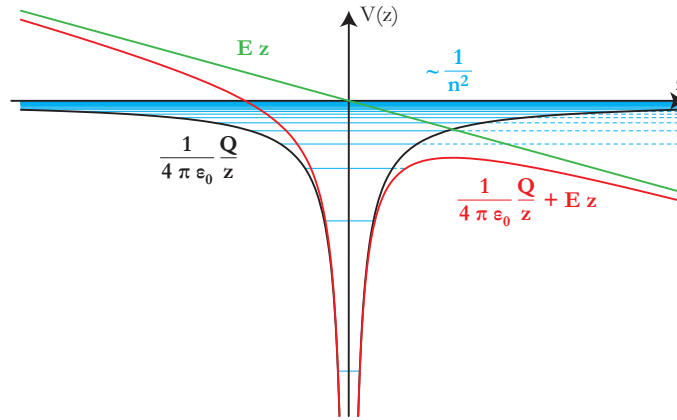


Figure 2.8: Superposition of an atomic Coulomb potential (black) and an external electric field (green). The lowering of the field barrier leads to ionization of the upper atomic energy levels (blue). Graph adopted from [44].

The resonant excitation process and the high number of possible ionization mechanisms with enhanced cross-sections lead to a high overall ionization probability of Rydberg states, usually much higher than for non-resonant ionization. However, most of the ionization mechanisms show a strong dependence on the conditions of the ionization volume. The strength of electric fields, the temperature of the ion source, or the collision rate can differ significantly for different experimental setups. Correspondingly, these conditions must be considered in detail when choosing the ionization step for an ionization scheme.

Autoionization

The third ionization step is shown in the upper center in figure 2.6. It uses the resonant excitation into an atomic state with a level energy greater than the IP, a so called autoionizing resonance. This is possible when the atomic state possesses two or more excited electrons, which store a total excitation energy greater than the IP. By internal coupling through Coulomb electron-electron interaction, the total energy can be transferred to the outermost valence electron. Its energy now exceeds the IP and it immediately leaves the atomic system, forming a positive ion. In most cases, electron wave functions have a significant overlap and thus, the energy transfer happens quite fast. As a consequence, these *autoionizing states* (AI states) are usually rather short-lived with lifetimes below nanoseconds. According to W. Heisenberg's uncertainty principle, the short lifetime of the state corresponds to an increased uncertainty of its energy. This causes a large spectral width of corresponding transitions, which can reach more than 100 GHz, exceeding the typical natural linewidths of ~ 10 MHz by many orders of magnitude. In addition, the observed resonance peaks in the spectrum often show a characteristic asymmetry which is caused by the interference of the excitation into the discrete AI state with the competing process of excitation into the continuum [45].

As the excitation is a resonant transition into an upper state, this excitation step offers higher efficiency and can exhibit saturation. In combination with the high probability of ionization, this fact results in ionization cross-sections about 10^4 times larger than those of non-resonant ionization. Detailed studies of the electronic configuration of those states are difficult, as the autoionization hinders any further transition. The underlying atomic configuration with multiple excited atoms is also non-trivial and hardly predictable by

theory. Therefore, for most elements, detailed documentation of AI states and reliable level assignments are missing in literature. Nevertheless, experimental observations confirm the expected high number of AI states in atoms with many open shells. Prominent examples are the lanthanides and actinides, which show exceptionally pronounced continuum structures with large numbers of AI states [46, 47, 48].

2.3.3 Line Shapes and Broadening Effects

Several effects influence the spectral line shape of an optical transition. The contribution of all effects add up to the experimental line shape which is observed in the recorded data. The relevant effects observed in the present work are typical for optical spectroscopy and therefore well studied. Detailed discussions can be found in a variety of textbooks, e.g. in [19, 20, 22]. The aim of this chapter is to concisely summarize these broadening effects and to recap their major properties and impact on experimental line shape. Throughout the present work, the word *linewidth* is always used in terms of the *full width at half maximum* (FWHM) of a peak.

Natural Linewidth

Excited atomic states show an essential broadening of their energy due to their finite lifetime. The resulting line shape in the frequency space is a Lorentzian profile,

$$I(\nu) = I_0 \frac{\gamma^2}{(\nu - \nu_0)^2 + \gamma^2} \quad , \quad (2.42)$$

where I_0 is the maximum intensity at resonance. The full width at half maximum of this profile is $\Delta \nu_{\text{natural}} = 2\gamma$. This value is linked to the lifetime τ of the excited state by

$$\Delta \nu_{\text{natural}} = \frac{1}{2\pi\tau} \quad . \quad (2.43)$$

For an optical transition between two atomic states, the lifetimes of upper and lower state, τ_i and τ_j , contribute to the broadening, leading to

$$\Delta \nu_{\text{natural}} = \frac{1}{2\pi} \left(\frac{1}{\tau_i} + \frac{1}{\tau_j} \right) \quad . \quad (2.44)$$

Typical atomic transitions address states with lifetimes of 1 ns - 1 μ s, which results in natural linewidths of about 160 kHz - 160 MHz.

Doppler Broadening

If an atom moves relatively to the source of the laser radiation, it experiences a *Doppler shift* of the laser frequency. The observed frequency is

$$\nu' = \nu \left(1 + \frac{v}{c} \right) \quad , \quad (2.45)$$

where ν is the initial laser frequency, v is the relative velocity of the emitter towards the atom, and c is the speed of light.

Like in most spectroscopy experiments, RIS addresses the atoms of interest in the gaseous phase, where the atoms' velocity distributions is described by the *Maxwell-Boltzmann distribution*. The direction of movement is randomly distributed, resulting in a broadening of the

absorption line, namely the *Doppler broadening*. The resulting line shape of the absorbed radiation is a Gaussian profile of the form

$$I(\nu) = I_0 e^{-\left(\frac{\nu - \nu_0}{\nu_0 \nu_w / c}\right)^2} . \quad (2.46)$$

The most probable speed is given by $\nu_w = \sqrt{2k_B T / m}$ while ν_0 is the initial center frequency of the absorption line, and I_0 the maximum intensity. The full linewidth at half maximum of the profile is

$$\Delta \nu_{\text{Doppler}} = \nu_0 \sqrt{\frac{8k_B T \ln(2)}{mc^2}} . \quad (2.47)$$

It is obvious that the width of the Doppler broadening depends on the mass of the atom, the temperature and the frequency of the transition, all being specified by the experimental settings. Naturally, the mass is associated with the isotope of choice. The other parameters T and ν_0 are bound to experimental conditions, like the temperature required for evaporation or the accessible transitions, but can be somewhat altered to manipulate the broadening.

The resulting linewidth for typical settings of $m = 20\text{-}200$ u, $T = 1400\text{-}2000$ °C, and transition wavelengths of $\lambda_0 = 400\text{-}800$ nm are $\Delta \nu_{\text{Doppler}} = 1\text{-}6$ GHz, which is several orders of magnitude larger than the natural linewidth. A special situation arises when the thermal velocity distribution is anisotropic, as presented in chapter 5. In this case, the observed Doppler broadening depends on the effective velocity spread along the laser axis.

Power Broadening

High intensity of the laser radiation can cause *power broadening*, also referred to as *saturation broadening*. For the sake of simplicity, this effect will be explained with the help of a simple two-level system with a lower state $|1\rangle$ and an upper state $|2\rangle$. The final excitation across multiple transitions introduces some additional constraints, but the two-level system offers a good description which applies to most cases. A more elaborate discussion of this topic can be found in [49, 50], while [51] provides a concrete experimental study of power broadening in an atomic two-level system.

As discussed in the previous section, the transition $|1\rangle - |2\rangle$ shows has a Lorentzian shape with a center frequency ν_0 and a natural linewidth of $\Delta \nu_{\text{natural}} = 2\gamma$. One can introduce the dimensionless saturation parameter S_0 , which describes the ratio of the pump rate p_{12} from $|1\rangle$ to $|2\rangle$ and the average relaxation rate r_2 of $|2\rangle$. It can also be interpreted as a standardized intensity

$$S_0 = p_{12}/r_2 = I/I_{\text{sat}} , \quad (2.48)$$

with the saturation intensity

$$I_{\text{sat}} = \frac{\pi \hbar c}{3\lambda^3 \tau} . \quad (2.49)$$

It can be shown that the population of the upper state $|2\rangle$ is given by

$$\rho_2 = \frac{S_0/2}{1 + S_0 + (\nu - \nu_0)^2/\gamma^2} \quad (2.50)$$

$$= \frac{S_0/2}{1 + S_0} \cdot \frac{\gamma^2(1 + S_0)}{\gamma^2(1 + S_0) + (\nu - \nu_0)^2} \quad (2.51)$$

$$= \frac{S_0/2}{1 + S_0} \cdot \frac{\gamma_s^2}{\gamma_s^2 + (\nu - \nu_0)^2} . \quad (2.52)$$

This is again a Lorentzian profile with a full width at half maximum of

$$\Delta \nu_{\text{sat}} = 2\gamma_s = 2\gamma\sqrt{1+S_0} \quad . \quad (2.53)$$

The linewidth depends on the strength of the transition (linked to γ) and the power and spot size of the focused laser in the interaction region. Under typical experimental conditions with powerful, pulsed laser systems as used in the present thesis, $\Delta \nu_{\text{sat}}$ can reach values up to several GHz.

The saturation can be also observed in the correlation between the used laser intensity I and the resulting ionization rate r or extracted ion current. When applying a RIMS excitation ladder, the correlation for any excitation step can be described as

$$r(I) = r_{\text{res}} \frac{I/I_{\text{sat}}}{1 + I/I_{\text{sat}}} + \alpha_{\text{nr}}I + r_0 \quad . \quad (2.54)$$

In this context, the saturation intensity I_{sat} represents the intensity which is needed to obtain half of the maximum ionization rate r_{res} . The linear term $\alpha_{\text{nr}}I$ reflects a contribution from non-resonant ionization. This term vanishes, if the photon energy $E(\nu)$ is smaller than the difference between the IP and any populated atomic state. A constant background of r_0 might be present, caused by non-resonant ionization due to laser radiation of previous steps in the excitation ladder or surface ionization in the ion source.

The Voigt Profile

As a result from the different broadening effects discussed above and the spectral line shape of the laser radiation used for excitation, the finally observed line shapes can differ, depending on the strength of the individual contributions. In the case of one broadening being dominant, the line shape can be well approximated with the respective Lorentzian or Gaussian profile. If the contributions from Lorentzian and Gaussian broadenings are of similar magnitude, the resulting line shape is described by a convolution of a Lorentzian and Gaussian profile, the so-called *Voigt profile*,

$$V(\nu) = (G * L)(\nu) = \int G(\nu')L(\nu - \nu')d\nu' \quad . \quad (2.55)$$

Unfortunately, there is no analytic solution to this integral. Therefore, numerical approximations are used in most cases. The drawback of this method is the high computational effort and the resulting high expenditure of time for fitting one or multiple Voigt profiles to experimental data.

To reduce the computational expense while enabling a precise determination of the line shape, a highly accurate and fast computation of the Voigt profile was implemented² in the present work. The fast algorithm is adopted from the work of Abrarov et al. and uses the Fourier expansion method to calculate points on a Voigt profile with high precision without the need of numerical computation [52, 53]. In this way, the time required for the fit procedure of a single spectrum with about 12-18 resonance peaks, as shown in in chapter 5, could be drastically reduced from multiple hours to only several minutes.

Due to the lack of an analytical solution for the Voigt profile, there is also no analytical expression for the full linewidth at half maximum (FWHM), which is of high relevance in the final experiment. A highly accurate approximation is presented in the work of Olivero

²All computation and data analysis in this work was done using *Wolfram Mathematica 9.0/11.0*

and Longbothum [54]. Using the FWHM of the underlying Gaussian and Lorentzian profile, f_G and f_L respectively, the FWHM of the Voigt profile can be calculated by

$$f_v = 0.5346f_L + \sqrt{0.2166f_L^2 + f_G^2} \quad (2.56)$$

This approximation shows an accuracy of 0.02%, which is smaller than all experimental accuracies and therefore well suited for the data analysis performed in this work.

EXPERIMENTAL SETUP

3.1 Laser System

One key element of a RIMS experiment is the laser system. It defines many important key parameters of the experiment, like accessible ionization schemes, selectivity, experimental linewidth, and ionization rate. As the individual experiments mostly have diverse objectives, the laser system needs to be adapted in order to meet the desired requirements. In some experiments, spectral resolution can be more important than maximum ionization rate, or vice versa. As the RIMS technique is now used for about two decades in the laboratory of the working group LARISSA, the laser system was meanwhile refined, adapted, and steadily optimized to meet further demands. This led to a set of different laser types within the Mainz laser system, which predominantly use titanium:sapphire crystals as active laser medium. The following sections will describe the individual laser types and emphasize their characteristics, similarities and peculiarities.

3.1.1 Standard Titanium:Sapphire Laser

As discussed in section 2.2, titanium-doped sapphire crystals as active laser medium offer a very broad spectral tuning range in the red to infrared region. They also feature the typical benefits of solid-state lasers, as for example stable long-term operation and very little maintenance. This makes pulsed Ti:sapphire lasers perfectly suited for the application in RIMS experiments (see section 2.3), where a large range of wavelengths is needed to allow access to as many chemical elements as possible. The first Titanium:sapphire laser in the group LARISSA were developed by Roland Horn in 2003 [55]. Continuous design updates improved the operation of that prototype, while the actual cavity design remained very similar. This laser type is used in nearly all experiments and is therefore referred to as the standard Ti:sapphire laser, whose basic design is schematically illustrated in figure 3.1 .

A pulsed frequency-doubled *Neodymium:yttrium aluminium garnet* (Nd:YAG) laser is used as a pump source, emitting 532 nm in p-polarization. A lens (PL) focuses the beam into the Ti:sapphire crystal inside a z-shaped standing-wave cavity. The crystals surface is oriented in the Brewster's angle to minimize losses in the p-polarized plane. The two curved mirrors (CM) create a focus of the laser mode inside the central arm, at the location of the crystal. This ensures best spatial overlap with region of high population inversion in the crystal, which is created by the pump beam. On the outer arms of the resonator, towards the *high-reflective* mirror (HR) and the *output coupler* (OC), the mode is almost parallel, ensuring a minimized divergence of the output beam. The reflectivity of the OC is 70–80 %, depending on the desired wavelength. Any uncontrolled optical feedback into the cavity

mode, i.e. from back reflections, would cause mode competition and hinder correct spectral control and proper frequency tuning. Therefore, the output coupler uses a wedged glass substrate, as shown in figure 3.1. The wedge angle of $0.5^\circ - 1^\circ$ between the reflective surface and the exit surface eliminates the possible optical feedback into the laser cavity. In addition, the exit surface has an anti-reflective coating to minimize losses by Fresnel reflection, when the laser beam exits the substrate.

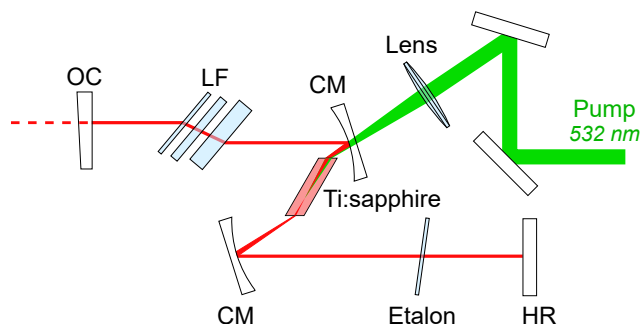


Figure 3.1: Schematic layout of the standard Ti:sapphire laser cavity. The output coupler (OC), curved mirrors (CM) and the high-reflective end mirror (HR) build the z-shaped standing-wave cavity. The pump laser beam is focused into the crystal with an anti-reflectively coated lens. A Lyot filter (LF) and a solid etalon are used for precise frequency selection. See text for detailed explanation.

The accessible tuning range of this laser is 690 – 960 nm with peak output powers at the gain maximum of the Ti:sapphire medium at about 800 nm. The selection of the output wavelength is achieved by a combination of mirror sets, a Lyot filter (LF) and a solid etalon. The mirrors of the cavity use dielectric coatings, which select a region of 50 – 100 nm width. Available are four mirror sets and a broadband mirror set which covers the complete Ti:sapphire tuning range. The Lyot filter uses three quartz plates, features a free spectral range of 100 THz, and narrows the laser output frequency down to about 100 GHz. The etalon is a 0.3 mm thick glass substrate with two plane-parallel, coated surfaces with a reflectivity of 40%. It has a FSR of 330 GHz and reduces the spectral linewidth of the laser to 3 – 5 GHz. The laser linewidth is also influenced by the amplification in the active medium and the number of passes through the frequency selective elements. Therefore, it depends on the wavelength and pump power. If the laser is pumped with high power and operated at a wavelength with high gain, the spectral laser linewidth will be broader, due to a smaller number of passes through the frequency selective elements. In contrast, small pump powers and wavelengths on the edges of the Ti:sapphire emission spectrum result in smaller linewidths. The laser wavelengths are monitored and recorded using a commercial HighFinesse WS6-600 wavelength meter, which uses five precisely calibrated and temperature-controlled Fizeau interferometers to determine the laser wavelength [56] with an accuracy of $\delta \nu(1\sigma) = 200$ MHz.

The specifications of the etalon were chosen to match the spectral linewidth with the typical Doppler broadening within the standard hot ion source. This allows efficient excitation of all velocity classes while operating in in-source geometry. At the same time, it is the limiting factor when higher resolution is desired. To overcome this drawback, a second etalon can be installed in the cavity, reducing the spectral laser linewidth to < 1 GHz [57, 58]. Currently, two types of etalon are used, where the first one is a 2 mm glass substrate with the identical 40% coatings, the second one is a 6 mm thick uncoated YAG substrate with a reflectivity of 8.5% resulting from Fresnel reflection. The first one has a larger FSR, which allows wider tuning without mode jumps, but the higher reflectivity induces more losses

and therefore decreases the output power. The YAG etalon allows higher output powers, but makes frequency tuning slightly more delicate. In any case, for a smooth and stable frequency scan in this *dual etalon* configuration, the thin standard etalon has to be tuned simultaneously with the second, thicker etalon.

The pulsed operation of the system provides high peak powers, which are needed to excite weaker atomic transitions, and allows efficient higher harmonic generation in non-linear optical crystals (see 3.1.4). As each atom inside the ion source has to be irradiated at least once before it leaves the laser interaction region, a high repetition rate is required. Therefore, the Nd:YAG pump laser is operated with a repetition rate of 10 kHz and pumps the water-cooled Ti:sapphire crystal with a power of 10 – 18 W. The output power of the Ti:sapphire laser is 2.5 – 4 W with a pulse length of about 50 ns. Both parameters are strongly correlated with the gain in the crystal and are therefore related to the pump power and desired wavelength. Under optimum conditions, output powers of up to 5 W and more could be demonstrated. As RIMS needs a set of synchronized laser pulses, temporal control of the laser output is required. An optional Pockels cell acts as a Q-switch and allows a precise and reliable way to delay the individual laser pulses by up to several hundreds of nanoseconds. An alternative approach is the variation of the individual pump power for each Ti:sapphire laser, which directly correlates to the gain and the delay between pump and laser pulse. This can be achieved by a combination of a $\lambda/2$ -waveplate and a polarizing beam splitting cube in the pump beam or by detuning the focusing of the pump beam into the Ti:sapphire crystal. Although this technique is reliably working, it is limited by the upper limit of reasonable pump power on one side and a significant loss in output power of the Ti:sapphire laser on the other.

The standard Ti:sapphire laser allows reliable and stable long-term operation, fast setting of new wavelengths, as well as continuous frequency tuning across a spectral range of about 300 GHz. Typically, after about 1 - 3 hours of warm-up time, all crucial parameters, i.e. the ISST parameters (see section 2.3.1), are very stable and the system can be operated for up to 24 hours and more without any further re-optimization. All this, led to an exceptional success and acceptance of the laser system within the RIMS community and gave rise to a multitude of international collaborations of the Mainz university LARISSA working group. Presently, this type of laser system is found at the majority of on-line radioactive ion beam facilities worldwide [5, 3] and in several other experimental projects [8]. In the framework of the present thesis, the design of standard Ti:sapphire laser was improved further. The footprint on the optical table was significantly reduced while additional features like optional intracavity doubling (see section 3.1.4) were added.

3.1.2 Grating-Assisted Ti:Sapphire Laser

The grating-assisted version of the standard Ti:sapphire laser provides continuous frequency tuning across the entire amplification range of the active medium. This is very advantageous for a variety of experiments, for example when conducting spectroscopy on Rydberg series or fast development of new ionization schemes. As shown in figure 3.2, the combination of a Lyot filter and an etalon as used in the standard laser is replaced by a diffractive blaze grating (BG), which selects the exact output frequency of the laser. The grating on a motorized rotation stage substitutes the high reflective end mirror. The grating is placed in Littrow geometry, reflecting the first diffraction order back into the cavity. Although the grating is optimized for this geometry and offers 80 % reflection into this order, the zeroth order is still a significant loss channel. This limits the maximum output power of the laser correspondingly. A prism beam expander (BE) in front of the grating enlarges the laser mode. It uses four anti-reflective coated prisms to expand the beam by a factor of about 8 in

horizontal direction. This lowers the intensity on the delicate grating surface and increases the number of illuminated grooves, which increases the spectral selectivity. Currently, a grating with 1740 lines/mm and a gold coating is used and a spectral linewidth of $2 - 3 \text{ GHz}$ can be achieved. A detailed discussion and analysis of the system and a full characterization can be found in the PhD thesis of C. Mattolat [28] and in the master thesis of P. Naubereit [59].

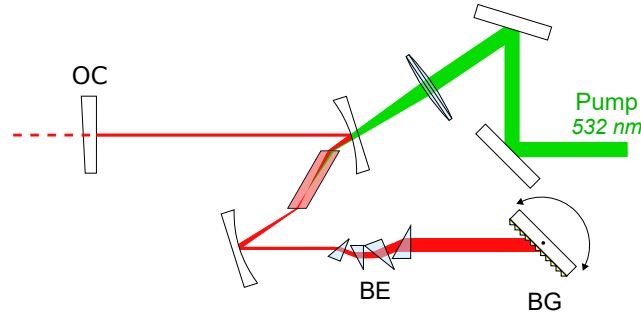


Figure 3.2: Schematic layout of the grating laser cavity. A diffractive blaze grating (BG) in Littrow geometry is used for frequency selection. A prism beam expander (BE) is used to increase the horizontal size of the laser mode, to increase spectral selectivity and avoid damaging of the sensitive grating surface. Continuous tuning is achieved by rotating the grating with a high-precision stepper motor. See text for detailed explanation.

The incident angle on the grating can be changed with a computer-controlled, high-precision stepper motor, tuning the wavelength as given by formula 2.39. It is evident, that for a constant rotation speed, the change in frequency will vary. While this is negligible for narrow range scans in the order of a few cm^{-1} , this has to be taken into account when performing wide frequency scans across the full tuning range.

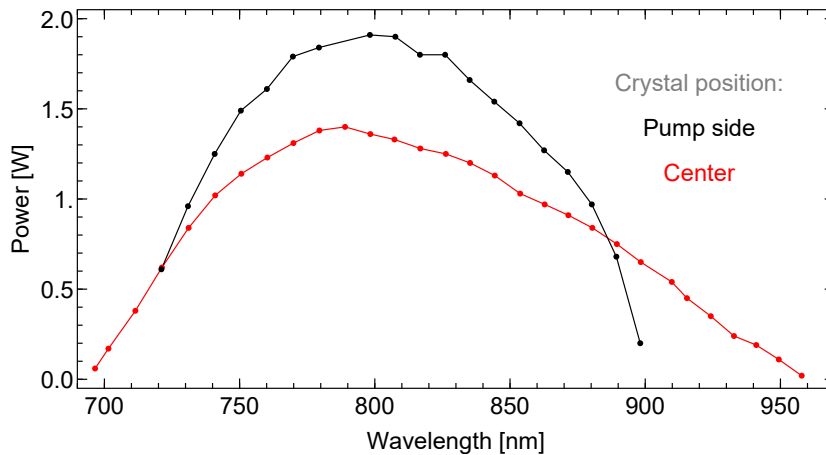


Figure 3.3: Tuning range of the grating-assisted laser for different positions of the Ti:sapphire crystal. Courtesy of P. Naubereit.

Figure 3.3 shows the output power across the accessible frequency range, taken at a constant pump power of 14.8 W . The position of the Ti:sapphire crystal within the central arm shows a clear influence on the maximum output power and the accessible tuning curve, which is discussed in the following paragraph. In general, the grating-assisted laser has lower output powers than the standard Ti:sapphire laser, about a factor of 2 lower at the peak and even worse towards the edges, due to the higher losses induced by the

grating and the prism beam expander. Degeneration of the grating, due to the relative high light intensities in the cavity, can lower the output power even further. As the gain of the Ti:sapphire crystal changes along the spectrum, the laser pulse length and the delay of the laser pulse in reference to the pump pulse change significantly during wide range scans. The latter has to be compensated by manual adjustment of the synchronization to the other lasers.

The influence of the Ti:sapphire crystal's position in the central arm on the output power applies to all laser types presented here, but is of special relevance for the grating-assisted laser. In the standard laser, the crystal is placed closer the curved mirror on the pump beam side as shown in figure 3.1. This allows the usage of higher pump powers as the pump beam is already absorbed partially before it reaches its focal point. Otherwise, the high laser intensity can cause critical damage of the crystal and its surfaces. Maximum output powers of the laser can be achieved in this configuration. If the crystal is placed exactly in the center between the two curved mirrors, the gain medium covers a region where the radius of laser mode is significantly smaller due to its focus. The waist of the pump beam stays the same. As a result, the laser mode overlaps only with the central part of the pump beam which exhibits a Gaussian profile in its cross section. This region offers the strongest inversion in the crystal. Consequently, the laser light experiences a stronger gain per pass. On the other hand, the overall output power will be slightly reduced, as a significant part of the deposited pump beam power does not overlap with the laser mode in the Ti:sapphire crystal and therefore is lost. The stronger gain leads to an extension of the accessible spectral tuning range on the low and high frequency side which is of special relevance for the grating laser as the losses from the grating and the beam expander must be compensated. As discussed in section 3.1.1, this effect has also an influence on the spectral linewidth of the laser radiation.

3.1.3 Injection-Locked Ti:Sapphire Laser

When aiming for smallest spectral linewidth to obtain best resolution in the experiment, the use of standing wave cavities pose an unfavorable limitation. Figure 3.4 illustrates the so-called *spatial hole burning* phenomena [60, 61, 62]. As a longitudinal standing wave of a cavity mode with order n has anti-nodes with a spacing of $\lambda/2$, the inversion in the Ti:sapphire crystal is not evenly depleted. Distinct areas of depleted and not-depleted inversion arise with an equal spacing of $\lambda/2$. In the center of the cavity, where the crystal is located, the standing waves of order $n \pm 1$ have their anti-nodes on exactly the locations, where the cavity mode of order n has its nodes. Therefore, the not-depleted inversion will always be available to amplify the neighboring cavity modes, making their suppression very difficult.

To accomplish the goal of operation with only one longitudinal cavity mode oscillating, referred to as *single longitudinal mode* or *single mode* (SM) operation, the formation of a standing wave pattern must be eliminated. This can be achieved by using a ring-shaped cavity, causing the resulting light wave to propagate steadily through the ring cavity which leads to an even depletion of the inversion along the entire crystal length. Due to microscopic vibrations, acoustic noise, and thermal fluctuations, it is complicated to keep the pulsed laser operating on the same cavity mode for each pulse. To overcome this problem, light from a stable narrowband *continuous wave* (CW) laser is injected into the cavity. These photons act as seed and cause an amplification cascade when the inversion in the active medium is built up by the pump pulse. For an efficient injection and lasing process, the cavity length has to be kept resonant to the frequency of the narrowband source. Therefore, one mirror is mounted on a linear piezo actuator and an electronic locking system stabilizes the cavity.

The basic layout of the injection-locked laser is shown in figure 3.5. The development

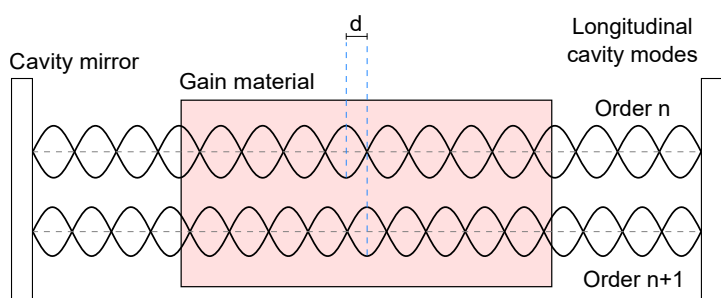


Figure 3.4: Schematic illustration of the hole burning in a simplified standing wave cavity. Neighboring longitudinal modes show different positions of their anti-nodes, resulting in different areas of the corresponding depletion of inversion inside the gain material. In the center of the cavity, the anti-nodes are separated by $d = \lambda/4$, meaning that the anti-nodes are located at the position of the nodes of the neighboring longitudinal mode. See text for further description.

and characterization of this design can be found in [63, 28, 29]. A stabilized *external cavity diode laser* (ECDL) acts as master laser and provides narrowband CW light. The sensitive laser diode has to be protected from the intense radiation of the Ti:sapphire laser, which reaches peak powers which are several orders of magnitudes higher. Therefore, the light passes a series of optical diodes (OD), which allow light transmission only in direction towards the Ti:sapphire laser. The CW light enters the Ti:sapphire cavity through the output coupler (OC). The ring cavity is bow tie-shaped and uses similar angles and curved mirror distances as the standard z-shaped cavity. The piezo-mounted mirror (PM) enables the precise tuning of the cavity's total length on a nm-scale. A highly amplified photo diode (PD) detects the tiny fraction of the light which leaks through the curved mirror. This signal is used by a commercial locking device (TEM LaseLock) to stabilize the cavity length via the piezo-mounted mirror to achieve resonance to the CW light. The voltage applied to the piezo-mounted mirror is modulated with a high frequency of about 42 kHz and a very small amplitude. This so-called *dithering* induces a corresponding modulation of the photo diode signal. A lock-in amplifier and a PID-regulator process the dither signal and the feedback of photo diode and stabilize the laser cavity on maximum resonance. For a correct response of the piezo actuator, it is crucial to choose a dither frequency well below the mechanical resonance frequency of the piezo actuator. As moved weight on the actuator lowers the resonant frequency of the system, a small 0.5" mirror was directly glued to a small mounting adapter to reduce the additional weight. The mirror features a high-reflective broadband coating which covers the complete Ti:sapphire tuning range. The other cavity mirrors are the same as for the standard z-shaped laser, which ensures optimum compatibility between the laser systems.

The typical pump powers are similar to those of the standard Ti:sapphire laser. The output powers are strongly depending on the alignment of the seeding CW mode. Without injected CW light, the laser radiation is emitted in both directions of the ring cavity, resulting in two output beams. Under optimum conditions, the injected CW light causes all of the available output power to be transferred into the seeded cavity mode, resulting in the emission of only one single laser beam. Correspondingly, this situation is referred to as a seed efficiency of 100%. In some cases, the total output power can even be higher than for a standard Ti:sapphire laser at similar pump power, as the lack of frequency selective elements reduces losses inside the cavity. Another consequence of the better amplification and the initial

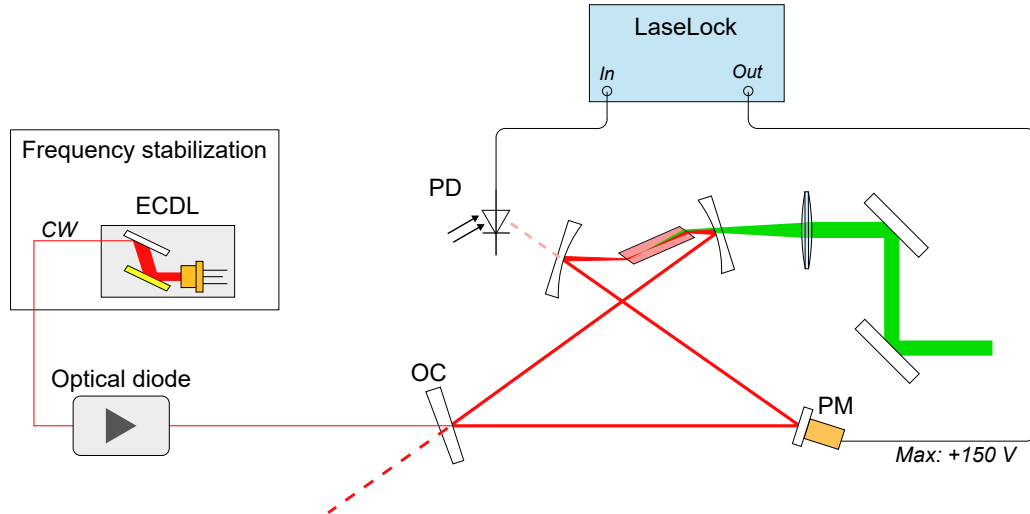


Figure 3.5: Schematic layout of the injection locked Ti:sapphire laser system. The narrowband CW radiation (thin, red) of an external cavity diode laser (ECDL) is injected into the bow tie cavity through the output coupler (OC). A commercial electronic locking device (LaseLock) uses the signal of a photo diode (PD) to stabilize the laser cavity to a resonant length by moving a piezo-mounted mirror (PM). See text for detailed explanation.

power in the seeded laser mode, which is already present when the inversion in the active medium starts to build up, is a relatively short delay between pump pulse and actual laser pulse. For this reason, a separate pump laser is required to synchronize the laser pulse of the injection-locked laser with the other excitation steps. If a TEM_{00} pump laser is used, the waist of the focus is much smaller, which can be helpful to avoid exciting other cavity modes. To avoid damaging the Ti:sapphire crystal surface with the high intensity of the small laser focus, the pump power has to be attenuated by about a factor of three to about 5 W. However, the loss in output power is somewhat compensated by the far better spatial overlap of pump beam and cavity mode inside the Ti:sapphire crystal. The narrowband CW ECDL system is described in detail in [43, 64, 47]. As laser diodes typically allow only a few nm tuning range, the investigated atomic transition must be properly chosen to match the accessible wavelength. This drawback can be overcome if a CW Ti:sapphire master laser is used [29].

The effective spectral linewidth of the external cavity diode lasers used in this work is dominated by the remaining jitter of the locking system, which is typically 3 MHz. Nevertheless, the spectral linewidth of the pulsed injection-locked laser is determined by the length and finesse of the laser cavity, Fourier-limitation and additional broadening effects stemming from the locking electronics and possibly chirp effects. In total, these result in a spectral linewidth of 10 – 20 MHz [29]. In comparison, the 3 – 5 GHz spectral linewidth of the standard Ti:sapphire laser's output is created by a total number of 30 - 50 individual cavity modes of different strength. Considering the similar output powers of injection-locked and standard laser, it becomes obvious that the latter provides a significantly higher spectral power density. This fact leads to a particularly high efficiency of nonlinear processes during frequency conversion, as well as significantly more pronounced power broadening when compared to broadband radiation.

3.1.4 Frequency Conversion

Higher harmonic generation (HHG) and frequency mixing with nonlinear optics is used to expand the accessible wavelength range of the laser system. This technique is well understood and is described in a variety of books [65, 22]. The basic principle is a nonlinear polarization response in a *nonlinear optical* (NLO) medium to the oscillating electromagnetic field $E(t, \mathbf{z})$ of the initially entering laser radiation. The medium's polarization density $P(t, \mathbf{z})$ can be described by the Taylor series

$$P(t, \mathbf{z}) = \varepsilon_0(\chi^{(1)}E(t, \mathbf{z}) + \chi^{(2)}E^2(t, \mathbf{z}) + \dots) \quad , \quad (3.1)$$

where $\chi^{(n)}$ is the susceptibility of the order n . In the general case of two interacting photons, $E(t, \mathbf{z})$ can be written as

$$E(t, \mathbf{z}) = E_1 \sin(\omega_1 t + \mathbf{k}_1 \mathbf{z}) + E_2 \sin(\omega_2 t + \mathbf{k}_2 \mathbf{z}) \quad . \quad (3.2)$$

As the nonlinearity of the medium implies $\chi^{(2)} > 0$, the corresponding quadratic term $E^2(t, \mathbf{z})$ gives rise to polarization density modulations, which include sum and difference frequencies, $\omega_1 + \omega_2$ and $\omega_1 - \omega_2$. At all points of the medium, the modulated polarization density induces oscillating electromagnetic fields, which can interfere constructively along the medium, resulting in a macroscopic beam of laser radiation. The constructive interference of the field with frequency $\omega_3 = \omega_1 \pm \omega_2$ requires the correct phase relationship between the electromagnetic fields, which is called the *phase matching condition*

$$\mathbf{k}_3 = \mathbf{k}_1 \pm \mathbf{k}_2 \quad . \quad (3.3)$$

In general, chromatic dispersion leads to a mismatch. The birefringence of a NLO crystal can be used to overcome this problem and to achieve correct phase matching. Commonly, two approaches are used: the so-called *noncritical phase matching*, where the temperature of the crystal is adjusted to match the refractive indices for the different polarizations; and the *critical phase matching*, where proper angular orientation of the crystal is used to adjust the extraordinary refractive index. The situation is called type-I phase matching if both initial photons have the same polarization, perpendicular to that of the resulting photon. In type-II phase matching the polarizations of the initial photons are perpendicular.

In the present work, critical phase matching and type-I phase matching is applied using beta barium borate (BBO) and lithium triborate (LBO) crystals as NLO material. The incident laser beam is focused into the NLO crystal. The outgoing laser beam passes a spherical and a cylindrical lens to optimize its beam shape. Due to the high intensities of the pulsed laser light, the process is quite efficient and reasonable powers can be obtained in second harmonic generation (SHG), third harmonic generation (THG) and fourth harmonic generation (FHG). Figure 3.6 visualizes the corresponding wavelength regions and typical maximum power levels. The conversion efficiency for SHG can reach up to 30 % and about 7 % for THG and FHG.

A recent development is the use of difference frequency generation (DFG) with the laser system, allowing access to the orange yellow-orange part of the visible spectrum. This technique is quite common for low repetition rate lasers with repetition rates well below 1 kHz and pulse energies in the range of several mJ. However, this technique is rarely used with repetition rates above 1 kHz, as the pulse energies are significantly lower and the typical pulse length is longer. This leads to relatively low powers of the resulting difference frequency wave, as its power is proportional to the product of the intensities of both initial waves. Nevertheless, powers of 10 mW were obtained with the LARISSA laser system [66, 67]. This is sufficient to saturate strong optical transitions and expands the

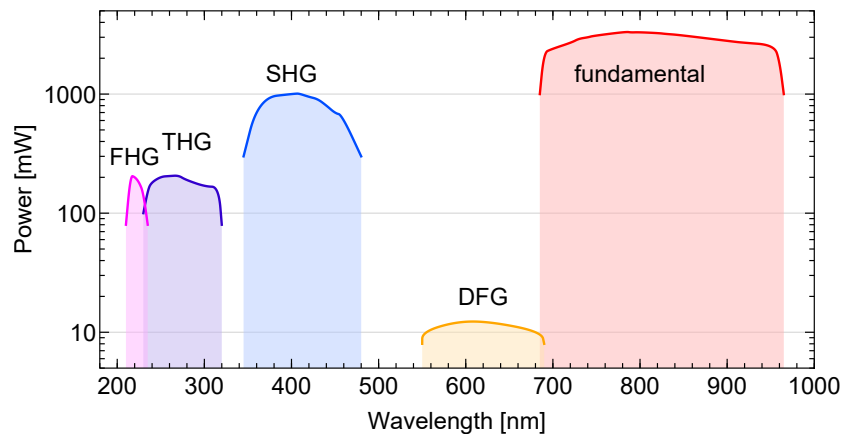


Figure 3.6: Accessible wavelength regions of the laser system in combination with frequency conversion. See text for details.

accessible wavelength region across the yellow-orange area of the visible spectrum.

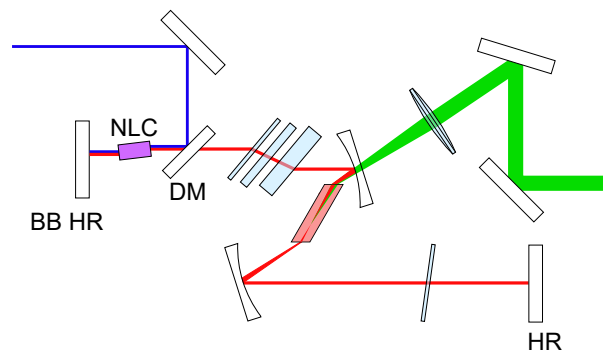


Figure 3.7: Schematic Layout of a standard Ti:sapphire laser cavity with intracavity SHG. The nonlinear optical crystal (NLC) is placed inside the laser cavity. A high-reflective broadband mirror (BB HR) replaces the output coupler and guarantees overlap of both SHG beams. A dichroic mirror (DM) separates the frequency-doubled light.

Some experiments may require a very high intensity in the higher harmonics regime, due to inefficient beam transport or involvement of weak atomic transitions. In those cases it is beneficial to use intracavity SHG as it offers much higher output powers. Here, the nonlinear crystal is placed inside the laser cavity. A position close to the end mirror or output coupler ensures highest intensities, as the laser mode is focused at these points. Figure 3.7 shows a sketch of the basic layout. The output coupler is replaced by a mirror which offers high reflectivity for the fundamental and frequency-doubled light, maximizing the power of the fundamental wave inside the laser cavity. The resulting high intensity and the continuous interaction between standing wave and the nonlinear medium leads to output powers of 1 – 3 W of frequency-doubled light [68, 67]. The photons of the laser mode pass the NLO crystal in both directions¹, resulting in two frequency-doubled laser beams which exit the NLO crystal on opposite sides. To overlap both beams, the nonlinear crystal is placed next to a mirror, which is high reflective for the fundamental and the frequency-doubled light. A dichroic mirror (M) installed under 45° separates the frequency-doubled laser beam from

¹When interpreting the laser mode as a wave, the anti-nodes of the standing wave interact simultaneously with the NLO material at multiple, spatially fixed locations inside the crystal.

the fundamental cavity mode. For this cavity setup, the conversion to frequency-doubled light can be seen as a power-dependent output coupler. It is mandatory to keep the SHG well optimized, to avoid too high power of the fundamental laser mode inside the cavity, which may damage the optics. Therefore, tuning and optimizing must be done carefully.

3.2 Mass Spectrometer

The experiments were performed using two different mass spectrometers at Mainz university. Each one was designed for a specific purpose, steadily improved and modified over the last years. The following sections give information about these two systems, their characteristics, differences and advantages.

3.2.1 RISIKO

The largest mass spectrometer setup of the LARISSA group is the RISIKO mass separator. The name is a German acronym for *Resonanzionisationsspektroskopie in kollinearer Geometrie*². Built in 1990, it was used for collinear spectroscopy and trace analysis on radioactive strontium [69]. After the end of the first project, the objectives changed and the collinear laser interaction region was dismantled. The separator frontend is nearly identical to the General Purpose Separator (GPS) at the on-line RIB facility ISOLDE (Isotope Separator On Line DEvice) at CERN [70, 71]. Figure 3.8 shows a sketch of the setup in its current status. The whole apparatus is operated at vacuum pressures in the 10^{-7} mBar region, which is maintained by a set of three turbomolecular and rotary vane pumps. It uses the same ion source frontend and initial beam-shaping ion optic geometry as the ISOLDE separator together with a 60° sector field magnet. The precisely tuned laser radiation enters the vacuum vessel through a window on the magnet and is focused into the ionizer tube of the ion source. After the selective resonance ionization process, the ions are extracted and accelerated to 30 keV. Ion optics shape the beam and ensure best transmission. The sector field magnet separates the masses spatially, before the ions of interest are detected by a Faraday cup (FC2) or a secondary electron multiplier (SEM), which allows single ion counting. The system characteristics include an isotopic abundance sensitivity of $S \approx 10^{-4}$ and a mass resolution of $R = \frac{M}{\Delta M} \approx 1000$.

Due to RISIKO's similarity to the ISOLDE separators, a variety of development activities can be carried out in the off-line laboratory in Mainz, as the tight beam time schedule at ISOLDE prohibits time consuming tests. This covers for example developments, tests and characterizations of ion source components, new ion optics, new techniques, as well as identification of new excitation schemes for resonance ionization. A full description of the latest status of the RISIKO mass separator can be found in the dissertation of S. Richter [44], which provides a comprehensive overview of all technical details. The recent addition of ion optics for beam re-focusing after the magnet section is described in [72]. Information on previous states of the setup can be found in earlier works like [69, 73]. The following subsections give a quick overview of the system and highlight the parts of special relevance as well as the new developments for this work.

Ion Source

The ion source heats and vaporizes the initial sample, which is the basic prerequisite for laser ionization. Depending on the experiment, ionization is achieved by surface ionization or resonant ionization through precisely tuned laser radiation. Figure 3.9 gives an overview

²English: Resonance ionization spectroscopy in collinear geometry

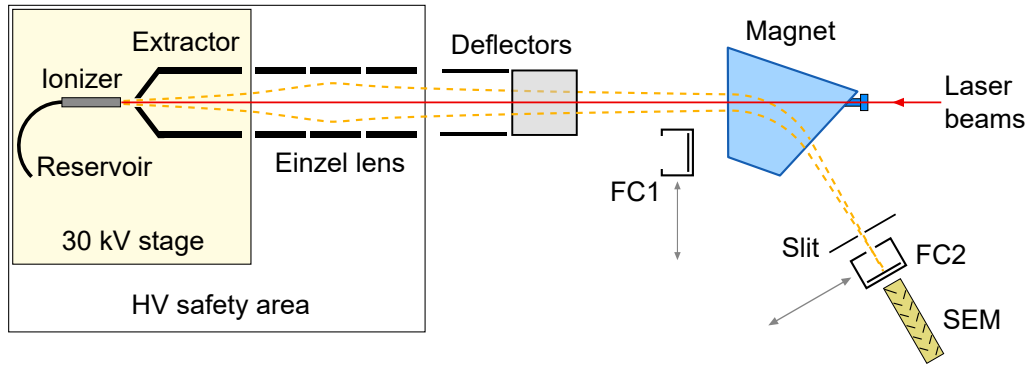


Figure 3.8: Schematic layout of the RISIKO mass separator. The ions are extracted from the ionizer and accelerated to 30 keV by a two-stage extraction. After beam-shaping, the ions enter the sector field magnet, where species with different momentum, respectively mass are spatially separated. A slit aperture selects the species of interest, which is then detected via a Faraday cup (FC2) or by a secondary electron multiplier (SEM). See text for a detailed description.

of the source components. The core parts of the RISIKO ion source are the larger ionizer tube (red) and a thin long reservoir capillary. The *ionizer tube*³ has an inner diameter of 2.5 mm and a length of 35 mm. Due to its high melting point and good machinability, tantalum is the standard material for the ionizer tube. However, some experiments favor other materials because of the sample's chemical and physical properties. Materials like graphite or tungsten can offer benefits in terms of resorption time or work function and the related surface ionization rate. Also quite exotic materials like special ceramics, coated metals or glassy carbon were investigated, but advantages apply only to some specific sample types and in most cases go along with higher price, fragility and/or bad machinability [73, 74, 75]. These aspects do usually not justify regular application.

The ionization tube is resistively heated to high temperatures of up to 2400 °C, corresponding to heating currents of about 300 A for the standard tantalum tube. The front and the back mounting parts are constructed to serve as current feeds. The mounting plate in the front (yellow) is connected to the grounded vacuum flange and is shaped in a special profile to reduce heat dissipation on the tip of the ionizer. The back of the ionizer tube is sitting in a mounting adapter made of tantalum, which also holds a heat shield (blue) for the tube. The electric current enters the vacuum chamber via a thick copper rod and reaches the rear mounting adapter by a set of joint tantalum strips (green). The latter serve as a spring, compensating thermal expansion and keeping the ionizer tube in place. The mount is hold in place by graphite elements, which hinder cementing at higher temperatures.

The thin reservoir capillary (gray), also made from tantalum, serves as an independently heated sample reservoir and is connected to the back of the ionizer tube. It is heated by an additional current which flows through the joint tantalum springs and the back of the reservoir capillary. For historical reasons, it is also called mass marker, which goes back to the original ISOLDE setup, where the reservoir capillary is used to supply additional samples of chosen elements to provide a reference in the complex mass spectra observed under on-line conditions. However, it is exclusively used as a sample reservoir in the RISIKO setup, containing the actual sample of interest. Its inner diameter is 1.1 mm and it is about 16 cm long, whereas it is tightly squeezed in the center to reduce the active volume to its half. Because of its smaller cross section in comparison to the ionizing tube, the maximum heating current is 100 A while temperatures up to 2100 °C can be reached. The sample is

³Also called hot cavity, transfer-line or line

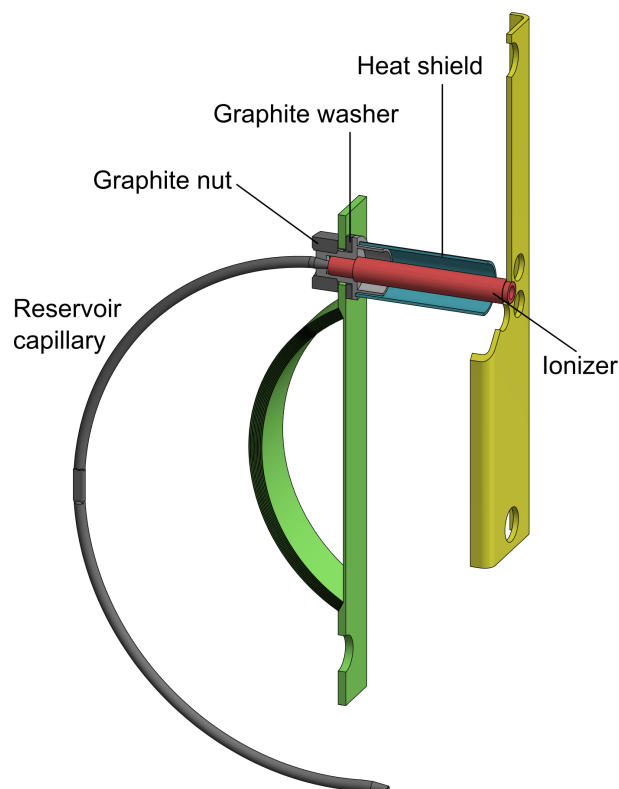


Figure 3.9: Technical drawing of the ion source. See text for description.

usually a small piece of metallic foil on which a few μl of liquid solution, containing the atoms of interest, has been evaporated. During the heating process, the material of the foil acts as reduction agent and prevents the formation of oxides, ensuring the evaporation of the sample into neutral atoms. Afterwards, the foil is folded and placed inside the *reservoir capillary* or alternatively directly inside the ionizer tube.

Solid copper connectors are used to provide the high heating currents which are required. Due to the low melting point of Cu, the must be water-cooled, causing temperature gradients, particularly in the region of the joint between ionizer tube and reservoir capillary, as well as at the front tip of the ionizer tube. The temperature distribution across the ion source components is of special relevance, as condensation of high melting samples on cold spots or thermal damage of the ion source components must be avoided. This aspect is discussed in more detail in section 4.3.5, as it was of relevance for the conducted efficiency measurements on palladium. Recent developments aim to improve the homogeneity of the heat distribution across the ion source by reducing the thermal black body radiation of the individual components of the ion source via proper choice of the used material and reduction of surface area [76, 72].

Ion Optics

The ion source unit and the vacuum housing up to the extractor is kept on +30 kV potential, which allows the rest of the vacuum chamber to be operated on ground potential. For safety reasons, all dangerous high voltage parts are located enclosed in a secure high voltage cage inside the LARISSA laboratory. The extraction design is adopted from the ISOLDE setup. It is a two-stage extraction in Pierce-geometry [77]. The distance between the exit of the ionizing tube and the extraction electrode, kept on +15–20 kV, is 4 cm. After extraction, the ions enter the Einzel lens with a kinetic energy of 30 keV. The Einzel lens unit is operated on 9–13 kV

and focuses the ion beam into the magnet, as illustrated in figure 3.8. Subsequently, two electrostatic deflectors, located directly behind the Einzel lens, are used to correct vertical and horizontal deviations of the ion beam from optimum. Mass separation is achieved by the 60° sector field magnet, which can provide a magnetic field up to 0.6 Tesla. In front of the detection, a horizontal slit in the focal plane of the magnet assures proper mass selection. All electrode voltages and the magnet current are remotely operated by a controlling computer.

Detection and Data Acquisition

As the vacuum chamber offers a variety of additional ports, the setup can be easily adapted for different requirements. The standard setup, which was used in this work, includes four different detectors. A wire scanner in front of the slit aperture at the focal plane of the magnet gives information on the ion beam width and shape along the horizontal axis, as well as intensity, and mass separation for a range of five to ten atomic mass units. These parameters are very useful, while optimizing the ion optics for best transmission and optimum mass resolution. As the effective detection area is small, the scanner's sensitivity is not very high and ion currents above 100 pA are needed for a sufficient signal. More sensitive detectors are two Faraday cups, one located in front of the magnet and one closely behind the slits. Both can be moved in and out of the ion beam path by pneumatic actuators. The first cup (FC1) has a large aperture of 30 mm. Its detection electrode is radially segmented and can be used to determine the size of the full ion beam in front of the magnet. As the second cup (FC2) is located behind the slit, it detects only the mass of choice and is the most frequently used detector in the RISIKO setup. It can measure currents as low as 40 fA and up to the μ A-region. Its aperture can be changed to meet the experimental requirements. During the experiments conducted in this work, the standard entrance aperture with an opening of 3 mm in diameter was installed. A complementary detector for lowest currents below the Faraday cup detection limit is the secondary electron multiplier (SEM). It is connected to a discriminator to allow for time resolved single ion counting, from which also the time structure of the impinging ion current can be extracted.

Nearly all experimental settings of the setup are computer controlled. The same PC also handles the data acquisition and first level data processing. All methods and the user interface are implemented in National Instrument's system design software Labview (currently version 2014). As the experimental system is highly flexible and its application is under constant development and optimization, the software is steadily modified in parallel. New features, which have been developed and improved in the framework of this thesis are for example a parameter monitoring system, which automatically takes safety precautions if required and an automated shutter control for the laser beams.

LIST

The *laser ion source and trap* (LIST) constitutes a special unit for the ion source, which adds the ability to suppress surface ionized species stemming from the ionizer [78]. The concept is particularly valuable for on-line ion sources, where a positive high energetic ion beam, most often composed of protons, hits a target material. The induced nuclear reactions, including fission, fragmentation, and spallation reactions, produce a large variety of isotopes from a wide range of chemical elements. As the production rates vary over several orders of magnitude with strong decrease towards the most exotic short-lived isotopes far off stability, an experiment on a rare isotope of interest can easily be impaired by strong background of surface ionized isobaric contaminations. Likewise, the same complication may arise in off-line spectroscopy experiments, in particular if carried out on smallest samples. To overcome this problem, the LIST offers an ionization volume which is not enclosed by hot

surfaces while surface ionized species from the hot ionizer tube are efficiently suppressed. It serves as add-on to the standard ion source where it is installed in front of the ionizer exit. Figure 3.10 shows a technical drawing of the current standard LIST as designed and used at Mainz University. Its repeller electrode allows the suppression of positive ions originated from the ionizer. The laser ionization volume inside the LIST is thus completely decoupled from the volume inside the hot ionizer tube. The investigation and characterization of the LIST was a key topic in the framework of previous PhD theses and is therefore well described in several dissertation theses [44, 79, 73, 80]. Its successful application at ISOLDE proved the usability under on-line conditions and demonstrated outstanding suppression of surface ionized isobaric contamination [81, 82, 83].

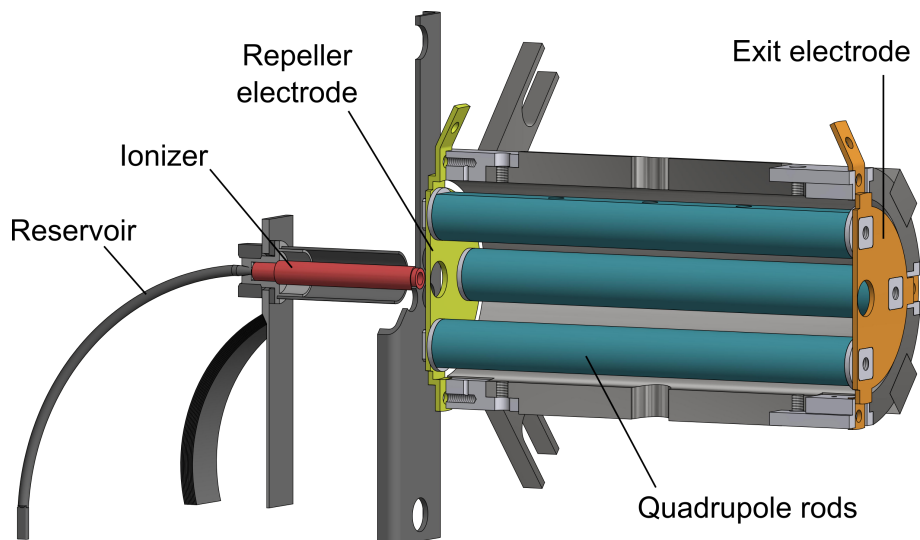


Figure 3.10: Technical 3D illustration of the conventional LIST unit installed in front of the ion source. The background due to surface ionization is strongly suppressed by the repeller electrode (yellow). The selective resonant ionization process takes place inside the linear quadrupole structure (blue), where the electrical RF field confines the transversal motion of the ions. The strong electrical field of the extraction electrode is shielded by the grounded housing and the exit electrode (orange).

The following description will describe the basic operation and highlight the parts of special relevance for this work and further development. The main parts of the LIST are the entrance electrode (yellow), a linear Paul trap (blue) [84, 85], the exit electrode (orange) and the housing. Its total length is 10 cm and the outer diameter of the housing is 5 cm. The circular entrance electrode, which is usually operated on a positive potential of +10 V, is located on the end facing towards the exit of the ionizer tube. This potential repels all positive ions from the ionizer tube, preventing them from entering the internal LIST volume. Neutral species can enter this region of the LIST structure, where they are exposed to a transversal radio frequency (RF) electric quadrupole field. Exposed to laser radiation, the neutral atoms can be resonantly ionized. In the LIST, they experience only a very weak electrical field instead of the strong field in front of the extractor without LIST. The field along the longitudinal axis is well below 10 V/cm , which is clearly exceeded by the transverse RF field with 20-100 V across the free field radius of 1 cm, which is usually still negligible regarding influences on atomic levels. In comparison, the electric field in the extraction region is about 3000 V/cm , which is not negligible anymore. Additionally, the corresponding spread of the maximum accelerating energy of the ions to lower values would result in a significant decrease in mass resolution. The oscillating quadrupole field confines the ions' lateral motion, increasing the ion transmission of the LIST unit. Once the ions reach the exit

electrode, they experience the acceleration of the extraction field penetrating through the 7 mm exit opening. The distance to the extraction electrode of 4 cm is the same as in the regular ion source setup.

The LIST can be operated in two characteristic modes, depending on the voltages on the entrance electrode. As described in the previous paragraph, if positive voltages of +5 V to +15 V are applied to the entrance electrode, it acts as a repeller and the selective laser ionization happens solely inside the LIST volume. In contrast, if the entrance electrode is on a negative potential, typically -10 V to -100 V, all positively charged species from the ionizer are extracted and transmitted through the LIST. It basically works as an ion guide (IG) and the system behaves very similar to standard laser ion source operation without the LIST. Correspondingly, these two operation modes are referred as LIST-mode and IG-mode. Figure 3.11 visualizes the relation between the ion current and the voltage of the repeller electrode. The red curve represents the ion current with lasers, the green curve the background which was recorded when the laser beams were blocked. The two shaded areas indicate the two different operation modes. Obviously, the LIST-mode offers a superior signal-to-noise ratio.

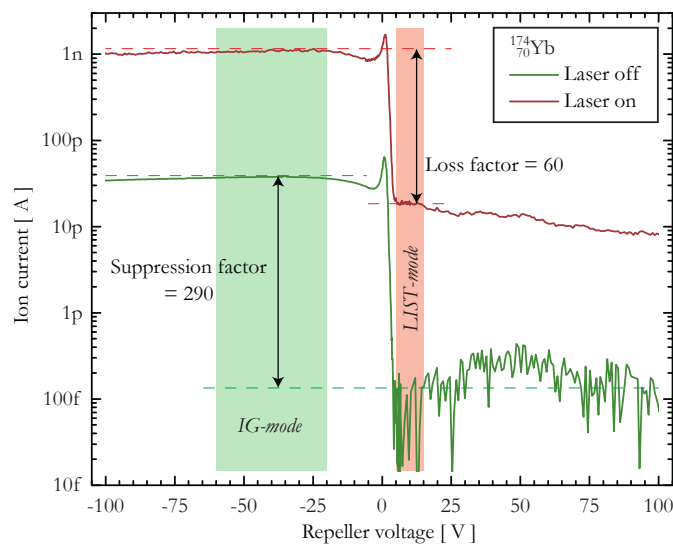


Figure 3.11: LIST repeller scans with the laser system tuned for resonance ionization of ytterbium.

In LIST-mode operation, positive repeller voltages of 5-15 V lead to a strong suppression of the surface ionized background. Graph adopted from [44].

The graph also shows two characteristic aspects of the LIST which are of special relevance for the individual experiments. The first one is the suppression of the laser-independent background, in particular caused by surface ions, in the LIST operation mode as indicated in figure 3.11. The background suppression factor between the IG-mode and LIST-mode is usually > 200 , but is clearly depending on the background level in IG-mode and the detection level in LIST-mode. The second characteristic parameter is the loss factor in the laser ionization signal if switching from IG-mode to LIST-mode operation. It is favorable to keep this number as small as possible, but obviously, the number of ions created inside the LIST volume will always be smaller than in IG-mode operation. This loss factor depends strongly on the optimization of the mass separator and especially the spatial alignment of the laser beams. Therefore, typical values range between 50 and 400.

The LIST unit was already used under off- and on-line conditions at Mainz University and at ISOLDE CERN. It is continuously refined, including several modifications. Measurements pointed out, that the ionization in the last part of the linear quadrupole does hardly contribute to the ion signal. This can be explained by the particle density, which roughly decreases by

$1/r^2$, while increasing distance to the ionizing tube exit r . Therefore a shorter LIST with 5 cm length was developed lately and tested at Mainz University. Recent experiments show no experimental drawbacks to the standard LIST, whereas the installation of the smaller device is much more convenient. Another version implies quadrupole rods of only 1 mm diameter, minimizing surfaces, which can cause contamination by radioactive decay of deposited radioisotopes. Another important development is the possible mass selective operation of the linear quadrupole trap, which was demonstrated in [44]. New findings and further developments in the framework of the present thesis will be presented in section 5.

3.2.2 MABU

The second RIS mass spectrometer at the LARISSA group is the Mainz atomic beam unit (MABU). It is a small table-top apparatus, developed for spectroscopic experiments and trace analysis. The first version was based on the apparatus used in the Ca-41 experiment [86, 87, 88, 89]. Its basic design, operation and upgrade to the present status are described in detail in the PhD thesis [47] and the diploma theses [90, 91]. As the MABU is well described in these references, the following section will just give a brief overview of the design, operation and key aspects, which are of special relevance for this work.

The design's primary goal is a compact footprint while providing access to two different ionization geometries. Figure 3.12 shows a sketch of the system. The sample is evaporated and ionized in small resistively heated oven, very similar as in the RISIKO setup. The ions are accelerated and guided into a quadrupole mass spectrometer (QMS) after which they reach the detector. The main difference to the RISIKO setup is the mass selection by a QMS which has significantly smaller dimensions than a comparable dipole magnet. In addition, it uses much smaller kinetic energies of the ions, which enables the operation of the ion optics on relatively low voltages. As a consequence, the whole system is much more compact compared to the RISIKO separator. The vacuum inside the apparatus is provided by a single turbomolecular pump and a rotary vane pump, which achieve a vacuum pressure in the order of 10^{-7} - 10^{-6} mBar. The following sections give a detailed description of some specific components and their operation.

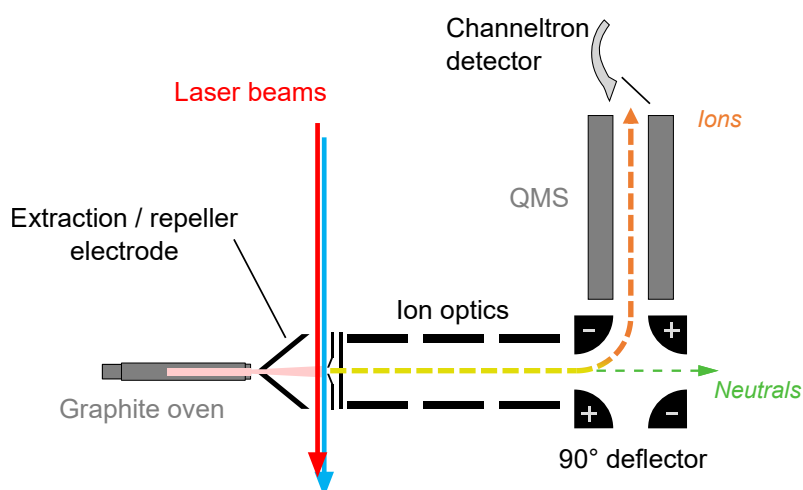


Figure 3.12: Schematic layout of the MABU spectrometer. After laser ionization, the ions (orange) are accelerated, separated from neutral species (green), and guided into a quadrupole mass filter (QMS). A channeltron detector enables sensitive single ion detection.

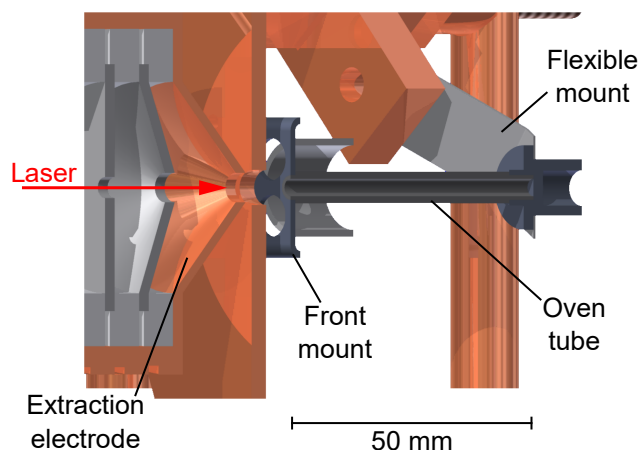


Figure 3.13: Sectional view of the MABU oven region with incoming laser beam. Graphic adopted from [91].

Ion Source

The sample is placed in a graphite tube, which can be resistively heated to about 2000 °C. Figure 3.13 shows that the tube's dimensions are similar to the ionizer tube of the RISIKO ion source. The oven tube has total length of 50 mm, an outer diameter of 4.3 mm, and an inner diameter of 2.2 mm. Likewise, the electrical heating current of up to 100 A requires water cooled feed throughs which in turns, leads to a slight temperature drop at the back and front of the oven tube. For compensation, the front tip is mounted in a specially designed holder with cut-outs to reduce heat dissipation, similar as in the RISIKO ion source. In addition, a small heat shield stretches across the first 10 mm to improve the homogeneity of the heat distribution towards the exit of the tube. A second, much larger, actively cooled heat shield surrounds the whole oven, protecting the rest of the apparatus from heat radiation.

Ion Optics

The ion optical system can be divided in four parts: extraction of the ions from the ionization region, beam shaping, separation from neutral species and the entrance into the quadrupole mass filter. A detailed description of the ion optics and simulations of the ion trajectories are given [90, 91]. The following paragraphs will briefly describe the components along the path of the ion trajectory.

The first part is the extraction region, where the ions are extracted from the ionization volume and accelerated to a moderate kinetic energy of 100 - 400 eV. The design enables modular exchange of the lens set, in order to switch between in-source ionization geometry and perpendicular ionization geometry. In in-source geometry, the overlapped laser beams enter the hot oven tube in longitudinal orientation, selectively ionizing the atoms with high efficiency. Here, all transitions show a Doppler broadening as described in section 2.3.3, increasing the spectral absorption linewidth to typically 1 - 5 GHz.

In the perpendicular ionization geometry, the first electrode is put on positive instead of negative potential, repelling all positive ions from the hot oven. Furthermore, the direction of the heating current flowing through the oven tube can be switched as well, which reverses the electric potential drop along the tube, inducing an additional suppression of positive ions created in the oven. The laser beam which exciting the transition of interest enters the region behind the repeller electrode in perpendicular orientation to the atom beam which effuses from the hot oven (see figure 3.12). As illustrated in figure 3.14, the thermal velocity

distribution along the laser axis is significantly reduced. The remaining Doppler broadening observed is typically in the order of about 100 MHz, allowing to study HFS and isotopic shifts in atomic transitions with high spectral resolution.

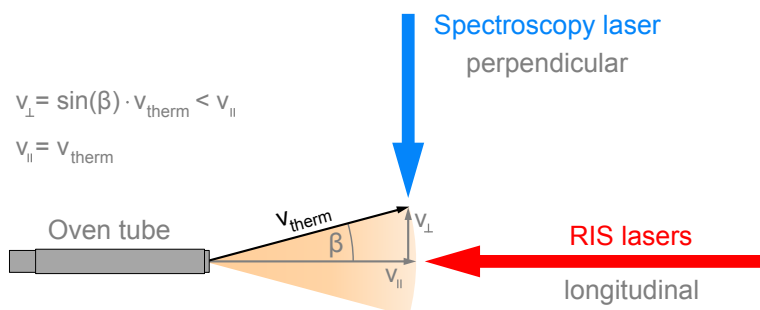


Figure 3.14: Illustration of the perpendicular ionization geometry and the reduction of the Doppler broadening. The thermal velocity v_{therm} distribution of the atoms causes a Doppler broadening of a few GHz. The full Doppler broadening is observed when probed with longitudinally aligned laser light (red arrow). If the laser beam is aligned perpendicularly to the atom beam (blue arrow), the velocity distribution along the corresponding axis v_{\perp} is significantly smaller, resulting in a reduced Doppler broadening. See text for more details.

The extraction region is followed by an Einzel lens and a telescope lens, which focuses the ion beam towards the electrostatic quadrupole 90° -deflector, where the ions are separated from the neutral species. A subsequent ring electrode is used to optimize the ion beam focusing into the quadrupole mass filter for most efficient transmission.

Quadrupole Mass Filter

An essential difference between the MABU and the RISIKO separator is the usage of a quadrupole mass filter, or *quadrupole mass spectrometer* (QMS) [84, 85]. It allows significantly smaller dimensions of the spectrometer setup as well as the use of a low-energetic ion beam. The QMS and its principle of operation is described in full detail in earlier works, e.g. [92, 93, 94, 47, 91]. This section will focus on a brief summary of the basic concept and highlight the experimentally relevant key characteristics in the MABU spectrometer.

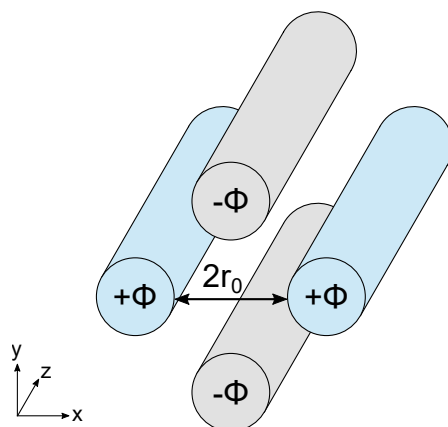


Figure 3.15: Rod arrangement of a QMS. The potential Φ is applied with different polarity to the two pairs of rods, creating an electric quadrupole field.

A QMS consist of four cylindrical rods in a parallel arrangement placed, as illustrated in figure 3.15. A combination of a direct voltage (DC) and a radio frequency alternating voltage (AC), $\Phi(t) = U + V \cos(\omega t)$, is applied to the rods. The pair of rods on opposite sides are kept on the same voltage Φ , while the different polarity $-\Phi$ is applied to the other pair of rods. The result is a superposition of static and alternating electric quadrupole field, which causes ions traveling along the z-axis to perform an oscillating motion in the x-y-plane. As shown in figure 3.16a, for ions with a certain mass-to-charge ratio m/q only a specific range of voltages U and V result in a stable oscillation in x- and y-direction, which show a characteristic triangular shape in the U - V -plane. Figure 3.16b visualizes the procedure of a mass scan where the DC and AC voltages are tuned with a proper ratio U/v , forming the so-called load line (dashed).

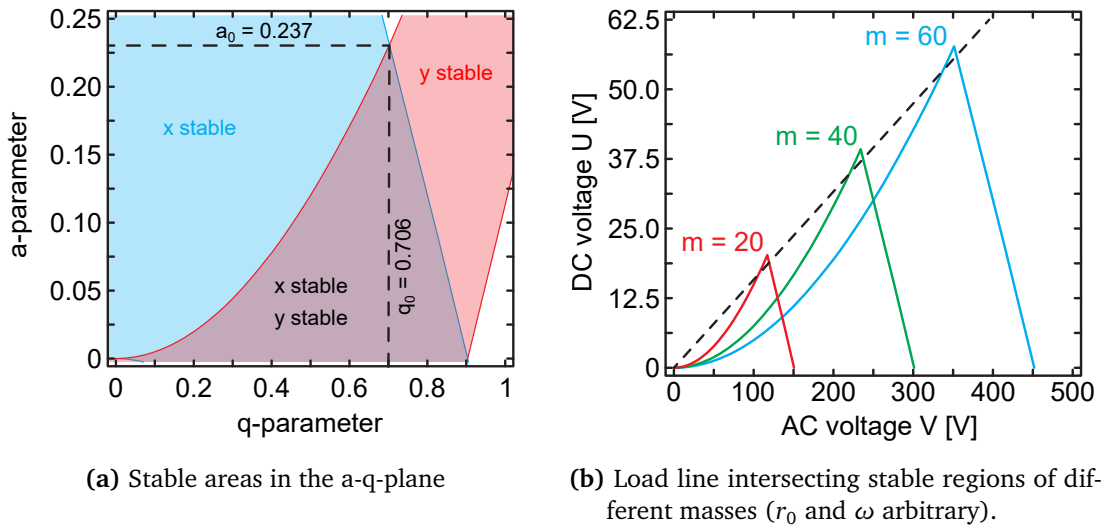


Figure 3.16: Stability diagrams of an ideal quadrupole mass filter. Figure (a) shows stable solutions of the oscillating motion, plotted in the plane of the stability parameters a and q which are proportional to the voltages U and V respectively. Figure (b) visualized a mass scan along the load line (dashed). Graphics adopted from [44]. See text for details.

The MABU uses a QMS with a length of 21 cm and a free field radius of $r_0 = 8.3$ mm. It uses an AC frequency of 1.2 MHz and is designed for a mass range of 0-300 atomic mass units. The MABU setup achieves a typical mass selectivity of about $m/\Delta m = 200$ while neighboring masses are suppressed by a factor of $\sim 10^5$. With settings optimized for optimum mass resolution, the transmission of the QMS is about 10 times lower compared to the sector field magnet in the RISIKO separator. As a result, the typical overall efficiencies obtained at the MABU spectrometer range from 0.5% to 2% [47, 90, 91].

Detection

As the MABU is designed for trace analytical measurements and spectroscopy on smallest samples, e.g. radioactive isotopes, a highly sensitive ion detection is installed. Therefore a single channel electron multiplier, or channeltron⁴ detector is used, which enables detection of smallest ion rates down to single ion counting.

A channeltron detector works similar to a secondary electron multiplier but lacks the cascade of individual electrodes. Instead, it uses a horn-shaped glass body which is coated with a high resistance material. As displayed in figure 3.17, a high voltage of about 2.5 kV is

⁴Channeltron is a registered trade name of Photonis - Burle - Galileo

applied between the larger entrance opening and the detector end, creating a continuously decreasing potential along the funnel. If a particle with sufficient energy hits the coating, secondary electrons are created and accelerated towards the positively charged end. These electrons hit the wall and generate multiple secondary electrons. The process triggers an avalanche, in which the number of electrons is amplified by up to a factor 10^8 . The curved shape of the funnel increases the number of collisions on the wall. As the high resistance coating is quite delicate and may undergo degradation when heavy ions directly impinge on the material, the MABU uses the channeltron in an off-axis configuration. Here, a small metal dynode (gray) is placed in front of the funnel opening and is kept on negative potential relative to the channeltron entrance. The ion beam is directly guided onto this electrode and only the kicked out secondary electrons enter the channeltron.

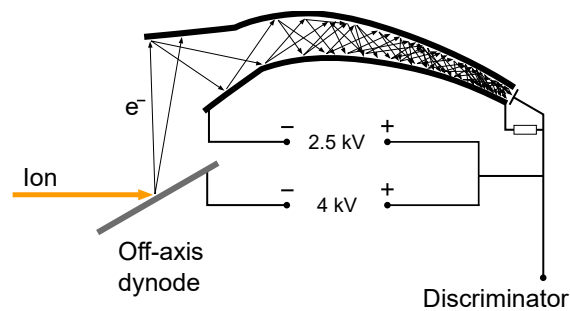


Figure 3.17: Channeltron detector

A discriminator unit converts the electric pulses on the detection side to 5 V TTL-pulses, which are then registered by a digital counter and recorded by a computer-based data acquisition system. When operated at suitable vacuum pressures of $\leq 10^{-6}$ mBar, the detector background, the so-called dark count rate, is well below 1 s^{-1} , while the detection efficiency is close to 100%. The minimum time between two distinct detected events, the dead time, is about $\approx 25 \text{ ns}$. A reasonable upper limit for the count rate to avoid dead time effects or damaging the channeltron is $2 \cdot 10^6 \text{ s}^{-1}$ for a continuous signal. Due to the pulsed laser system, the ions are produced in short bunches of only μs duration with a kHz repetition rate, which reduces the safe upper limit of the ion count rate to about $2 \cdot 10^5 \text{ s}^{-1}$.

IONIZATION EFFICIENCY: IONIZATION SCHEME DEVELOPMENT IN PALLADIUM

This chapter presents the development and characterization of a new highly efficient resonance ionization scheme for palladium. As discussed earlier in the introduction in chapter 1, the development of such an ionization scheme was requested, as planned experiments at ISOLDE aim to perform high-precision mass measurements at very rare neutron-rich Pd isotopes. The selective and highly efficient resonance ionization of Pd is a prerequisite for accessing these isotopes far off stability at RIB facilities like ISOLDE. Different 2-, 3-, and 4-step excitation schemes, suitable for the titanium:sapphire laser system as currently used at the major RIB facilities worldwide, were developed and compared in terms of ionization efficiency, in order to obtain a well suited excitation ladder for highest ionization rates. This subject is covered in section 4.1, while the subsequent section 4.2 highlights the spectroscopic investigation on Rydberg series above the ionization potential, which played an important role in the development process of the ionization scheme. After the identification of the most efficient schemes, the individual efficiencies were studied in extensive series of measurements which were conducted under off-line laboratory conditions using quantified samples of natural Pd. This activity is presented in section 4.3. Outstanding overall efficiencies of 54.3(14)% could be demonstrated at the RISIKO separator at Mainz university and 59.7(21)% at the IRIS2 separator at Oak Ridge National Laboratory (ORNL), proving the high performance of the ionization scheme. Parts of this chapter were published in [4].

Palladium ($Z = 46$) is part of the transition metal group and was first discovered in 1803 by chemist and physicist William Hyde Wollaston, who named his new discovery after the asteroid Pallas. As shown in figure 1.1, it is part of the periodic table's d -block and can also be assigned to the group of the platinum metals, which are Ru, Rh, Pd, Os, Ir, and Pt. Figure 4.1 shows a section of the chart of nuclides around Pd, including the natural isotopic abundances of the six stable Pd isotopes [95]. The nuclear spin I of Pd is $0+$ for all isotopes with even A and $5/2+$ for the ^{105}Pd isotope. Palladium's atomic ground state configuration $[\text{Kr}] 4d^{10}$ has a completely closed d -shell acting as its valence shell without any outer s - or p -shell being populated, a unique peculiarity, which is not found in any other element. In contrast, the other elements in group 10 of the periodic table, i.e. Ni, Pt, and Ds, have the same number of valence electrons, but exhibit different ground atomic state configurations, in which the corresponding s -shell is fully or partially filled. Comparable atypical configurations of the valence shell within the corresponding group of the periodic table can be found in other elements of the 5th period within the d -block, namely niobium

($Z = 41$) with $[\text{Kr}] 4d^4 5s$, ruthenium ($Z = 44$) with $[\text{Kr}] 4d^7 5s$, and rhodium ($Z = 45$) with $[\text{Kr}] 4d^8 5s$.

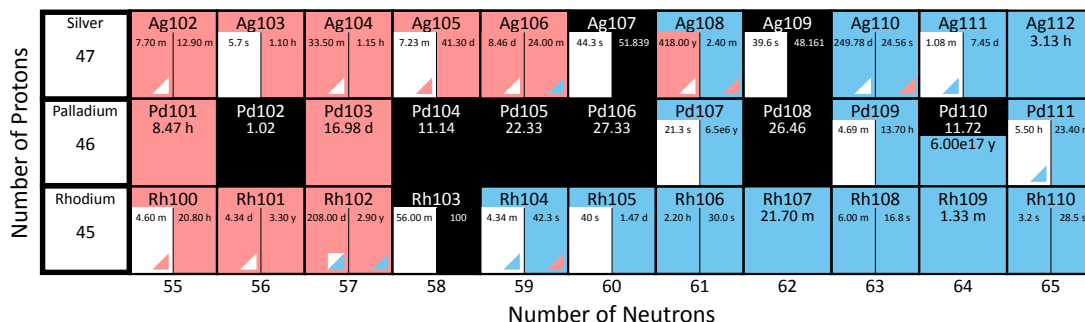


Figure 4.1: Pd region in the charts of nuclides with the natural abundance of the stable isotopes in percent [95].

The atomic level structure of neutral palladium has been studied in some detail in the past [96, 97, 98, 99, 100, 101, 102]. The most recently reported value for the ionization potential, representing the ion ground state Pd II ($4d^9 2D_{5/2}$), is $67241.3(8) \text{ cm}^{-1}$, which was determined by Baig et al. [98]. The energetically higher lying fine structure component of the ion ground state Pd II ($4d^9 2D_{3/2}$) appears in the Pd I spectrum as an additional limit for Rydberg series at $70779.8(8) \text{ cm}^{-1}$ [98]¹. This is sometimes referred to as second ionization limit. Several Rydberg series converging towards the ionic ground state with $J = 5/2$ have been studied, as well as some members of autoionizing Rydberg series that converge to the energetically higher lying fine structure level with $J = 3/2$ [96, 98, 100, 97, 99]. Nevertheless, precise data on higher Rydberg levels, especially concerning autoionizing levels with $n > 17$, is completely missing. The present work also comprises a detailed study of this region of the atomic spectrum (see section 4.2), which provides essential information to identify an efficient resonant final ionization step in a RIS excitation scheme.

4.1 Ionization Scheme Development

Several ionization schemes for Pd were developed and studied, using the RISIKO mass separator at Mainz university, described in section 3.2.1. For the spectroscopic investigations, a few μg of solid Pd were placed in the ionizer tube. This relatively large sample was used for several weeks of intensive measurements without showing signs of significant depletion. A Faraday cup was used for the detection of the ion current, which was typically in the range of 100 – 5000 pA. Figure 4.2 gives a typical mass spectrum of the Pd region, exhibiting very low background of well below 1 pA. All individual isotopes could be perfectly resolved and the observed signal ratios were in excellent agreement with the natural isotope abundance of Pd.

First tests with resonance ionization on palladium were already performed earlier in the context of a diploma thesis [104]. As visualized in figure 4.3, these experiments compared two 3-step schemes with different second excitation steps and a non-resonant ionization step. The first excitation step was a strong transition at 244.9 nm with $A = 1.1 \cdot 10^7 \text{ s}^{-1}$ [103], leading from the $4d^{10} 1S_0$ ground state to the excited state $4d^9 (2D_{3/2}) 5p^2 [1/2]_1^0$ at $40838.874 \text{ cm}^{-1}$. This UV wavelength was provided by the frequency-tripled radiation of a Ti:sapphire laser operating at 734.6 nm. It should be noted that the state assignments

¹The value of $70779.8(8) \text{ cm}^{-1}$ is taken from [98] according to the NIST database [103]. However, within the article [98] the value is also quoted to be $70779.7(8) \text{ cm}^{-1}$, which seems to be a typing error.

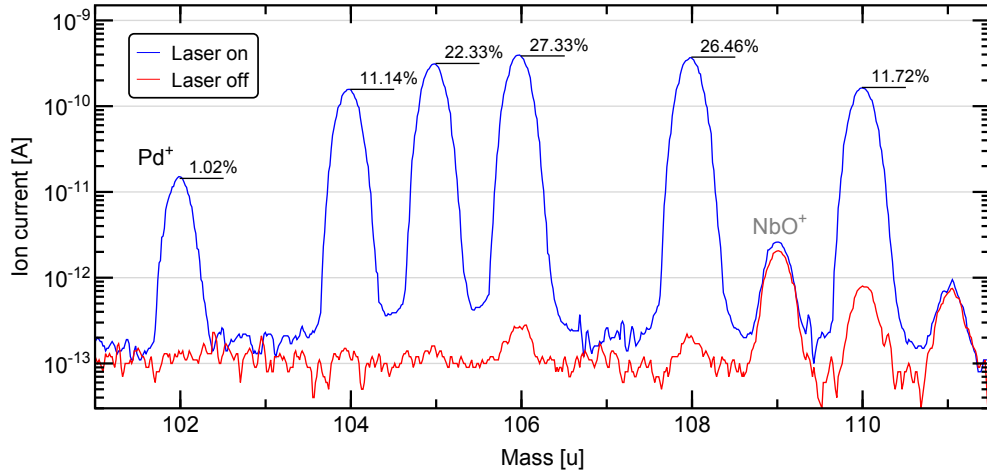


Figure 4.2: Typical mass spectrum in the Pd region at the RISIKO mass separator. The experimentally observed intensity ratios of the laser-ionized species (blue) are in excellent agreement with the natural abundance (see markers) of Pd as given in [95]. The background (red) shows the presence of a small amount of surface ionized NbO^+ at 109 u. The origin of the surface ionized fraction at 110 u and 111 u could not be clearly identified.

used here are based on the J_1K coupling scheme as proposed in [101], while [104] used less suitable assignments based on LS coupling. See section 2.1.4 for a description of both coupling schemes. Two second excitation steps were tested, the 715.1 nm transition to the $4d^9(^2D_{5/2})5d^2[3/2]_1$ state at $54823.051 \text{ cm}^{-1}$, and the 706.2 nm transition populating the $4d^9(^2D_{5/2})5d^2[5/2]_2$ state at $54998.664 \text{ cm}^{-1}$. Both excitation steps showed a rather similar gain in ionization rate. Saturation powers of 68(12) mW for the 706.2 nm transition and 126(32) mW for the 715.1 nm transition were obtained, so that both could be saturated with the available laser powers of about 800 mW. The values for the saturation powers might be less accurate as stated, as the evaluation suffered from a small number of data points and significant deviations between the data points and the resulting fit were observed. A search for an efficient third step transition to autoionizing states was conducted, but an accessible transition within the covered frequency range was not found. Correspondingly, non-resonant ionization into the continuum was used as third step with wavelengths of $< 805.3 \text{ nm}$ or $< 816.8 \text{ nm}$, respectively. As discussed in section 2.3.2, this ionization process has quite low cross-sections, resulting in considerably smaller ionization efficiencies compared to the use of resonant transitions to autoionizing states.

The final efficiency measurements at a simple atomic beam unit suffered from severe problems in the ion transmission and resulted in a very poor overall efficiency of about $4 \cdot 10^{-7}$. The heavy transmission losses made it impossible to estimate a meaningful value of the ionization efficiency or to compare the result to data obtained at a suitable mass separator setup like the RISIKO separator. However, a quite low efficiency was expected to some extent, as the scheme relied on the inefficient non-resonant ionization step. Therefore, this ionization scheme was not suitable for any further application on smallest samples and consequently was not investigated further in the framework of the present thesis.

The goal of the study presented here, is the development of a new ionization scheme with highest ionization efficiency, suitable for the high repetition rate Ti:sapphire laser system as used at Mainz university and the majority of RIB facilities world wide. This poses certain requirements, which have to be kept in mind during the development process. The chosen atomic transitions must have wavelengths suitable for the tuning range of Ti:sapphire laser systems. In order to obtain highest excitation efficiency, the transitions need sufficiently high

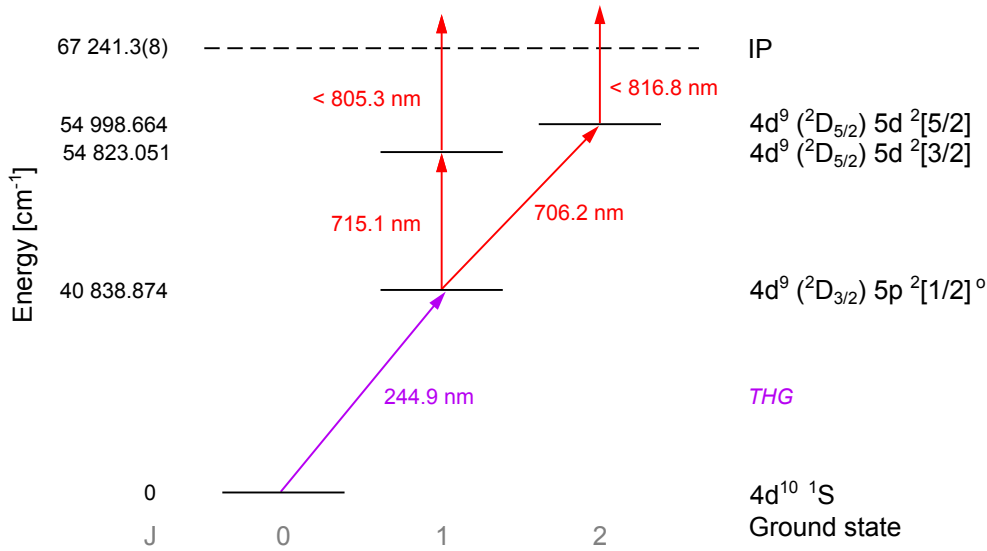


Figure 4.3: Non-resonant Pd ionization schemes investigated in the earlier work [104].

transition strengths, which corresponds to low saturation intensities, ensuring significant saturation of the transition with typical laser powers. Another issue is the possibility of optical pumping into so-called dark states, where an intermediate excited state decays spontaneously into another lower lying state. In this case, the atom cannot be excited further preventing it from proper ionization. Therefore, high decay rates might cause severe losses, hindering an efficient ionization process. Experimental tests of the suggested ionization schemes are mandatory to check for the presence of this effect and to characterize the strength and saturation behavior of the involved transitions.

Figure 4.4 summarizes the newly developed excitation schemes, which were investigated in the present work. As various different intermediate and final excitation steps were tested for each scheme, the figure shows only the most efficient excitation ladders for the 2-step, 3-step, and 4-step ionization scheme.

4.1.1 Resonant 2-Step Scheme

The first attempt was the development of a resonant 2-step scheme, using two UV transitions. Two-step schemes are of special interest, as the reduced number of excitation steps implicate less work for setting up and operation the laser system. In addition, the small number of free parameters allow easy monitoring of the operation parameters and optimization of the whole setup, which constitute clear benefits for the reliable operation of an ion source.

The $4d^{10} 1S_0 - 4d^9 ({}^2D_{5/2}) 5p^2 [3/2]_1^o$ transition at 276.4 nm was chosen as the first excitation step. This transition is promising, as it is the strongest documented ground state transition in Pd [103, 101]. Transition probabilities are reported as $A = 1.5 \cdot 10^7 \text{ s}^{-1}$ [105] or $A = 1.7 \cdot 10^7 \text{ s}^{-1}$ [103, 106]. The UV radiation was provided by frequency-tripling of the fundamental laser wavelength of 829.2 nm, which is close to the gain maximum of the Ti:sapphire gain medium. Consequently, the high laser powers allowed efficient frequency conversion, resulting in typical laser powers of up to 200 mW of UV laser radiation. An efficient resonant transition to an autoionizing state was desired as second step to achieve a high ionization rate. Several autoionizing Rydberg states are reported in [98, 96]. The corresponding Rydberg series converge towards the energetically higher ionic

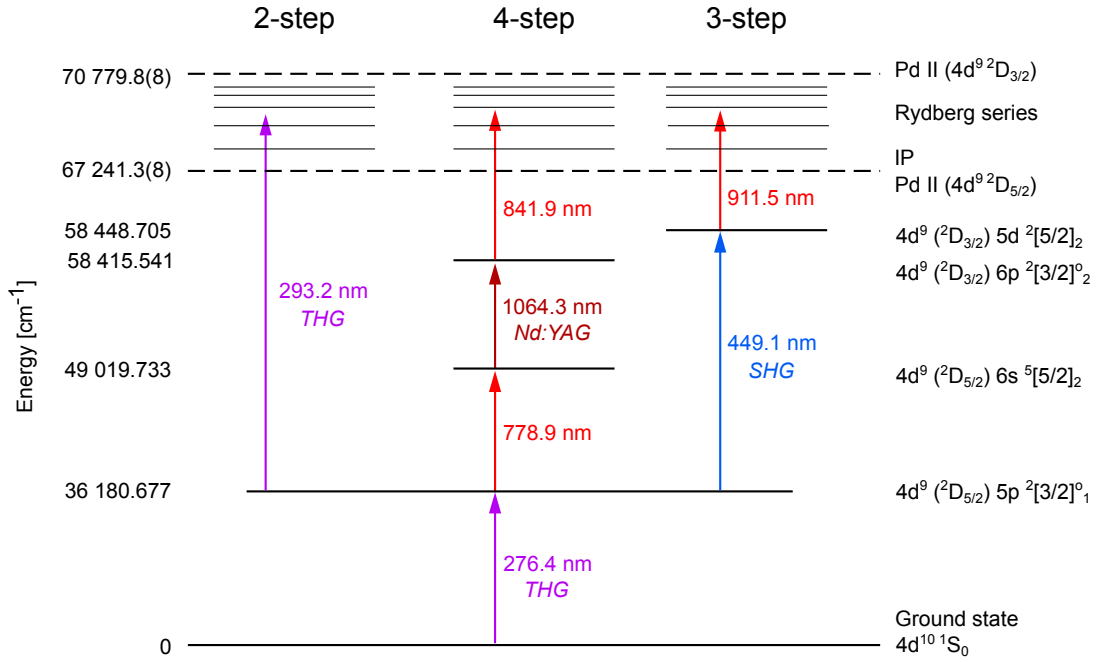


Figure 4.4: Overview about the Pd excitation schemes investigated in this project. The given excitation steps and levels are the most efficient ones of all tested combinations. The third step in scheme B was excited by the fundamental radiation of a Nd:YAG laser, while all other transitions were excited with Ti:sapphire lasers and HHG. Level assignments and energies are based on [101, 98].

state Pd II ($4d^{9^2}D_{3/2}$) at $70779.8(8) \text{ cm}^{-1}$, which lies well above the ionization potential at $67241.3(8) \text{ cm}^{-1}$, which corresponds to the ion ground state Pd II ($4d^{9^2}D_{5/2}$). To reach this energy region of the spectrum, the wavelength range for the second step was about 270 – 300 nm, which could again be provided by the frequency-tripled radiation of a Ti:sapphire laser.

Those atomic Rydberg states with one highly excited valence electron at high principal quantum number n and the atomic core in the excited ionic state Pd II ($4d^{9^2}D_{3/2}$) have a very high energy, which can easily exceed the IP. Such autoionizing Rydberg states² above the IP are excellent candidates regarding high ionization efficiency. They enable strong resonant transitions and very efficient subsequent ionization, as the states combine the strong ionization mechanisms of autoionizing states and Rydberg states as discussed in section 2.3.2, which makes them perfectly suited as final excitation step.

The first excitation step at 276.4 nm showed a low saturation power of about 2 – 5 mW with a laser beam spot size of $\approx 0.7 - 1 \text{ mm}$ diameter^{3,4}. This low saturation power agrees well with the transition probabilities quoted above. Figure 4.5 visualizes frequency scans of the excitation steps in the 2-step ionization scheme. On the right hand side, saturation curves show the saturation behavior of the ion current in regard to increasing laser power of the corresponding excitation step. A curve as described in formula 2.54 in section 2.3.3 was fitted to the data to determine the saturation power P_S . The first step transition could be easily saturated, with available laser powers of up to 170 mW ⁵, resulting in power

²Also referred to as AI Rydberg states or Rydberg AI states.

³This and all following diameters are given in terms of full width at half maximum, also noted as FWHM.

⁴All power values given here and in the following correspond to the measured laser power in front of the entrance window of the mass separator.

⁵The saturation curve in figure 4.5 was recorded with attenuated laser power during a direct comparison with the 4-step scheme which required different laser pulse timing leading to lowered output power. However,

broadening which can be seen in figure 4.5. The broadening of up to 24 GHz full width at half maximum is advantageous, as it minimizes the influence of frequency drifts of the laser during long-term experiments.

As presented in the following section 5.3.3, the first excitation step was also investigated in the context of another experiment, aiming for high spectral resolution with a special ion source setup and laser system. These measurements showed, that the isotope shift across all stable isotopes is less than 700 MHz. This size can be neglected when compared with the spectral linewidths of more than 20 GHz in the present chapter.

As indicated in figure 4.4, this first excitation step was also used in all other ionization schemes. A second photon of this first step provides enough energy to overcome the gap between first excited state and ionization potential, leading to a non-resonant ionization signal using solely the laser for first step. Provided that frequency and intensity for the first excitation step are kept stable, this non-resonant signal can be used as reference across all tested ionization schemes. The ratio between ion current produced by solely the UV radiation of the first excitation step and the ion current produced with the full set of excitation lasers can be defined as the relative intensity

$$r_{\text{rel}} = \frac{I_{\text{all steps}}}{I_{\text{1st step only}}} , \quad (4.1)$$

which enables comparison of the different schemes among each other. It can be seen as a figure of merit which gives the increase in ionization rate of the further excitation steps following the first step.

To find the most suitable second excitation step, several ultraviolet transitions to different autoionizing Rydberg levels of even parity with $n' = 12 - 20$ were tested with regard to resulting ion current, relative intensity, and their saturation behavior. Additional Rydberg levels could not be investigated, as the tuning range of the frequency-tripling setup for the second step was technically limited to a few cm^{-1} . A more detailed analysis of the spectrum is provided in section 4.2. For each n' , a group of Rydberg resonances belonging to different series, were observed as shown in the upper left of figure 4.5. The transition with the highest ionization rate was found at 293.2 nm and lead to a specific autoionizing Rydberg state at 70292.96 cm^{-1} with $n' = 15$.

Unfortunately, none of these second step transitions could be properly saturated, as the available laser power was limited to about 120 mW by the required frequency-tripling. This circumstance results in low excitation rates, hampering high ionization efficiencies. Therefore, this type of ionization scheme is not suited for application with the present high-repetition Ti:sapphire laser system. However, it might be suitable for dye laser systems, which can provide significantly higher laser powers of up to several Watts in this frequency range.

To overcome this limitation, it was suggested to replace the second excitation step by three transitions with fundamental Ti:sapphire wavelengths. This would drastically improve the chance to fully saturate all steps of the excitation ladder, as each individual step could be excited with laser powers up to 3 Watts. In addition, a final excitation step with fundamental laser frequency allowed the continuous, wide frequency scan with the grating-assisted Ti:sapphire laser, which could not be realized in the 2-step scheme. This enable the search for additional autoionizing states and a more comprehensive study of the Rydberg series above the IP. This is a major advantage for the development of an ionization scheme and contributes to a conclusive understanding of the atomic level structure in Pd.

the available power was enough to clearly show the strong saturation.

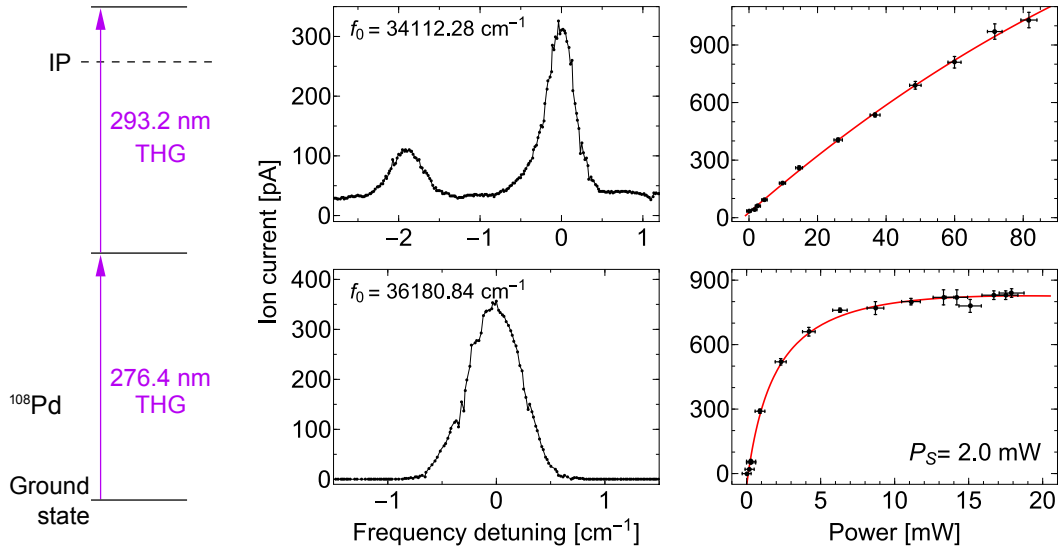


Figure 4.5: Frequency scans (left) and the corresponding saturation curves (right) of the 2-step ionization scheme in Pd. The scan in the second step clearly shows an additional autoionizing resonance which belongs to a different Rydberg series. The red curve shows fits of formula 2.54 to the data to determine the saturation power P_S .

4.1.2 Resonant 4-Step Scheme

The results obtained from the investigation of the 2-step scheme indicated possible advantages of a 4-step scheme. The fundamental idea was to use the same first excitation step, followed by three transitions which can be addressed with fundamental Ti:sapphire laser radiation instead of one excitation step, which would require frequency-tripling. This allows much higher power for each of the upper excitation steps, increasing the chance to find a set of strong, significantly saturated transition. In addition it provides the possibility to use the grating-assisted Ti:sapphire, which is described in section 3.1.2, to perform wide, continuous frequency scans of the last excitation step in order to search for suitable transitions.

The resulting scheme is shown in the center of figure 4.4. The second excitation uses the transition $4d^9(^2D_{5/2})5p^2[3/2]_1^o - 4d^9(^2D_{5/2})6s^2[5/2]_2$ at 778.9 nm to excite the $5p$ -electron into the $6s$ -orbital. The transition probability is expected to be suitably strong, as L and J increase by $+1$. Figure 4.6 shows a frequency scan in the second transition and the corresponding saturation measurement. The observed low saturation power of 42 mW confirms the strength of the transition. In comparison, the laser system provided up to 3 W of laser power for this transition, which made it easy to achieve strong saturation for the planned efficiency measurements.

The search for a suitable transition of the third step was quite complicated, as the most promising transitions were outside the accessible wavelength range of the Ti:sapphire laser system. Fortunately, the transition $4d^9(^2D_{5/2})6s^2[5/2]_2 - 4d^9(^2D_{3/2})6p^2[3/2]_2^o$ corresponds to a photon wavelength of 1064.3 nm and could be excited with radiation from the prominent 1064 nm line of a fundamental Nd:YAG laser. Therefore, a spare pump laser (Northrop Grumman Mirus) was included in the laser system. In this way, a maximum power of 25 W at a 10 kHz repetition rate with a pulse length of about 100 ns and a TEM_{00} mode profile could be provided. The laser radiation had a relatively broad spectral linewidth of about 52 GHz [107]. In order to enable some frequency control, the linear laser cavity of the Nd:YAG laser was equipped with an additional solid etalon from a standard Ti:sapphire laser. The large temporal jitter of this Nd:YAG laser made proper synchronization to the other Ti:sapphire lasers complicated. Since this temporal jitter in the order of 50 ns was

similar to the pulse length of the standard Ti:sapphire lasers, it caused increased fluctuations of the detected ion current. As up to 7 W of laser power were available at the entrance of the mass separator, the excited transition could be well saturated. As a drawback, the laser frequency of this step could not be scanned smoothly across the whole resonance.

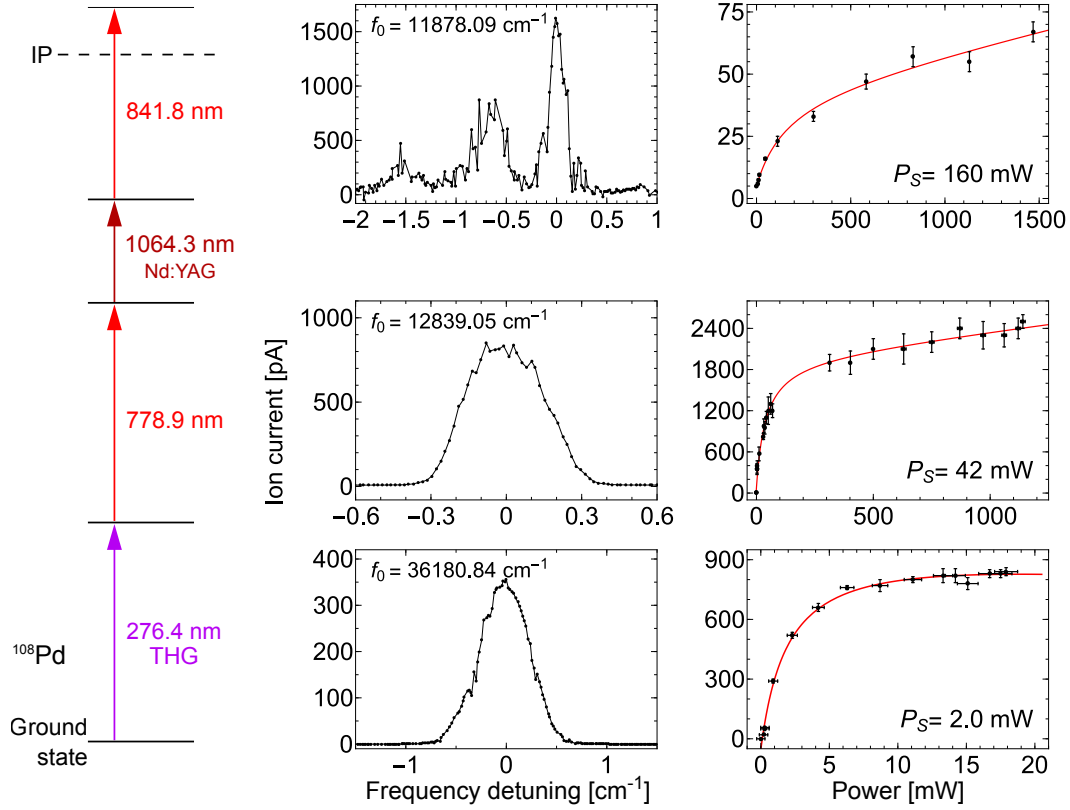


Figure 4.6: Frequency scans (left) and the corresponding saturation curves (right) of the 4-step ionization scheme in Pd. The red curves on the right show fits to the data to determine the saturation power P_S . The third step could not be properly scanned, due to the provisional spectral control of the used Nd:YAG laser. The frequency scan in the fourth step clearly shows additional autoionizing resonances which belong to different Rydberg series.

A first test with manual tuning of a standard Ti:sapphire as a fourth step, confirmed the accessibility of the autoionizing Rydberg levels of even parity above the ionization potential, which was already observed with the 2-step scheme. As a next step, the grating-assisted laser was used to scan a frequency range of 805 – 880 nm, covering the range of 69770 – 70820 cm^{-1} between the ionic ground state Pd II ($4d^9 2D_{5/2}$) and the higher lying Pd II ($4d^9 2D_{3/2}$) state. Section 4.2 provides a closer look on the acquired spectrum and the observed autoionizing resonances. Many members of the Rydberg series as well as a second Rydberg series, which was weaker, could be observed. Most of the strong resonances showed significant saturation broadening, an indicator for an efficient excitation into the autoionizing state. After comparing the strongest resonances of the spectrum under stable ion source conditions, the strongest transition of the fourth step was found to be at a photon energy of 11878.09 cm^{-1} , populating the autoionizing Rydberg state at 70293.64 cm^{-1} , also corresponding to $n' = 15$. The measured saturation power of only $P_S = 160$ mW indicates a high transition probability and was easily exceeded by up to 3 Watts of available laser power.

The 4-step scheme proved suitable ionization rates, a factor of 9.5 higher in direct comparison to the 2-step scheme. On the other hand, it showed several disadvantages. First of all, the simultaneous operation and control of four lasers generally comes with more experi-

mental expenditure and adds significantly more possible complications. The temporal and especially the spectral control of the Nd:YAG pump laser was rather complicated, especially with regard to long-term operation over several hours, which was needed for the extensive efficiency measurements in section 4.3. The temporal jitter resulted in significant fluctuations of the ion current, which made optimization of the whole system quite difficult. Another point which must not be forgotten is the fact that not all on-line laboratories can provide the additionally required fundamental Nd:YAG laser radiation, especially in combination with proper spectral control, which prevents the planned application on radionuclides.

4.1.3 Resonant 3-Step Scheme

To overcome the drawbacks of the 4-step scheme, a 3-step scheme was developed, replacing the last three excitation steps in the fundamental Ti:sapphire frequency range with one transition in the frequency-doubled frequency range followed by a transition excited by fundamental laser radiation. As laser powers of up to 3 Watts (see section 3.1.4) were available after frequency-doubling, it was expected to achieve proper saturation the second excitation step. Similar to the development of the 4-step scheme in the previous section, the use of a fundamental Ti:sapphire laser to excite the last step, enabled wide range frequency scans with the grating-assisted laser, in order to search for strong resonant transitions to AI states. As the 2-step and 4-step schemes showed clear presence of many strong transitions to autoionizing Rydberg states of even parity in this energy region of the spectrum, it was expected to also find a number of suitable transitions to autoionizing Rydberg states of odd parity. In addition, such autoionizing Rydberg series of odd parity were reported by M. A. Baig as well as Karamatskos [98, 96].

The first objective was to test and compare suitable second steps, which can be well excited by frequency-doubled Ti:sapphire laser radiation. As visualized in figure 4.7, a set of four promising transitions in the easily accessible wavelength range of 446 nm to 456 nm was selected for experimental investigations. Starting from the first excited state $4d^9(^2D_{5/2})5p^2[3/2]_1^o$, this led to population of the levels $4d^9(^2D_{3/2})5d^2[3/2]_2$, $4d^9(^2D_{3/2})5d^2[3/2]_1$, $4d^9(^2D_{3/2})5d^2[5/2]_2$ and $4d^9(^2D_{5/2})7s^2[5/2]_2$, respectively⁶. Correspondingly, the difference in total angular momentum was $\Delta J = 0, +1$, which should allow suitably transition strength. All transitions could be properly saturated and autoionizing Rydberg states above the ionization potential were found as expected.

Starting from the different second excited levels, once again the region between the ionization potential, the ionic ground state Pd II ($4d^9\ ^2D_{5/2}$), and the higher lying ionic state Pd II ($4d^9\ ^2D_{3/2}$) was investigated. Wide range frequency scans were conducted in the third excitation step using the grating-assisted Ti:sapphire laser. The investigated wavelength range from 700 nm to 950 nm, almost entirely covered the range between the two fine structure components of the Pd II ground state configuration. The resulting spectra in the energy range of 68690 cm^{-1} up to 72840 cm^{-1} showed an excellent signal-to-noise ratio and revealed a large number of sharp resonances, corresponding to transitions to members of different autoionizing Rydberg series of odd-parity, which converge towards the energetically higher ionic state Pd II $4d^9\ (^2D_{3/2})$. The present section will focus on the development of the most efficient ionization scheme, while section 4.2 presents the analysis of the spectra. Consistently, in all spectra, the most intense resonances were found on the lower energy side, closer to the first ionization potential or, in other words, the ionic ground state Pd II ($4d^9\ (^2D_{5/2})$). The peak ionization rates slowly decreased along the Rydberg series when

⁶Please note, in agreement to [103], the level assignments here are based on [101], but some inner couplings are corrected, as they were incorrectly listed as ($^2D_{5/2}$), instead of ($^2D_{3/2}$), in the original publication.

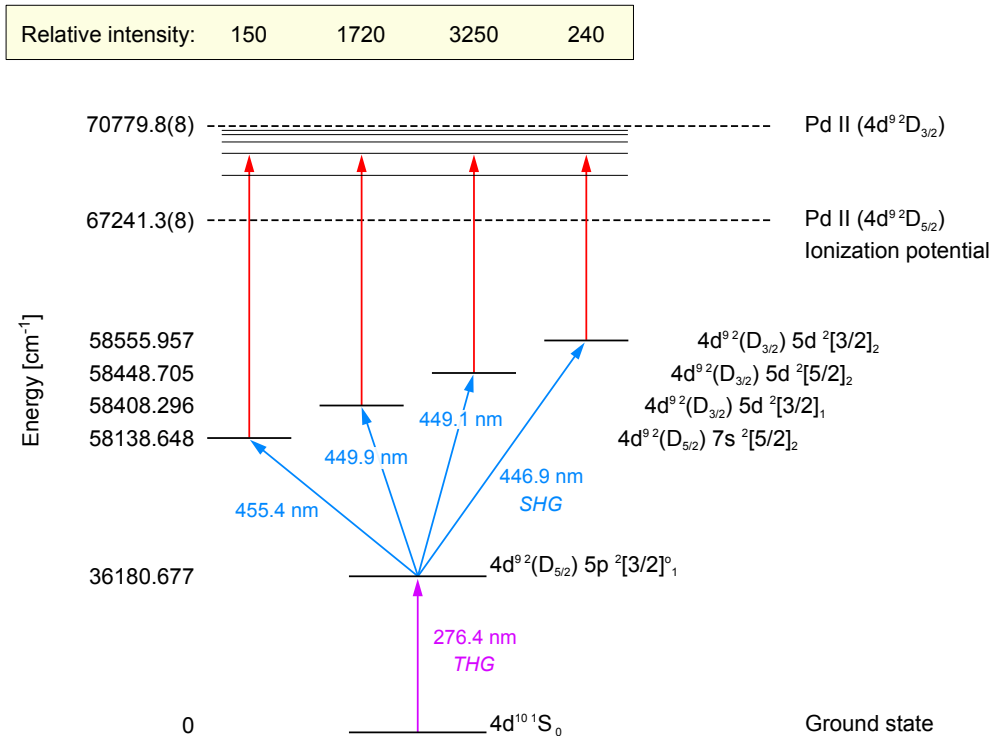


Figure 4.7: Different second excitation steps for the 3-step ionization scheme in Pd

going towards the corresponding limit, the higher lying ionic state Pd II ($4d^9\ ^2D_{3/2}$), a trend which was also observed during the investigation of the 2-step and 4-step scheme.

For each second excitation step, several of the strongest third step transitions were studied with a standard Ti:sapphire laser with full laser power in order to compare maximum ionization rate and saturation power. Figure 4.7 also gives the highest relative intensity for each second excitation step, which was achieved when using the strongest available third step transition. Excitation ladders involving the second step transition to the $4d^9(^2D_{5/2})7s^2[5/2]_2$ yielded the lowest ionization rates which is attributed to the fact that the $^2D_{5/2}$ core configuration does not match the $^2D_{3/2}$ configuration of the autoionizing Rydberg states addressed in the third excitation state. However, even this weak 3-step excitation ladder is comparable with the 2-step scheme. The strongest excitation ladder showed a relative intensity of $r_{\text{rel}} = 3250$, clearly outperforming the 2-step and 4-step ionization schemes, which yielded $r_{\text{rel}} = 950$.

Figure 4.8 presents the deduced 3-step excitation scheme, which showed the highest ionization rate. The graphs on the left side show the frequency scans of the excitation steps, while the graphs on the right hand side show the corresponding saturation behavior of the ion current in regard to increasing laser power. The final excitation step at 10971.41 cm^{-1} addresses an autoionizing Rydberg state at 69420.16 cm^{-1} . According to [98, 96, 27] this state may be identified with the $n' = 9$ member of the Rydberg series $4d^9(^2D_{3/2})np$ or nf , respectively $4d^9(^2D_{3/2})12p$ or $4d^9(^2D_{3/2})9f$.

The second and third transitions in this scheme showed a saturation power of only 7 mW and 61 mW, when the laser beams were focused to a spot size of $\approx 1.5\text{ mm}$ diameter (FWHM) at the entrance of the ionizer tube. The associated spatial profiles of the laser beams can be found in the appendix, in figure A.2. These represent very low saturation power levels for transitions in the medium to higher energy part of a atomic level spectrum, in particular regarding the third excitation step. Usually, saturation powers of well above 50 mW up to

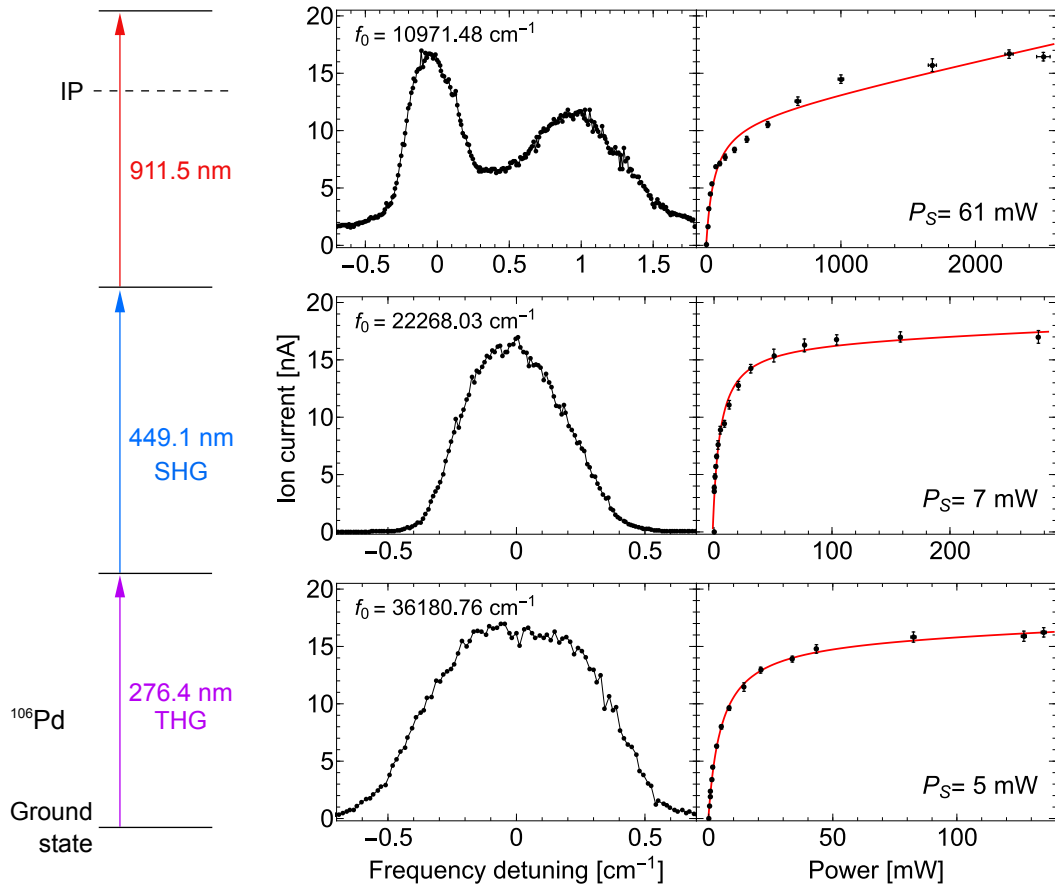


Figure 4.8: Frequency scans (left) and corresponding saturation curves (right) of the 3-step ionization scheme in Pd. The red curves on the right show fits to the data to determine the saturation power P_S . In agreement to the saturation measurements on the right, strong saturation broadening was observed in all excitation steps. The frequency scan in the last excitation step revealed additional Rydberg resonances nearby, which are discussed in more detail in section 4.2.

a couple of Watts are observed under the experimental conditions at the laboratory. The exceptional strengths of these transitions into autoionizing Rydberg states are ascribed to the peculiarity of the higher excitation steps in the Pd I spectrum with a single valence electron and the coupling to the strongly interacting one-hole electronic core configuration $4d^9 2D_{3/2}$. In this situation both the np and nf configurations form sublevels of total angular momentum of $J = 2$ and 3 (as well as additional $J = 0, 1$ sublevels for the np and $J = 4, 5$ for the nf levels), which may be efficiently populated from the second excited state with $J = 2$. This leads to strong and rather comparable transition strengths, in particular for higher excited states, where shifts between and splittings of individual configurations are no longer completely resolved due to their shrinking with high powers of the principal quantum number. As a result, all three transitions could be well saturated, as the available laser system provided typically 170 mW, 400 mW and 2500 mW for the first, second and third steps, respectively. Correspondingly, this resonant 3-step scheme seems highly suitable for highly efficient, selective ionization of palladium.

4.2 Analysis of the Rydberg Series

This section will take a closer look on the high-lying Rydberg series which were observed during the development of the ionization schemes in section 4.1. As mentioned above, the autoionizing Rydberg series converge to an excited state of the ion, i.e. the higher-lying fine structure component Pd II ($4d^9\ ^2D_{3/2}$) of the ion ground state Pd II ($4d^9\ ^2D_{5/2}$). This section will discuss the observed series and evaluate their limit in order to determine the ionization potential precisely.

As discussed in the beginning of this chapter, Rydberg series in that energy region of the spectrum were already studied by Karamatskos et al. and Baig et al. [98, 96]. Both experiments started from the Pd ground state $4d^{10}\ ^1S_0$, thus allowing dipole-transitions to the autoionizing Rydberg levels $4d^9\ (^2D_{3/2})\ np\ [1/2]_1^o$, $4d^9\ (^2D_{3/2})\ np\ [3/2]_1^o$, and $4d^9\ (^2D_{3/2})\ nf\ [3/2]_1^o$. In the work of Karamatskos et al. a total of 11 Rydberg resonances corresponding to $n' = 5.99 - 16.0$ were reported. As the spectral linewidth in this experiment was 0.12 nm, corresponding to $\sim 57\text{ cm}^{-1}$, the different states could not be resolved. The work of Baig et al. comprise the observation of 10 resonances with $n' = 4.95 - 13.99$ with significantly better spectral resolution.

The energy of Rydberg states in general is given by formula 2.33. This formula can be used to calculate the effective principal quantum number n' by the formula

$$n' = n - \delta = \sqrt{\frac{-R_{y,\text{mod}}}{E_{\text{lim}} - E_n}} \quad (4.2)$$

Here, E_{lim} is the energy of the series limit and $R_{y,\text{mod}} = R_\infty \mu/m_e$ is the mass-corrected Rydberg unit of energy.

The work of Fano et al. provides fundamental descriptions of atomic Rydberg states and their properties [45, 27]. For high principal quantum numbers n , the quantum defect δ is expected to approach a constant value, which depends on the orbital angular momentum l . Fano carried out calculations using the phase shift, here denoted as δ_l , which differs to the quantum defect, here denoted as μ , by a factor of π . Figure 4.9 shows a graph from Fano's work [27], presenting the predicted phase shift and quantum defect for $l = 0, 1, 2, 3$ at the binding energy $E = 0$, meaning for $n \rightarrow \infty$, as a function of the atomic number. The values of the quantum defect are used in the following to identify the members of the different Rydberg series in the observed spectra.

4.2.1 Even Parity Series

The frequency scans in the final excitation step in the 2-step scheme and 4-step scheme, as depicted in figure 4.4, allowed investigation of the energetic region between the IP and the fine structure component of the ion ground state Pd II ($4d^9\ ^2D_{3/2}$). This part of the atomic spectrum is dominated by autoionizing Rydberg series converging to the Pd II ($4d^9\ ^2D_{3/2}$) limit. Several members of these Rydberg series with even Parity could be populated, by using either the 2-step scheme or alternatively the 4-step scheme as described in the previous section 4.1. Table 4.1 summarizes the Rydberg states which were accessible via dipole-transitions.

In the 2-step scheme, a continuous wide frequency scan could not be realized in the final excitation step starting at $4d^9\ (^2D_{5/2})\ 5p\ ^2[3/2]_1^o$, as it was technically not possible to properly tune the required frequency-tripling. Therefore, distinct frequency ranges of about 30 cm^{-1} width were scanned to cover resonances corresponding to Rydberg states with $n' = 12$ to $n' = 20$. In contrast, the 4-step scheme used a final excitation step in the fundamental

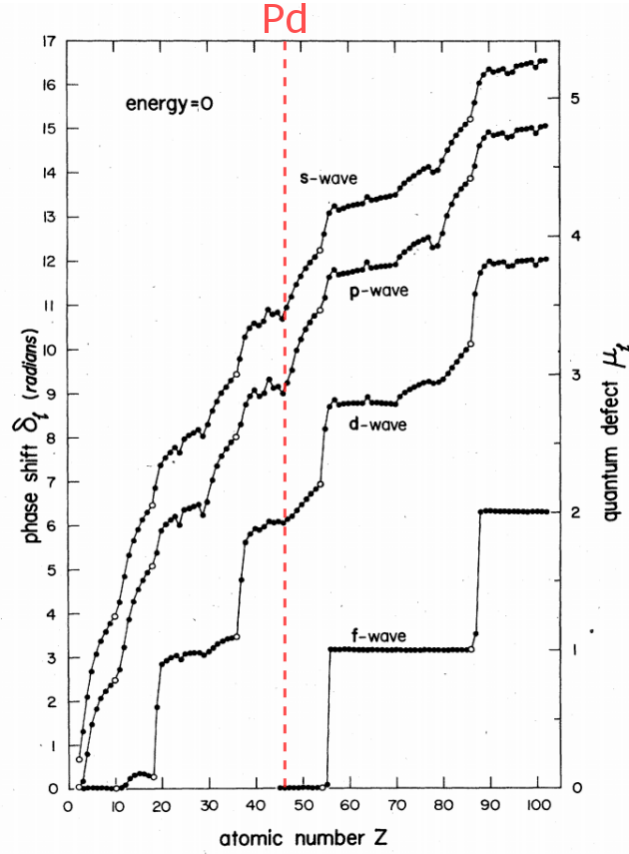


Figure 4.9: Quantum defect and phase shift for $l = 0, 1, 2, 3$ as a function of atomic number. Graph adopted from [27].

Table 4.1: Compilation of upper Rydberg states of even parity in Pd which can be accessed by dipole-transitions starting from the initial states as given on the left hand side.

Initial state	Upper states $4d^9 ({}^2D_{3/2})$
$4d^9 ({}^2D_{5/2}) 5p^2 [3/2]_1^o$	$ns^2 [3/2]_{1,2}$ $nd^2 [1/2]_{0,1}, nd^2 [3/2]_{1,2}, nd^2 [5/2]_2$
$4d^9 ({}^2D_{3/2}) 6p^2 [3/2]_2^o$	$ns^2 [1/2]_{1,2}$ $nd^2 [1/2]_1, nd^2 [3/2]_{1,2}, nd^2 [5/2]_{2,3}, nd^2 [7/2]_3$

frequency range of the Ti:sapphire laser. Therefore, the grating-assisted laser could be used to perform a continuous frequency spanning across 805 – 880 nm enabling access to Rydberg states with $n' = 10$ to $n' = 40$ in the range from 69779 to 70838 cm^{-1} . However, some variations in output power and temporal stability of the laser were unavoidable due to technical reasons. The resulting spectra of both measurements are illustrated in figure 4.10. The positions of the resonances in the two different excitation schemes are in good agreement, with deviations of less than 0.05 cm^{-1} . The dominant resonances have n' close to integer values, which agrees with Fano's predictions for nd -series. The continuous scan in the 4-step scheme revealed an additional series, which is given by the smaller peaks in the red colored spectrum. The positions of these smaller peaks correspond to half-integer values of n' and δ , which indicates significantly weaker transitions to the $ns^2 [1/2]_{1,2}$ series according to 4.9.

Figure 4.11 shows a section of the spectra at 70020 cm^{-1} . The top axis of the graph shows

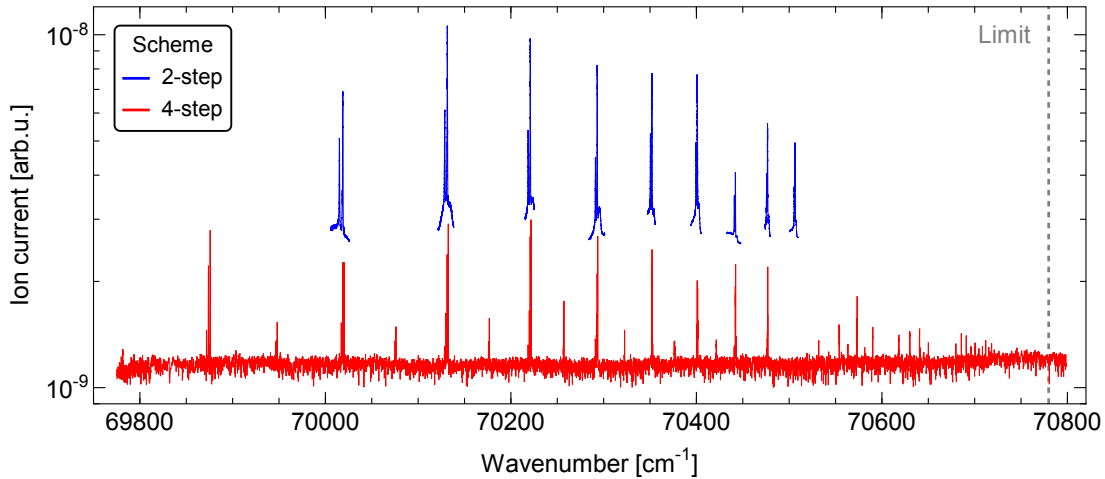


Figure 4.10: Spectrum of even parity in Pd obtained with the 2-step (blue) and 4-step scheme (red). In the 2-step scheme, the resonances were scanned individually, as a continuous frequency scanning across the complete range was technically not possible. The initial state for the 2-step scheme was the first excited state $4d^9(^2D_{5/2})5p^2[3/2]_1^o$ at 36180.677 cm^{-1} , while the scan in the 4-step scheme started from the state $4d^9(^2D_{3/2})6p^2[3/2]_2^o$ at 58415.541 cm^{-1} . The ion current data was scaled for a better view.

n' according to formula 4.2, calculated using the series limit as determined in the following section 4.2.3. The section presents the area around $n' = 12$ with the nd -components with $n = 10$, as δ for d-series is $\simeq 2$. Here, the individual components could be well resolved, while the convergence of the Rydberg series at higher n' caused overlapping of the peak structures. The graph includes a first assumption of possible assignments. However, a clear identification of the individual components remains difficult. Information cannot be taken from the earlier works of Baig et al. and Karamatskos et al., as these investigated only the odd parity spectrum starting from the ground state with $J = 0$. Information on states with

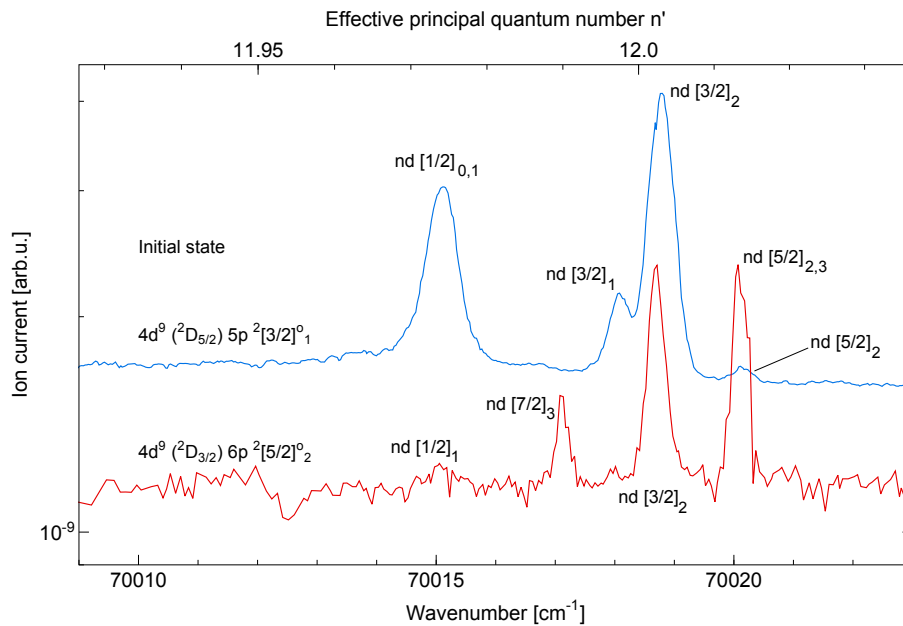


Figure 4.11: Low-energy section of the even parity Rydberg spectra in Pd. A first assumption of possible assignments is shown. Further measurements are required for a clear identification of the Rydberg states.

similar configuration and lower n , well below the IP, is rare and does not contribute to a clear identification at the here studied energy range [101]. Correspondingly, further spectroscopic investigations are required for a clear assignment of the Rydberg states.

4.2.2 Odd Parity Series

Using different 3-step schemes as shown in figure 4.7, three continuous wide frequency scans were performed in the ionization step, covering a wavelength range of 700-950 nm and addressing states of odd parity. The starting levels were $4d^9(^2D_{5/2})7s^2[5/2]_2$, $4d^9(^2D_{3/2})5d^2[3/2]_1$, and $4d^9(^2D_{3/2})5d^2[5/2]_2$. A continuous frequency scan starting from the state $4d^9(^2D_{3/2})5d^2[3/2]_2$ was not conducted, as the ionization rate of that particular scheme was rather low and data from two other starting levels with $J = 2$ was already available. With an spectral linewidth of 10 GHz most of the different components of the Rydberg states could be fully resolved. Figure 4.12 provides two spectra as example, each one containing about 250 individual resonances.

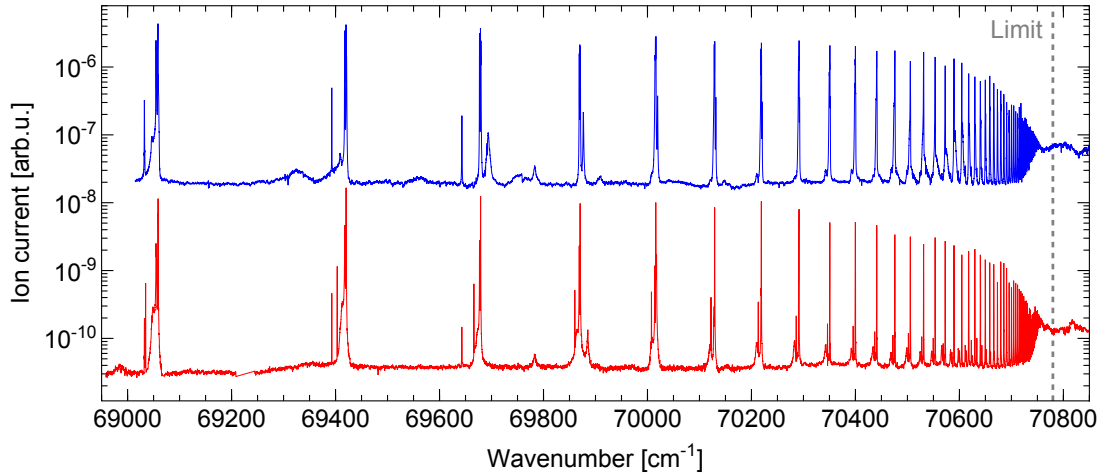
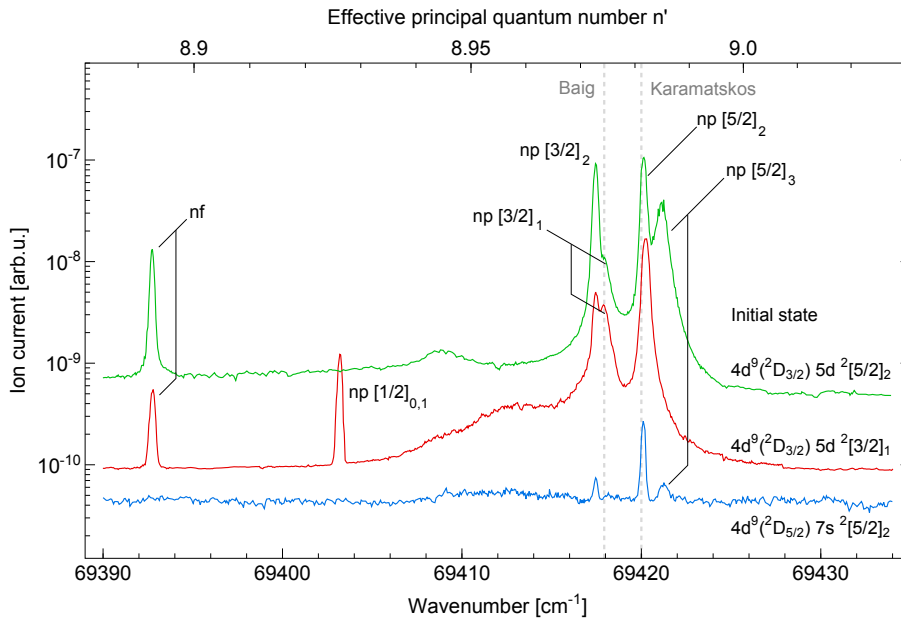


Figure 4.12: Rydberg spectra of odd parity from the frequency scans in the 3-step excitation schemes. The scans started from the states $4d^9(^2D_{3/2})5d^2[3/2]_1$ at 58408.296 cm^{-1} (red) and $4d^9(^2D_{3/2})5d^2[5/2]_2$ at 58448.705 cm^{-1} (blue). The ion current was scaled for a better view.

Table 4.2 compiles the Rydberg states, accessible from the initial states in this experiment. Figure 4.13 shows a section of the low-energy region of all three spectra, presenting the region where the effective principal quantum number n' is relatively small and the different components of the Rydberg series are well separated. As expected from 4.9, all np and nf resonances have n' close to integer values. Several peaks can be observed in all three spectra, indicating a np series which can be access from the $7s$ as well as from the $5d$ electron. In comparison, Karamatskos et al. [96] reported an unresolved resonance at $69420(14)\text{ cm}^{-1}$ with an spectral width of about 57 cm^{-1} . Therefore it was not possible to resolve the nf and np series and the resonance was assigned to a superposition of the states with $n' \approx 9$, namely $4d^9(^2D_{3/2})12p[1/2]_1^o$, $4d^9(^2D_{3/2})12p[3/2]_1^o$, and $4d^9(^2D_{3/2})9f[3/2]_1^o$. The experiments of Baig et al. [98] achieved a significantly higher resolution, reporting a resonance for at 69417.93 cm^{-1} which was assigned to $4d^9(^2D_{3/2})12p[1/2]_1^o$ and $4d^9(^2D_{3/2})12p[3/2]_1^o$. However, for the present spectra, as shown in figure 4.13, the situation is similar as for the even parity Rydberg series. A first assumption of possible assignments is shown in the graph, but an absolutely clear identification of all individual components can not be made on the basis of the available data. Further spectroscopic measurements are required to obtain more information which allows unambiguous assignments for all observed Rydberg states.

Table 4.2: Compilation of upper Rydberg states in Pd which can be addressed by dipole-transitions starting from the initial states given on the left hand side.

Initial state	Upper states $4d^9 ({}^2D_{3/2})$
$4d^9 ({}^2D_{5/2}) 7s^2 [5/2]_2$	$np^2 [1/2]_1^o, np^2 [3/2]_{1,2}^o, np^2 [5/2]_{2,3}^o$
$4d^9 ({}^2D_{3/2}) 5d^2 [3/2]_1$	$np^2 [1/2]_{0,1}^o, np^2 [3/2]_{1,2}^o, np^2 [5/2]_2^o$ $nf^2 [3/2]_{1,2}^o, nf^2 [5/2]_2^o$
$4d^9 ({}^2D_{3/2}) 5d^2 [5/2]_2$	$np^2 [1/2]_1^o, np^2 [3/2]_{1,2}^o, np^2 [5/2]_{2,3}^o$ $nf^2 [3/2]_{1,2}^o, nf^2 [5/2]_{2,3}^o, nf^2 [7/2]_3^o$

**Figure 4.13:** Low-energy section of the odd parity Rydberg spectra in Pd. The dashed gray lines indicate the energy of the resonances accessed from the $4d^{10} 1S_0$ ground state, observed by Baig et al. and Karamatskos et al. [98, 96]. A first assumption of possible assignments is shown. Further measurements are required for a clear identification of the Rydberg states.

4.2.3 Graphical Analysis of the Rydberg Series Limits

The limit of the observed Rydberg series was evaluated using a graphical evaluation method, similar to the analysis in [108, 48], which are in turn based on the work of Fano et al. [109, 27]. The approach is described in the following. Formula 4.2 can be used to plot the complete spectrum against the effective principal quantum number n' , as shown in figure 4.14 for the spectrum accessed from the state $4d^9 ({}^2D_{3/2}) 5d^2 [3/2]_1$ at $58408.296 \text{ cm}^{-1}$ and the accurate series limit, determined at the end of this section.

Without knowing the exact principal quantum number n of each Rydberg state, it is not possible to determine the precise value of δ . This problem can be overcome by making use

of the discrete nature of n . The remainder of δ can be calculated using the modulo function

$$\begin{aligned}\delta_{\text{re}} &= \delta - k \quad \text{with } k \in \mathbb{N} \\ &= \text{mod}_1(\delta) \\ &= \text{mod}_1(n - n') \\ &= \text{mod}_1(-n') \quad .\end{aligned}$$

This approach equals an assumption of a principal quantum number of

$$\begin{aligned}n_{\text{re}} &= n - k \\ &= n' + \delta_{\text{re}} \\ &= \lceil n' \rceil\end{aligned}$$

These variables will be referred to as the reduced quantum defect δ_{re} and the reduced principal quantum number n_{re} in this work.

The Rydberg spectrum can now be visualized by plotting the observed ion current against δ_{re} and n_{re} . During the computation, the n' spectrum was binned in intervals of 0.002, in order to reduce the computation time. Figure 4.15 shows such a 2D-plot for the frequency scan starting from the state $4d^9(^2D_{3/2})5d^2[3/2]_1$ at $58408.296 \text{ cm}^{-1}$, when using the literature value of 70779.8 cm^{-1} for the IP energy E_{lim} in formula 4.2. The display range is extended to $\delta_{\text{re}} > 1$ for a better view of the series. The strong ionization signal from the autoionizing Rydberg states is clearly visible, starting at about $\delta_{\text{re}} = 0$, respectively $\delta_{\text{re}} = 1$, indicating a close to integer value of δ , typical for the observed np - and nf -series. Due to the relation $\delta_{\text{re}} \propto (\sqrt{E_{\text{lim}} - E_n})^{-1}$, the resonances appear broader for higher n_{re} which leads to a growth of the width of the Rydberg series along the δ_{re} -axis in the plot. Furthermore, the plot reveals two significantly weaker series, which exhibit a change of δ_{re} from 0 to 1 in the region of about $n_{\text{re}} = 10$ -40, a peculiarity which is currently not completely understood. Further spectroscopic studies are required to allow a proper identification of this series.

The quantum defect δ is expect to stay constant, especially for higher n , resulting in a straight line for Rydberg series in the 2D-plot. In some cases, the Rydberg series can be disturbed by an interfering resonance in the spectrum, affecting the quantum defect and resulting in a sharp, local kink of the line. This is not observed in any spectrum obtained in the present work. Good examples of strong perturbation of Rydberg series can be found in [48, 110]. Figure 4.15 shows a significant trend of the calculated δ_{re}^* of the Rydberg resonances to lower values when using the value of $E_{\text{lim}} = 70779.8 \text{ cm}^{-1}$. This feature is consistently observed when visualizing all other spectra in the same way. This is a clear indication that this value is too low. The energy of the series limit can now be derived

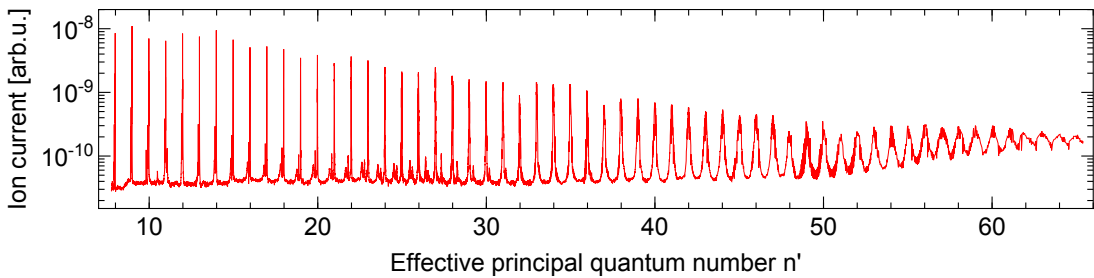


Figure 4.14: Spectrum of the frequency scans starting from the state $4d^9(^2D_{3/2})5d^2[3/2]_1$ at $58408.296 \text{ cm}^{-1}$, plotted against the effective principal quantum number n' . See text for more details description.

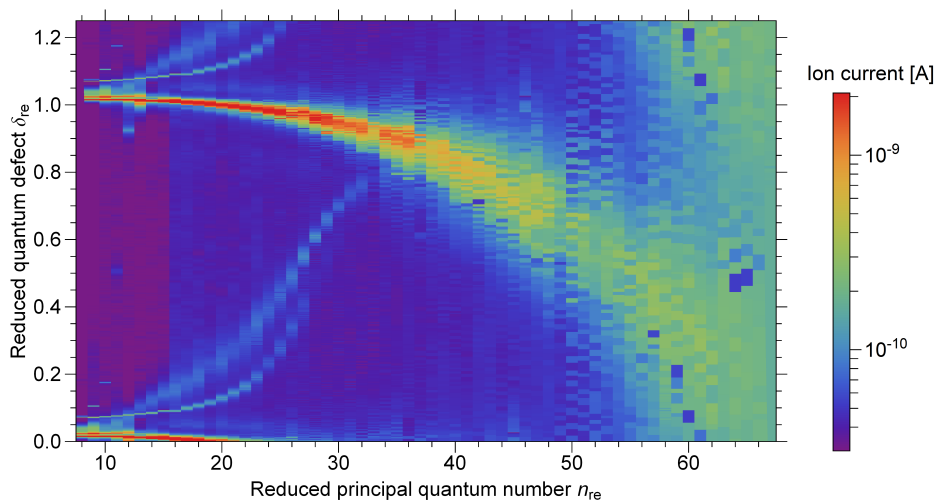


Figure 4.15: Color-coded 2-dimensional visualization of the spectra obtained with frequency scans starting from the state $4d^9(^2D_{3/2})5d^2[3/2]_1$ at $58408.296 \text{ cm}^{-1}$. The literature value of 70779.8 cm^{-1} was used as input parameter E_{lim} during the computation. The clear trend of the Rydberg series to smaller δ_{re} indicates that this energy is too low. See text for further description.

by altering the value for E_{lim} used in the computation of δ_{re} . The shape and horizontal alignment of the Rydberg series in the resulting graphs can be used to precisely determine the energy of the series limit. In addition, the logarithmic visualization of the same data projected onto the δ_{re} -axis can be used as further assistance to evaluate the straightness in the 2D-plot. The Rydberg series appears as clear peak, while any trend to higher or lower δ_{re} causes a clear asymmetry.

As an example, figure 4.16 shows 2D-plots for the determined series limit E_{lim} and for $E_{\text{lim}} \pm \delta E$, with δE being twice the estimated error. The corresponding projections of the data onto the δ_{re} -axis are shown in figure 4.17. Additional figures, showing the graphs of the other spectra, are given in the appendix in section A. With the well resolved spectra of the initial states $4d^9(^2D_{3/2})5d^2[3/2]_1$ and $4d^9(^2D_{3/2})5d^2[5/2]_2$, the value of E_{lim} with optimum horizontal alignment can be determined within $\pm 0.08 \text{ cm}^{-1}$. This is comparable to the precision of earlier experiments in the LARISSA laboratory, even though these experiments used evaluation methods which require time-consuming precise fitting of all individual peaks in the Rydberg spectrum. The resulting limits and their estimated uncertainty are summarized in table 4.3.

Table 4.3: Resulting energy limits of the graphical evaluation of the high-lying autoionizing Rydberg series in Pd.

Initial state	State energy [cm^{-1}]	E_{lim} [cm^{-1}]
$4d^9(^2D_{3/2})6p^2[3/2]_2^0$	58415.541	70780.50(12)
$4d^9(^2D_{5/2})7s^2[5/2]_2$	58138.648	70780.40(16)
$4d^9(^2D_{3/2})5d^2[3/2]_1$	58408.296	70780.46(8)
$4d^9(^2D_{3/2})5d^2[5/2]_2$	58448.705	70780.48(8)

The weighted mean of the different values in table 4.3 is used as final result for E_{lim} . In addition to the statistical errors in the table, a conservative systematic error of $2.5 \text{ GHz} \approx 0.08 \text{ cm}^{-1}$ is considered to account for possible systematic effects stemming from the waveme-

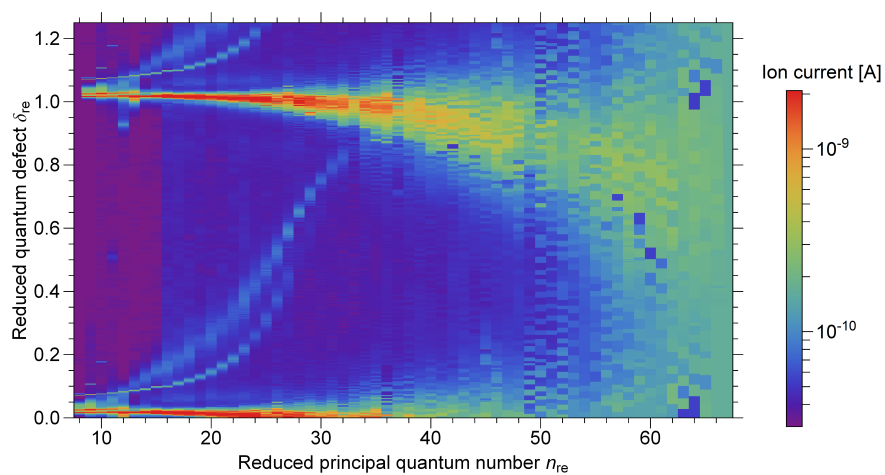
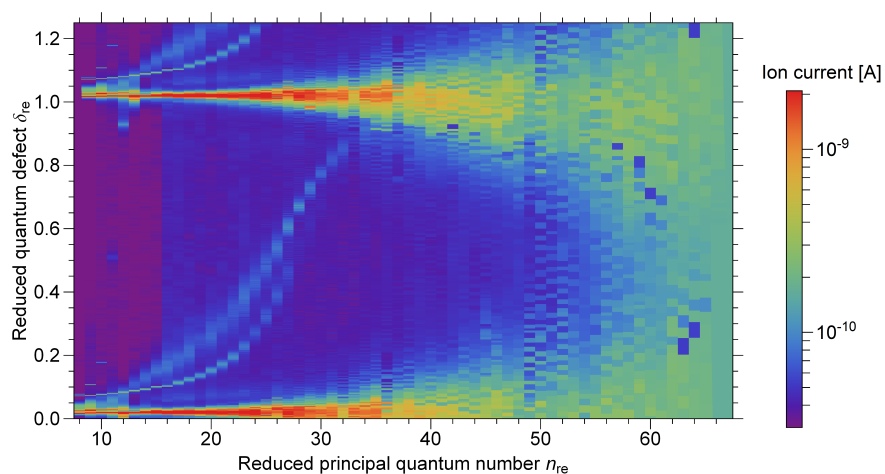
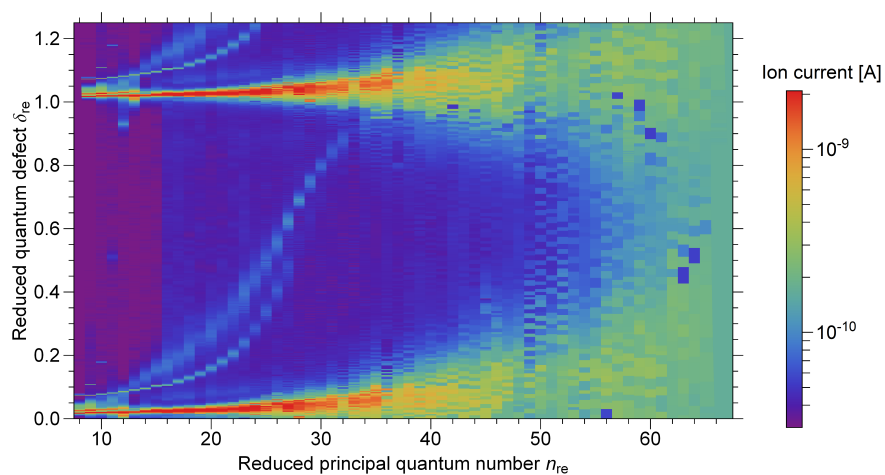
(a) $E_{\text{lim}} = 70780.26 \text{ cm}^{-1}$ (b) $E_{\text{lim}} = 70780.46 \text{ cm}^{-1}$ (c) $E_{\text{lim}} = 70780.66 \text{ cm}^{-1}$

Figure 4.16: Color-coded 2-dimensional visualization of the spectra obtained with frequency scans starting from the state $4d^9(2D_{3/2})5d^2[3/2]_1$ at $58408.296 \text{ cm}^{-1}$. The three graphs were generated for the different values of E_{lim} as given. See text for more details.

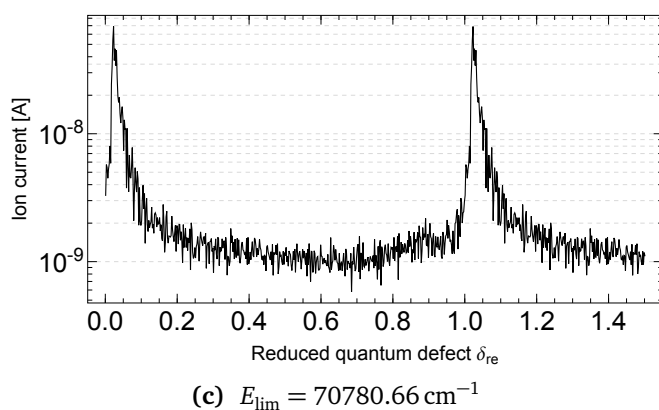
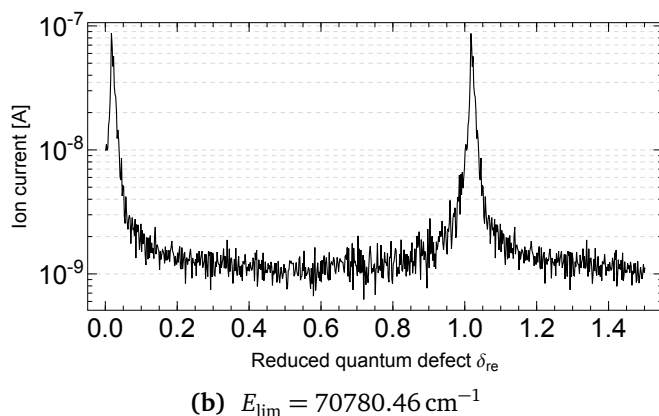
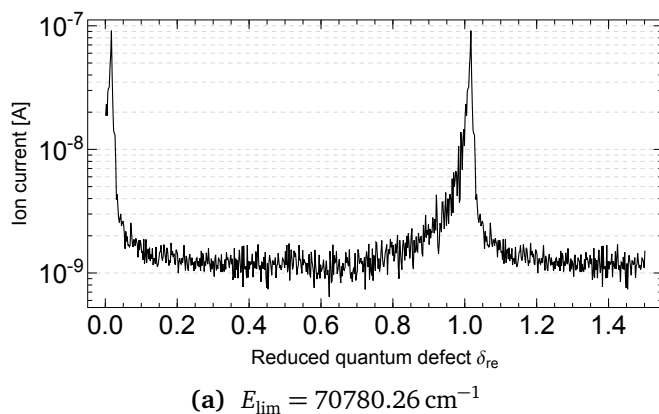


Figure 4.17: Projection of the data shown in the 2D-plots in figure 4.16 onto the δ_{re} -axis. The three graphs correspond to the same values of E_{lim} as given in figure 4.16. The asymmetry of the peak from the Rydberg series can be used to determine the straightness of the series in the corresponding 2D-plots. See text for more details.

ter or the literature values of the energy of the initial states considered. Hence, the final result for the series limit, representing the ionic state $4d^{9\ 2}D_{3/2}$, is $70780.47(8)_{\text{sys}}(5)_{\text{stat}} \text{ cm}^{-1}$. This is consistent with the previously reported values of $70779.8(8) \text{ cm}^{-1}$ and $70780.9(10) \text{ cm}^{-1}$ by Baig et al. [98] and Callender et al. [111], respectively, but increases the precision by about one order of magnitude.

In the ionic spectrum, the energy of the corresponding state $4d^{9\ 2}D_{3/2}$ was measured by Litzen et al. by the analysis of spectra from hollow cathode discharges, resulting in 3539.242 cm^{-1} [112]. An exact error of the energy is not directly stated in the article, but it can be assumed to be about $\pm 0.005 \text{ cm}^{-1}$, when considering the number of observed lines to this state and their stated uncertainty. Subtracting this energy from the series limit derived in the present work, one obtains an energy of $67241.23(9)_{\text{sys}}(5)_{\text{stat}} \text{ cm}^{-1}$ for the IP of atomic Pd, which is in very good agreement with the energy of $67241.3(8) \text{ cm}^{-1}$ determined by Baig et al. [98], but once again about one order of magnitude more precise.

4.3 Investigation of the Efficiency

Dedicated experiments are needed to investigate and compare the ionization efficiency of different ionization schemes. However, in general, this quantity cannot that easily be quantified individually. Therefore, it is reasonable to compare the ionization schemes with regard to the overall efficiency, the ratio between the detected ions and the well known number of atoms in the initial sample. This was done for the resonant 4-step and 3-step scheme for Pd, which were discussed in the previous section.

The overall efficiency ϵ is affected by several process and may be split up as

$$\epsilon = \epsilon_{\text{atomization}} \cdot \epsilon_{\text{ionization}} \cdot \epsilon_{\text{transmission}} \cdot \epsilon_{\text{detection}} \quad (4.3)$$

The first term describes the generation of neutral atoms in the gas phase inside the heated ion source. This strongly depends on chemical and physical characteristics of the sample. The atoms of interest might not be accessible in a sufficient quantity if the temperature for evaporation cannot be reached or if a significant formation of oxide molecules takes place. Correspondingly, the combination of the reduction agent in use, the ion source material, temperature, and the element of interest have major impact which cannot be predicted precisely. The ionization efficiency $\epsilon_{\text{ionization}}$ is usually the dominating variable in this equation. It depends on the excitation scheme, the laser powers used, and the thermal population of the addressed ground state. Also the relationship between the spectral linewidth of the atomic transition, typically broadened to several GHz, and the spectral linewidth of the exciting laser radiation have an significant influence. The latter is of special relevance when using isotopes with large HFS splitting. Also the ionization geometry is of major concern, as it determines interaction time and spectral coverage. Ion beam extraction and the ion transmission through the mass separator define the transmission efficiency $\epsilon_{\text{transmission}}$. Proper settings of the ion optics are essential for high transmission. Typically, magnetic mass separators with high acceleration voltages of several kV, like the RISIKO separator used here, reliably achieve transmission efficiencies well above 90 %. The last term, $\epsilon_{\text{detection}}$, describes the detection efficiency. As all conducted measurements used ion current detection on a Faraday cup, the detection efficiency can be assumed to be very close to 100 %. However, electron sputtering from the detection electrode must be reliably prevented, as it would artificially increase the read ion current. Considering all that, the overall efficiency is a benchmark for the ionization scheme as well as for the complete experimental setup.

4.3.1 Sample Preparation Process

All efficiency measurements were performed on samples of natural Palladium with the isotopic abundances as given in figure 4.1. A well defined amount of several micro liters of a certified standard solution, were dropped onto a small metallic foil and volatilized at gentle temperatures of about 50 °C. The water of the solution evaporated, leaving behind a well known amount of Pd on the surface of the foil. The metallic foil served for two purposes. First, it acted as a substrate safely mounting the deposited, microscopic sample, which would not enter any solid form with sizes well below 10^{16} atoms. Secondly, the material of the foil acts as a reduction agent in the later heating and atomization process inside the ion source. Afterwards, the foil was folded three to five times and placed in the reservoir capillary of the RISIKO ion source (see section 3.2.1). The folding ensures a complete enclosure of the sample which is needed to guarantee maximum interaction probability between the Pd atoms and the reduction agent. Figure 4.18 shows photographs of the sample during different stages of the preparation process.



Figure 4.18: Photographs of the sample preparation process. From Left: Drop of acid solution containing the natural Pd on a $5 \times 5 \text{ mm}^2$ metallic Zr foil. Center: Sample after evaporation of the solution. The residue of the solution is visible as dark spot. Right: Folded sample, length 2.5 mm. See text for further description.

Two kinds of solution have been used. The first⁷ was an *atomic absorption standard* (AAS) based on 5 % hydrochloric acid (HCL), the second⁸ was based on 5 % nitric acid (HNO₃). The latter was not available at the beginning of the experiments and was acquired to test possible positive effects to counteract the slow release of the Pd which was observed during the first efficiency measurements. During the experiment, no difference in release or efficiency between the two solutions was found. Well defined aliquots of the AAS solution were directly dropped onto the metallic foil, or diluted with purified water beforehand to get smaller atom numbers per sample. After the evaporation process, the Pd atoms remained on the foil surface in the chemical form of palladium chloride PdCl₂ or palladium nitrate Pd(NO₃)₂, respectively. These salts decompose during the heating process, releasing Pd or Pd oxide, which is then reduced by the metallic foil.

Titanium and zirconium foil were tested as reduction agents for Pd, as they offer suitable chemical properties, similar for both elements as they are isoelectronic and have analog atomic ground states of [Ar]3d²4s² and [Kr]4d²5s², respectively. However, they differ in regard to their melting points, which is crucial for proper operation of the ion source. Basically, the melting point should be higher as the melting point of the sample, to ensure a proper reduction process at higher temperatures, when the sample is being released. Palladium has a melting point of 1555 °C, whereas the melting point of Ti is 1668 °C and 1855 °C for Zr. As the melting point is only about 100 °C higher in the case of Ti, it is likely that it will evaporate quickly during the measurement. Therefore it was expected to obtain a more stable ion current at high temperatures when using Zr.

The resulting uncertainty of the number of Pd atoms in each sample was dominated by the uncertainty of the pipetting process. It was estimated to be 3 - 5 %. The evaporation process as well as the folding of the foil were considered not to change the number of atoms deposited on the foil significantly. Other uncertainties, like the Faraday cup readout, were significantly smaller and therefore could be neglected. Therefore, a conservative relative uncertainty of the number of atoms of 5 % was considered for each individual sample. For each measurement, an uncontaminated reservoir capillary, either new or stemming from earlier experiment which did not use Pd as sample, was installed in the ion source and the sample was inserted.

4.3.2 Measurement Analysis

The overall efficiency is defined by the ratio between the number of atoms of the selected isotope in the initial sample and the number of ions detected with the Faraday cup detector.

⁷SIMGA-ALDRICH, Palladium atomic absorption standard solution

⁸Alfa Aesar, Palladium plasma standard solution, Specpure

The initial number of atoms per isotope on the sample is determined using the total number of Pd atoms from the sample preparation and the natural isotope abundances. The number of ions detected with the Faraday cup was determined by integrating the recorded ion current over time.

Laser-independent processes can cause non-resonant ionization. This background is primarily created by non resonant surface ionization in the hot ion source. In the thermal equilibrium, the ratio of neutral atoms and ionized atoms can be described using the Saha-Langmuir equation for singly ionized atoms:

$$\frac{n_i}{n_0} = \frac{g_i}{g_0} \exp \left[\frac{E_W - E_{IP}}{k_B T} \right] . \quad (4.4)$$

Here, n_0 and n_i are the densities of ionized and neutral atoms and g_i and g_0 are the degeneracies of ionic and atomic states. The difference between the ionization potential E_{IP} and the work function E_W of the material of the hot surface is of special importance as it defines if the exponent is positive or negative. If the work function of the surface material exceeds the ionization potential, the volatilization from the hot surface as ion is energetically favored, resulting in a high surface ionization rate. As the ionization potential of Pd of 8.3 eV is relatively high and exceeds the work function of the ion source's tantalum material $E_{W,Ta} = 4.2$ eV significantly, the corresponding surface ionization current was very low, typically less than 0.1 % of the overall ion signal.

During the individual measurements, the level of laser-independent background ion current was quantified by a regular blocking of the laser beams. In this way, the ratio of laser ion current and laser-independent background current was monitored over the course of the measurement. This data was used to calculate a continuous background current by scaling the smoothed⁹ laser ion current accordingly. This procedure also accounts for fast increases of the background current due to an increase of the ion source temperature, which would not be considered by a simple linear interpolation between the measured levels of the background current. However, when comparing both approaches, the difference in the number of accumulated background ions for the complete measurement is quite small, corresponding to less than 0.01 % of the initial number of atoms in the sample, which is negligible when compared to the uncertainty introduced by the sample preparation process. The background signal was not included in the final efficiency. Hence, the background current was subtracted from the laser-induced ion current before calculating the final efficiency.

If mass scans were performed during the long lasting periods with stable ion current, the data was adapted to consider the produced ions of the isotope of interest and to exclude ion signal of other masses. When the laser beams entered the ion source, causing resonance ionization, the ion current level was extrapolated for the duration of the mass scan. In this case, the maximum of the corresponding mass peak in the mass spectrum was used as well. During periods without laser beams entering the ion source, the corresponding background level was assumed as no atoms were resonantly ionized in the source. This is a conservative approach as for the duration of this period a larger amount of neutral atoms could leave the source compared to operation with the laser beams resonantly ionizing in the source. However, the depletion of the gaseous sample is slowed down without laser beams, as the source provides a slightly better buffer capability for neutral atoms than for ions. This can be clearly observed on the data in figure 4.19, which shows the behaviour of the ion current when blocking the laser beams. After unblocking the laser beams, the ion current increased and exceeded the ion current level before the blocking, clearly indicating an accumulation of Pd atoms inside the ionizer tube during the period with blocked laser beams. As shown

⁹The data was smoothed using a floating median average.

in the graph, the ion current normalized over the period of several seconds up to about one minute.

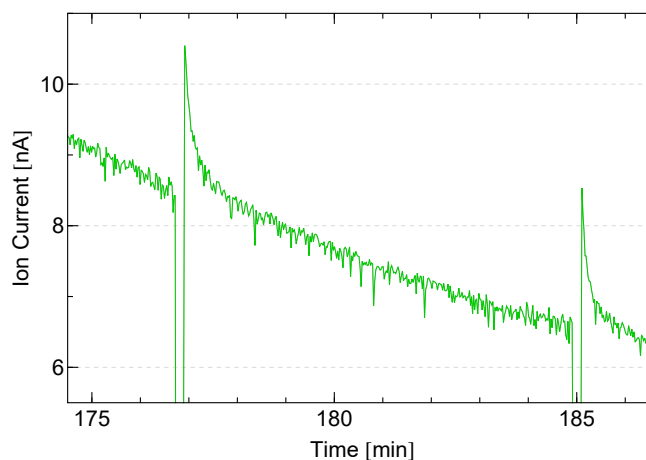


Figure 4.19: Typical overshoots of the ion current after blocking of the laser beams. See text for details.

The accumulation of neutral atoms in the ionizer can be partially explained, as the neutral atoms do not experience the force caused by electrical field across the ionizer tube, which is created by the resistive heating and the corresponding voltage drop of about 2 V. Therefore depletion of the ionizer volume is strongly enhanced with the laser ionization. In addition, the higher overall concentration of neutral Pd without laser radiation can cause an increase of adsorption on the interface of the tantalum material of the ionizer tube as this is an equilibrium process. When the laser ionization takes place after such an accumulation period, the concentration of Pd atoms in the ionizer is decreased, leading to a re-evaporation of the adsorbed Pd. This re-evaporation takes several seconds, whereas the depletion of the Pd in the gaseous phase happens within a few laser pulses over the course of a few hundred to thousand microseconds. The description of the adsorption process at high temperatures is quite complex and depends strongly on the adsorption enthalpy of the material combination, the temperature, and the microscopic texture of the solid surface. Unfortunately the adsorption enthalpy of palladium on solid Ta is not well characterized in literature. More complexity is added to the problem, as the temperature across the tube is not completely homogeneous and the interface is curved which introduces possible effects from surface tension.

4.3.3 Measurements at the RISIKO Separator

The following subsection describes the efficiency measurements at the RISIKO mass separator at Mainz university which was described in section 3.2.1. The spacing of the slit behind the sector field magnet was set to about 1.5-2 mm. The typical process of an efficiency measurement at the RISIKO separator can be described in successive steps and phases. In a first step, the heating current of the ionizer tube was smoothly heated to a maximum of 320 A, which corresponds to a temperature of about 2400 °C. For technical reasons, this also introduced a small current of about 15 A draining through the reservoir capillary, resulting in a gentle heating of the capillary and the sample. In most cases, this heating and the heat from the hot ionizer tube were sufficient to evaporate very small amounts of Pd, resulting in small ion currents of Pd in the range of a few pA, observed when the laser beam entered the source and were correctly tuned on resonance. In case of no observable signal, the current for the resistive heating of the reservoir capillary was smoothly turned up to about 40 A. This

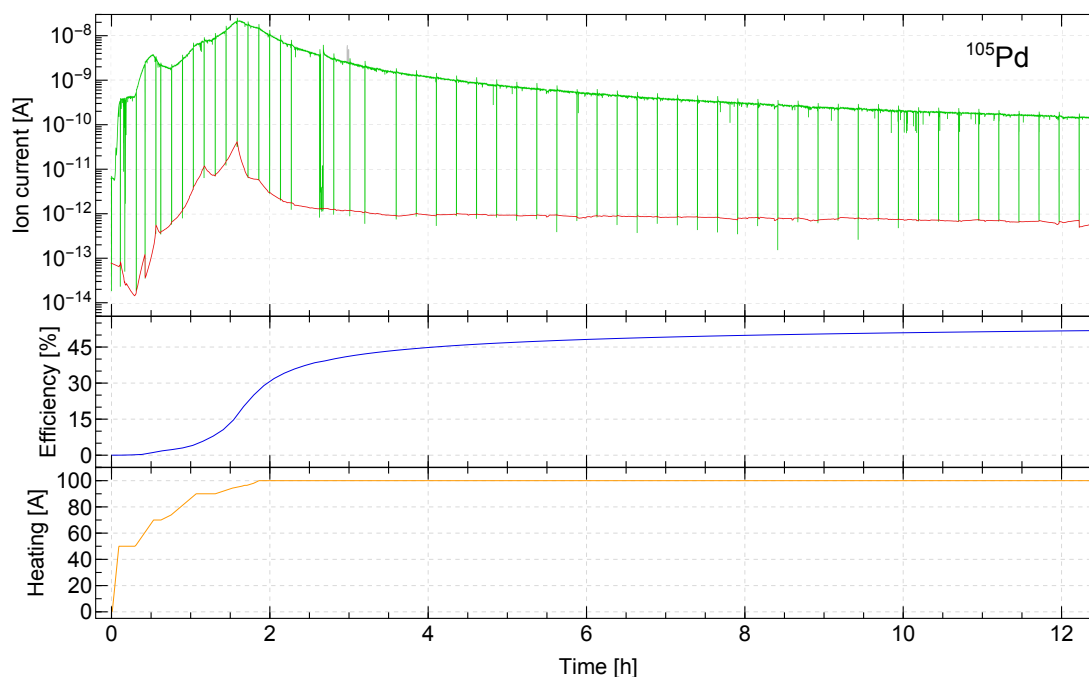


Figure 4.20: Course of a typical efficiency measurement on ^{105}Pd on the RISIKO mass separator. The ionization scheme used here was the 3-step scheme as depicted in figure 4.8. The upper graph show the ion current in green and the underlying laser-independent background in red. Gray sections indicate ion current which was not taken into account for the determination of the overall efficiency. See text for details.

resulting ion signal was used for the first optimizations, which included a full optimization of all ion optical settings, fine tuning of the mass separation, and the optimization of all ISST-parameters of the laser radiation. The recording was typically started at a total ion current of 0.5 to 5 pA on the mass of choice. A typical course of an efficiency measurement is shown in figure 4.20.

In the next phase, the heating current of the reservoir capillary was slowly and smoothly increased, while the heating current of the ionization tube was kept at its maximum. The resulting increase of temperature of the sample led to an according increase of the detected ion current. Regular checking and optimization of the previously mentioned settings ensured optimal operation conditions and maximization of the ion current. As explained in the previous section 4.3.2, the background due to non-resonant surface ionization was regularly determined by blocking of the laser beams in front of the separator. Please note, due to the long overall timescale of the experiments, the decrease in ion current due to the blocking appears as sharp vertical lines in the graph. Due to the logarithmic scaling and a slight negative overshoot in the Faraday cup readout, some lines reach lower than the actually observed background current.

An important point was reached at a capillary heating current of about 80 A. At this point the ion current started to increase significantly, even when the heating current was kept constant, and showed a high sensitivity to every little increase of the of the heating current, i.e. the temperature of the reservoir capillary. Systematic studies of the temperature distribution in the ion source showed that at this heating current, the part of the capillary where the sample was placed heats up to about 1700 °C [76, 113]. Correspondingly, the sample's temperature exceeded the melting point of Pd of 1555 °C. The significant release of the sample when reaching the sample's melting point is a typical effect observed at laser ion sources when using such samples or macroscopic amounts of the element of interest.

Due to the low pressures in the order of 10^{-6} mbar inside the mass separator, the boiling point is significantly reduced, resulting in a significant transition rate into the gas phase when reaching the melting point of the sample.

After this initial point of release, the capillary's heating current was successively increased to its maximum value of 100 A, while the ion optic settings and the ISST-parameters were still regularly inspected to ensure optimal operation conditions. Typically the maximum heating current was reached after about 2.5 hours of operation. Using higher heating currents above 100 A, would have a high risk of fatal damage for the reservoir capillary. In addition, above 95 A, the ion current showed only minor response to further increase of the heating current. At maximum temperature, the total ion current reached its maximum of a few nA. The following phase is characterized by the depletion of the sample and a corresponding decrease of the total ion current. As shown in figure 4.20, this observed decrease in ion current was very slow when compared to earlier efficiency measurement of other elements, for example ytterbium or holmium [44, 113, 114], where the measurement was typically completed after 2 – 4 hours. The present measurements were stopped when the ion current reached a lower limit of about 100 pA or less, as further accumulation did only contribute very little to the overall efficiency. Due to the very slow depletion rate, each measurement took about 10 – 20 hours in total. This issue of the exceptional slow depletion is addressed separately in section 4.3.5. The complete setup proved excellent stability over the course of these long-term operations. Ion optical settings and the ISST parameter of the laser system were also inspected during the long-lasting depletion phase, but required none to only minor corrections.

Results for the 4-Step Scheme

The efficiency measurements presented here used the 4-step scheme from figure 4.6. The measurements were performed on the isotope ^{108}Pd for two reasons. First, it offer similar high abundance as the most abundant isotope ^{106}Pd . This ensured a suitably strong signal, while the total amount of Pd in the sample could be kept low. This was favorable as it avoided unnecessary palladium contaminations of the separator setup. Secondly, as shown in the mass spectrum in 4.2, the ion signal on mass 106 is free from any measurable contributions from the neighboring masses 107 and 109, which could have affected the detected ion current on mass 106. This precaution was very conservative, as the RISIKO mass separator reliably achieved a suppression of the neighboring masses well above 10^4 at this mass range. Therefore, contributions from neighboring masses were absolutely negligible compared to the uncertainty of the initial number of atoms in the sample.

The results of the measurements are summarized in table 4.4. It must be mentioned that the data needed some special treatment due to technical difficulties. After the measurement campaign, it was found that the cable for the repeller electrode inside the Faraday cup was broken. During normal operation, the negative potential of this electrode suppresses the sputtering of electrons from the detection electrode, induced by the impact of the 30 keV ions. If electrons may leave the detection electrode, the detected positive current is artificially increased. On the other hand, the electrons emitted by the detection electrode led to a negative charge on the unconnected repeller electrode, as illustrated in figure 4.21, which counteracted the emission of electrons from the detection electrode. Therefore, the situation was unclear but considerably different to operation with repeller electrode on 0 V ground potential, which showed improper enhancement factors of about 2 – 3 in the detected ion current, in agreement with observations in earlier experiments. After the repair of the cable, the effect of an unconnected repeller electrode was investigated during the following measurements using the 3-step scheme in Pd. Figure 4.22 shows the result

of these measurements. The maximum observed ion currents during the 4-step efficiency measurements were below 2 nA. The corresponding amplification factor due to the sputtered electrons was determined to be 1.60(16). To account for this problem, all detected ion currents during the measurements with the 4-step scheme were divided by 1.60 and an additional relative uncertainty of 10 % was taken into account. After the repair, the correct function of the repeller electrode was verified regularly in the following measurements for the 3-step scheme.

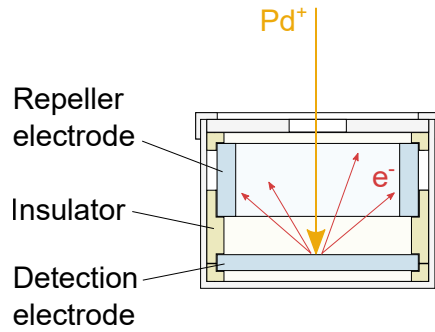


Figure 4.21: Cross-section of the Faraday cup, visualizing the sputtered electrons due to the impinging 30 keV Pd ion beam. See text for more details.

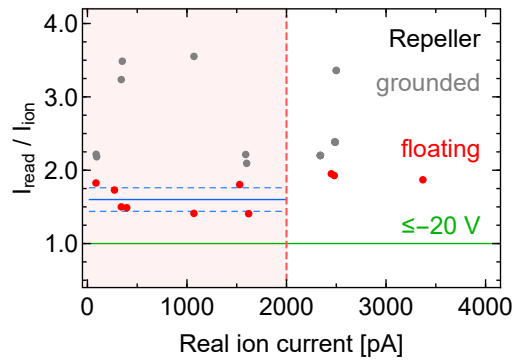


Figure 4.22: Influence of grounded, floating, and properly working repeller electrode. The Faraday cup readout I_{read} is artificially increased when operating with floating (red) or grounded (gray) repeller electrode. During the efficiency measurements using the 4-step scheme ion currents of 2000 pA and below were observed (light red colored area) while a technical failure caused a floating repeller electrode. The blue line indicates the corresponding mean value of 1.60(16) and the corresponding error interval. Under proper conditions, with ≤ -20 V applied to the repeller electrode, the correct current is observed (green).

Table 4.4 gives an overview of the conducted efficiency measurements with the 4-step scheme. It includes the total number of Pd atoms in the sample, the corresponding number of atoms of the ^{108}Pd isotope, the total time of the recorded ion current, and the corrected value of the overall efficiency ϵ . As mentioned, the contribution of the laser-independent background was subtracted. During all measurements, this surface ionized background was about three orders of magnitude smaller than the total ion current. On average, the accumulated background current yielded well below 0.01 % of the initial number of ^{108}Pd atoms in the sample. As mentioned above, this originated from the low surface ionization rate of Pd due to its high ionization potential. As mentioned above, the Nd:YAG laser used in the

third excitation step showed a significant temporal jitter. It is possible that this unfavorable situation caused a slight reduction of the overall efficiency, but this influence could not be investigated as no other suitable laser was available. The efficiencies in table 4.4 result in a mean value of 14.6(13)%, which is reproduced quite well in the three measurements. In earlier efficiency studies on other elements, the obtained efficiency values scattered typically up to $\pm 10\%$ of the mean value. In contrast, the present measurements series shows only small relative variations of about $\pm 2\%$, which indicates a reliable operation at optimum conditions of laser system, ion source, and mass separator. This also includes a good reproducibility of alignment and assembly of the ion source, when changing the reservoir capillary and the sample. The reproducibility of the efficiency might benefit from the fact, that the majority of the Pd was released during the long depletion phase at maximum ion source temperature, when the setup reached a state of high stability.

Table 4.4: Results of the efficiency measurement using the 4-step scheme at the RISIKO mass separator. In all measurements, the overall efficiency ϵ was determined using the isotope ^{108}Pd . See text for more details.

#	Total amount Pd	^{108}Pd	Duration [h]	ϵ [%]
1	$2.83 \cdot 10^{15}$	$7.49 \cdot 10^{14}$	13.3	14.5(22)
2	$2.83 \cdot 10^{14}$	$7.49 \cdot 10^{13}$	7.5	14.8(22)
3	$2.83 \cdot 10^{14}$	$7.49 \cdot 10^{13}$	7.9	14.6(22)
Mean				14.6(13)

Results for the 3-Step Scheme

The three most abundant isotopes ^{105}Pd , ^{106}Pd , and ^{108}Pd were used for the efficiency measurements for the 3-step ionization scheme which is illustrated in figure 4.8. Several reasons led to the change of the isotopes of interest. First, it was intended to identify possible isotope specific effects on the ionization efficiency. Such effects, could influence the ionization rate of even-A and odd-A isotopes when using broad-band laser radiation and were repeatedly reported in the past [115, 116]. This phenomenon can be explained by the influence of HFS splittings of a transition and the resulting variation in the absorption of the available spectral power density. However, no evidence for this effect was observed during the measurements on Pd, in agreement with the fact that no significantly large HFS splitting was observed and all transition could be highly saturated. The final efficiency measurements were carried out on ^{105}Pd . This was due to the change of the metallic foil of the sample from titanium to zirconium. The latter was suggested as better suitable reduction agent with similar chemical and reduction properties as Ti, but higher melting point. Correspondingly, it was expected to improve the depletion of the ion source during the long-lasting period on maximum temperature which led to further extended measurement times of more than 12 hours. Due to its lower melting point, it was likely that all the Ti might be evaporated from the ion source before the Pd was completely depleted. However, no measurable difference in efficiency or depletion rate was found when using Ti or Zr. However, the usage of Zr offered a slightly smoother gain of the ion current, when heating the reservoir capillary from 75-100 A, a noticeable benefit for the optimization procedure. Unfortunately, the change from Ti foil to Zr foil introduced a strong background of surface ionized ZrO in the mass spectrum at $m = 106-112$ u. The surface ionized ZrO background, as shown in figure 4.23 in red, clearly reproduced the natural abundance of the Zr isotopes. The rate of surface

ionized ZrO behaved significantly different with regard to ion source temperature than for Pd, making a precise quantification of the contribution of ZrO^+ to the detected ion current at the most abundant Pd masses 106 u and 108 u quite difficult. Consequently, the isotope ^{105}Pd became the most suitable one for the present efficiency measurements.

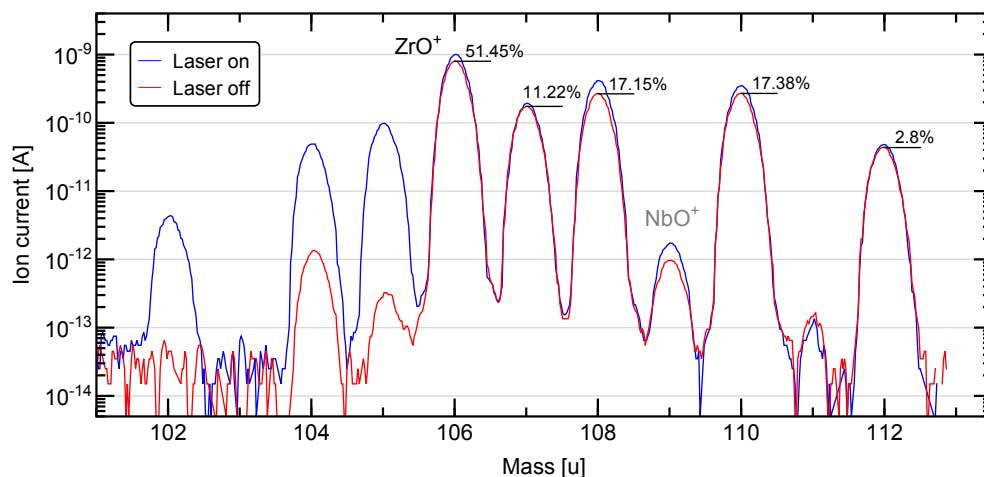


Figure 4.23: Mass spectrum of the Pd region at the RISIKO mass separator when using Zr foil in the sample. A strong background due to surface ionized (red) zirconium oxide is clearly visible. The black markers indicate the isotopic abundance of natural ZrO, taking into account the dominant presence of the ^{16}O isotope which has a natural abundance of 99.8% [95]. These expected ratios are in excellent agreement with the experimentally observed ratios. A linear plot is provided in figure A.1 in the appendix.

Table 4.5 summarizes the results of the efficiency measurements obtained by using the 3-step ionization scheme. It also indicates significant changes of the experimental setup, like major improvements of the ion optic voltages or a physical re-adjustment of the ion optic electrodes. The same data is illustrated graphically in figure 4.24. Several dedicated measurements on blank samples were performed between the efficiency measurements and confirmed the absence of unwanted Pd contaminations. In addition, during the preparation of each measurement, the ionizer tube was heated with active laser beams, while keeping the freshly installed reservoir capillary unheated, in order to check for any unexpected signal in the Pd mass region. These tests also proved the absence of any additional sources of Pd. Further details of the blank measurements are discussed at the end of this section. The first three efficiency measurements were performed directly after the measurements using the 4-step scheme. Therefore, they were also affected by the broken cable of the Faraday cup repeller, as described in the previous section. To determine the correct efficiency, the number of detected ions was corrected correspondingly and a larger error assumed. After measurement # 3, the measurement campaign was interrupted for several month after a total breakdown of the primary turbomolecular pump in the vacuum system.

After resuming the experiment, overall efficiencies from 21.4% to 36.1% could be achieved in measurements # 4 - # 10. These are already decent values compared to efficiency experiments on other elements. As previously mentioned, replacing the Ti foil by Zr foil in measurement # 7 introduced an unexpected, large background, requiring the use of the isotope ^{105}Pd in the subsequent measurements. The rise of the background while increasing the ion source temperature can be seen in the diagram of the measurement in figure A.9 in the appendix. It cannot be completely excluded, that the result of measurement # 7, on ^{105}Pd might be affected by the strong background, which exceeded the laser ionized fraction during some phases of the measurement.

Table 4.5: Chronological overview of the efficiency measurements performed with ^APd using the 3-step scheme at the RISIKO mass separator.

#	Total Pd	A	Duration [h]	ϵ [%]	Comment
1	$2.8 \cdot 10^{15}$	108	10	17.7(27)	Optimization of setup
2	$2.8 \cdot 10^{15}$	108	23	41.8(63)	
3	$5.7 \cdot 10^{15}$	108	25	34.3(51)	
Breakdown of turbomolecular pump					
4	$5.7 \cdot 10^{15}$	106	25	11.5(6)	Optimization of setup
5	$5.7 \cdot 10^{15}$	106	29	29.0(14)	
6	$5.7 \cdot 10^{15}$	108	18	21.4(11)	Contact problem of reservoir capillary
7	$5.7 \cdot 10^{15}$	108	16	36.1(18)	Potentially influenced by strong ZrO background
Adjustment of ion optics and magnet settings					
8	$5.7 \cdot 10^{15}$	105	17	23.2(12)	} Mean: 23.1 %
9	$5.7 \cdot 10^{15}$	105	20	21.7(11)	
10	$7.9 \cdot 10^{15}$	105	20	24.3(12)	
Optimization of ion optical settings					\Rightarrow 50 % higher ion transmission $\Rightarrow \epsilon \approx 34.7$ % expected
11	$4.5 \cdot 10^{15}$	105	23	34.2(17)	
12	$4.5 \cdot 10^{15}$	105	5	22.6(11)	Reservoir capillary lost contact
Replacement of ion source parts and re-alignment					New ionizer, mounting plate and heat shield Mechanical difficulties during alignment
13	$4.5 \cdot 10^{15}$	105	15	21.4(11)	Evidence of misalignment and Reservoir capillary lost contact
Replacement of mounting plate					Modification of screw holes Extensive adjustment of ion optics
14	$4.5 \cdot 10^{15}$	105	18	60.1(30)	
15	$4.5 \cdot 10^{15}$	105	16	52.6(26)	
16	$4.5 \cdot 10^{15}$	105	20	54.8(27)	
17	$4.5 \cdot 10^{15}$	105	20	52.6(26)	

As already mentioned, due to the exceptional slow depletion rates, it was required to operate the ion source at highest temperatures for more than 15 hours, causing a high level of thermal stress for the ion source. In some cases, it was required to replace distorted parts of the ion source and re-optimize the axial alignment of ion source and ion optics, in particular the extraction electrode. A precise spatial alignment with offsets less than 1 mm is an important prerequisite to guarantee optimal ion extraction from the ion source and a maximum ion transmission through the separator setup. The axial alignment was thoroughly evaluated with the help of a theodolite. A cause for the slow depletion and the long-term operation was the temperature distribution within the ion source itself. This issue is discussed in the following section 4.3.5.

During measurements # 12 and # 13, the ion source could not be properly operated, as the reservoir capillary slowly lost contact to the ionizer tube, preventing further transport of the evaporated Pd as well as proper resistive heating. This eventually led to an early abortion of the measurement. However the overall efficiency values were about 22 %, which

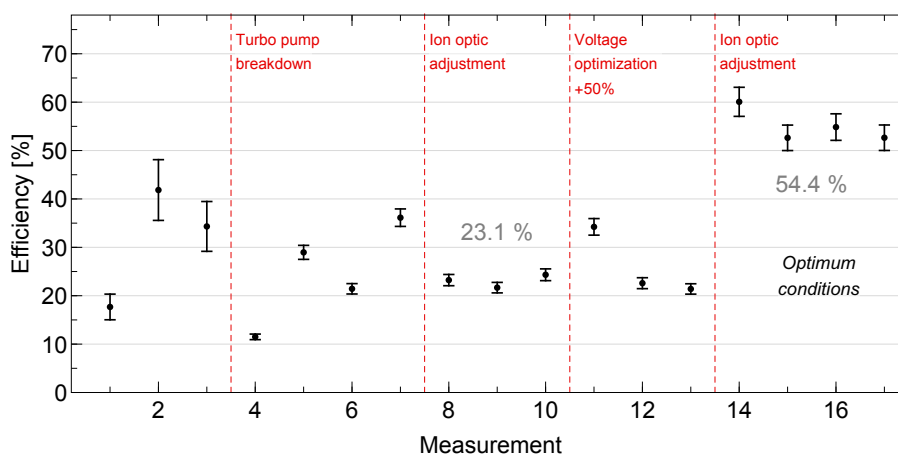


Figure 4.24: Graphical representation of the overall efficiency values for Pd obtained using the 3-step scheme from table 4.5. The dashed red lines indicate major changes of the setup which influenced the overall efficiency significantly.

already indicated a high overall efficiency under proper conditions. After measurement # 13, several parts of the ion source were replaced due to significant thermal distortion and the extraction electrode was re-aligned again very carefully. In addition, the mounting plate was mechanically modified to achieve best possible alignment, as this was a limiting parameter in previous alignment procedures. In particular, the axial alignment could be significantly improved compared to the previous measurements. Subsequently, the set of voltages applied to the ion optics as well as the magnetic field in the sector field magnet were extensively re-optimized, resulting in a significant increase of the ion extraction and transmission through mass separator. This led to an improved overall efficiency during the subsequent measurements # 14 - # 17, yielding an outstandingly high average value of about 55 %. Graphical presentations of these four measurements are provided in section A in the appendix.

Similar to the measurements with the 4-step scheme, the scatter of the obtained efficiency values in these final measurements is relatively small, indicating a proper operation of setup in terms of laser system and mass separator. For example, the absolute scatter of the efficiencies obtained in measurements # 8 - # 10 is only $\pm 1.3\%$, corresponding to a relative scatter of about $\pm 6\%$ of the corresponding mean value. The overall efficiencies obtained in the last four measurements # 14 - # 17 span from 52.6 % to 60.1 %, which also resembles a similarly relative scatter of $\pm 7\%$. These are small variations compared to earlier experiments, where relative scatters of 20 % and more were observed.

Measurements on blank samples were performed regularly between the efficiency measurements. These confirmed the absence of any Pd contaminations within the tantalum material of the ion source, the metallic sample foils, or introduced by the sample preparation process. In addition, an independent measurement using *neutron activation analysis* (NAA) of a ^{165}Ho sample on the same kind of Ti foil was carried out at the *Institute of Nuclear Chemistry* at Mainz university [117, 114, 118]. The results based on this completely different experimental approach also proved the absence of any measurable quantities of Pd in the Ti foil or introduced by the sample preparation. The measurements on blank samples were also used to characterize the minor amount of Pd which remained in the ionizer tube after an efficiency measurement. This memory effect must be accepted as a complete depletion of Pd down to the fA-level would have required several days of time. The ionizer tube is the only element where a significant amount of Pd might remain, as each measurement

used a new, uncontaminated reservoir capillary. This minor memory effect was found to correspond to an amount well below 2% of the initial sample size and was correlated to the final ion current at the end of the finished measurement.

To account for this effect, the last four measurements with efficiency values above 50% were corrected during the data analysis. Figure 4.25 illustrates the correction procedure. For each measurement, the number of ions corresponding to the remains of the previous measurement were subtracted and added to the number of detected ions of the corresponding previous measurement. It is clear that this treatment only exchanged certain number of ions between the efficiency measurements and did not alter the total number of ions detected during the measurements. As the measurements were finished at similar ion currents and were conducted using equal sample sizes, the amount of remaining Pd in the ion source was similar, leading to only minor changes of ϵ . The corrected results for the overall efficiency $\epsilon_{\text{corrected}}$ are presented in table 4.6 together with the final mean value of the overall efficiency for the 3-step scheme of 54.3(14)%. As expected, the correction procedure decreased the scatter of the individual values. It also decreases the mean values, as the correction also erases the contribution of the residual amount of Pd stemming from measurement # 13, being slightly larger as this measurement was stopped at a slightly higher ion current level.

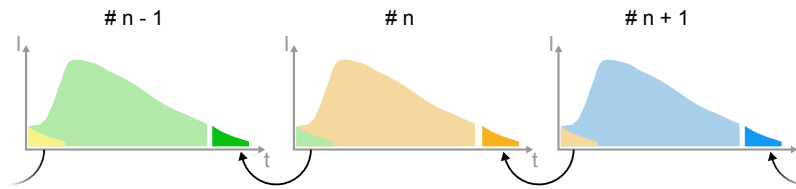


Figure 4.25: Schematic visualization of the correction of the efficiency values, due to minor amounts of Pd remaining in the ionizer tube. The residual amount of Pd after a measurement subject to the final total ion current was determined with measurements on blank samples. In this way the corresponding amount could be determined for each measurement and was assigned to the correct measurement. See text for detailed explanation.

Table 4.6: Correction of the final overall efficiency values for the 3-step scheme. See text for explanation.

#	ϵ [%]	$\epsilon_{\text{corrected}}$ [%]
14	60.1(30)	57.5(29)
15	52.6(26)	53.4(27)
16	54.8(27)	53.9(27)
17	52.6(26)	52.6(26)
Mean	55.0(14)	54.3(14)

4.3.4 Efficiency Measurements at the IRIS2 Separator at ORNL

The measurements using the 3-step scheme at the RISIKO mass separator at Mainz university yielded an excellent overall efficiency of 54.3(14) %. In order to confirm these exceptionally high efficiency values, a series of efficiency measurements was conducted at a different RIMS setup at the *Oak Ridge National Laboratory* (ORNL) in the United States using identically prepared samples. The experiment used the laser ion source installed at the *Injector for Radioactive Ion Species* (IRIS2) mass separator, part of the *Holifield Radioactive Ion Beam Facility* (HRIBF) [119].

As the experimental setup at the ORNL is in many aspects rather similar to the RISIKO setup at Mainz university, this section will only discuss essential aspects of and differences between both setups. A more detailed description of the ion source, the mass separator, and the laser system at ORNL can be found in [120]. As illustrated in figure 4.26, the geometry of the hot-cavity ion source of the IRIS2 separator exhibits some differences to the ion source of the RISIKO separator which is described in section 3.2.1. The dimensions of the ionizer tube are similar, with a diameter of 3 mm and a length of 30 mm. It is also made from tantalum. The major difference to the RISIKO ion source unit is the sample reservoir, also being made of Ta, but being straight and significantly larger. Its inner diameter is 8.5 mm and its length about 100 mm. The ion source was also resistively heated by a current of up to 380 A flowing through both parts, ionizer tube and reservoir and resulting in similar maximum temperatures as the ion source of the RISIKO setup. Before the experiment, the ionizer tube and reservoir were replaced by new parts to avoid any contaminations from previous experiments. Earlier experiments within the ongoing collaboration between the LARISSA group at Mainz and the ORNL laboratory indicated that the ORNL mass separator setup is by trend capable to achieve 10 – 20 % higher overall efficiencies compared to the RISIKO separator [46]. This is ascribed to the differences of the ion sources and will be discussed further below. Therefore, overall efficiency values in the range of 50 – 65 % were expected.

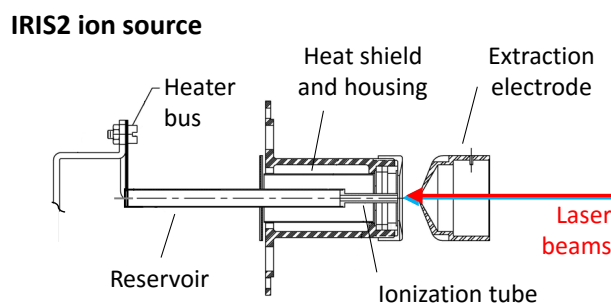


Figure 4.26: Schematic view of the ion source at the IRIS2 separator at ORNL. Laser beams entered the ionization tube in collinear orientation, while the ionization tube and reservoir were resistively heated up to about 2000 °C.

The basic layout of the IRIS2 mass separator setup is sketched in figure 4.27. The ion source is operated on an acceleration potential of 40 kV. After extraction, the ions are guided and separated by two sector field magnets and an equivalent set of ion optical elements, which made the ion transport optimization slightly more complex than at the RISIKO separator at Mainz university. After the laser beams passed a view port at magnet number one, they directly entered the ion source in collinear geometry, similar as at the RISIKO setup. The ion current was also detected using a Faraday cup.

The laser system at the ORNL laboratory consisted of three commercial Ti:sapphire

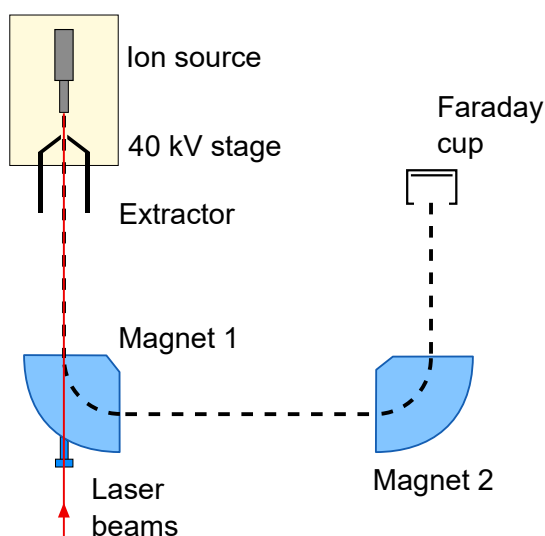


Figure 4.27: Schematic view of the basic layout of the IRIS2 separator at ORNL. See text for description.

lasers from the company Photonics Industries, each one pumped by an individual compact frequency doubled Nd:YAG laser. The Ti:sapphire lasers used a diffraction grating for frequency selection, similar to the design of the grating-assisted Ti:sapphire laser at Mainz university (see section 3.1.2), leading to a comparable spectral laser linewidth of ~ 3 GHz. The laser repetition rate of 10 kHz and the pulse length of about 50 ns were identical to the specifications at Mainz university. Frequency doubling, tripling, and quadrupling were also available by the use of NLO crystals. The foci of the laser beams at the ionizer tube were adjusted for maximum ionization signal. Even though the laser powers at ORNL were about a factor of three smaller when compared to the measurements at the RISIKO separator, each of the three transitions of the 3-step scheme was well saturated, as shown in 4.28. The saturation powers resulting from the fits were 3.4, 2.6, and 45 mW, respectively. They were comparable to the values obtained at the RISIKO setup, but showed a trend to smaller values, indicating a slightly smaller laser beam spot size. Despite of the fact that the distance from laser system to the ion source was 18 m, about three times larger than at the RISIKO setup, the spatial alignment of the laser beams was sufficiently stable.

The samples used for the efficiency measurements were prepared at Mainz university using the same nitric acid AAS solution and the same Zr foil to ensure identical conditions to prove the performance of the 3-step ionization scheme and the IRIS2 mass separator. Five samples were brought to the ORNL laboratory, all with a total amount of $2.26(11) \cdot 10^{16}$ Pd atoms each. Due to the surface ionized background of ZrO, all measurements were performed on the ^{105}Pd isotope, like the last measurements at Mainz university. The process of the measurements was also very similar to the measurements at the RISIKO separator. Figure 4.29 shows an example of a measurement, while graphs of other measurements are provided in section A in the appendix. As a first step, the complete mass separator setup and the ISST parameters of the laser system were well optimized using the initial, small ion signal available at medium temperatures. Subsequently, the ion source was smoothly heated up to its maximum temperature, while the optimum setting of all parameters was regularly inspected. Like during the measurements at the RISIKO separator, Pd was released predominantly after the ion source reached its maximum temperatures of about 2000 °C. The subsequent decline of the laser-induced ion current, indicating the depletion of the sample, was similar or even slower compared to the measurements at the RISIKO separator,

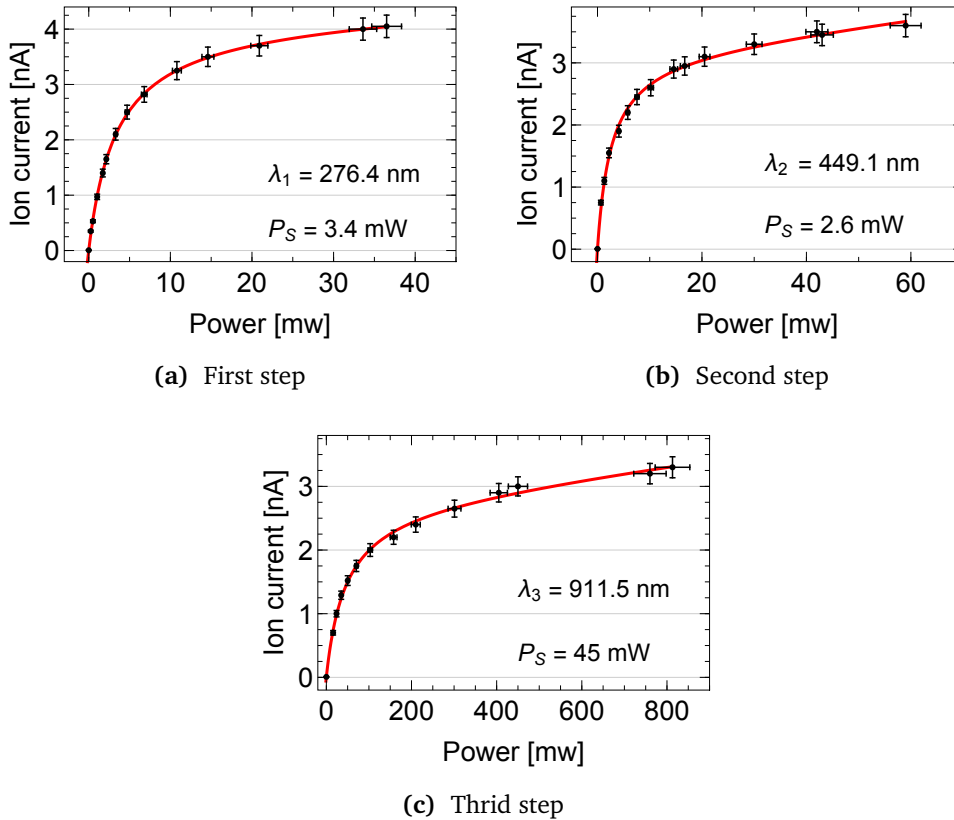


Figure 4.28: Saturation curves obtained during efficiency measurement # 3 at the ORNL setup. All steps of the 3-step scheme could be well saturated with the laser powers provided by the commercial ORNL Ti:sapphire laser system.

leading to long measurement times of up to 19 hours.

The resulting efficiency values of all efficiency measurements are summarized in table 4.7. The first samples were used to refine and carefully re-optimize all parameters of the mass separator and the laser system. A small misalignment of the extraction electrode during the first two measurements and technical difficulties during the optimization of the ion optics' voltages hampered the optimal performance of the separator setup during the first three measurements. After an extensive optimization procedure of the ion optics and magnet settings at the very beginning of measurement # 4, a fully satisfying optimization was achieved and measurements # 4 and # 5 could be performed under identical conditions. Similar to the experiments at Mainz university, the surface ionization of Pd was relatively weak, leading to a contribution of only about 0.1 % of the observed total ion current.

After final optimization of the complete setup and solving of all technical problems, measurements # 4 and # 5 could be conducted under optimum conditions, leading to significantly higher results. However, the fact that efficiencies between 22.2 % and 44.7 % were achieved under non-optimum conditions confirms the high ionization efficiency of the applied 3-step scheme. The outstanding efficiencies of 59.3 % and 60.23 % yield a mean value of 59.7(21) %. This is a relative enhancement of about 10 % compared to the results obtained at the RISIKO separator, which is in good agreement with the initial expectations. It should be noted that the ion current could not be recorded during the periods of optimization of the ion optics at the very beginning of each measurement. The amounts of ^{105}Pd ions which were overlooked in this way, can be estimated to be about 2 % for measurement # 4 and about 1 % for measurement # 5 in terms of absolute contributions to the overall efficiency.

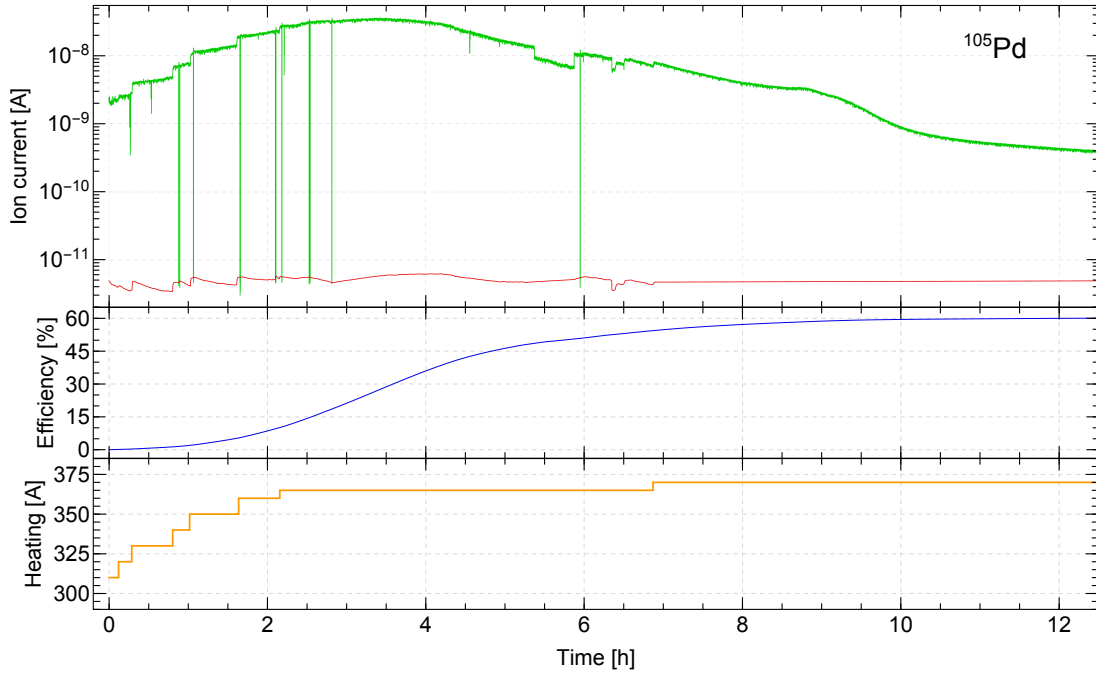


Figure 4.29: Course of efficiency measurement # 5 on ^{105}Pd at the IRIS2 mass separator at ORNL. The ionization scheme used here was the 3-step scheme as depicted in figure 4.8. The observed decline of the laser-induced ion current (green) after reaching its maximum was similar or even slower compared to the measurements at the RISIKO separator (see figure 4.20).

Consequently, in the best scenario, the final mean overall efficiency at the IRIS2 separator might even be about 1.5 % higher, if the setup could have been completely optimized before the measurement, allowing complete recording when operating under optimum conditions.

The higher overall efficiency of the IRIS2 separator compared to the RISIKO separator is attributed to the geometry of its ion source. The volume of reservoir and ionizer tube in the IRIS2 ion source was about 40 times larger, while the exit aperture was similarly sized

Table 4.7: Chronological overview of the efficiency measurements performed with ^{105}Pd using the 3-step scheme at the IRIS2 mass separator at ORNL. See text for discussion.

#	Duration [h]	Overall efficiency ϵ [%]
1	18.5	28.3(14)
2	19	44.7(22)
Extraction electrode found to be off-axis → Re-alignment and optimization of ion optical settings		
3	17.5	22.2(11)
Ion optical settings found to be not fully optimized → Re-optimization → Significant improvement of ion transmission		
4	17	59.3(30)
5	13	60.2(30)

as in the RISIKO setup. Therefore, the ORNL ion source provides a much larger atom-laser interaction region. In addition, due to the larger ratio between volume and exit aperture,

the residence time of atoms inside the ion source is expected to be significantly increased, reducing the probability of Pd atoms leaving the source before being ionized. Both aspects contributed positively to the achievable overall laser ionization probability for Pd atoms.

4.3.5 Influence of the Temperature Distribution

Independent from the ionization scheme applied or the mass separator setup used, all measurements shared one common characteristic. The evaporation of Pd required maximum ion source temperature and the depletion rate after the ion current reached its maximum was very slow, causing the measurements to last for 12 hours and even more. This feature did not change when using different metallic foils as reduction agents. The fundamental reason for this behavior seems to originate from the relatively high melting point of palladium of 1555 °C, which leads to quite similar properties as the refractory metals. As a result, the ion source of the RISIKO and the IRIS2 setup had to be operated at maximum temperatures of about 2300 °C. In most measurements even higher temperatures would have been favorable in order to achieve a faster depletion of the sample. Unfortunately, this could not be realized as it would have posed serious threat to the structural integrity of the ion source unit.

A fundamental problem in this situation was the fact that the temperature was not completely homogeneous along the whole structure of the ion source. This was caused by different thermal resistances between the individual parts and the variation in the heat dissipation via black body radiation across the ion source unit. In the case of the RISIKO ion source, recently conducted computer simulations provided valuable information on the temperature distribution in the ion source. The resulting temperatures agree well with experimentally observed temperatures of the ion source. A detailed description of the investigation can be found in [76, 113]. The simulation were based on the *finite element method* and were carried out using the software *Autodesk CFD 2016*.

The simulation model was used to evaluate the temperature distribution of the RISIKO ion source unit with the settings used during the Pd efficiency measurements. This means maximum heating currents for the ionizer tube and the reservoir capillary, which correspond to $I_{\text{ionizer}} = 320 \text{ A}$ and $I_{\text{reservoir}} = 100 \text{ A}$, respectively. The results are illustrated in figure 4.30. In this situation, the temperature of the middle part of the ionizer and the reservoir capillary reach respective temperatures of 2000 °C and 2400 °C, whereas the front and the back part of the tube have slightly lower temperatures. Especially, the region around the interconnection between ionizer and reservoir capillary showed a significantly lower temperature of only about 1600 °C, just slightly higher than the melting point of Pd. As a consequence, a significant fraction of the Pd atoms, evaporated in the reservoir capillary, could condense at the interconnection region during the beginning of the efficiency measurements, when the ion source was slowly heated to maximum temperatures. After the heating currents reached their maximum, the temperature of the colder interconnection region slightly exceeded the melting point of Pd and the condensed fraction started to slowly re-atomize. But due to the temperature being only slightly higher than the crucial temperature, the evaporation rate was very small, leading to the slow depletion which was observed during all efficiency measurements.

Slow depletion rates were also observed at ORNL, where a slightly different ion source and heating technique was used. As shown in figure 4.26, there was no additional heating connection between reservoir and ionizer tube. Consequently, a single electric current, flowing through both parts, was used to heat the ion source. This design eliminates the need of an additional power connection between the two parts, thus avoiding cold spots in that area. However, there was still a significant temperature gradient along ionizer tube and reservoir, caused by the difference in diameter and conductivity of the ionizer tube

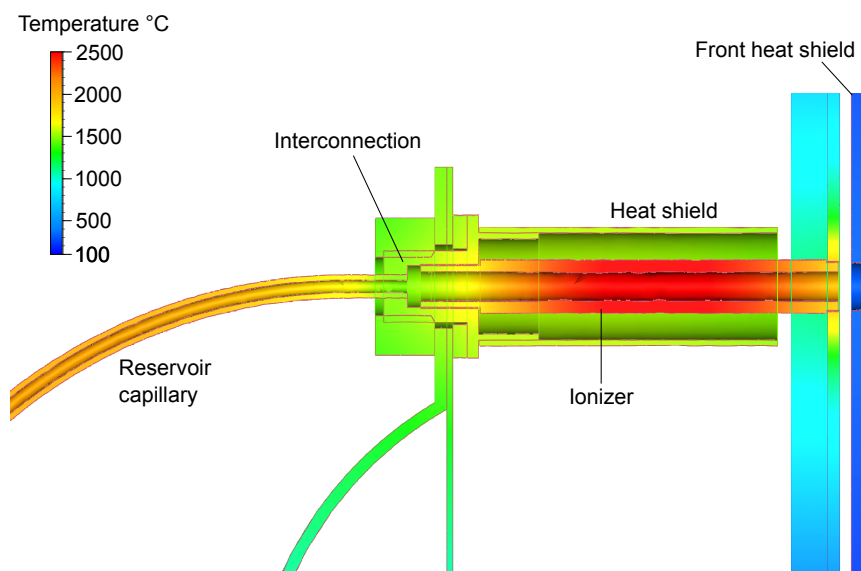


Figure 4.30: Computer simulated temperature distribution of the RISIKO ion source. Simulation adopted from [76, 113].

and the reservoir tube. The smaller material cross section of the ionizer tube resulted in a effectively higher resistance, which caused a stronger power deposition and correspondingly stronger heating in the ionizer tube. In addition, the smaller outer surface introduced less losses due to thermal black body radiation. This effect was further enhanced by the heat shield, which did not completely cover the reservoir. The outcome of this was a significant lower temperature of the reservoir's back compared to the ionizer tube. When operated at maximum heating current, the ionizer tube reached about 2100 °C while the reservoir back reached only about 1600 °C. This created a similar situation as in the RISIKO ion source at maximum temperature, which explains the similar depletion rates during the experiments at Mainz university and ORNL.

Based on the computer simulations and results from other experiments, the ion source at the RISIKO separator was recently modified in order to reduce power losses and to improve the homogeneity of the temperature profile [76, 72]. Minimization of hot outer surfaces and the use of material offering less emissivity served to minimize power losses due to thermal black body radiation at the interconnection region. Figure 4.31 illustrates the simulation results for different configurations of the ion source. The improved design clearly reduces the temperature drop in the interconnection region, while on the other side the overall temperature is increased. The simulations were conducted considering a heating current of 320 A but neglecting the influence of a second heat shield, causing a slightly lower maximum temperature in comparison to the Pd efficiency measurements performed. These findings are confirmed by first experimental results. When using samples with high melting points, like Pd, the new ion source design can significantly reduce the duration of efficiency measurements, as the sample can be depleted much faster. In addition, possible memory effects are reduced as well, as the amount of atoms remaining at colder regions is significantly lowered.

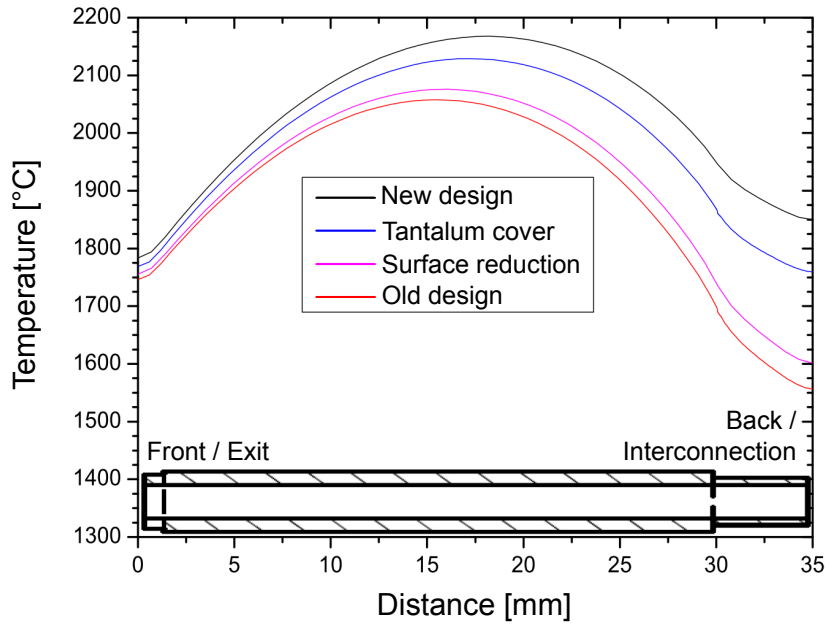


Figure 4.31: Comparison of the temperature along the ionizer tube for the ion source design used in the Pd efficiency measurements (blue) and after the reduction of heat dissipation by thermal radiation (black). The new design clearly reduces the temperature drop in the interconnection region, while on the other side the overall temperature is increased. Figure adopted from [76].

4.3.6 Summary

The final values for the overall efficiency using the best 2-step, 4-step and 3-step ionization schemes are summarized in table 4.8, while figure 4.32 provides a graphical representation of the individual measurements, as well as the corresponding arithmetic mean values. The three measurements at the RISIKO separator using the 4-step scheme resulted in an average efficiency of 14.6(13)%, whereas the significant measurements using the 3-step scheme yielded high efficiency of 54.3(14)%. The ratio of these two values agrees well with the ratio of the observed relative intensities, when comparing the ionization rate produced by solely the first step. No dedicated efficiency measurement was performed with the 2-step scheme, as the final ionization step could not be properly saturated. By using the ratio of the measured relative intensities of the 2-step scheme and the 4-step scheme the overall efficiency of the 2-step scheme was estimated to be about 1.5(5)%. Here, an additional estimated relative uncertainty of 15% was included in the error to account for the indirect determination of this value.

Table 4.8: Relative intensities and average overall efficiencies of the best 2-step, 4-step and 3-step ionization schemes, as shown in figure 4.4. *This value was calculated via the corresponding relative intensities. See text for details.

Scheme	Rel. Intensity	Separator	ϵ [%]
2-step	100	RISIKO	1.5(5)*
4-step	950	RISIKO	14.6(13)
3-step	3250	RISIKO	54.3(14)
3-step	-	IRIS2	59.7(21)

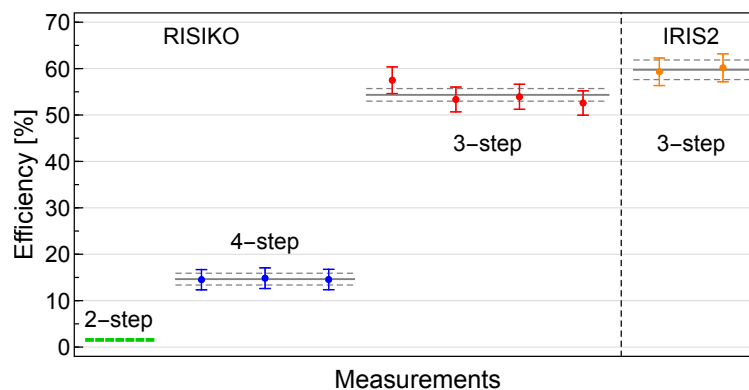


Figure 4.32: Overall efficiencies of the investigated schemes in Pd, as listed in table 4.8. The value for the 2-step scheme was estimated, while the efficiencies for the 4-step and 3-step scheme were measured at the RISIKO separator and IRIS2 separator, respectively. Mean values and their one σ uncertainties are given by the solid and corresponding dashed lines.

The efficiency achieved by the use of the 3-step scheme is more than three times larger than the value of the 4-step scheme. This is mostly due to the set of extraordinarily strong transitions in the 3-step scheme. This is also represented by the significantly lower saturation powers compared to those of the 4-step scheme. In general, the saturation powers of only a few mW of step two and three in the 3-step scheme were exceptionally low in comparison to typically observed saturation powers of transitions in the medium to high energy region in the atomic spectrum of other elements. This enabled a very efficient excitation as well as ionization. As mentioned above, both overall efficiency values of the 3-step scheme, namely 54.3(14)% and 59.7(21)%, measured at two independent mass separator units, confirm each other and are presently the highest efficiency values reported for resonance ionization laser ion sources.

SPECTRAL RESOLUTION: HFS SPECTROSCOPY IN TECHNETIUM

5.1 Development of a High-Repetition Rate Single Mode Laser

Spectral resolution is one of the key aspects when studying HFS and isotope shifts of optical transitions. A typical HFS comprises several individual transitions between the different F levels, which are typically spread across a spectral range of 100 MHz up to 30 GHz. Correspondingly, laser linewidths well below 1 GHz are required in order to completely resolve the individual components, allowing the precise determination of the characteristic parameters of atomic HFS. The typical length of a Ti:sapphire resonator, as used at the Mainz LARISSA laboratory or at the on-line laser ion sources worldwide, is about 0.5 m, resulting in a spectral spacing of the individual longitudinal cavity modes of about 330 MHz. Consequently, single longitudinal mode operation of the laser is mandatory to reduce the laser linewidth to below 1 GHz.

In order to provide pulsed laser radiation in a single longitudinal cavity mode, an injection-locked laser which is seeded by a CW master laser is typically used. One example is the injection-locked Ti:sapphire laser system in the LARISSA laboratory as described in section 3.1.3. Despite the fact that several outstanding spectroscopic results have been achieved using this approach [121, 122, 29, 123], it goes along with several experimental complications. The laser setup is rather complex and significantly more difficult to operate compared to a standard stand-alone Ti:sapphire laser (see section 3.1.1). It requires an additional, frequency stabilized master laser system, proper mode matching of the CW radiation to the resonator mode of the pulsed laser, and a dedicated electronic setup for the locking of the Ti:sapphire laser cavity to the injected CW light. Furthermore, the accessible frequency range is restricted to the frequency range of the available master laser system. This is of special relevance when a diode laser is used as master laser, as it is currently implemented in the Mainz LARISSA laboratory, since these lasers typically cover only narrow wavelength ranges of a few tens of nm in specific spectral regions.

This section presents the development of a first prototype of an unseeded, stand-alone pulsed single mode Ti:sapphire laser which aims to combine the simplicity of the standard laser design with the high spectral resolution of single mode operation. First results obtained with this laser in spectroscopic experiments on Cu are summarized briefly at the end of this section, while the following section 5.2 provides a more detailed discussion of HFS spectroscopy on Tc.

5.1.1 Laser Resonator Design

The basic idea of the frequency selection is similar to that of the standard Ti:sapphire laser in dual etalon configuration as described in 3.1.1. However, the second etalon must feature a significantly higher frequency selectivity in order to achieve selection of a single longitudinal resonator mode. Similar as for the injection-locked Ti:sapphire laser, single mode operation implies the use of a ring cavity in order to avoid spatial hole burning (see section 3.1.3). The laser design includes a piezo mounted mirror, enabling precise control of the cavity length, which is prerequisite for smooth tuning and stabilization of the laser frequency. These fundamental requirements lead to a basic laser design which is based on a bow tie-shaped cavity as sketched in figure 5.1. The folding angle α of the cavity is of special relevance for the following section 5.1.2 as it acts as a crucial design parameter.

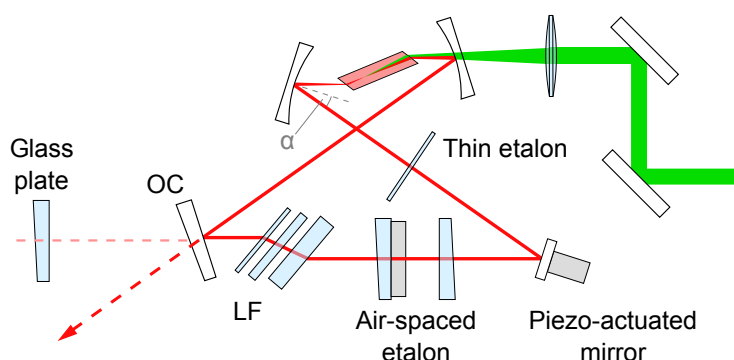


Figure 5.1: Cavity layout of the unseeded single mode Ti:sapphire laser. The bow tie-shaped cavity is equipped with a birefringent Lyot filter (LF) and a thin etalon with identical specifications as in the standard Ti:sapphire laser. An additional air-spaced etalon provides selection of a single longitudinal cavity mode and can be tuned using a piezo actuator (gray). A second actuator is used to tune the length of the laser cavity itself.

The laser uses a set of dichroic mirrors, a birefringent Lyot filter, and an etalon with the same specifications as in the standard Ti:sapphire laser. To achieve a higher frequency selectivity with the second etalon while using suitable reflectivities below 50 %, the *FSR* is decreased by choosing a larger distance d between the two reflective surfaces. This is accomplished by a so-called *air-spaced etalon* (AE) which consists of two wedged glass substrates with plan-parallel aligned partially reflective surfaces. A low-power helium-neon laser is used for precise optimization of the plan-parallel alignment for best contrast in the resulting interference pattern. The reflective surfaces are provided by two broadband mirrors¹ with 30 % reflectivity across 700-1100 nm and an anti-reflective coating on the wedged back surface. The two mirrors are mounted on a rail system, allowing to adjust the distance from 0 to 20 mm. For frequency control, one mirror is mounted on a linear piezo actuator, enabling precise tuning of the AE distance by applying voltages up to +150 V.

Figure 5.2 visualizes the selection of a single longitudinal cavity mode using a proper combination of frequency selective elements. The transmission curves, based on formula 2.37, were calculated with the following settings: cavity length: 630 mm; thin etalon as described in 3.1.1; AE reflectivity: 30 %; AE distance: $d = 12$ mm; number of round-trips through the ring cavity: 100. The laser threshold of about 10 % is an empirical value, stemming from comparison of experimental observations and calculations. Unfortunately, the linewidth of the transmission peaks of the AE cannot be decreased arbitrarily by using

¹Thorlabs, part number: BSS11

higher reflectivities or increasing the distance d , as this results in relatively high losses, primarily caused by the spatial walk-off of the individual internal reflections in perpendicular direction to the propagation axis [124, 22]. The corresponding loss factor for each pass is proportional to d . As a result, the laser showed severe power losses resulting in unstable operation and hindering proper single mode operation when using distances larger than $d = 15$ mm. This trade-off between spectral selectivity and losses in the cavity is crucial and a key aspect in the whole laser design. To achieve optimum suppression of the neighboring cavity modes for a given frequency selectivity of the AE, one can increase the FSR of the cavity, i.e. the spectral spacing of the individual cavity modes. Therefore, the length of the laser cavity must be reduced, which is in turn limited by the space required by the frequency selective elements. The reduction of the dimensions requires also optimization of other geometrical parameters using the ray transfer matrix formalism, which is discussed in the following section 5.1.2.

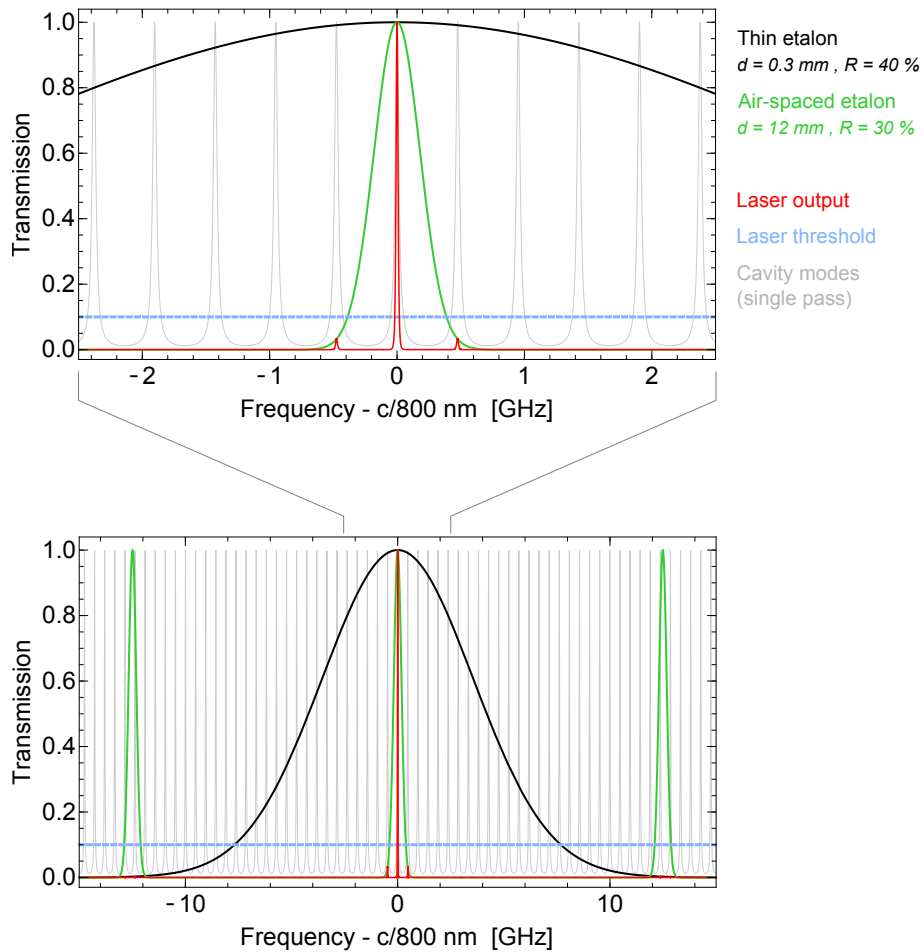


Figure 5.2: Selection of a single longitudinal cavity mode using the combination of thin and air-spaced etalon. See text for details.

Without seed photons in the cavity, defining the lasing direction in the injection-locked Ti:sapphire laser, the unseeded laser produces two counterpropagating laser beams, exiting the output coupler in two different angles. In general, unidirectional laser operation can be achieved by introducing a combination of Faraday rotator and a second polarization rotator, e.g. a waveplate, in the cavity. This concept was also successfully tested, but discarded as the relatively large space required to accommodate the Faraday rotator and the waveplate

increased the resonator size significantly. In addition, unfavorable etalon effects caused by the surfaces of the crystal inside the rotator were observed, hindering proper spectral control of the laser. Instead, the surface reflection of $\sim 4\%$ on a wedged glass substrate was used to feed $\sim 0.8\%$ of the output beam of one direction back into the laser cavity. This small feedback is sufficient to favor laser amplification in one direction during the build-up of the laser pulse [125]. Using this feedback, the power ratio of 0.5:0.5 in two-beam operation could be reliably changed to about 0.03:0.97, almost completely eliminating the laser amplification in one direction. Etalon effects caused by this concept were not observed with properly optimized setup. This is due to the very low percentage of power reflected back into the cavity and the low finesse of the interferometer formed by the output coupler and the glass plate due to the low reflectivity of the latter. However, if the glass plate feedback has to be removed for any reason, the reduction in output power in the favored direction of about a factor of two is usually not critical as the beam is attenuated anyway to avoid power broadening effects.

5.1.2 Ray Transfer Matrix Analysis

The ray transfer matrix analysis, or ABCD matrix analysis, is a mathematical method to calculate the propagation of light rays and Gaussian beams through an optical setup, typically used to design optical systems and laser resonators. The characteristic concept is the representation of the geometric parameters of a simple ray or a Gaussian beam as a 2-dimensional vector q and optical components as 2x2-dimensional matrices M . An optical system is characterized by the product of the transfer matrices of its individual components. A stable laser resonator requires the geometrical parameters of the light beam to be reproduced after each full resonator round-trip², leading to an eigenvalue problem

$$M_{\text{resonator}} \circ q_{\text{beam}} = q_{\text{beam}} \quad (5.1)$$

which can be solved mathematically. More detailed descriptions of the ray transfer matrix analysis can be found in various optics textbooks like [126, 65] or in recent theses, e.g. [59, 29].

The first prototype of the laser cavity was constructed using available optics and an optical breadboard. The size of the laser cavity could be reduced to a total geometrical length of 625 mm, corresponding to a FSR of 470 MHz. In a next step, the ray transfer matrix formalism was used to optimize the distance between the two curved mirrors and the folding angle α of the cavity (see figure 5.1). The curved mirrors act as focusing elements in the cavity and therefore are crucial regarding stability of the resonator as well as the radius of the laser mode. The latter aspect is very important for the amplification in the Ti:sapphire crystal as well as for the frequency selection processes. The folding angle compensates the astigmatism caused by the Brewster-cut Ti:sapphire crystal. The main goal of the optimization is to create a circular beam shape inside the laser cavity while completely compensating the astigmatism in order to produce a circular output beam with minimum divergence and improve the output power and stability of the laser. In addition, the beam divergence in the region of the frequency selective elements should be minimized, as they achieve maximum frequency selectivity for perfectly parallel beams.

Figure 5.3 shows the evolution of the beam radius in tangential (horizontal) and sagittal (vertical) direction along the laser resonator for non-optimized cavity parameters, i.e. a folding angle of 18.50° and an optical distance of 90 mm between the curved pump mirrors. The thermal lens inside the Ti:sapphire crystal, caused by heating due to the pump laser beam,

²For standing wave resonators, this implies the pass through the resonator in back and forth direction.

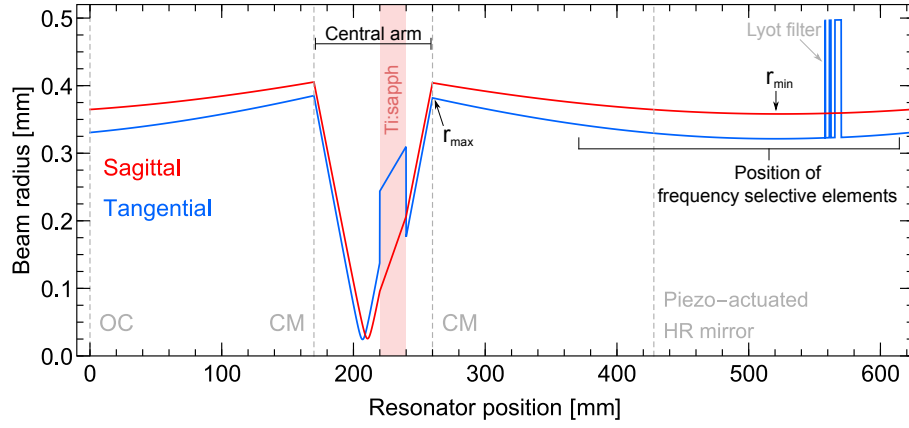


Figure 5.3: Evolution of the beam radius in the ring cavity at 800 nm when using non-optimized cavity parameters, i.e. a folding angle of 18.50° and an optical distance of 90 mm between the curved mirrors. These settings produce a slight mismatch in tangential and sagittal direction, representing an elliptic beam shape. See text for details.

was estimated with a focal length of $f = 10$ m. As shown in figure 5.3, these settings produce a slight mismatch in tangential and sagittal direction, representing an elliptic beam shape. The correlation of both parameters was investigated by using the difference of the shape in tangential and sagittal plane. A figure of merit δr was constructed by adding up the differences in radius along the length of the resonator in a step size of 0.5 mm,

$$\delta r = \sum |r_{\text{sag}} - r_{\text{tan}}| \quad . \quad (5.2)$$

As the mode usually exhibits astigmatism in the central arm between the curved mirrors, this section is not included in δr . Obviously, this parameter is zero for a perfectly circular beam. The resulting 2D map is presented in figure 5.4. The region with almost no difference between the beam shape is characterized by an approximately linear correlation between curved mirror distance and the folding angle. Figure 5.5a visualizes the corresponding minimal waist radius in the tangential plane in the region of the frequency selective elements. Here, a trend to a smaller waist radius, meaning an unfavored, harder focus of the mode, is observed at larger distances between the two curved mirrors.

In order to obtain the favored circular beam shape mentioned above while decreasing the sensitivity to small misalignments of the cavity the broad part of the red colored area in figure 5.4 around 90-93 mm was selected. In addition, this region provides a less pronounced focus of the mode which allows the optimum use of the frequency selective elements. Therefore, a curved mirror distance of 91 mm and a folding angle of 17.35° was chosen as optimum parameters for the laser cavity setup, as indicated with marker B in figure 5.4. Figure 5.6 shows the resulting evolution of the beam shape which features an almost identical radius in both planes.

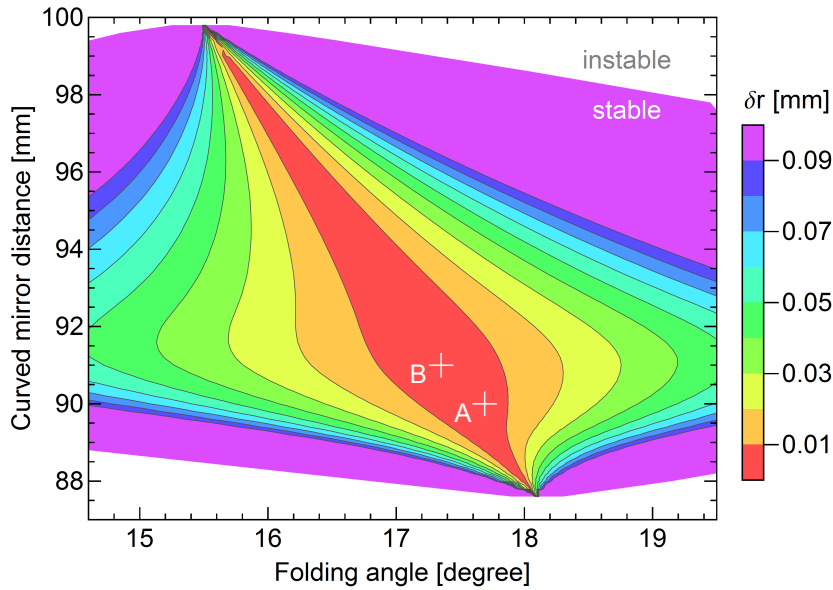
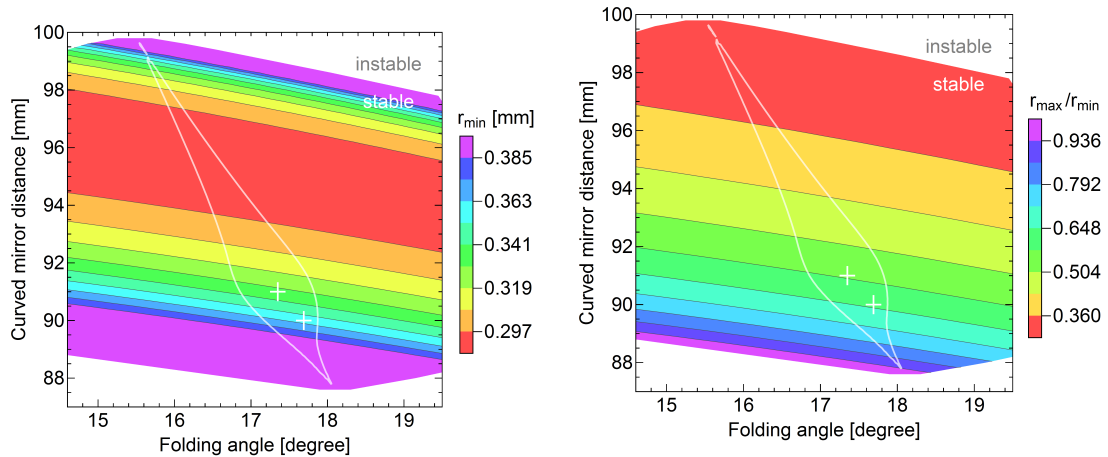


Figure 5.4: Influence on the circularity of the laser mode cross section. The sum of differences in radius in tangential and sagittal direction along the length of the resonator is used as figure of merit. Smaller values of δr indicate a more circular beam shape. The marker A and B indicate the settings of the standard Ti:sapphire laser and the optimized settings for the ring cavity, respectively.



(a) Influence on the beam waist radius. The white contour highlights the region of interest regarding an optimum beam cross section as shown in figure 5.4.

(b) Influence on the ratio of maximum beam radius to waist radius. The white contour highlights the region of interest regarding an optimum beam cross section as shown in figure 5.4.

Figure 5.5: Influence of curved mirror distance and folding angle on beam shape parameters outside the central arm between the curved mirrors. See text for details.

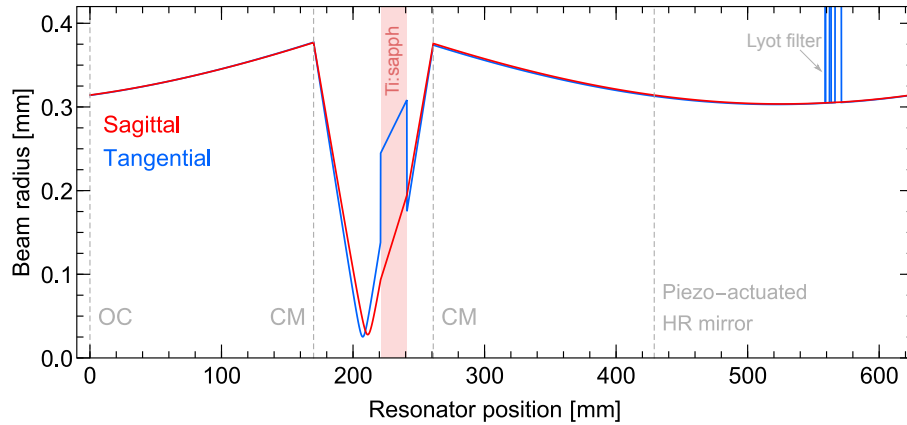
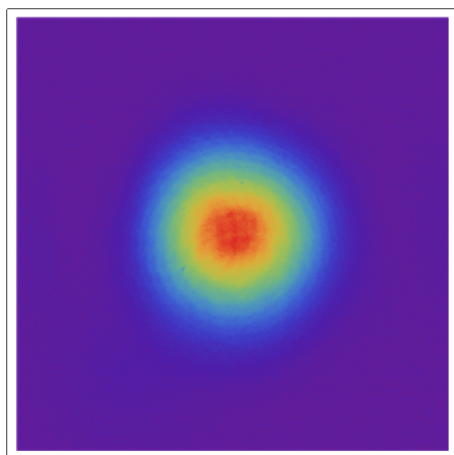


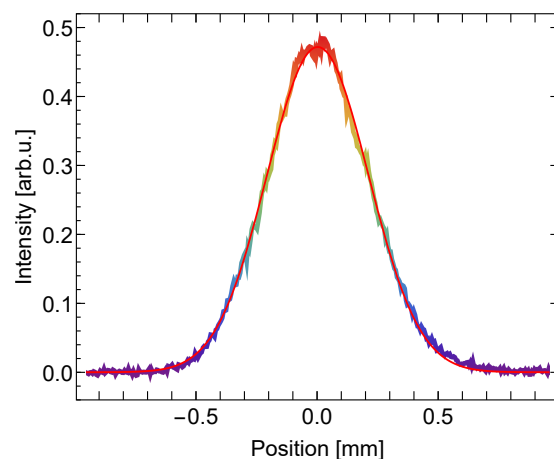
Figure 5.6: Evolution of the beam radius in the ring cavity at 800 nm with optimized parameters. The folding angle was set to 17.35° and the optical distance between the curved mirrors to 91 mm, corresponding to marker B in figure 5.4. The resulting beam shape is equal in both planes. See text for details.

5.1.3 Characterization and First Spectroscopic Application

Without the air-spaced etalon, the laser operates with very similar specifications as the standard Ti:sapphire laser design. The same tuning ranges and overall output powers were demonstrated during use in several RIMS experiments in the Mainz LARISSA laboratory. However, the spatial beam profile obtained with the ring cavity was in general superior to the beam profiles obtained from the z-cavity lasers. The beam featured an almost perfect Gaussian profile, as shown in figure 5.7, and allowed a very good focusing. This is most likely due to different symmetrical properties of z-cavity and ring cavity. A more detailed investigation of this feature as well as a full determination of the M^2 -parameter of the beam, which describes how close the beam is to a theoretical Gaussian beam, is subject to future studies.



(a) 2D beam profile of the laser output of the ring laser cavity.



(b) Cross-section of the beam profile in (a). A Gaussian profile (red) was fitted to the data.

Figure 5.7: Typical spatial beam profile of the output of the ring laser cavity. The beam showed an excellent Gaussian profile. The profile was taken while the air-spaced etalon was installed in the ring-shaped laser cavity.

With the AE installed in the laser to achieve single longitudinal mode operation, the output power was significantly reduced due to losses caused by the AE as mentioned above. For usual pump powers of about 15 W, this resulted in a typical laser power of 800-1000 mW in the region of the peak gain around 800 nm, which is well above the requirements of typical high-resolution spectroscopy experiments. For wavelengths in lower gain regions, for example > 850 nm, the AE must be equipped with less reflective mirrors to ensure a stable operation of the laser. As this in turn reduces the frequency selectivity, careful alignment and tuning of the laser is required to achieve a proper suppression of the neighboring cavity modes.

The fundamental linewidth of the laser was analyzed using a scanning Fabry-Pérot interferometer with a FSR of 4 GHz. As shown in figure 5.8, the observed transmission fringes at 785 nm exhibited a FWHM of 45(5) MHz. However, this is an upper limit for the intrinsic laser linewidth, as the finite finesse of the interferometer itself caused a considerable contribution to the observed linewidth. The FPI spectrum shows another important aspect, the occurrence of neighboring side modes in some of the laser pulses. This concerns only a minor fraction of the pulses, about five laser pulses in the whole spectrum, but can create some artificial signal during the spectroscopy on atomic transitions.

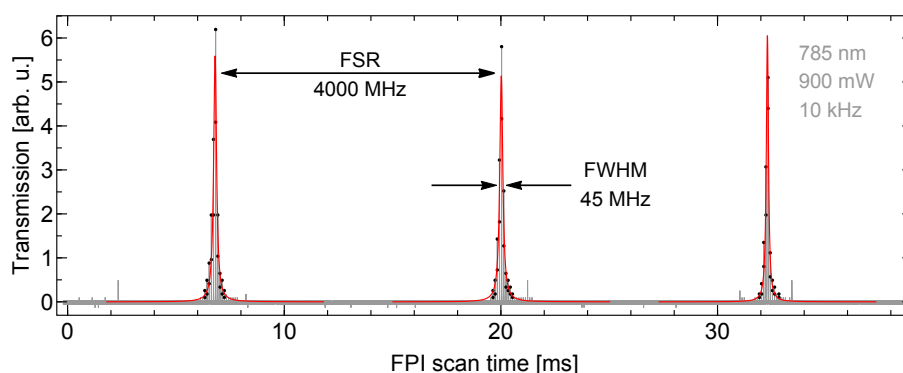


Figure 5.8: Determination of the spectral linewidth of the unseeded single mode Ti:sapphire laser, using a scanning FPI ($FSR = 4$ GHz). One scan cycle is shown. The photodiode signal (gray) shows the individual laser pulses. A set of Lorentzian profiles (red) were fitted to the maxima of the laser pulses (black dots) in each transmission peak. The corresponding FWHM was determined by repeating this measurement for many FPI scan cycles resulting in an average value of 45(5) MHz.

Spectroscopy in Cu

The performance of the unseeded single mode laser was first demonstrated in a high-resolution HFS spectroscopy experiment on the stable copper isotopes $^{63,65}\text{Cu}$ at the MABU spectrometer. The results of these experiments were published in [127].

The three-step ionization scheme used is scheme II in figure 5.9. In order to reduce the thermal velocity distribution along the laser axis, i.e. the Doppler broadening, the spectroscopy was performed using a perpendicular alignment of the laser beams relative to the atomic beam leaving the oven (see section 5.2). The frequency of the single mode laser was manually controlled via the voltages supplied to the piezo actuators of AE and cavity. Figure 5.10 shows sections of the obtained HFS spectrum, which were well resolved with total linewidths of 150(3) MHz. This value is consistent with estimations considering a residual Doppler broadening corresponding to 1200 °C and a laser linewidth of 45 MHz. The spectrum also shows some small artificial peaks caused by the occurrence of side

modes (dashed lines) from the laser. However, these could be easily identified and were correspondingly handled in the final fitting procedure.

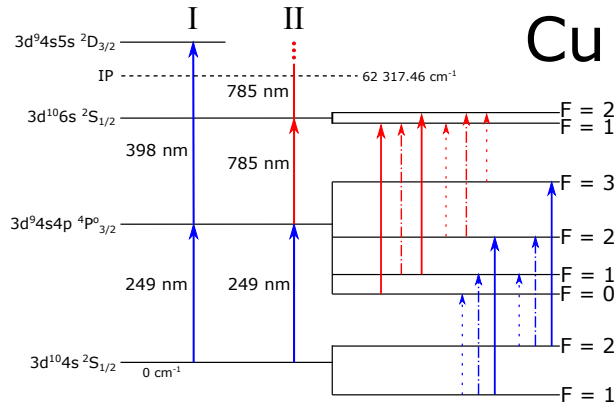


Figure 5.9: Diagram of the electronic levels (labeled by their total angular momentum F) and transitions used in this work. Dashed lines indicate weak transitions ($\Delta F = -1$), dash-dot lines indicate stronger lines ($\Delta F = 0$) and full lines represent the strongest excitation paths ($\Delta F = +1$). The three-step scheme II was used for the double resonance 2D mapping. Graphic adopted from [127].

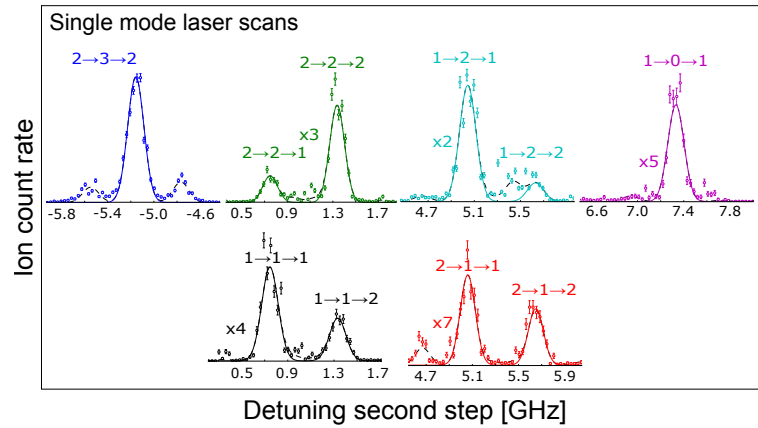


Figure 5.10: Frequency scans of the second excitation step (785 nm) in Cu at fixed first step (249 nm) frequencies, taken with the single mode laser system. Symbols are the experimental points, the solid lines are the best fitting curves. The labels near the peaks display the angular momenta F of the states involved in the RIS excitation pathway. Dashed lines indicate effects from possible side modes which were considered in the fitting process. Graphic adopted from [127].

Evaluation of Performance and Limitations

The results of the first applications showed that the unseeded pulsed Ti:sapphire laser is well suited for RIS-based HFS spectroscopy. The narrow laser linewidth of about 45 MHz enables full resolving of typical HFS. It is about the same size as the residual Doppler broadening which is observed when the probing laser beam is aligned in perpendicular orientation. This situation is favorable as further reduction of the laser linewidth primarily decreases the ionization efficiency while the total linewidth is hardly reduced as the Gaussian part σ_{total} is then dominated by the Gaussian contribution of the Doppler broadening, due to the relation

$$\sigma_{\text{total}} = \sqrt{\sigma_{\text{Doppler}}^2 + \sigma_{\text{laser}}^2}$$

The spectral laser linewidth consists of two major parts. The first one is the intrinsic spectral linewidth of a single laser pulse, which is expected to be equal to that of the injection-locked laser, about 10-20 MHz, as both lasers operate on a single longitudinal mode of an almost identical cavity. The second contribution is caused by small spectral deviations of each individual laser pulse due to vibrations, thermal drifts, and acoustic noise. This spectral pulse-to-pulse jitter increases the linewidth to an effective laser linewidth of about 45 MHz when averaged over several thousand pulses. In contrast to the injection-locked laser or other CW-based laser systems, each individual laser pulse is completely independent from the previous laser pulse, as the oscillating laser mode completely vanishes before the start of the next laser pulse. As a result, the stand-alone single mode laser exhibits a slightly higher sensitivity to fluctuations, which cannot be easily eliminated in this laser design.

From the measurements performed in the framework of this thesis, one can identify certain limitations of this laser prototype in its current design. An essential issue is the ratio between the relatively strong losses introduced by the AE and the considerably lower gain for wavelengths outside the peak gain region, $\lambda < 750$ nm or $\lambda > 850$ nm. Future developments will address the reduction of the walk-off effect in order to decrease the associated loss and increase the finesse of the AE, which in turn allows the use of mirrors with lower reflectivity.

Furthermore, an automated active stabilization and frequency control is desired which can be divided into two parts. First, the AE must be stabilized to achieve proper single mode operation with full suppression of the neighboring cavity modes. This could be achieved by using the back reflection of the AE as feedback. Alternatively a fast, software-based evaluation of the transmission pattern of a scanning FPI could be implemented. The second part is the stabilization of the laser frequency to counteract the remaining frequency drift after implementation of the single mode stabilization. In addition, linking the frequency stabilization system to a PC would enable computer-controlled frequency scanning. Frequency stabilization can be achieved by adapting conventional stabilization techniques for pulsed lasers, as for example by locking to a precise wavemeter or a stabilized reference cavity or by fringe-offset locking to a stabilized laser source. Obviously, the overall stability can be enhanced further by optimizing the final laser design in terms of thermal, acoustic and vibration isolation.

5.2 Spectroscopy in Tc at the MABU

As described in chapter 1, precise characterization of HFS and isotope shifts in Tc are of special interest for atomic and nuclear physics as well as for the ongoing RIMS-based ultra trace analysis project at the institute of nuclear chemistry. This section presents the spectroscopic study of these important attributes in different transitions for the two radioactive isotopes ^{97}Tc and ^{99}Tc . Furthermore, this experiment gave another opportunity to demonstrate the performance of the newly developed unseeded single mode laser, enabling full resolving of the HFS in selected first and second step transitions.

5.2.1 Experimental Setup

The experiment was performed using the compact MABU spectrometer, which was described in section 3.2.2. The laser system was composed of three standard Ti:sapphire lasers, as described in section 3.1, and the prototype of the unseeded single mode Ti:sapphire laser as presented in the previous section 5.1. The layout of the setup is sketched in figure 5.11.

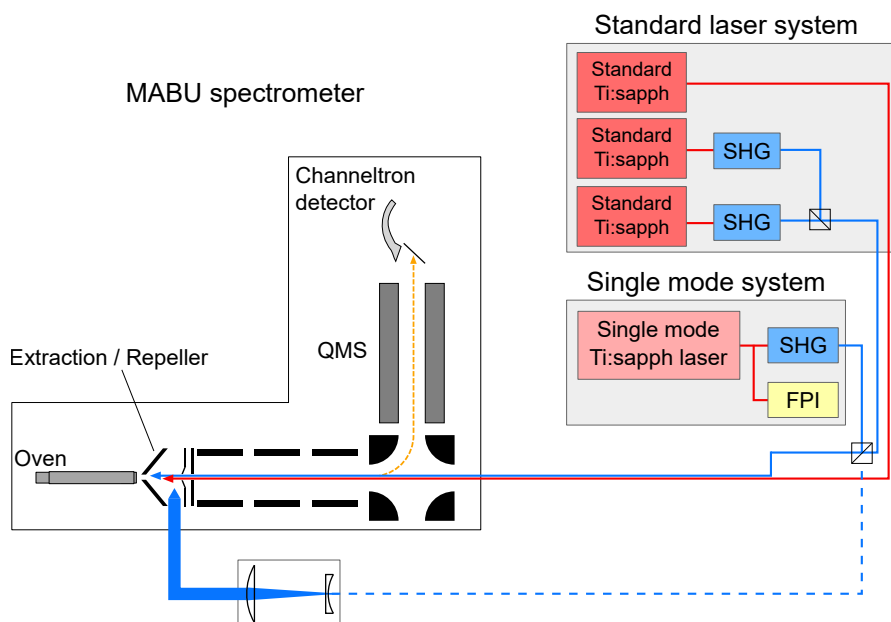


Figure 5.11: Basic layout of the experimental setup for Tc spectroscopy in the MABU spectrometer. See text for description.

The standard laser system was used for basic broadband excitation. It produced excellent maximum powers of up to 730 mW, 960 mW, and 3.6 W for the first, second, and third excitation step, respectively. As described in section 3.1.1, one of the standard Ti:sapphire lasers could be equipped with a second etalon to reduce the spectral linewidth of the fundamental laser radiation to about 1 GHz. In this dual etalon configuration, the scan of the laser frequency was done manually by careful and accurate, simultaneous tilting of both etalons. The single mode Ti:sapphire laser was also tuned manually and provided up to 800 mW of narrowband radiation, resulting in a peak power of 20 mW after the second harmonic generation. The frequencies of the standard Ti:sapphire lasers were monitored with a *HighFinesse WS6-600* wavemeter. A *HighFinesse WSU-30* wavemeter provided a more precise frequency readout for the single mode laser, while a scanning Fabry-Pérot-Interferometer with an *FSR* of 4 GHz was used to inspect the spectral profile and check for proper single mode operation.

The MABU spectrometer allowed two different ionization geometries. The first is, conventional in-source geometry, in which all lasers beams enter the heated oven in longitudinal orientation. As a result, the full Doppler broadening is observed in all excited transitions. In the second, the laser beam(s) of interest can be aligned in perpendicular orientation to the atomic beam which exits the graphite oven tube. Here, the velocity spread along the laser axis is reduced significantly, resulting in a residual Doppler broadening of about 250 MHz FWHM. In order to maximize the ionization efficiency, the laser beam of interest was enlarged with a telescope, to a diameter of about 25 mm, to cover the complete accessible ionization volume. The ionization geometry could be changed within a few seconds, using magnetic detachable mirror mounts.

The radioactive samples of ^{97}Tc and ^{99}Tc were kindly provided and prepared by the institute of nuclear chemistry of Mainz university. A solution, containing the Tc atoms in the form of ammonium pertechnate, NH_4TcO_4 , was dropped onto a small metallic foil of zirconium or platinum with the size of a few mm^2 , which acted as reduction agents inside the heated graphite oven. In agreement with findings from [73], it was found that the use of Pt resulted in a more reproducible and more stable ion signal. Table 5.1 lists the specifications of the samples used in the experiment.

Table 5.1: List of Tc sample used at the MABU spectrometer for the HFS spectroscopy. It should be mentioned, that the observed isotope ratios at the MABU differed from the amount listed here, possibly due to an inaccuracy in the sample preparation process.

Number	Amount of atoms		Foil
	^{97}Tc	^{99}Tc	
I	-	$1.4 \cdot 10^{13}$	Pt
II	$2.2 \cdot 10^{13}$	$5.6 \cdot 10^{13}$	Zr
III	$8.8 \cdot 10^{13}$	$5.6 \cdot 10^{13}$	Zr
IV	$8.8 \cdot 10^{13}$	$5.6 \cdot 10^{13}$	Zr

With proper operation of the quadrupole mass filter (QMS), both isotopes could be well suppressed against each other, as shown in the mass spectrum in figure 5.12. The background due to the dark count rate of the ion detection was on average about $1.8(2) \text{ s}^{-1}$, a typical value obtained at this spectrometer. Even though it did not affect the spectroscopic measurements, it should be mentioned, that the observed isotope ratio of ^{97}Tc and ^{99}Tc differed from the ratios quoted by the preparation laboratory. As depicted in the graph, the amount of ^{97}Tc was about a factor 7 smaller than the amount of ^{99}Tc . This fact was observed for all samples used and indicated a systematic inaccuracy in the sample preparation process.

5.2.2 Study of the Ionization Scheme

The objectives of the present study were a comparison of alternative excitation ladders with regard to ionization efficiency and a precise characterization of the corresponding isotope shifts and underlying hyperfine structures. This is essential for the identification of possible frequency dependent effects of the simultaneous excitation and ionization of ^{97}Tc and ^{99}Tc with a broadband laser system. In addition precise data of HFS and nuclear moments of Tc is still rare or even unknown for both isotopes.

The basic atomic level structure of Tc was studied by W. R. Bozman et al. and Patrick Palmeri and Jean-Francois Wyart [128]. The ionization potential has been determined by precise evaluation of Rydberg series using RIMS [129]. As mentioned above, precise data on

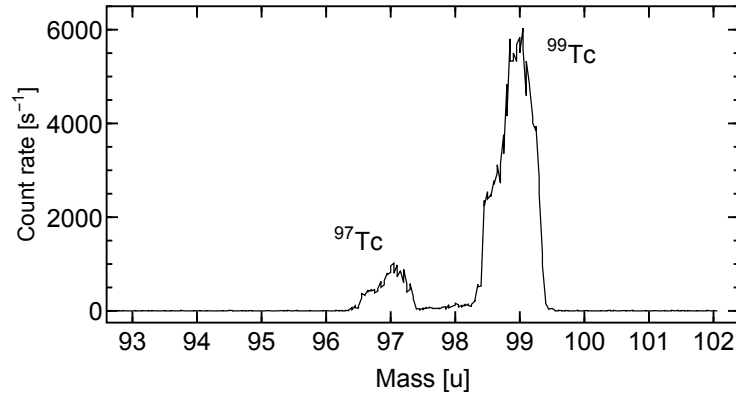


Figure 5.12: Tc mass spectrum obtained at the MABU spectrometer. Both isotopes, ^{97}Tc and ^{99}Tc , are well separated. See text for additional information.

the HFS in Tc is very rare. The transitions used in the present work were only studied in ^{99}Tc by Wendlandt et al. [130] which will serve used as main reference throughout this chapter.

Figure 5.13 summarizes the investigated excitation ladders. Three strong transition to the $4d^5(^6S)5s(^7S)5p^6P^o$ fine structure triplet was used as first step. The transition strength to the $J = 3/2, 5/2,$ and $7/2$ component are $3.8 \cdot 10^7, 4.0 \cdot 10^7,$ and $4.2 \cdot 10^7 \text{ s}^{-1}$, respectively. From these first excited states a set of suitable transitions leads two the fine structure components of the $4d^6(^5D)5d^6P$ state, with fundamental wavelength close to the Ti:sapphire gain maximum enabling high laser powers. All first and second excitation steps required frequency doubling of the laser light (SHG). Subsequently, four different autoionizing states were used for efficient ionization. This set of excitation steps defined a multitude of possible excitation ladders, which were characterized and compared. The respective wavelength of the first, second, and third excitation steps lie closely together, which enabled fast switching between different schemes. The excitation ladder which is currently used in the ultra trace analysis project is on the right side of figure 5.13 and is highlighted with orange asterisks. It uses the transitions 429.8 nm, 395.2 nm, and 841.7 nm and will be referred to as the ultra trace analysis ionization scheme throughout the present work.

In a first step, all possible excitation ladders were briefly compared in terms of ionization efficiency. The ultra trace analysis ionization scheme with the first step leading to the $J = 7/2$ state, showed the highest ionization rates. In comparison, the use of the alternative AI transition at 838.2 nm yielded a 10% smaller ionization rate, while the schemes using the 423.9 nm first step transition to the $J = 3/2$ state gave the smallest ionization efficiencies. This observation is in good agreement with the expectations based on the different transition strengths of the first excitation steps, which usually plays a major role regarding the ionization efficiency.

Figure 5.14 visualizes the clear difference between in-source spectroscopy with the standard laser configuration (blue) and the narrowband dual etalon configuration (red). The isotope ^{99}Tc was used in both spectra. As a result of the reduced spectral laser linewidth in the dual etalon configuration, the experimental linewidth in the spectrum is reduced correspondingly from a full width at half maximum of 30 GHz to about 3.7 GHz FWHM, respectively. The larger splitting of the upper state $^6P_{5/2}^o$ with a reported HFS coupling constant of $A = 892(4)$ MHz could be partly resolved for the hyperfine states with higher F , while the significantly smaller splitting of the $^6S_{5/2}$ ground state with $A = -109.1(9)$ MHz could not be resolved [130].

As an example, figure 5.15 presents the frequency scans for all three transitions in

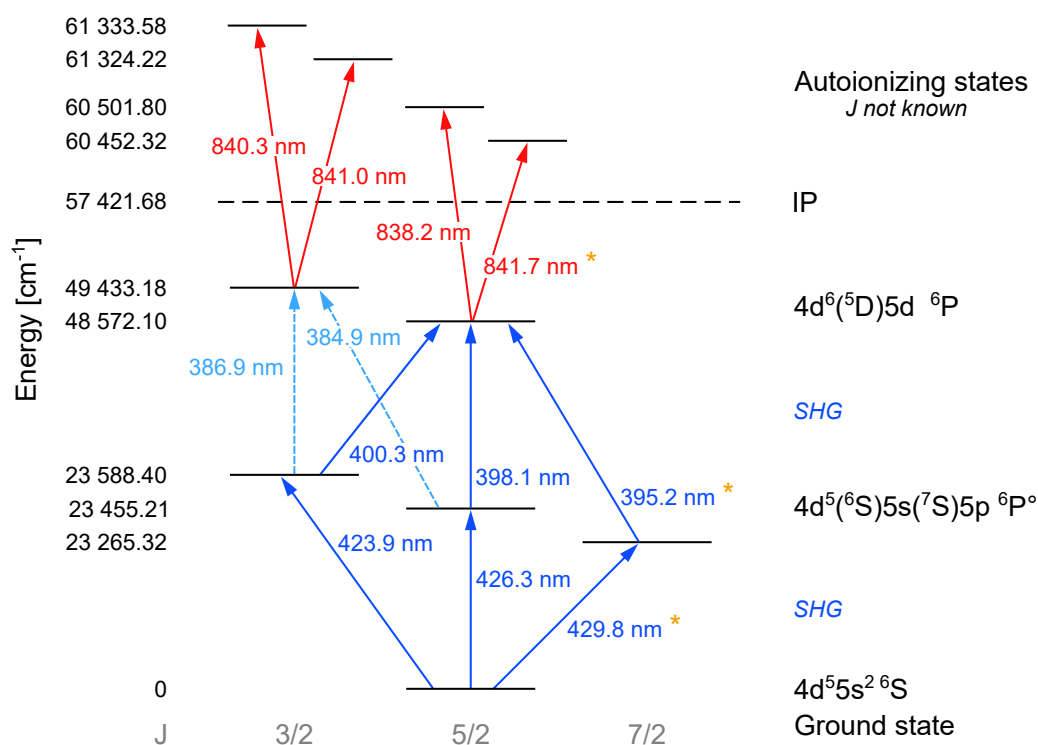


Figure 5.13: Ionization schemes for Tc. The strong transitions to the different ${}^6P^{\circ}$ fine structure states in the first ionization step enable a multitude of suitable ionization schemes. The respective wavelengths of the first, second, and third excitation steps lie closely together, allowing fast switching between the different schemes. The ionization scheme currently used in the ultra trace analysis project is indicated by the orange asterisks. See text for further description.

both isotopes of the ultra trace analysis ionization scheme using the dual etalon laser configuration and in-source ionization geometry. A full compilation of frequency scans for all investigated transitions is given in the appendix in section B. Several conclusions can be drawn from the frequency scans. Although the HFS could only be partially resolved, the observed structures are very similar for both isotopes, ${}^{97}\text{Tc}$ and ${}^{99}\text{Tc}$, corresponding to similar A coupling constants, which in turn indicate a similar magnetic dipole moment of the nuclei. The observed splittings in the first excited states ${}^6P^{\circ}$, which are partly resolved in the scans of the first step transitions, agree with the values for the A factors reported in [130]. Only a minor frequency shift is observed in all spectra, indicating a relatively small isotope shift of about 300 MHz, which is negligible when using high power broadband radiation from the standard laser configuration. Also in the transition to the AI state at 60452.32 cm^{-1} , depicted in the upper graph in figure 5.15, some HFS structure could be observed, a feature which is usually completely covered by the typically broad linewidth of the resonance. A full analysis of the hyperfine structure will be performed with the significantly better resolved spectra from the scans with the single mode laser in the following section.

These results show ideal conditions for the resonance ionization of both isotopes of interest as performed in the ultra trace analysis project. The wide hyperfine structure and the negligible isotope shift are completely covered when using high power broadband radiation from the standard Ti:sapphire laser system. This allows simultaneous ionization of both isotopes without the need to adjust the laser frequency for each isotope. Here, the HFS was not completely resolved, as the total experimental linewidth was limited by the

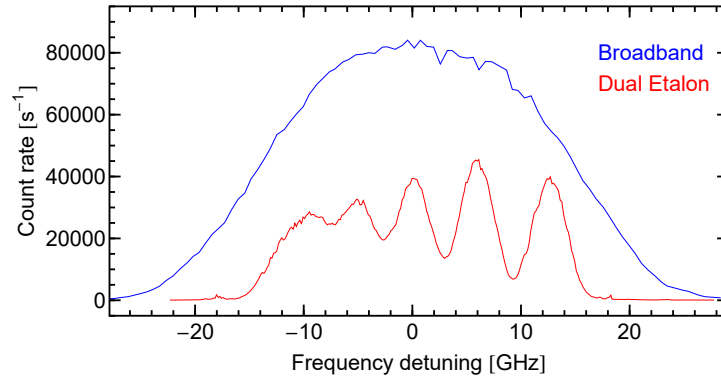


Figure 5.14: Comparison of spectra from ^{99}Tc in in-source spectroscopy with standard laser configuration (blue) and dual etalon configuration (red). The spectra shown are from the first step transition with $J = 5/2 - J' = 5/2$. The spectral linewidth is clearly reduced from 30 GHz to 3.7 GHz FWHM when using the dual etalon configuration, partly resolving the underlying HFS. The blue spectra was scaled for a better comparison. See text for more information.

laser linewidth of the dual etalon lasers and the Doppler broadening, which were about the same size. To overcome this drawback, the unseeded single mode laser was used for precise spectroscopy in some selected transitions.

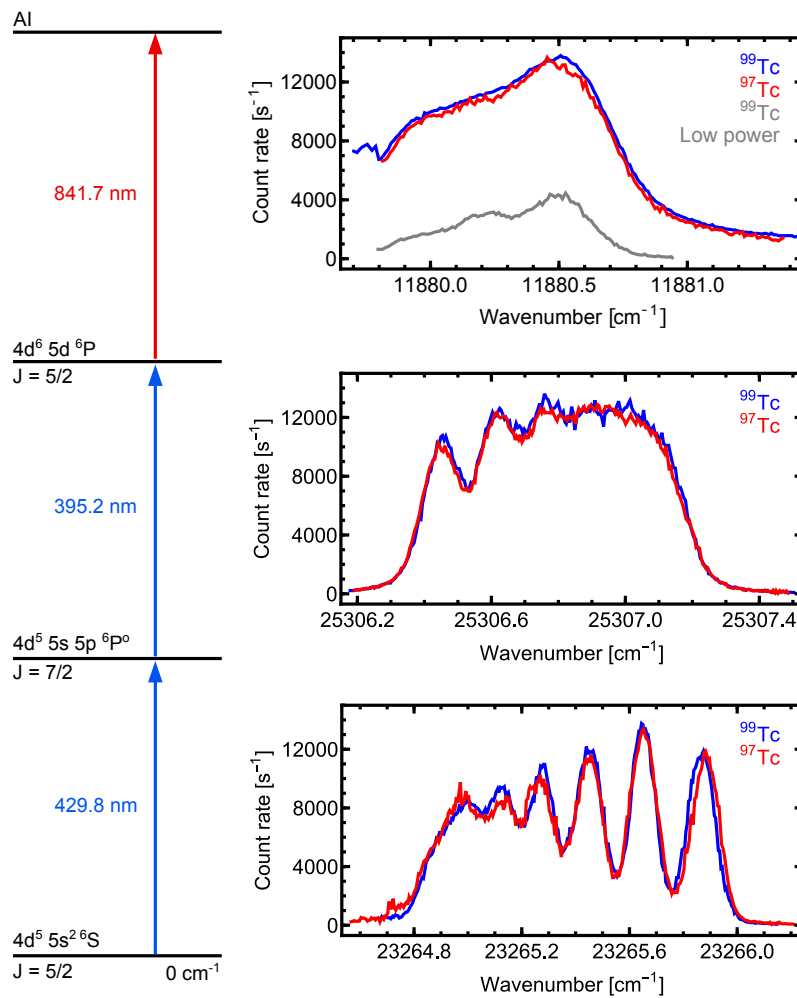


Figure 5.15: Frequency scans with dual etalon laser configuration in the excitation steps of the ultra trace analysis ionization scheme for both Tc isotopes. The count rate of the scans in ^{97}Tc have been scaled for better comparison. See text for further discussion.

5.2.3 High-Resolution HFS Study of the First and Second Excitation Steps

A selection of first and second step transitions were investigated with the single mode Ti:sapphire laser, as described in section 5.1, in order to fully resolve the HFS spectra. As the single mode laser was still in an early development stage, frequency tuning as well as stabilization were performed by manual control of the voltages applied to the two piezo actuators inside the air-spaced etalon and the ring cavity. The fringe pattern of the scanning FPI provided precise information of the relative frequency and visualized the occurrence of possible side modes. Due to the complexity of the manual control, mode jumps or brief appearance of side modes could not be completely avoided. However, most of the affected data points were easily identified as the FPI provided clear information on the spectral profile. In addition, the affected points are clearly separated in the spectrum by a fixed offset which equals one FSR of the ring cavity, about 470 MHz. The identified data points were excluded from final analysis.

In order to avoid tampering the strength of the individual hyperfine transitions in the investigated first or second excitation steps, the respective second or first step transition was excited with a standard Ti:sapphire laser without thin etalon. This increased the fundamental laser linewidth significantly to about 50 – 100 GHz, leading to an equal excitation of all individual HFS transitions across the entire hyperfine structure.

As a result from the manual stabilization and due to the sensitivity of the single mode laser prototype, the raw data showed a relatively large scatter, primarily cause by power fluctuations of the laser. Therefore, each multiplet structure was scanned two to six times for each isotope, resulting in about 25000 to 50000 data points for each spectrum. In each spectrum, one resonance peak was chosen as a reference and scanned several times over the course of the measurement. This was used later in the analysis to identify the relative strength of the signal, as the absolute signal decreased over the course of the measurement due to depletion of the sample. Finally the count rate was corrected correspondingly and the spectrum quantized via data binning along the frequency axis.

Study of the First Excitation Step

Two first step transitions were investigated, the ${}^6S_{5/2} - {}^6P_{7/2}^o$ transition at 429.8 nm and the ${}^6S_{5/2} - {}^6P_{3/2}^o$ transition at 432.9 nm. The single mode laser was used for the spectroscopy in the first excitation step, the second step was excited by the broadband radiation of a standard laser without an etalon as mentioned above, and the third step was excited by a Ti:sapphire laser in standard configuration. To avoid power broadening in the first excitation step, the laser power was reduced to about 1.0 mW of frequency doubled light in a 3 cm² spot before entering the MABU apparatus in perpendicular orientation to the atomic beam. For excitation step two and three, the power was 800 mW, and 2.0 W, respectively.

Figure 5.16 shows a comparison of the spectra in the ${}^6P_{7/2}^o - {}^6P_{5/2}$ transition in ⁹⁹Tc obtained with the dual etalon laser (black) and with the single mode laser. Here, the gray dots represent the raw data of the single mode scan while the red curve shows the binned data. The increase in resolution in the spectra of the single mode laser is very clear, showing linewidth of about 250 MHz FWHM. The graph also illustrates the mentioned, relatively large scatter of the raw data, caused by power fluctuations and frequency jitter of the single mode laser on a ms time scale, which could not be compensated completely by the manual stabilization. As for the following spectra, the data from the scans using the single mode laser was binned in intervals of 30 MHz widths.

The splitting of the two investigated transitions ${}^6P_{5/2} - {}^6P_{7/2}^o$ and ${}^6P_{5/2} - {}^6P_{3/2}^o$ are illustrated in figure 5.17. As a result, a total number of 18 and 12 transitions are expected,

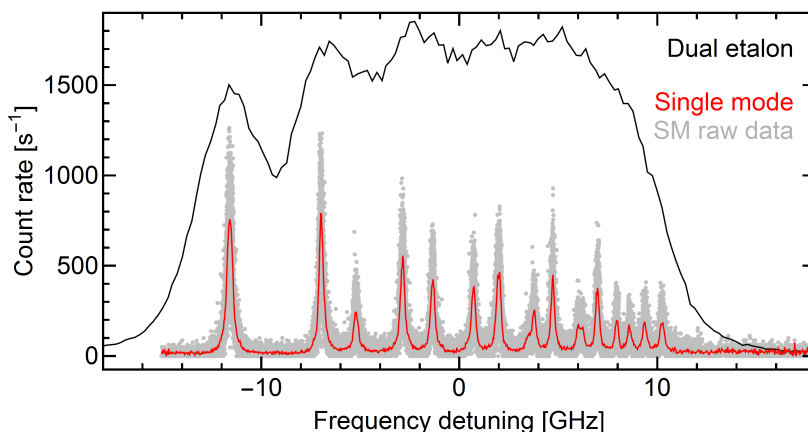


Figure 5.16: Comparison of frequency scans with dual etalon laser and single mode laser of the second step transition ${}^6P_{7/2}^o - {}^6P_{5/2}$ in ${}^{99}\text{Tc}$. The solid lines in black and red represent the binned data of the dual etalon scan and the single mode scan, respectively. The gray points show the raw data of the scan using the single mode laser. The center frequency corresponds to 25306.80 cm^{-1} . The data of the dual etalon scan was scaled for a better comparison.

respectively. According to formula 2.18 and the discussion in section 2.1.3, a set of Voigt profiles, as described in 2.3.3 was fitted to the binned data. Each resonance peak features a free peak height and Lorentzian width. In order to keep the number of free fit parameters in a reasonable ratio to the observed statistic scatter of the data points, a single Gaussian width was used for each spectrum, as the Doppler broadening is expected to effect each component in the same way. The resulting fits for the two first step transitions are shown in figure 5.18.

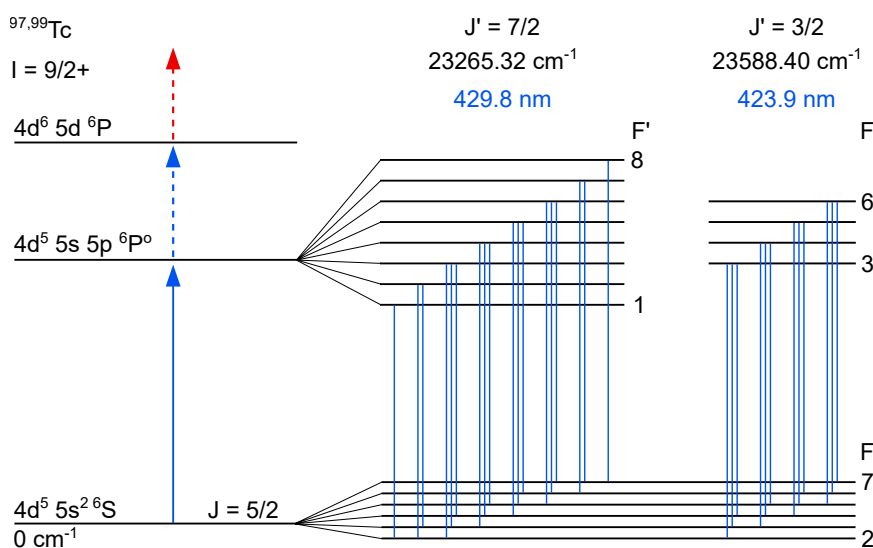
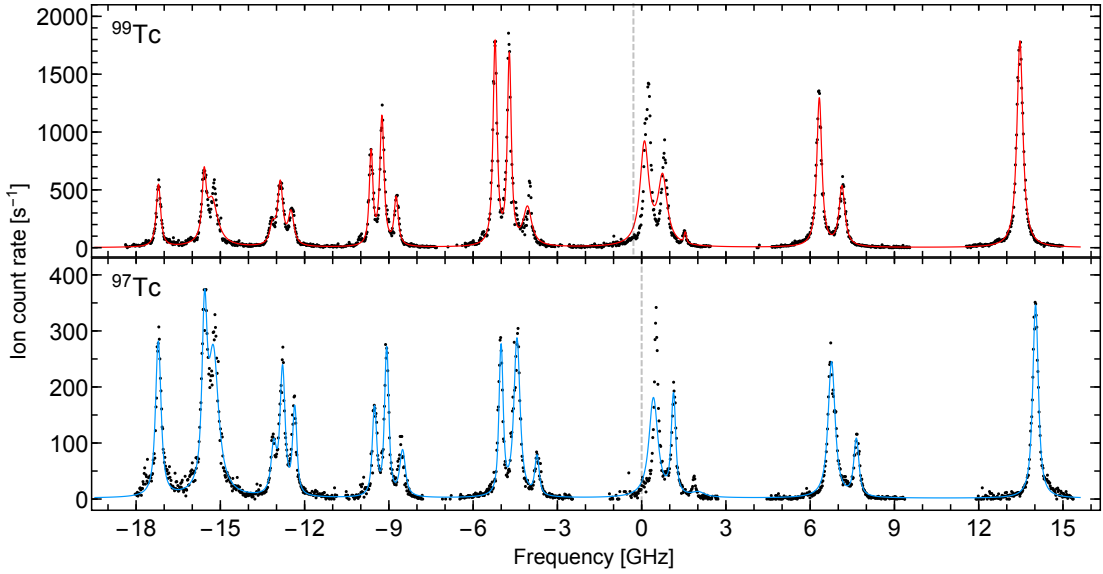
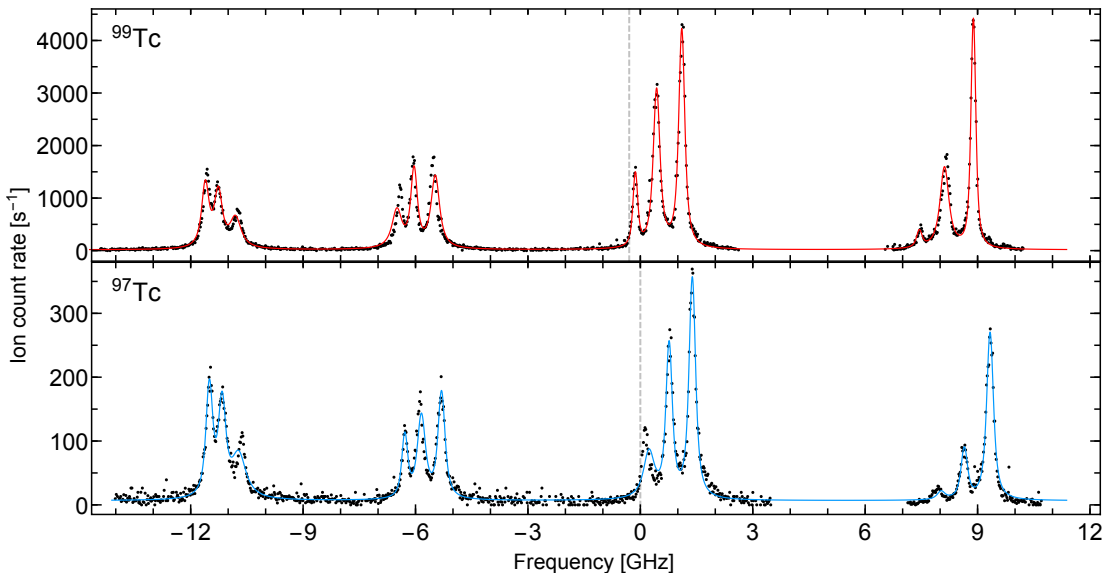


Figure 5.17: Schematic illustration of the hyperfine splitting of the first step transitions ${}^6S_{5/2} - {}^6P_{7/2}^o$ and ${}^6S_{5/2} - {}^6P_{3/2}^o$ at 429.8 nm and 423.9 nm, respectively, in Tc.



(a) Fit to the experimental data of the ${}^6S_{5/2} - {}^6P_{7/2}^o$ transition at 429.8 nm. The center frequency corresponds to $23265.379 \text{ cm}^{-1}$.



(b) Fit to the experimental data of the ${}^6S_{5/2} - {}^6P_{3/2}^o$ transition at 423.9 nm. The center frequency corresponds to $23588.421 \text{ cm}^{-1}$.

Figure 5.18: Binned experimental data (black) of the HFS structure in the first step transition in ${}^{97}\text{Tc}$ and ${}^{99}\text{Tc}$. The single mode laser was used for the spectroscopy, while broadband lasers were used for the subsequent excitation steps. As shown in red and blue, hyperfine spectra based on Voigt profiles were fitted to the data. The resulting curves show slight discrepancies to the experimental data, caused by a technical malfunction of the wavemeter. See text for further discussion.

In general, all spectra show a good spectral resolution with full separation of almost all individual hyperfine transitions. The contributions to the full width at half maximum of the Voigt profiles are summarized in table 5.2. The mean widths of the full peak are about 240 MHz, while the most narrow peaks of the spectra show reach linewidths below 200 MHz. Each multiplet in the spectra was alternately scanned on mass 97 u and 99 u, resulting in identical oven temperature and laser alignment for both isotopes.

Table 5.2: Contributions to the full width at half maximum of the resonance peaks in the first excitation step spectra shown in figure 5.18. The values are derived by fitting of a set of Voigt profiles. All values are given in MHz.

	FWHM	Gaussian	Lorentzian	Total
${}^6S_{5/2} - {}^6P_{7/2}^o$				
${}^{97}\text{Tc}$		100	197	243
${}^{99}\text{Tc}$		67	211	233
${}^6S_{5/2} - {}^6P_{3/2}^o$				
${}^{97}\text{Tc}$		99	194	239
${}^{99}\text{Tc}$		87	195	232

The fitted curves show slight discrepancies to the experimental data, visible at the multiplets at -15 GHz and 1 GHz in the ${}^6S_{5/2} - {}^6P_{7/2}^o$ spectra and -11 GHz and -6 GHz in the ${}^6S_{5/2} - {}^6P_{3/2}^o$ spectra. The spacing of the individual peaks of the multiplets seems well reproduced for most multiplets but differs for some multiplets. It is important to note, that this effect is independent from the chosen isotope and shows its major impact at the same regions of the spectra of each transition.

The origin of this discrepancy could be identified, but unfortunately only some weeks after the actual experiment. The apparent shifting of some peaks is caused by a technical malfunction of the WSU30 wavemeter, which showed a systematic, periodical deviation in the readout, as illustrated in figure 5.19, where the difference of the wavemeter readout to the input laser frequency is plotted against the input frequency. The reference laser radiation was provided by a CW diode laser system, frequency stabilized to $< \pm 5$ MHz. A brief description of this laser system is given in section 3.1.3. The periodic discrepancy reached values up to 80 MHz in the fundamental laser frequency, resulting in a corresponding shift of up to 160 MHz in the final spectrum after frequency-doubling. This matches the observed frequency mismatch between the fit and some peaks in the experimental data in Tc. Unfortunately, the deviation changed considerably each time the wavemeter was calibrated (see curves in figure 5.19), preventing a proper correction of the data points in the final analysis after the problem was discovered. As a consequence, the fit model used does not properly reproduce the experimental data and relatively large errors have to be assumed for the extracted HFS coupling constants A and B , as well as for the center frequency of the unperturbed transition.

Table 5.3 summarizes the HFS coupling constants A and B and the isotope shifts $\delta \nu$ derived from the fits. The ground state parameters of each isotope differ by up to 14 MHz while the A'/A ratio, which is expected to be very similar for each isotope for a given transition shows significant deviations. Due to the considerably better signal-to-noise ratio, the errors from the spectra in ${}^{99}\text{Tc}$ are estimated to be slightly smaller than for ${}^{97}\text{Tc}$. However, the A and A' of ${}^{99}\text{Tc}$ match the values given by Wendlandt et al. [130] within ± 4 MHz. The obtained B coupling constants are strongly influenced by the malfunction of the wavemeter as the introduced shifts are about the same size as the effect of B . Consequently, the values

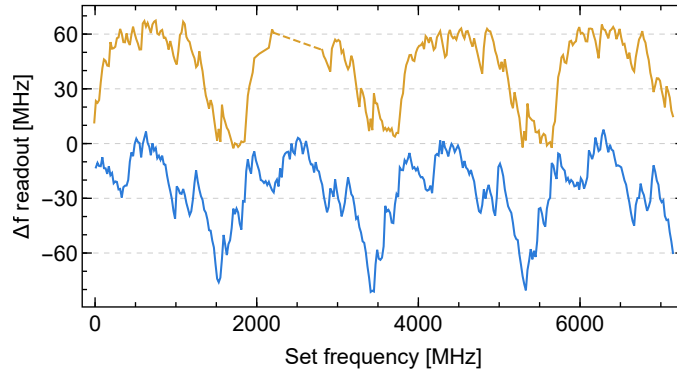


Figure 5.19: Visualization of the periodic systematic deviation of the wavemeter frequency readout. The difference of the wavemeter readout to the input frequency is plotted against the input frequency, which was provided by a CW diode laser, frequency stabilized to $< \pm 5$ MHz [64, 43]. Each curve features an arbitrary offset in Δf -direction.

of ^{99}Tc differ significantly to the literature values and the errors are estimated to be about ten times larger than the errors for the A constants. It should be noted that the ground state splitting in [130] could not be resolved and therefore a value for B was not given.

Despite the relatively large error due to wavemeter malfunction, the data provide important results with regard to the resonance ionization for ultra trace analysis using the $^6\text{S}_{5/2} - ^6\text{P}_{7/2}^o$ transition. The A coupling constant for both isotopes, ^{97}Tc and ^{99}Tc , are similar within a few percent and the resulting nearly identical hyperfine structures of the transition span across 32 GHz, while the isotope shift $\delta\nu$ is only $-321(40)$ MHz. As already discussed at the end of the previous section 5.2.2, this poses ideal conditions for the ultra trace analysis measurements, since effects due to HFS structure and isotope shifts can be completely neglected when using broadband laser radiation.

Table 5.3: Summary of the HFS coupling constants A and B and the isotope shifts $\delta \nu$ as derived from the fit presented in figure 5.18. The literature values for ^{99}Tc are taken from [130]. It should be noted that in [130], the ground state splitting could not be resolved and a value for B was not given. In this context, the errors given for A in [130] seem to be underestimated. See text for further information. All values are given in units of MHz.

Parameter	^{97}Tc	^{99}Tc	$^{99}\text{Tc}_{\text{lit}}$
Transition ${}^6S_{5/2} - {}^6P_{7/2}^o$			
A	-118(10)	-106(7)	-109.1(9)
A'	808(12)	801(10)	798.6(36)
B	-128(120)	-138(85)	-
B'	-217(120)	-177(85)	-57(17)
A'/A	-6.9(6)	-7.5(5)	-7.32
$\delta \nu$	-321(40)	0	-
Transition ${}^6S_{5/2} - {}^6P_{3/2}^o$			
A	-104(10)	-112(7)	-109.1(9)
A'	1214(10)	1178(7)	1182(4)
B	-33(120)	-83(85)	-
B'	92(120)	32(85)	-12(12)
A'/A	-11.6(11)	-10.5(7)	-10.8
$\delta \nu$	-297(40)	0	-

Study of the Second Excitation Step

The two second steps transitions ${}^6P_{7/2}^o - {}^6P_{5/2}$ at 395.2 nm and ${}^6P_{5/2}^o - {}^6P_{3/2}$ at 384.9 nm were investigated using the single mode Ti:sapphire laser. As for the scans in the first excitation steps, the laser power in the probed step was reduced to about 1.0–2.2 mW in a 3 cm² spot before entering the MABU to avoid power broadening. The first step transition was excited with 210 mW of frequency-doubled laser radiation and 1.9 W were used for the third step transition.

Figure 5.20 provides a visualization of the hyperfine splitting in the upper and lower state. A total number of 18 and 12 individual HFS transitions are expected for the two transitions. As for the spectra in the first excitation step, a set of Voigt profiles was fitted to the experimental data. The results are shown in figure 5.21.

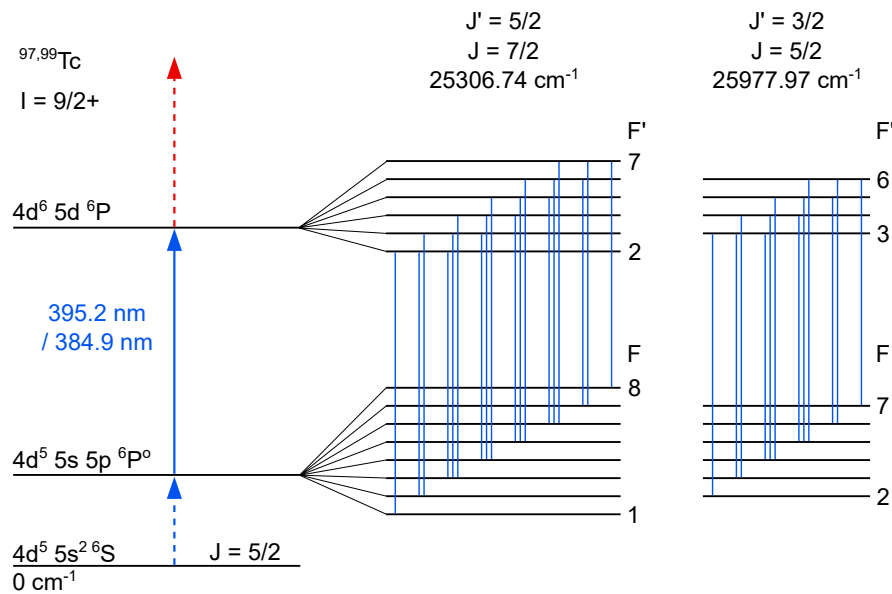
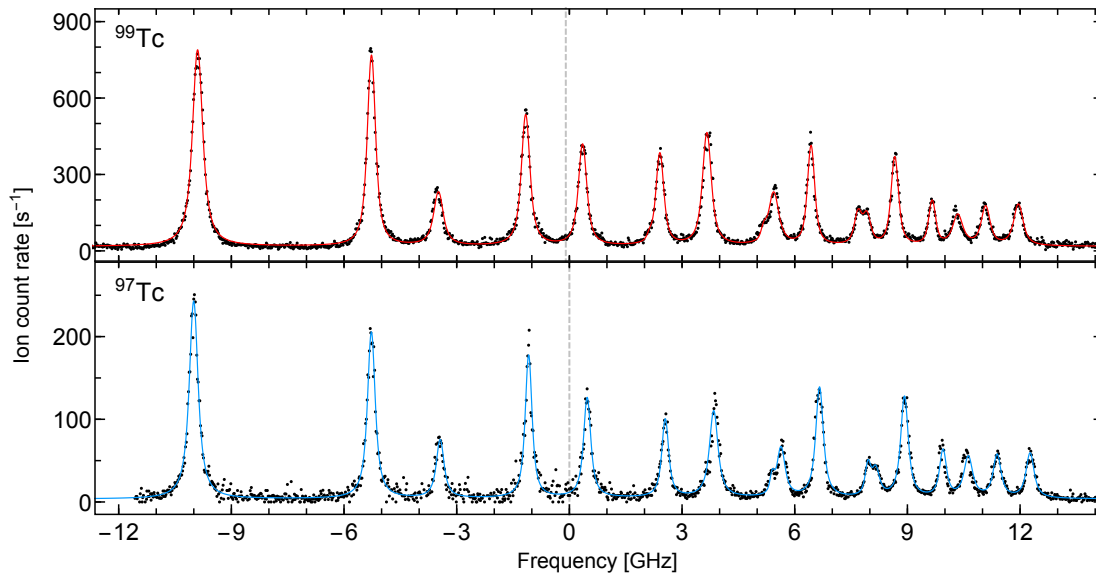


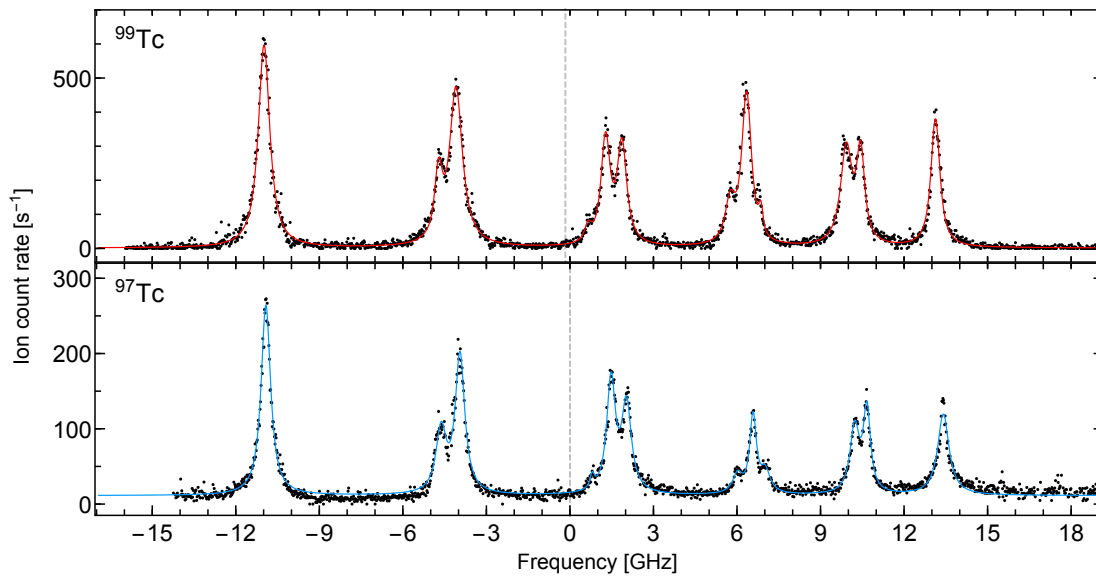
Figure 5.20: Schematic illustration of the hyperfine splitting of the second step transitions ${}^6P_{7/2}^o - {}^6P_{5/2}$ and ${}^6P_{5/2}^o - {}^6P_{3/2}$ at 395.2 nm and 384.9 nm, respectively, in Tc.

The spectra of the second excitation step show similar resolution as the spectra of the first excitation steps. Almost all of the individual hyperfine transitions could be resolved. Table 5.4 summarizes the contributions to the full width at half maximum of the Voigt profiles. As expected, the Gaussian contributions are comparable to the Gaussian contributions of the first step spectra. As a similar laser power of 1.0 mW was used for the ${}^6P_{7/2}^o - {}^6P_{5/2}$ transition, the Lorentzian contributions also agree well with the Lorentzian contributions of the first step scans. As the available time for scanning the ${}^6P_{5/2}^o - {}^6P_{3/2}$ transition was limited, a higher laser power of 2.2 mW was used to increase the ionization rate and to achieve sufficient statistics. The resulting increase in power broadening is clearly visible in graph 5.21b and is also expressed in the almost doubled Lorentzian FWHM listed in table 5.4. As a result, the mean FWHM of the Voigt peaks are about 250 MHz for the ${}^6P_{7/2}^o - {}^6P_{5/2}$ transition and significantly higher, about 400 MHz, for the ${}^6P_{5/2}^o - {}^6P_{3/2}$ transition. Similar to the results from the first step spectra, the most narrow peak in the spectra of the ${}^6P_{7/2}^o - {}^6P_{5/2}$ transition showed a FWHM of only 160 MHz.

Also here, the resulting fits show deviations to the experimental data, caused by the incorrect frequency readout of the wavemeter. In comparison to the first step spectra, it seems that the effect has less impact. This might be caused by the operation at a slightly



(a) Fit to the experimental data of the ${}^6P_{7/2}^o - {}^6P_{5/2}$ transition at 395.2 nm. The center frequency corresponds to $25306.743 \text{ cm}^{-1}$.



(b) Fit to the experimental data of the ${}^6P_{5/2}^o - {}^6P_{3/2}$ transition at 384.9 nm. The center frequency corresponds to $25977.965 \text{ cm}^{-1}$.

Figure 5.21: Binned experimental data (black) of the HFS structure in the second step transition in ${}^{97}\text{Tc}$ and ${}^{99}\text{Tc}$. The single mode laser was used for the spectroscopy, while broadband lasers were used in the first excitation steps. As shown in red and blue, hyperfine spectra based on Voigt profiles were fitted to the data. Compared to the fits in the first step transition, the resulting curves show less discrepancies to the experimental data. See text for further discussion.

Table 5.4: Contributions to the full width at half maximum of the resonance peaks in the second excitation step spectra shown in figure 5.21. The values are derived by fitting of a set of Voigt profiles. All values are given in MHz.

FWHM	Gaussian	Lorentzian	Total
${}^6P_{7/2}^o - {}^6P_{5/2}$			
${}^{97}\text{Tc}$	94	204	243
${}^{99}\text{Tc}$	134	189	263
${}^6P_{5/2}^o - {}^6P_{3/2}$			
${}^{97}\text{Tc}$	94	377	401
${}^{99}\text{Tc}$	108	371	403

different wavelength region, about 30 nm lower than for the first step transitions, where the discrepancy of the wavemeter readout might be less pronounced.

Table 5.5 summarizes the parameters derived by the fit. The determined coupling constants of ${}^{99}\text{Tc}$ agree well with the available values from Wendlandt et al. [130]. The values of the ${}^6P_{7/2}^o$ state from the ${}^6P_{7/2}^o - {}^6P_{5/2}$ transition also agree with the corresponding values obtained from the ${}^6S_{5/2} - {}^6P_{7/2}^o$ first step transition.

The ${}^6P_{7/2}^o - {}^6P_{5/2}$ transition, which is used as the second excitation step in the ultra trace analysis ionization schemes provides the same suitable features as the first step transition. Both characteristics of the transition, the HFS which is quite similar for both isotopes and the observed isotope shift of only $-95(30)$ MHz can be neglected when using a high power broadband laser system with spectral linewidth well above 10 GHz.

Table 5.5: Summary of the HFS coupling constants A and B and the isotope shifts $\delta\nu$ derived from the fit presented in figure 5.21. The literature values for ^{99}Tc are taken from [130]. All values are given in units of MHz.

Parameter	^{97}Tc	^{99}Tc	$^{99}\text{Tc}_{\text{lit}}$
Transition ${}^6P_{7/2}^o - {}^6P_{5/2}$			
A	822(10)	804(7)	798.6(3,6)
A'	260(7)	252(5)	-
B	-16(120)	-46(60)	-57(17)
B'	40(120)	44(60)	-
A/A'	3.17(9)	3.19(7)	-
$\delta\nu$	-95(30)	0	-
Transition ${}^6P_{5/2}^o - {}^6P_{3/2}$			
A	906(12)	896(10)	892(4)
A'	-112(10)	-114(7)	-
B	-97(120)	-1(85)	93(18)
B'	-12(120)	86(85)	-
A'/A	-8.1(7)	-7.9(5)	-
$\delta\nu$	-165(40)	0	-

2D Mapping of the Second Excitation Step

In the ${}^6P_{7/2}^o - {}^6P_{5/2}$ transition the splitting of the upper and the lower state exhibit similar sizes. In this case, the multiplets in the observed spectra, as shown in figure 5.21a, start to overlap which can cause individual peaks to overlap, as for example at 5.5 GHz or at 8 GHz. In some cases, this might affect the correct identification of the peaks, especially when the nuclear spin I or the total angular momentum J is not known. Additional information can be gained when using specific excitations in the first and second step. This results in a full 2-dimensional map of first and second step or alternatively in specific slices through the corresponding 2D plane. This approach is referred to as *2D mapping* and was already demonstrated for example in [43] and in [127].

A sliced 2D frequency map for the ${}^6S_{5/2} - {}^6P_{7/2}^o$ and the ${}^6P_{7/2}^o - {}^6P_{5/2}$ transition in ^{99}Tc is shown in figure 5.22. The first step transition was excited with a Ti:sapphire laser in dual etalon configuration, similar to the measurements presented in section 5.2.2. This enabled the selective addressing of a specific multiplet, populating a particular hyperfine level with corresponding F of the first excited state ${}^6P_{7/2}^o$. The single mode laser was used in the second excitation step, to probe the transitions starting from the populated hyperfine level with high resolution. In this way, the spectrum was disentangled revealing overlapping peaks and allowing a clear assignment of the observed peaks.

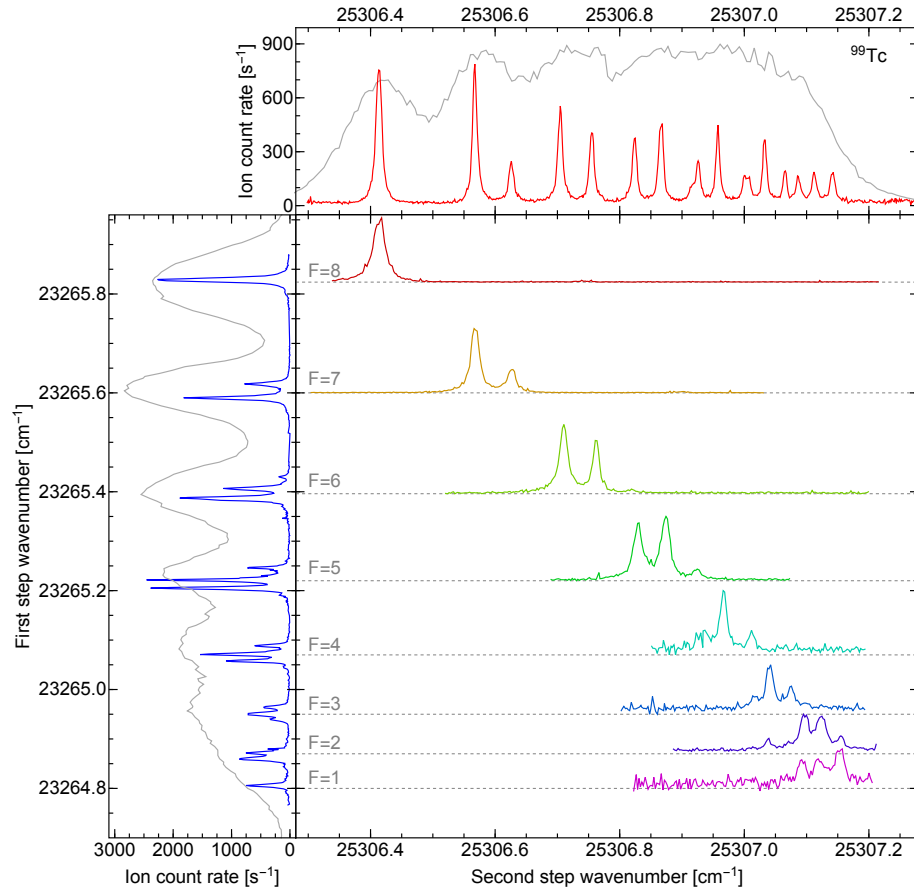


Figure 5.22: Visualization of the 2D frequency space of the first step transition ${}^6S_{5/2} - {}^6P_{7/2}^o$ and second step transition ${}^6P_{7/2}^o - {}^6P_{5/2}$. The left and upper panel show 1D frequency scans in the first and second excitation step, using the dual etalon laser (gray) or the single mode laser (blue/red) respectively. The center panel shows frequency scans in the second excitation step while the first step transition was excited using a laser in dual etalon configuration, leading to the populating of a particular hyperfine level F (gray labels). The single mode Ti:sapphire laser was used for the subsequent second excitation step, probing the individual multiplets of the second step spectrum (red) with high resolution.

5.3 The PI-LIST: A New Tool for High-Resolution Spectroscopy

As mentioned in the previous sections, the atomic spectroscopy on rare radioactive samples is essential for a comprehensive understanding of atomic and nuclear structure. Usually, the size of radioactive samples is limited due to legal regulations, restricted availability, and the health risk for the experimentalists. This is of special relevance when dealing with radioactivity in an off-line laboratory, like the one of the LARISSA working group. In addition the handling of radioactivity comes with a significant higher complexity of the experiment and can also increase the financial costs. Consequently, it is of highest interest to maximize the experimental overall efficiency as well as to reduce the sources of background in order to increase the experimental sensitivity. This becomes even more important, when high spectral resolution is required, as this always goes along with a significant reduction of the efficiency.

In the case of RIS experiments at the LARISSA laboratory, the sample size is usually limited to about 10^9 - 10^{14} atoms per sample. Depending on that number and the efficiency of the accessible ionization schemes, the realization of high-resolution spectroscopy in order to inspect the HFS can easily become a challenging task. Numerous developments of the LARISSA group aimed to push the boundaries of technical feasibility for these high-resolution RIMS experiments, e.g. [43, 122, 127]. In general the use of a high energy magnetic mass separator, like the RISIKO separator as described in section 3.2.1, is favored over spectrometers using quadrupole mass filters, as the former offer a significantly higher ion transmission, which is at least ten times larger. This section will describe the development of a next step towards highly sensitive high-resolution spectroscopy, paving the way for future off-line experiments and future applications at on-line RIB facilities like ISOLDE.

5.3.1 Development of the PI-LIST

As mentioned above, the RISIKO separator at the LARISSA laboratory offers significantly higher ion transmission compared to the MABU spectrometer, a significant advantage when dealing with small samples. As described in 3.2, both setups are capable of sensitive single ion detection by using either a secondary electron multiplier or a channeltron detector. Until now, the RISIKO separator allowed laser ionization only in longitudinal in-source geometry, resulting in a significant Doppler broadening due to the temperature in the hot ion source with spectral linewidths of 1-5 GHz. Obviously, this is too large to resolve most HFS splittings in atomic spectra sufficiently.

In general, there are three ways to overcome this barrier. First, relative reduction of the Doppler velocity spread by (anti-)collinear spectroscopy on an accelerated ion beam, which was demonstrated in the past [131, 132, 133, 134], but is presently not available at the LARISSA laboratory. Second, implementation of an ionization geometry with the laser beams of interest oriented perpendicularly to the directed Doppler velocity spread in the atomic beam emerging from the ionizer tube as illustrated in 3.14. And third, the application of Doppler-free two-photon spectroscopy. The latter was successfully demonstrated in the element silicon, achieving experimental linewidths below 100 MHz at the MABU spectrometer [122]. Due to the much lower cross-section of the two-photon absorption process, this technique needs substantially higher laser intensities, suffers from relatively low ionization efficiency, and comes with larger experimental expenditure. In addition, new ionization schemes must be developed as the two-photon absorption is constrained by different selection rules, like $\Delta J = 0, \pm 2$ and $\Delta \pi = 0$, and different accessible frequencies compared to conventional one-photon transitions.

At the RISIKO separator, it was desired to reduce the complexity to a minimum in order to

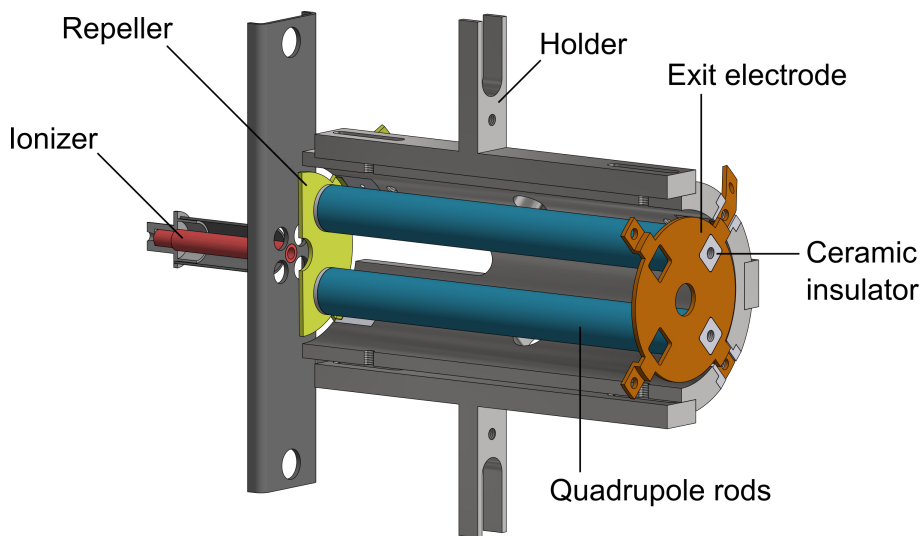
ensure reliable long-term operation with best conditions for high-resolution spectroscopy, an important aspect regarding the long-term goal of an implementation at the ISOLDE on-line facility. The targeted combination of linewidths well below 1 GHz and high transmission efficiency would provide the foundation for a multitude of new high-resolution applications. In this case, the best suited approach to suppress the thermal Doppler broadening was the implementation of a perpendicular alignment of the laser beam of interest, as mentioned above. Consequently, the laser interaction volume must be located outside the hot ionizer tube, enabling perpendicular orientation of the probing laser beam and the atomic beam emerging from the ionizer tube. A suitable environment for such a setup is realized by the LIST, presented in section 3.2.1, as it provides a laser interaction region separated from the hot ion source and a shielding from the strong electric fields in the extraction region. In addition, the quadrupole provides spatial confinement for the ionized atoms, improving the ion transmission, while the repeller enables suppression of background due to surface ionized species. The key objectives and benefits of this concept can be summarized as follows:

- **Reduced Doppler broadening** by perpendicular ionization geometry, allowing spectral linewidths well below 1 GHz,
- **Nearly field-free** ionization region as the strong electric extraction field is shielded by the LIST,
- **High efficiency** due to the combination of high ion beam energy and magnetic mass separator and the additional transversal spatial confinement within the LIST, and
- **Enhanced signal-to-noise ratio**, as surface ions can be well suppressed by the LIST.

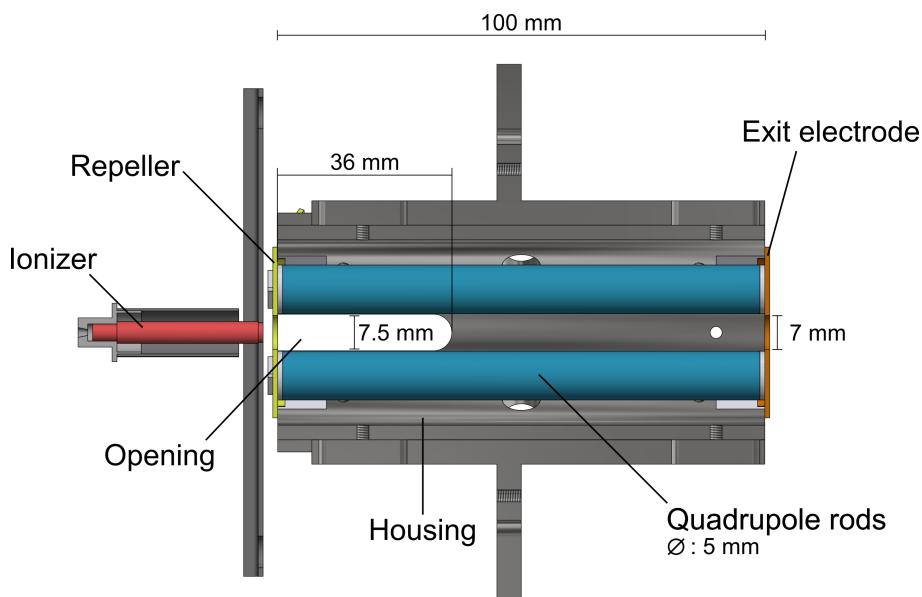
As already mentioned, the full Doppler broadening inside the hot ionizer tube is typically 1-5 GHz. If the ionization is performed inside the LIST, only atoms moving in the direction of the ionizer tube's exit can enter the laser interaction region, resulting in the observed transition lines being slightly blue-shifted and featuring less Doppler broadening. Along the perpendicular axis, the thermal velocity spread of the atomic beam is significantly smaller and not shifted as the symmetric expansion of the atomic beam causes both positive and negative velocity components along the axis. Based on earlier experiments [43], the opening angle was estimated to be about $\beta = 13^\circ$ which corresponds to a remaining Doppler broadening of about 500 MHz FWHM. In addition, the size of the longitudinally aligned laser beams for further excitation and ionization, can be reduced, resulting in a smaller laser interaction region. As a consequence, the opening angle and the residual Doppler broadening can be reduced further, leading to spectral FWHM of less than 100 MHz.

The standard LIST design, described in section 3.2.1, was used as a starting point. Some essential modifications were made to allow a perpendicular ionization geometry inside the LIST's RF quadrupole structure. Due to the perpendicular ionization geometry, the new device was named *perpendicularly illuminated LIST*, short PI-LIST or π -LIST. Figure 5.23 shows a 3D technical drawing of the PI-LIST with the two horizontal slit openings on the sides of the housing, enabling access to the inner LIST volume in perpendicular orientation. As shown in figure 5.23b, the openings were located directly behind the entrance, formed by the repeller electrode, giving access to the region with highest atom density in the atomic beam. The PI-LIST can be operated in the same manner as the conventional LIST. The electric RF quadrupole field on the longitudinal axis is not significantly altered as the housing and the quadrupole rods provide good shielding from external fields.

The vertical width of the openings was chosen to match the vertical distance between the upper and lower pair of quadrupole rods of about 7.5 mm to give access to the entire



(a) Perspective sectional view of the PI-LIST



(b) Lateral sectional view of the PI-LIST

Figure 5.23: 3D CAD model of the PI-LIST. Figure (a) provides an overview of the full geometry. The lateral view (b) clearly illustrates the position and shape of the additional openings in the housing, which allows the perpendicularly aligned laser beam to access to the atomic beam effusing from the ionizer (red). The dimensions and functionality of the repeller (yellow), quadrupole rods (blue), and exit electrode (orange) were not changed compared to the standard LIST design, which is described in 3.2.1.

region behind the repeller electrode. The horizontal length of the openings of about 36 mm was determined by the accessible free aperture of the vacuum viewports (30 mm) and some additional tolerance. As the pulsed laser system operates with repetition rate of 10 kHz, this length has to be compared to distance which the atoms travel between each pulse, to estimate possible losses due to the duty cycle of the system. A typical atom of mass 100 u at a thermal velocity³ at 2000 °C travels about 60 mm in the 100 μ s gap between to laser pulses. In principle, the shorter length of the openings would therefore result in a loss of up to a factor of two when operating in perpendicular ionization geometry compared to conventional LIST operation with longitudinal ionization geometry. However, no significant duty cycle losses were expected with the 30 mm long interaction region, as earlier experiments and simulations indicated that the major part of the ionization occurs in the region of the first 20 mm behind the repeller where the atoms enter the LIST volume [44]. This is due to the transversal expansion of the atomic beam, causing a rapid decrease of the atom density with increasing distance r to the exit opening of the ionizer tube. This issue will be addressed in more detail in the context of a systematic characterization of the PI-LIST in section 5.4.2.

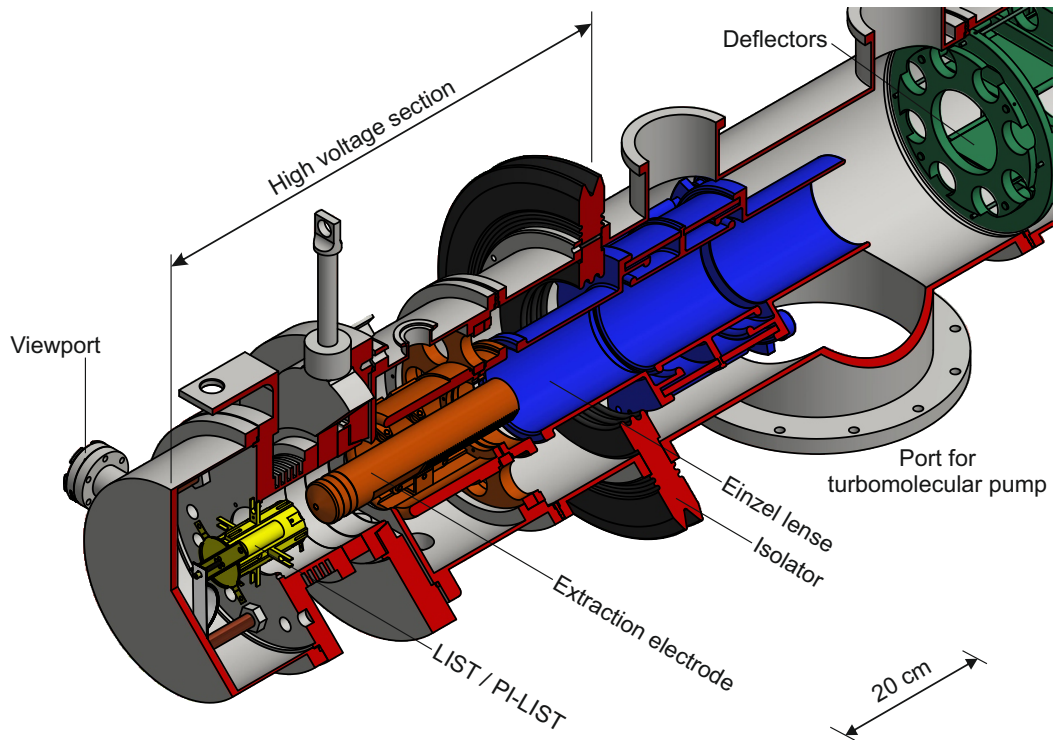


Figure 5.24: PI-LIST installed at the RISIKO frontend. Graphic adopted from [135].

Figure 5.24 shows a sectional CAD view of the RISIKO frontend with installed PI-LIST, while figure 5.25 shows a photograph of the real ion-source and PI-LIST. Two vacuum viewports were installed on the left and on the right side of the vacuum chamber of the ion source unit. In comparison to the standard LIST setup, the PI-LIST had to be positioned closer to the rear side of the ion source unit to place the side openings of the LIST in direct line-of-sight to the opening in the vacuum housing. Correspondingly, all major components of the ion source itself (see figure 3.2.1) were positioned about 52 cm backwards with custom-built spacers. The holders of the PI-LIST were slightly modified to allow a displacement

³Most probable speed of the corresponding Maxwell-Boltzmann distribution.

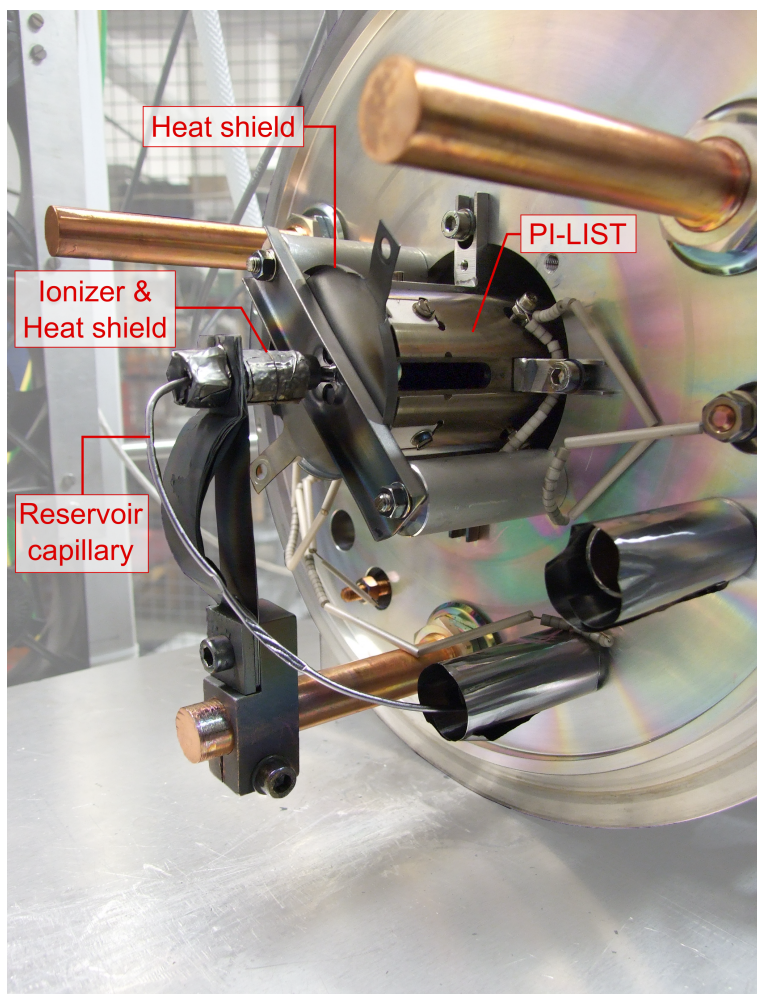


Figure 5.25: Photograph of the PI-LIST setup installed at the RISIKO ion source. The components of the usual ion source (e.g. ionizer tube and reservoir capillary) are located on the left side. The PI-LIST is placed in front of the ionizer's exit opening. The wires which can be seen are isolated with temperature stable ceramic pieces and supply the voltages for the electrodes.

of 45 mm. In addition, elongated holes gave an extra clearance of ± 7.5 mm for spatial optimization. A commercial high-vacuum-compatible ConFlat viewport⁴ was installed to serve as entrance window. It comprised a 1.5" uncoated fused silica window, providing optimum transmission over the complete accessible wavelength range and a high damage threshold. In addition, a wedge of 0.5° between both surfaces of the window eliminated the risk of possible interference effects. In the framework of a bachelor's thesis, a second repeller was added to the PI-LIST in order to suppress background induced by negative species which was encountered during the measurements on Tc [135]. More details can be found in section 5.4.1.

⁴Thorlabs, part number: VPCHW42

5.3.2 First Test Run with Pd

A first test run of the PI-LIST at the RISIKO separator was conducted to test the technical concept and to briefly characterize the operation. Palladium was the test element of choice, as its behavior in the RISIKO ion source was well-known and a suitable laser system was available from the efficiency measurements, which were presented in chapter 4. In addition, as mentioned earlier, the use of zirconium foil as reduction agent caused a strong isobaric background due to surface ionized ZrO, which gave optimal conditions to test the suppression capability of the PI-LIST. The ionization scheme used was the resonant 3-step scheme shown in figure 4.4, which could be well saturated in all transitions with the available laser powers.

The PI-LIST was installed as shown in figure 5.25. Ionizer, PI-LIST, and ion optics were precisely aligned with the help of a theodolite. In a first step of the experiment, the conventional LIST operation, as presented in 3.2.1, was investigated. A quick test using surface ionized cesium confirmed good transmission of ions through the RF quadrupole field without any difficulty up to ion currents of about 2 nA of the stable isotope ^{133}Cs . Also, the suppression of surface ionized Cs worked as expected and the ion current could be well suppressed to the background level, when applying a positive voltage of +10 V to the repeller electrode at the entrance of the PI-LIST unit. Using conventional in-source ionization with longitudinal ionization geometry and the LIST's ion guide mode, a first Pd ionization signal was easily obtained. As discussed in detail in section 4.3, the Zr sample foil caused a strong, laser-independent background signal due to surface ionization of ZrO in the ion source. As shown in figure 5.26a, this background was also observed here, when using the IG mode. When switching into LIST mode operation by applying a positive potential to the repeller electrode, all positively charged ions stemming from the ion source were repelled and the isobaric background was well suppressed to the background level of the detection, as shown in figure 5.26b. The strong suppression of isobaric background increases the signal-to-noise ratio tremendously, resulting in a significant enhancement of the overall quality of the signal. This is of special relevance for experiments with limited sample size or other restrictive constraints where only low signals can be obtained.

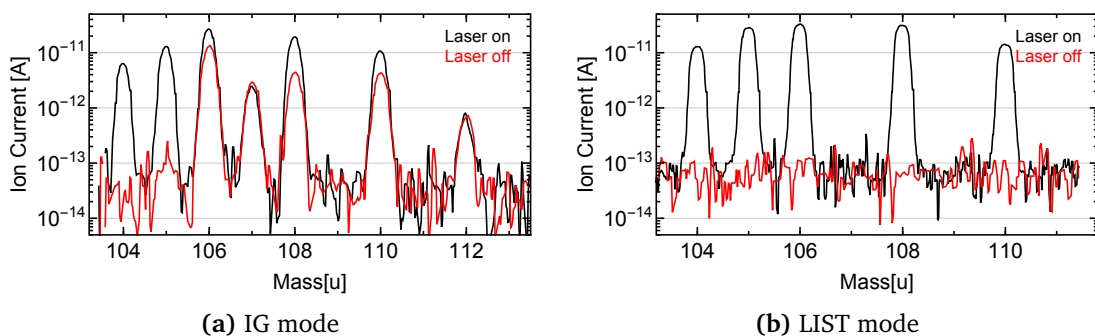


Figure 5.26: Mass spectra with the PI-LIST in two operation modes. Both graphs show the mass spectra with laser beam entering the separator (black) and with blocked laser beams (red). Figure (a) shows the operation with longitudinally aligned lasers in ion guide mode, featuring a strong, laser-independent background due to surface ionized ZrO. Figure (b) shows the operation in LIST mode, suppressing the surface ionized species from the source to background level. The absolute height of the ion signal is not of relevance, as scan (b) was performed at higher ion source temperature.

In a next step, the laser beam for the first step excitation was aligned in perpendicular orientation, while the other laser beams remained in longitudinal alignment. Before the laser beam of the first excitation step entered the vacuum chamber through the viewport, it was expanded horizontally to an elliptical spot of about 15 mm x 20 mm, in order to achieve

best illumination of the entire interaction region behind the repeller. As expected, a resonant ionization signal was detected immediately, without requiring optimization of the spatial alignment of the laser beams. This confirmed a good alignment of the PI-LIST unit, the ion optics of the separator, and all laser beams. The change from longitudinal to perpendicular ionization geometry in LIST mode operation came along with a decrease of the ion current from 10 pA to 8 pA, which was in agreement with the expectations due to the smaller laser interaction region in the perpendicular geometry.

A detailed investigation of the first step transition was performed to test the spectroscopic properties of the PI-LIST operation with perpendicular laser beam alignment. Figure 5.27 shows the comparison of frequency scans in the first excitation step performed with different spectral linewidths and powers of the laser radiation. The isotope of choice was ^{106}Pd . The first scans were performed using the standard laser configuration with a fundamental linewidth of about 5 GHz. The following scans were done with the Ti:sapphire laser in dual etalon configuration, as presented in section 3.1, reducing the fundamental laser linewidth to about 1 GHz FWHM. The subsequent frequency tripling of the laser beam increases the spectral linewidth by about a factor of $\sqrt{3}$, resulting in an estimated spectral linewidth of about 8.7 GHz or 1.7 GHz, respectively. As shown, the frequency scans were repeated at different laser powers to study potential saturation broadening. The resulting resonance curves in the graph were normalized for each operation mode, to allow a better evaluation of their spectral width and shape.

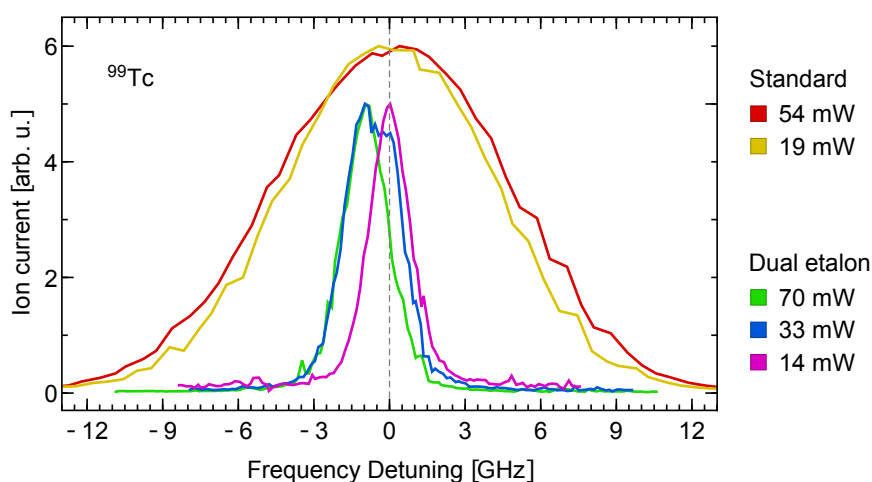


Figure 5.27: Comparison of frequency scans of the first excitation step in Pd. See text for discussion.

In the perpendicular ionization geometry, the laser beam of the first step was enlarged to achieved proper illumination of the ionization volume. As a result, the applied laser intensities were more than 200 times lower than the corresponding intensities presented in section 4.1, preventing significant saturation when using the standard laser configuration. In contrast, the spectral power density of the narrowband laser is about a factor of 10 higher, due to its smaller spectral linewidth. However, this is still significantly smaller than the factor 200 decrease of the laser intensity due to the increased spot size. A linear correlation between laser power and ion current up to 100 mW showed that the laser powers with the standard laser configuration were below the saturation level. Correspondingly, the scans with laser powers of 54 mW and 19 mW showed almost no difference of the spectral linewidth. By fitting of a Gaussian function to the data, the spectral linewidth (FWHM) were determined to be 10.8(2) GHz and 9.6(2) GHz, respectively, proving that the experimental linewidth is dominated by the laser linewidth of about 5-8.5 GHz. When performing the scan with the narrowband dual etalon configuration and laser powers of 70 mW, 33 mW, and 14 mW, the

observed FWHM decreased slightly from 2.2 GHz to 1.9 GHz.

The narrowband scans in figure 5.27 show a unusual feature. The resonance peak shifts clearly over the course of three subsequent measurements while the laser power was lowered step-wise. Such a type of shift was never observed previously, neither at the RISIKO separator nor at the MABU spectrometer. The first scan (green) at 70 mW seems normal. The peak from the following scan (blue) at 33 mW shows an underlying substructure on the right side, while its top follows the shape of the previous scan. The shape of the last scan (magenta) at 14 mW shows no underlying structure, but its position is shifted relative to the first scan, but its right slope agrees with the right slope of the previous scan at 33 mW. This effect cannot be attributed to the change of the laser power. If it would be power dependent, it might explain a shift, but it cannot explain the occurrence of the substructure which vanished again at even lower laser power.

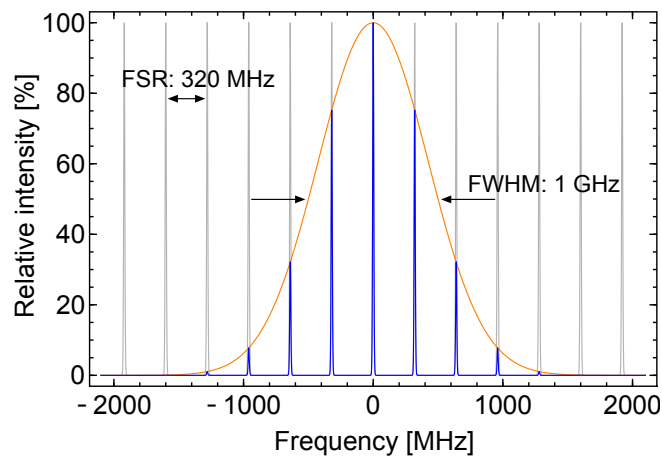


Figure 5.28: Simplified spectrum of the fundamental radiation of Ti:sapphire laser in dual etalon configuration. The gray curve represents the different longitudinal cavity modes of the laser with a free spectral range of about 320 MHz. The blue curve represents the oscillating cavity mode. The orange colored envelope with a linewidth of 1 GHz visualizes the time-averaged spectral laser spectrum observed in usual experiments, where Doppler broadening leads to absorption linewidth of ≥ 1 GHz. It is important that this representation is only correct when seen as average over a large number of laser pulses at time scales > 100 ms. The spectral structure of single laser pulses may differ. See text and in section C for detailed explanation.

An explanation can be found when considering the spectral structure of the laser radiation. Due to the laser cavity, the laser radiation is composed of several cavity modes, which are equally spaced in the frequency space. Figure 5.28 shows a simple picture of the cavity modes present in dual etalon configuration, which add up to an envelope with FWHM of about 1 GHz. The interval between the cavity modes is the free spectral range of the cavity, which is about 320 MHz for the used z-cavity. As the length of the cavity itself could not be controlled, the frequency of these cavity modes could not be scanned. They are fixed except for length changes induced by temperature drifts. During a frequency scan with the etalons, only the intensity ratio of the oscillating cavity modes are changed, moving the spectral center of gravity of the laser radiation. In the case that the atomic absorption linewidth is smaller than the spectral distance between the cavity modes, a continuous spectral shift of the cavity modes, caused by the thermal drift of the laser cavity length, would result in the occurrence of a mode hop in the spectroscopic data, as observed. That is the main reason, why this effect was not observed in previous experiments, as the absorption line is typically broadened to values of 1-5 GHz and more by the Doppler broadening. This explanation is supported by the time between first and last scan of 17 minutes, which fits

well to typical timescales of thermal drifts. The fit of Gaussian profiles to the first and last scan reveals a frequency shift of 947(5) MHz. When considering the frequency-tripling in the first excitation step, this corresponds to a spectral spacing of about 316(2) MHz in the fundamental radiation, which agrees well with the estimated free spectral range of the laser cavity of about 320 MHz.

Albeit this looks like a reasonable explanation at first glance, there is one more detail which has to be considered to fully understand this effect. In return, this provides an important piece of information on the laser radiation which was not found out earlier. Usually, frequency mixing processes in NLO material induce additional modes through sum frequency generation of the individual cavity modes of the initial laser radiation, resulting in additional modes and leading to the same mode spacing in the frequency-tripled radiation as in the fundamental radiation. In this case, the scans should have shown a shift of 320 MHz, instead of the observed 947 MHz. This discrepancy was caused by a strong suppression of the additional modes in the frequency mixing process, which can be traced back to special properties of the laser radiation of the dual etalon Ti:sapphire laser. A detailed explanation of the cause of this mode suppression is relatively complex and leads further away from the actual topic of the present chapter. Therefore, a comprehensive discussion is given in the appendix in section C.

The suppression of additional side modes in the spectrum of frequency-tripled or frequency-doubled laser radiation is an important fact, as this property of the dual etalon laser setup was not observed previously. It would be worthwhile to study the spectral structure of the narrowband laser radiation after SHG, THG and FHG in more detail to obtain a conclusive understanding. A suitable approach for the analysis would be the use of a scanning Fabry-Pérot interferometer in combination with time-resolved data acquisition. Furthermore, the Fourier-transformed signal of a fast photo diode could also be used to investigate the spectral structure of a single laser pulse via the observed mode-beating pattern. The other key result of this very first spectroscopy using the PI-LIST in perpendicular ionization geometry, is the fact that the spectral linewidth of the absorption line of the first step, still broadened by the residual Doppler and power broadening, is well below 1 GHz. In order to prevent the mode hop effect as observed here, it is essential to use a continuously tunable single mode laser for proper spectroscopic studies.

5.3.3 Investigation of the Isotope Shift in Pd

During the spectroscopic measurements in Pd, as presented in chapter 4, the investigated transitions showed no significant isotope shift. Here, the spectroscopic setup was operated with broadband lasers at full power and using in-source ionization geometry, which broadened the optical resonances to about 25 GHz. Using the PI-LIST setup and the dual etalon laser, the first step transition of the Pd ionization scheme was investigated again more precisely in order to confirm the previous observations. The setup enabled a significantly higher resolution, even though a relatively large uncertainty of ± 950 MHz had to be assumed, due to influences of the mode hop effect as discussed in the previous section 5.3.2.

Figure 5.29 shows the resulting spectra for all Pd isotopes obtained with the first step laser in dual etalon configuration (see section 3.1) taken in perpendicular ionization geometry using the PI-LIST. Experimental linewidths of only 2 GHz FWHM were demonstrated. The typical fundamental laser linewidth for this wavelength and laser power was about 1-1.3 GHz, which was broadened by the frequency tripling process by a factor $\sqrt{3}$, resulting in a spectral linewidth of 1.7-2.3 GHz. Obviously, the observed experimental linewidth of 2 GHz was clearly dominated by the spectral linewidth of the exciting laser radiation. As a consequence, the residual Doppler broadening must be well below 2 GHz, which agrees well with the

initial expectation of only a few hundred MHz and the observations in the previous section 5.3.2.

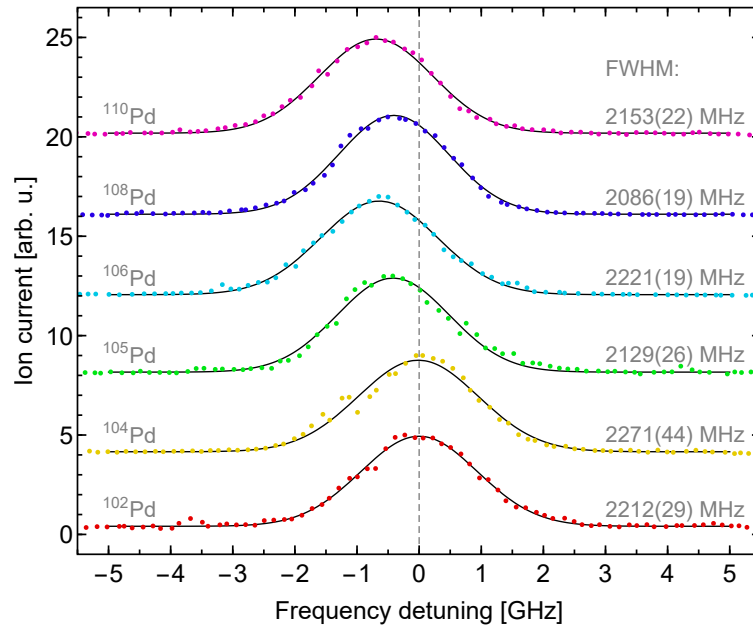


Figure 5.29: Frequency scan of the first excitation step for all stable Pd isotopes with higher resolution. The PI-LIST was used in perpendicular ionization geometry for the first excitation step while steps two and three were kept in longitudinal orientation. The center frequency of $36180.734(20)\text{ cm}^{-1}$ of the isotope ^{102}Pd was chosen as zero of the x-axis. The data points represent the raw data with 150 MHz binning and normalized ion current. Gaussian profiles (black) were fitted to the data points. The resulting linewidths (FWHM) and corresponding standard errors from the fit procedure are given on the right. See text for details.

The center frequencies clearly follow a trend to lower frequencies for increasing mass number. The individual resonance curves look smooth and do not show any evidence of a substructure as in figure 5.27, but it cannot be excluded that a similar shift occurred between the scans, preventing a precise evaluation of the isotope shifts. The center frequencies, as extracted from the fits, shift by only $692(5)\text{ MHz}$ or less, showing that the isotope shift can be completely neglected when operating the laser ion source with standard lasers at high power and in-source geometry.

Due to its odd number of neutrons, ^{105}Pd , is the only isotope with a nuclear spin and therefore the only isotope with a HFS splitting. The corresponding scan in the graph shows no evidence of an underlying substructure, indicating that the size of the splitting must be well below 1 GHz. In addition to the small isotope shifts, this is also favorable for the conventional ion source operation with broadband lasers.

5.4 High-Resolution HFS Spectroscopy in Tc

Extensive high-resolution spectroscopy was carried out using the newly developed PI-LIST. The aim was to precisely study the HFS in atomic transitions of Tc in order to characterize HFS and isotope shift as well as to demonstrate the capabilities of the PI-LIST under realistic experimental conditions. In comparison to the measurements in section 5.2, a completely different ion source and spectrometer were used and an additional first step transitions was investigated. Another important aspect is the availability of a third isotope, ^{98}Tc ($\tau_{1/2} = 4.2 \cdot 10^6$ y), which enabled the study of the evolution of HFS, isotope shift, and nuclear moments in a sequence of three subsequent isotopes.

The following sections give a quick overview of the experimental setup, followed by a first systematic investigation of characteristic properties with regard to optical spectroscopy performance. The last sections will present and evaluate the results from the high-resolution study of HFS and isotope shift in three ground state transitions in Tc for the three isotopes ^{97}Tc , ^{98}Tc , and ^{99}Tc .

5.4.1 Experimental Setup

The setup used is sketched in figure 5.30. The laser system consisted of two major components, a set of three standard Ti:sapphire lasers for the basic, broadband excitation of the resonant 3-step ionization scheme, and the injection-locked single mode Ti:sapphire laser system. A detailed descriptions of the individual lasers as well as the RISIKO separator is given in chapter 3. The broadband laser system provided high powers of up to 480 mW, 690 mW, and 2.5 W for the first, second, and third excitation step of the excitation ladders presented in 5.13. As described in section 3.1.3, the single mode laser system used the output of a frequency-stabilized narrowband CW diode laser system to seed the injection-locked Ti:sapphire laser cavity. The generated high-power, pulsed laser radiation could be scanned smoothly and continuously across the desired frequency regions with a narrow linewidth of about 15 MHz, which was essential to demonstrate the full potential of the PI-LIST setup.

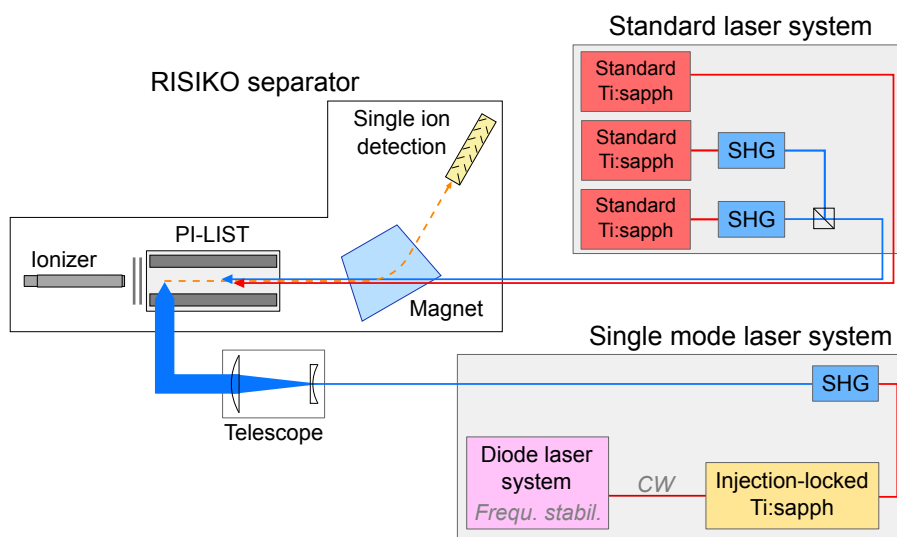


Figure 5.30: Basic layout of the experimental setup for the HFS spectroscopy in technetium. See text for description.

The power of the initial CW laser radiation in front of the injection-locked cavity was 0.2-1.0 mW, which was more than sufficient for reliable locking and seeding of the Ti:sapphire

laser at wavelengths around 860 nm. The injection-locked, bow tie-shaped laser provided narrowband laser radiation with an output power of up to 1 W at 10 kHz repetition rate and an estimated linewidth of 15 MHz. The pulsed laser light was frequency doubled using single-pass SHG in a NLO crystal (BBO), resulting in an output power of up to 40 mW. Due to the narrow linewidth and the associated high spectral power density, the laser beam had to be attenuated to about 0.5 mW for most measurements, in order to avoid power broadening. A cylindrical telescope was installed close to the entrance window of the vacuum chamber at the RISIKO separator. It allowed a horizontal expansion of the laser beam to about 30 mm, as shown in figure 5.31, for a full coverage of the accessible laser interaction region behind the repeller of the PI-LIST. During a frequency scan with the single mode system, the seeding diode laser was scanned in steps of 5-10 MHz and data was taken for about 3-6 s on each setpoint. The frequency setpoint as well as the diode laser frequency, measured with a HighFinesse WSU2 wavemeter, were recorded.

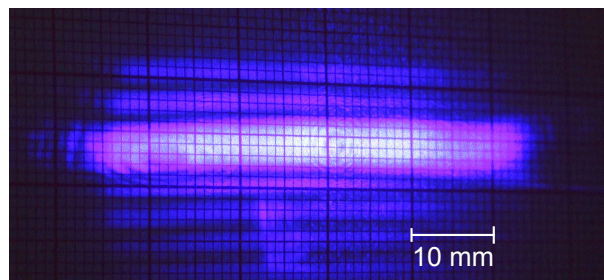


Figure 5.31: Photograph of the spectroscopy laser beam after horizontal expansion for the perpendicular alignment. Scaled millimeter paper was used for reference.

The PI-LIST (see section 5.3) was used to enable perpendicular access to the Tc atomic beam. Graphite tubes were used as ionizer tubes, as findings from previous experiments indicated an unfavorable, high adsorption of Tc onto tantalum [73]. The samples were provided and prepared by the institute of nuclear chemistry at Mainz university. The sample sizes are listed in table 5.6. As observed during the experiment at the MABU spectrometer, described in section 5.2, some samples showed a slightly different $^{97}\text{Tc}:^{99}\text{Tc}$ isotope ratio as stated from the preparation laboratory which is ascribed to an yet unexplained incorrectness in the sample preparation process. For the sample preparation, a solution, containing the Tc atoms in the form of ammonium pertechnetate, NH_4TcO_4 , was dropped onto a small metallic foil of zirconium or platinum with the size of a few mm^2 and evaporated. The metallic foil acted as reduction agent during the atomization process inside the hot ion source. It was found that Pt allowed a smoother and more reliable atomization of the Tc sample. After folding the metallic foil, the sample was directly placed inside the ionizer tube, as no separate reservoir capillary was required. The use of a secondary electron multiplier allowed efficient and sensitive single ion detection of the small amounts of ionized Tc.

The measurements also included an extensive study of the ion transmission characteristics of the PI-LIST, carried out in the framework of a bachelor's thesis [135]. This work also provides a comprehensive description of additional, technical details as well as a simulation of the electric field inside the PI-LIST. First tests showed the presence of an unexpected, strong laser-independent background in LIST mode operation, as shown in figure 5.32a. In previous experiments, all ions stemming from the ionizer could be completely suppressed in this operation mode. The disturbing effect was attributed to electron impact ionization in the entrance region of the PI-LIST when electrons emitted from the hot ionizer tube are accelerated towards the positive potential the repeller. This effect was not discovered previously, as earlier experiments used the LIST only in combination with a significantly

Table 5.6: Overview of the samples used for this experiment. The isotopes ^{97}Tc and ^{98}Tc stemmed from the same main solution with a fixed ratio of about 10/1. ^{99}Tc was added from a separate solution. See text for additional details.

Number	Amount of atoms			Foil
	^{97}Tc	^{98}Tc	^{99}Tc	
I	-	-	$1.4 \cdot 10^{13}$	Pt
II	$8.8 \cdot 10^{13}$	$8.8 \cdot 10^{12}$	$5.6 \cdot 10^{13}$	Zr
III	$9.5 \cdot 10^{11}$	$9.5 \cdot 10^{10}$	$9.5 \cdot 10^{11}$	Pt
IV	$9.5 \cdot 10^{11}$	$9.5 \cdot 10^{10}$	$9.5 \cdot 10^{11}$	Pt
V	$1.1 \cdot 10^{13}$	$1.1 \cdot 10^{12}$	-	Pt

less sensitive Faraday cup detector and higher laser ion currents. In addition, the electron emission rate of the hot ion source may also depend on the material of the ionizer tube, e.g. graphite or tantalum. This problem was solved by installing a second repeller electrode at the entrance of the LIST, as illustrated in figure 5.33. A small negative voltage at the first repeller rejects all negative species from the source while the second repeller suppresses the positive ions. Figure 5.34 shows scans of the voltage applied to the second repeller for different voltages of the electron repeller. Negative voltages of 5 – 10 V allowed a complete suppression of the electron impact ionization, reducing the background to the level of the dark count rate of the detection. The suppression is also reflected in the very clean mass spectrum as shown in figure 5.32b. More details of the dual repeller design can be found in [135]. For the following spectroscopy measurements, repeller voltage sets of $-5/+5$ V to $-10/+10$ V were chose to obtain optimum signal-to-noise ratios, as indicated in gray shaded areas in figure 5.34.

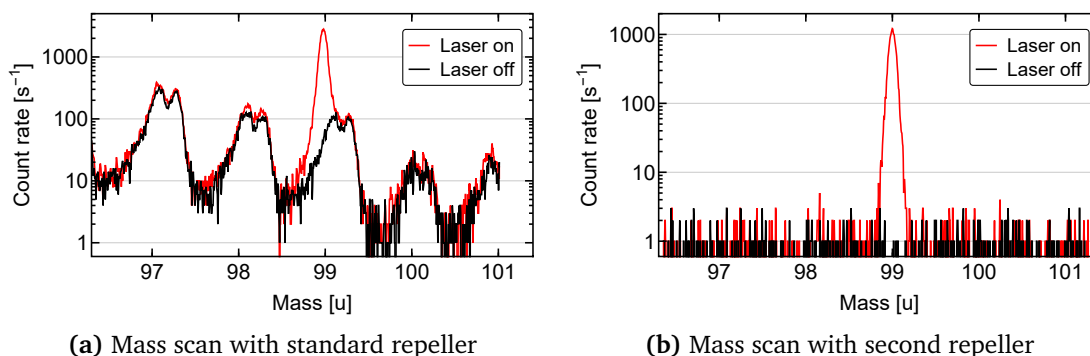


Figure 5.32: Mass scans with and without second repeller in LIST mode operation. In addition to the laser ionized ^{99}Tc in figure (a), a strong laser-independent background was observed which was traced back to electron impact ionization inside the LIST due to electrons emitted from the graphite ionizer. As shown in figure (b), this could be completely eliminated by installing a second repeller electrode which was used to hinder electrons from entering the LIST volume.

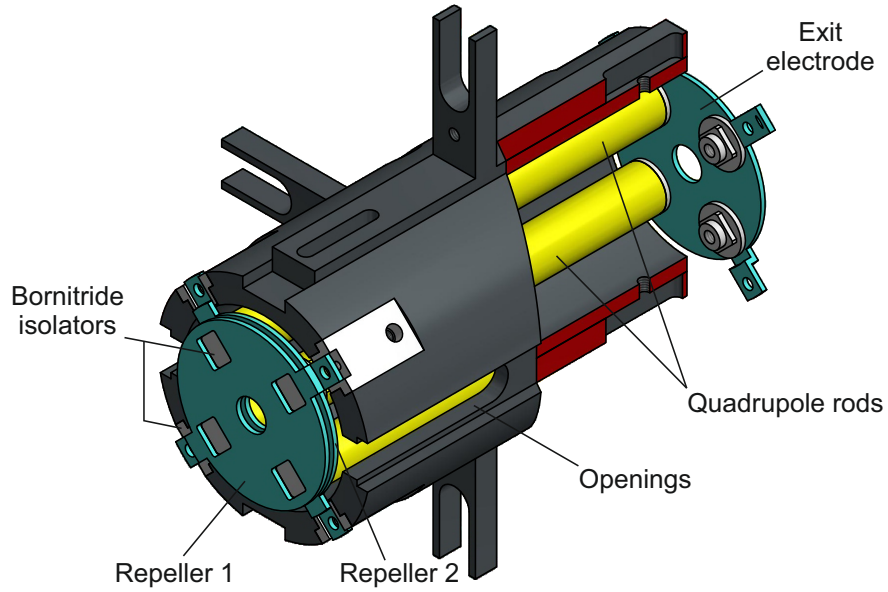


Figure 5.33: 3D computer model of the PI-LIST with dual repeller. See text for details. Figure adopted from [135].

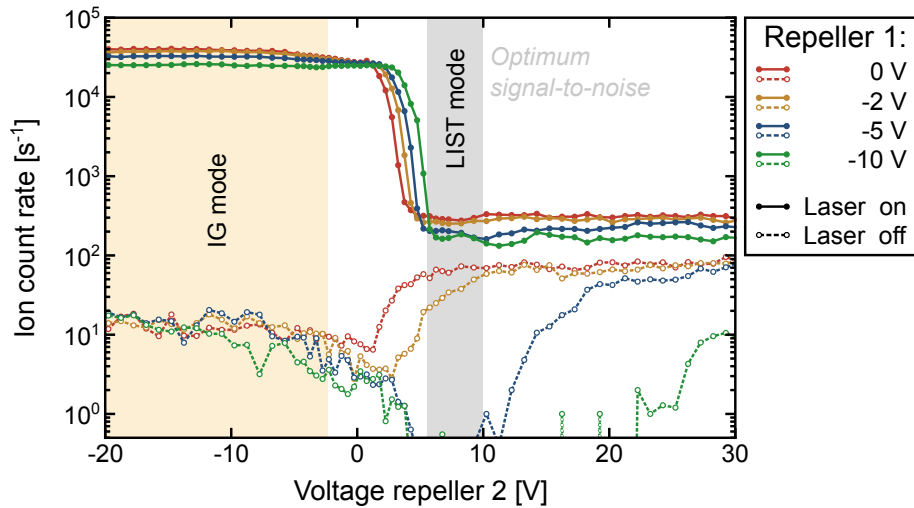


Figure 5.34: Scans of repeller voltages in dual repeller configuration performed with longitudinally aligned laser beams. Repeller labeled as shown in figure 5.33. The voltage of repeller 2 was scanned from negative, where ions from the ion source can pass the LIST (left side), to positive, where positive ions from the source are repelled (right side). These two distinct operation modes correspond to the IG mode and the LIST mode as described in section 3.2.1. The laser-independent background in LIST mode when repeller 1 is at 0V is significantly suppressed with voltages of -5 V to -10 V as electrons are repelled preventing electron impact ionization. Graph adopted from [135]. See text for more details.

5.4.2 Characterization of the Spectroscopic Performance of the Setup

In the present experiment, the PI-LIST setup was used for the very first time in combination with a fully operational single mode laser system, allowing a systematic characterization with regard to high-resolution spectroscopy on smallest samples. The investigation of the relation between spectral linewidth, ionization efficiency, and signal-to-noise ratio are essential for a detailed understanding of the PI-LIST operation as well as for identifying aspects for future developments. The findings of these measurements, obtained using ^{99}Tc , were used to determine the optimum operation settings for the detailed study of the HFS, which are presented in the following section 5.4.3. The singlet transition at $23265.8362\text{ cm}^{-1}$ of the HFS in the $4d^5 5s^2 6S_{5/2} - 4d^5 5s 5p^6 P_{7/2}^o$ transition was used for the investigation presented here as it offers a single peak without nearby resonances or spectral substructure. The results were confirmed by additional measurements using a HFS triplet in the $4d^5 5s^2 6S_{5/2} - 4d^5 5s 5p^6 P_{3/2}^o$ transition at 23588.42 cm^{-1} , which are not included in the present section.

Power Broadening

As described in section 2.3.3, power broadening can reduce the spectral resolution in the obtained spectrum significantly. Therefore, it is mandatory to characterize this influence and to choose a suitably low power level to maximize the resolution. On the other hand, lower laser intensities reduce the ionization efficiency and consequently the signal-to-noise ratio, which is a very important aspect when studying smallest samples. Consequently, the choice of laser power is always a trade-off between ionization efficiency and spectral resolution.

Figure 5.35a shows frequency scans across the HFS singlet resonance for different laser powers in the first excitation step. As expected, the peak is significantly broadened at the full laser power of 23 mW, while the linewidth is reduced for lower laser powers. The significant difference of the spectral linewidth between the scan at 23 mW (green) and the one at 9 mW (red), with 700 MHz and 450 MHz FWHM, respectively, indicated that the former was affected by power broadening. This was confirmed by the fact that the power attenuation by a factor of 2.6 reduced the peak ion count rate from 255 cps to 200 cps, which corresponds to a factor of only 1.3. Such a non-linear correlation is characteristic for laser powers above the saturation level. The scans at 9 mW and 4 mW showed only a minor influence of broadening, in agreement with a correspondingly linear decrease of the count rate. Consequently, a laser power of 6 mW was chosen for the next measurements, as a compromise between resolution and ionization rate.

The laser pulses of the different excitation steps of a ionization scheme are typically synchronized to optimal temporal overlap in order to achieve maximum ionization rate. Through the simultaneous excitation of first and second transition, a strong power broadening of the second step transition can also induce a spectral broadening of the first transition [49]. This can be explained in a simply picture by the second excitation step strongly depopulating the first excited state which reduces its effective lifetime, causing a broadening of its energetic uncertainty and consequently increasing spectral linewidths of corresponding transitions. The frequency scan of the first step was repeated with different laser powers in the second step, while the power of the first step laser was kept at 6 mW. The results are shown in figure 5.35b. The first scan at the full laser power of 239 mW showed a slightly larger linewidth, when compared with the scan at 75 mW. The graphs show a trend to smaller linewidths for lower laser powers, but the effect is small compared to the influence of the power in the first step. To minimize this broadening, a laser power of 50 mW in the second step was chosen as setting for the subsequent measurements.

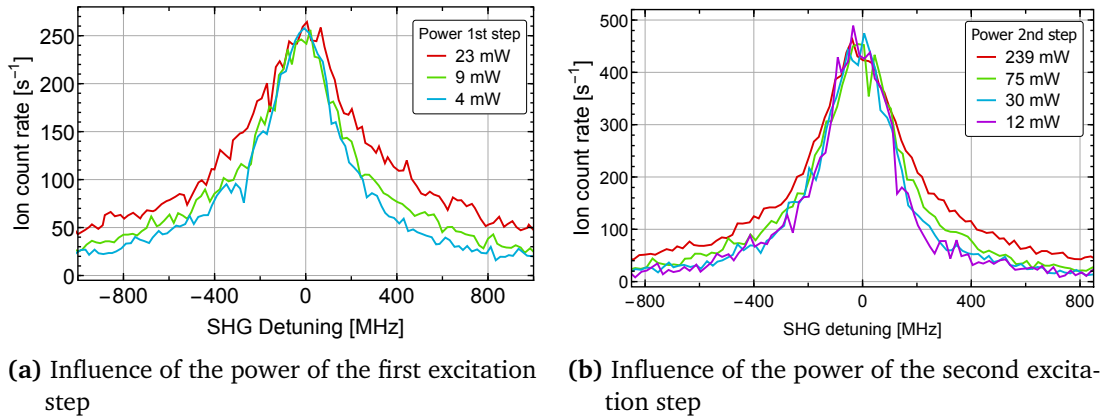


Figure 5.35: Influence of the laser power on the spectral profile of the singlet transition at $23265.836 \text{ cm}^{-1}$. Graph (a) shows frequency scans of the first excitation step with different laser power, while the power in the second excitation step was constantly kept at maximum. A reduced spectral linewidth was observed for smaller laser powers in the first excitation step. Graph (b) shows frequency scans of the same transition with different powers in the second excitation step, while the power in the first step was kept at constant 6 mW. The data in both graphs was normalized for a better comparison of the spectral linewidth. See text for discussion.

Temporal Separation of Laser Pulses

Besides intensity of the laser radiation, the use of pulsed laser light adds another adjustable parameter, the timing of the individual laser pulses. Usually, the pulses are synchronized for maximum ionization efficiency and the excitation and ionization happen almost simultaneously. As already discussed, this comes with the consequence that broadening effects or any perturbation of the atomic energy levels, caused by the second step, might be observed in the spectrum of the first excitation step. A theoretical approach to this topic, including simulations, detailed discussions, and an experimental example is presented in the master's thesis of R. de Groot [49] and in the article [50]. In this work, a basic two-step ionization scheme with a non-resonant ionization step is described, but the same principles apply for an excitation step followed by a second excitation step with a subsequent ionization step, which form a three step ionization scheme.

A major outcome of this work is the aspect that any observed influences on the first excitation step can be completely canceled, if the laser pulse of the second excitation step interacts with the atom after the first excitation pulse passed. In this way, any power broadening or perturbation caused by the second step will not affect the spectrum of the first excitation step. The atomic states still get broadened or disturbed, but only after they are probed by the first step laser. Therefore, the spectrum of the first step will not be affected. In addition, the power broadening induced by the first step laser itself can be partially reduced. The latter can be explained by an adiabatic population return after the pulsed excitation for a small frequency detuning from the resonance. These findings were supported by experimental results in the mentioned work [49] and in the PhD thesis of V. Sonnenschein [29].

In experiments with limited samples, the trade-off between the benefits of temporal pulse separation and a related loss of ionization rate, induced by the spontaneous decay of the excited state depending on the state's lifetime, must be considered. It might be counter-intuitively at first, but the use of weak transitions with excited state lifetimes in the order of $\sim 10^{-7} \text{ s}$ can be advantageous in this context. Their weaker decay rate allow a larger temporal delay between the excitation pulses without sacrificing an unacceptable amount

of ionization efficiency, thus enabling optimum temporal pulse separation.

Temporal pulse separation was also investigated in the present study on Tc. Figure 5.36 shows frequency scans of the HFS singlet for different delays δt between the first step laser pulse and the laser pulses for excitation steps two and three. The delay of 0 ns corresponds to the initial synchronization for optimum ionization rate. The delay was adjusted with the trigger of the separate pump laser for the injection-locked laser. The laser power in the first excitation step was set to 6.0 mW, while the laser power for the second and third step were kept at maximum power, 239 mW and 2.5 W, respectively. The ion count rate was normalized for a better comparison of the spectral linewidth. When interpreting the different delays, it has to be considered that the pulse duration of the individual laser pulses was about 50 ns. For a better visualization, figure 5.37a shows the corresponding full widths at half maximum, extracted by fitting Lorentzian profiles to the data. Figure 5.37b shows the corresponding absolute ion count rate at the peak maximum of the resonance.

The spectral linewidth could be significantly reduced, from an initial FWHM of 613 MHz for no delay down to 252 MHz for a delay of 70 ns. The reduction follows a clear linear trend for delays larger than 20 ns. For a delay of 20 ns, the extracted linewidth shows no reduction, when compared to 0 ns. This means that the laser pulses of 50 ns duration are still well overlapped with each other. It cannot be excluded that the pulse of step two was a few ns earlier than the pulse of step one at the $\delta t = 0$ ns mark. This aspect is also reflected in the observed ion count rate, which is only reduced by about 8 %, while the count rate reduction for larger delays is almost constant at 30 % per 20 ns. Due to the spontaneous decay of the atomic state, an exponential decrease of the ion count rate is expected in graph 5.37a. The corresponding lifetime is rather short and can be expected to be below 24 ns. However, the graph shows a linear trend, which is due to the laser pulses of 50 ns FWHM still being slightly overlapped for the examined delays up to 70 ns.

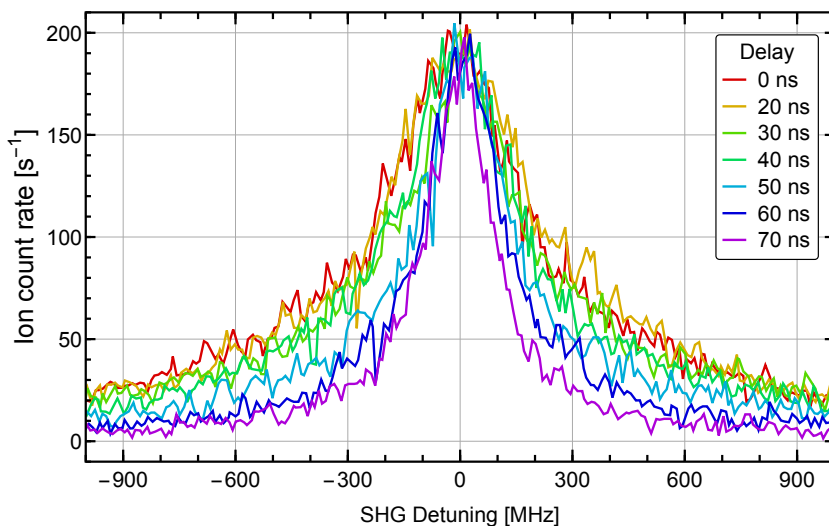


Figure 5.36: Influence of temporal separation of the laser pulse of the first step and the pulses for steps two and three. The delay of 0 ns corresponds to the first step pulse being temporally optimized for maximum ionization rate, considered to be nearly simultaneous laser pulses. The spectral linewidth was clearly reduced by up to a factor of 2.5 when delaying the laser pulses for step two and three. The ion count rate was normalized for a better comparison of the spectral linewidth.

The presented evaluation agrees well with the findings in [49, 29] and shows that the control of the delay between the laser pulses can be used to improve the spectral resolution when conducting spectroscopy experiments. The benefits of this method are strongly dependent on the lifetime of the first excited state and the linked loss in ionization efficiency. Therefore, this aspect must be properly investigated for each transition and should be combined with suitable reduction of the laser power. For comparability, the following measurements in this section were all performed with a delay of $\delta t = 0$ ns.

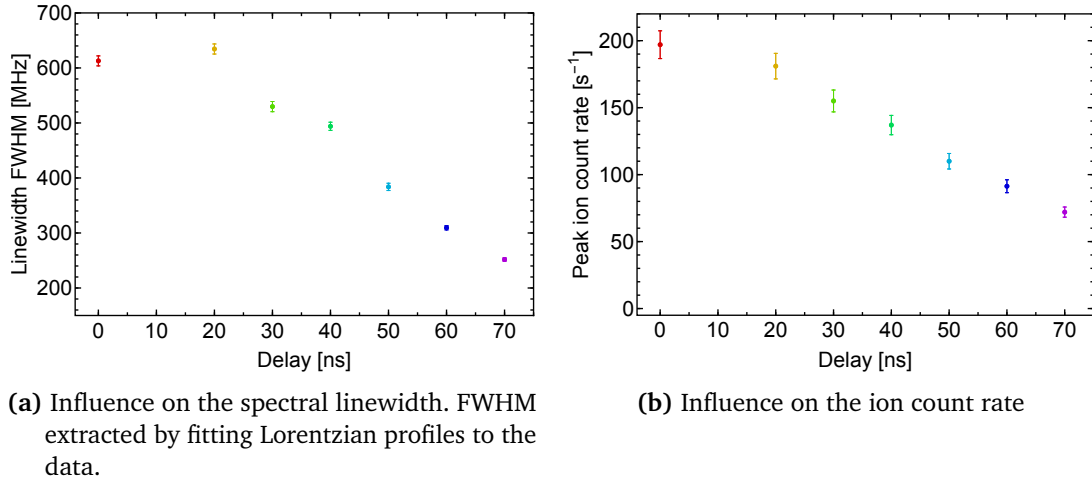


Figure 5.37: Influence of temporal pulse separation on the spectral linewidth and ionization rate for the data shown in figure 5.36. The choice of color of the data points is equal to the coloring in figure 5.36.

Beam Size of the Second Step Laser

When using perpendicular ionization geometry with laser beams for the subsequent ionization steps aligned in longitudinal orientation, the size and shape of the latter are important as their cross section have a major influence on the observed residual Doppler broadening. Together with the perpendicular laser beam, they define the laser interaction volume in which the atoms can be resonantly ionized. Relative to the exit opening of the ionizer tube, this volume defines the solid angle which is covered and therefore has a direct influence on the projection of the thermal Doppler spread on the perpendicular axis. As sketched in figure 3.14, this defines the finally observed Doppler broadening. As a consequence, the influence of the spot size of the laser beams for the second and third step and possible side effects of their shape were investigated.

In theory, laser beams are described by a Gaussian intensity profile in the spatial cross section. In reality, laser beams often show some deviation from an ideal Gaussian beam. Distortions can have several reasons, such as imperfections of reflecting surfaces in the optical path, spherical aberrations of lenses or side effects caused by NLO optics. In some cases the laser beams show a weak halo around the actual beam, especially after SHG or THG as used in the second excitation step here. Typically, only a negligible fraction of the laser power is contained within this halo. Nevertheless, this might cause a wider laser interaction volume, possibly increasing the residual Doppler broadening. Figure 5.38 shows two frequency scans across the singlet transition performed with full laser beam and with an iris blocking the halo of the longitudinal aligned laser beams for excitation step two and three. As expected, no evidence of any influence on the shape or the height of the resonance peak were observed due to the very weak laser intensity within the halo which does not

give a the measurable contribution to the ionization rate.

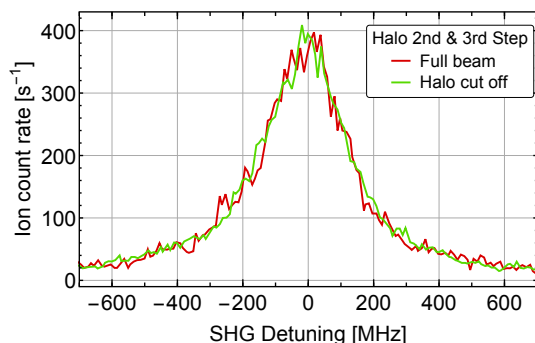


Figure 5.38: Influence of the laser beam halo on the spectral structure. No difference in the spectrum was found after repeating the frequency scan, while blocking the halo of the laser beam of the second and third excitation step. See text for details.

In a next step, the spot size of the second step laser in the interaction region was decreased to reduce the width of the laser interaction volume inside the PI-LIST and therefore reduce the residual Doppler broadening. It is clear that this has also a big effect on the intensity of the laser radiation at the interaction region, which made it necessary to re-evaluate the impact of power broadening. The laser spot size in the interaction region was reduced from approximately 3 mm in diameter to roughly 1 mm diameter, increasing the intensity by roughly a factor of 10. The plot in figure 5.39 shows a first comparison of a frequency scan of the first step with unaltered spot size (green) and with reduced spot size (red) of the second step. The first step was kept at 6 mW while the power of the second step was set to 3 mW for a proper comparison to the scan with previous spot size at 30 mW. A clear reduction of the spectral linewidth, from about 300 MHz down to 250 MHz, was observed with the smaller spot size.

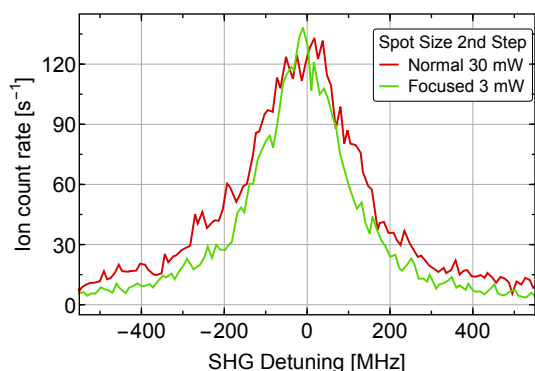


Figure 5.39: Frequency scans of the first excitation step with different spot sizes of the second step laser. See text for details.

With the focused second step laser, the ionization signal showed clear saturation for second step laser powers above 3 mW due to the increased laser intensity. In order to check for power broadening induced in the first step transition, the first step frequency was scanned with laser powers of 3.0, 1.45, and 0.7 mW in the second step, while the laser power of the first excitation step was kept at 6.0 mW. The resulting resonance curves, presented in figure 5.40a, showed no significant influence on the spectral linewidth in the first step, which is in agreement with the findings from the first investigation in this section (see figure 5.35b).

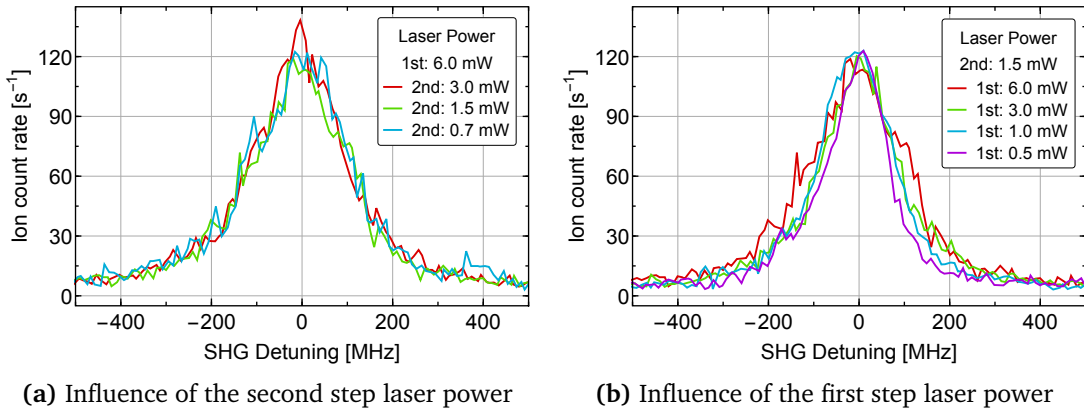


Figure 5.40: Re-evaluation of power broadening in the first step transition after the reduction of the laser spot size of the second step. Frequency scans of the first excitation step were performed at different laser powers. The data in both graphs was normalized for a better comparison of the spectral linewidth. See text for details.

As shown in figure 5.39, the focusing of the second step reduced the broadening of the atom absorption line significantly, indicating a corresponding reduction of the laser interaction volume. Consequently, the effective cross section of the first step laser beam in the interaction volume was similarly reduced. Due to the laser beam's spatial intensity following a Gaussian profile, this results in a higher laser intensity when averaged over the complete interaction volume. As a consequence of this, also the influence of the first step laser power was checked again, as it might cause power broadening. Figure 5.40b shows the corresponding frequency scans for different laser powers in the first excitation step. The spectral linewidth could be decreased further, starting at 250 MHz FWHM at 6.0 mW, down to only 150 MHz FWHM at 0.5 mW.

Influence of PI-LIST Voltage Settings

The voltages applied to the electrodes of the PI-LIST define the electric field which the atoms experience within the laser interaction region. Consequently, the occurrence of any undesired influences on the observed spectra was investigated. As the LIST as well as the PI-LIST were initially designed to provide a nearly field free laser interaction volume, shielding the atoms from the strong extraction field and using only weak electric fields inside the (PI-)LIST, such an influence was not expected. Graph 5.41 shows frequency scans across the HFS singlet in the first step transition at different voltage settings of the PI-LIST. Neither the potentials of the repeller electrodes nor the amplitude of the RF voltage on the quadrupole rods showed any measurable effect on the spectrum. Consequently, the parameters could be simply optimized on optimum extraction and transmission of the ions, resulting in maximum ion count rate. In the presented case, the settings of the red scan with repeller voltages of -5 V and $+5$ V and a RF amplitude of 130 V yielded the highest ion count rate and were used in the previous measurements of this section.

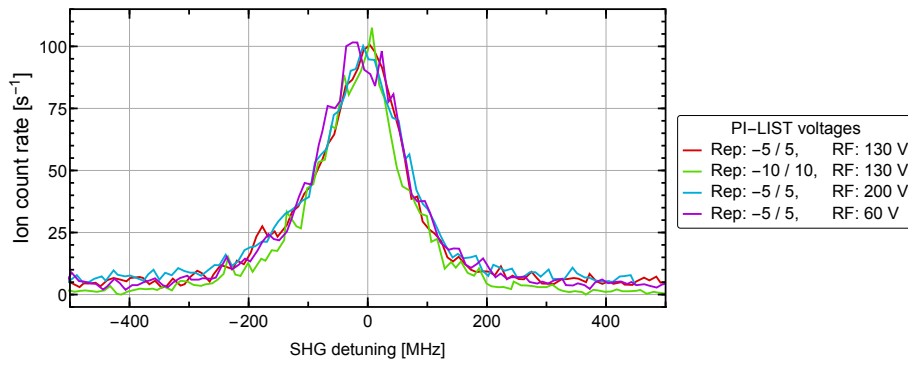


Figure 5.41: Frequency scans for different electric LIST settings. No influence on the spectral structure was observed. The ion count rate was normalized for a better comparison of the peak shape. See text for discussion.

Atom Density in the Ionization Volume

An important aspect for a full understanding of the ionization process within the laser interaction volume is the spatial ionization rate. This is an essential characteristic of the PI-LIST as ion source and fundamental for the proper operation and future developments of the PI-LIST as well as the conventional LIST. As discussed in the previous section 5.3, it was expected that the majority of the laser ions are produced within the first 20 mm behind the repeller electrode. This is a finding from an earlier investigation of the time structure of the laser ion bunches, from which the initial ionization position on the longitudinal axis could be derived [44]. This study used the fact that atoms which are ionized in front of the ionizer tube do not experience the full extraction potential and as a result, gain a slightly lower kinetic energy compared to those atoms which are ionized inside the ionizer tube. Consequently, they reach the ion detector later and appear at lower masses in the mass spectrum, which allows to probe the longitudinal ionization position with the help of time-resolved mass scans. Figure 5.42 shows the determined decrease of the ionization rate with increasing longitudinal distance z from the ionizer exit. This is caused by a corresponding decrease of the atom density inside the expanding atomic beam. To confirm this effect, the ion production was directly examined using the PI-LIST in perpendicular ionization geometry. A slit-shaped aperture of 2.5 mm width was moved horizontally through the expanded perpendicular laser beam of the first excitation step. In this way, it was possible to precisely shift the ionization region along the longitudinal axis of the PI-LIST. The results are shown in figure 5.43. The position with the highest ion count rate was set as $z = 0$ mm, corresponding to the situation that the perpendicular laser beam passed directly behind the repeller electrode, where the atom density has its maximum. The gray points represent positions, in which the laser beam is partly blocked by the repeller itself or the housing of the PI-LIST. The slope of the black data points agrees well with the observations from figure 5.42, confirming the fast decrease of the atom density along the longitudinal axis.

Two simple models were fitted to the decreasing slope of the experimental data, using the fit function

$$I(z) = \frac{I_0}{(z - z_0)^2} \cdot (1 - m \cdot z) \quad , \quad (5.3)$$

where the first term represents the approximated z^{-2} decrease of the atom density by the expanding atomic beam. The position z_0 corresponds to the point of origin of the isotropic expansion of the atomic beam, which is located a few mm inside the ionizer tube. The last term, $(1 - m \cdot z)$, accounts for a potential decrease of the laser intensity along the horizontal

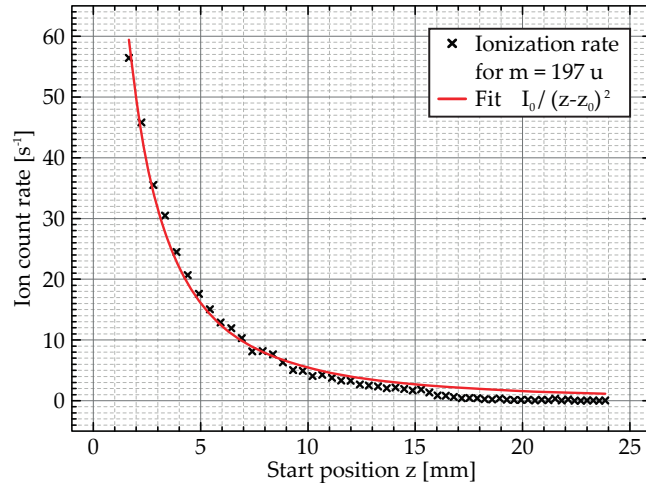


Figure 5.42: Spatial dependence of the ion count rate in the extraction field derived from investigation of the time structure of the laser ion bunches. The start position z is the position of ionization relative to the exit of the ionizer tube located at $z = 0$ mm. The strong decrease in the ion count rate for increasing distance corresponds to a reduction of the atom density. See text for details. Graphic adopted from [44].

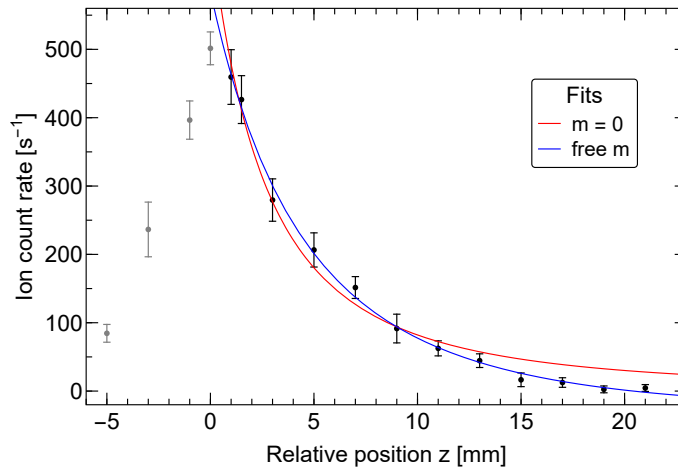


Figure 5.43: Spatial dependence of the ion count rate inside the PI-LIST derived by irradiation of specific regions along the longitudinal z -axis. The relative position of $z = 0$ mm corresponds to ionization directly behind the repeller electrode, yielding maximum ionization rate. Two models, approximating the spatial ionization rate, were fitted to the experimental data. See text for details.

axis. It is a simple linear approximation for a section of the Gaussian intensity profile of the expanded laser beam, whose maximum was located closely behind to the repeller electrode about $z = 0$ mm.

The fit function in figure 5.42 uses $m = 0$, as the laser were in longitudinal orientation, ensuring a constant power along the z -axis. In figure 5.43, the red curve neglects the linear term ($m = 0$) and differs clearly from the experimental data. In contrast, the blue curve, representing the fit with a free m -parameter, matches the data much better. The resulting point of origin from the blue plot is $z_0 = -9(2)$ mm. When considering the distance between the repeller's backside and the exit of the ionizer of about 4(1) mm, this corresponds to a starting point of the atomic beam expansion located 5(3) mm inside the ionizer tube. This value is reasonable and in fair agreement with the results in [44] where 2.0(1) mm were

obtained from the fit.

Estimation of the Overall Efficiency

The overall efficiency of the experimental setup is of high interest, especially when the sample size is limited due to availability or legal regulations. It is defined as the ratio between the number of detected ions to the initial number of atoms in the sample. Unfortunately, technical difficulties prevented a direct determination of the overall efficiency for Tc with the PI-LIST. However, some efficiency values can be estimated on the basis of known efficiencies, measured ratios of signal strength between individual operation modes, and the consumption of sample during the measurements presented in this and the following sections.

The estimated efficiency values for the different operation modes are listed in table 5.7 and are briefly explained in the following. In general, the RISIKO mass separator offers a high ion transmission, which results in high overall efficiencies of up to about 55 % as shown in chapter 4. The overall efficiency depends strongly on the ionization efficiency of the ionization scheme and the evaporation process of the sample into neutral atoms inside the hot ion source. In the case of Tc, an efficiency of 4 % was demonstrated by F. Schweltnus [73] with the ultra trace analysis ionization scheme (see figure 5.13). This is in good agreement with the sample consumption observed during the present work, where several days of measurement could be performed on a single sample despite the small sample size.

Table 5.7: Overview of estimated values of the overall efficiency in different operation modes. See text for more details.

Operation mode	Efficiency [%]
RISIKO in-source	
- General (e.g. Dy, Yb, Ho, Pd)	1-55
- Tc	4
PI-LIST - Tc	
- IG mode	1-2
- LIST mode	0.01-0.02
- PI-LIST mode	0.0001-0.02

When the LIST is installed at the ion source and used as an ion guide (IG mode), the efficiency is typically decreased by about a factor of 2. The difference in signal strength in LIST mode operation with longitudinal alignment of the laser beams is very sensitive to spatial alignment. The resulting reduction was typically about a factor of 50-150, which is in fair agreement with findings from earlier measurements on the element ytterbium [44]. Consequently, the overall efficiency can be estimated to be in the range of 0.01-0.02 %. These estimations were confirmed with dedicated efficiency measurement on Tc, yielding an efficiency of 1.4(1) % in IG mode and 0.014(1) % in LIST mode operation. However, technical difficulties with the ion source caused premature termination of the efficiency measurements, preventing a complete depletion of the sample in the ion source.

The overall efficiency using the PI-LIST in perpendicular ionization geometry depends on a set of parameters. The use of a narrowband laser source, attenuation of laser power to avoid power broadening, and the partial coverage of the full spectral width of the entire HFS structure lead to a significant reduction of the ionization rate. For the spectroscopic measurements presented in the following section, this was a decrease of about a factor of 100. On the other hand, if the spectral width of the laser radiation can cover the complete

HFS structure, ionization efficiencies can be equal to those of conventional LIST mode operation as the relevant volume behind the repeller, of about 20 mm in length, can be completely covered by the perpendicular laser beam. This is supported by the observations in 5.3.2 and in the present systematic study of the spectroscopic performance, where only 20 % loss was demonstrated when switching between proper optimized longitudinal and perpendicular first step laser alignment when using full power broadband laser radiation.

5.4.3 High-Resolution HFS Study of the First Excitation Steps

Highly resolved optical spectroscopy was performed in all three first excitation steps, namely the transitions from the $4d^5 5s^2 6S_{5/2}$ ground state to the states of the $4d^5 5s 5p^6 P^o_{3/2,5/2,7/2}$ fine structure triplet, in the three technetium isotopes available, ^{97}Tc , ^{98}Tc and ^{99}Tc . The available excitation ladders are shown in figure 5.13. Proper settings were chosen on the basis of the findings from the systematic characterization presented in the previous section 5.4.2. The following section presents the obtained spectra, their analysis, and the determined characteristic parameters of the HFS and isotope shifts.

All frequency scans with the injection-locked Ti:sapphire laser system were performed by scanning the fundamental CW diode laser from lower to higher frequencies. First, a wider area around each individual multiplet was scanned with 10 MHz step size. Afterwards, the peak structure of the multiplet was scanned multiple times with an increased resolution of 5 MHz in step size. Please note that the step sizes correspond to 20 MHz and 10 MHz, respectively, after the frequency-doubling of the pulsed laser radiation. Depending on the average ion count rate, the scan was repeated two to four times, while data was recorded for 3 – 6 s at each frequency setpoint. Because of the relative large HFS splitting across several GHz, the laser frequency in the second excitation step was re-optimized on each multiplet. The HighFinesse WSU2 wavemeter, used for the precise determination of the fundamental laser frequency of the CW diode laser, was calibrated to a stabilized HeNe laser⁵ before recording a new spectrum. For the evaluation, the data of all individual scans of a spectrum was combined and binned in intervals of 10 MHz width. The mass spectrum presented in figure 5.44 shows well separated mass peaks for all three isotopes, proving that the individual optical spectra are not affected by the neighboring isotopes.

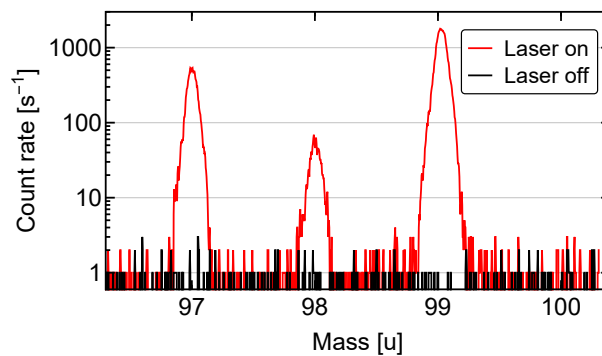


Figure 5.44: Mass spectrum of the Tc region at the RISIKO separator using the PI-LIST in LIST mode with longitudinal laser alignment

Figure 5.45 visualizes the splitting of ground state and first excited state. The black colored values for F correspond to the isotopes $^{97,99}\text{Tc}$ with nuclear spins $I_{97,99} = 9/2$, while the gray colored labels correspond to ^{98}Tc with $I_{98} = 6$. In the following, the evaluation of the $J = 5/2$ to $J' = 7/2$ transition acts as an example to describe the process of the analysis

⁵SIOS Messtechnik - SL03/01

in full detail, in particular the fitting procedure. The other two transitions to $J' = 3/2$ and $J' = 5/2$ were evaluated in an identical manner. Additional plots of these two transitions can be found in the appendix, section D.

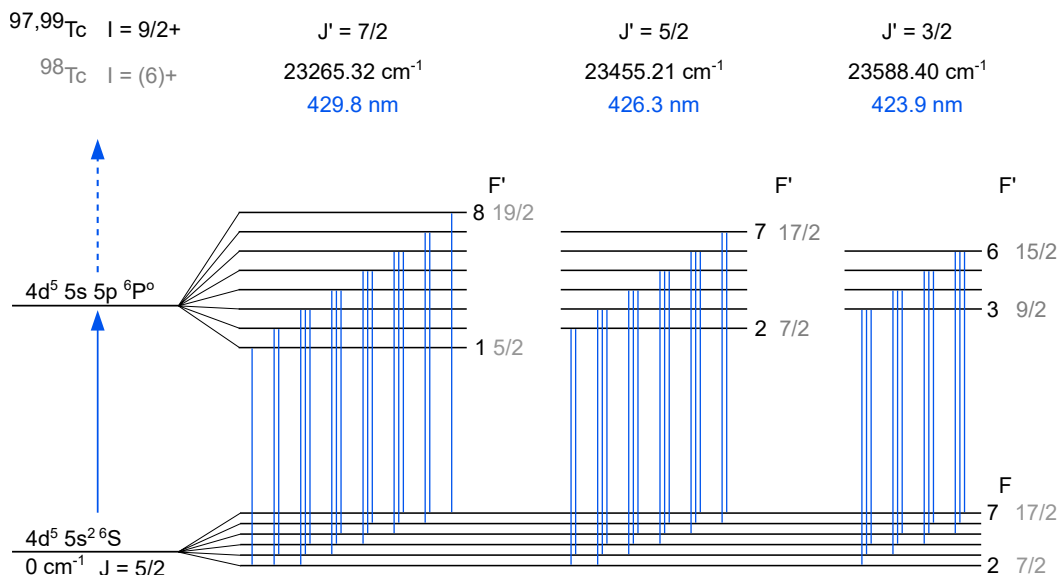


Figure 5.45: Schematic illustration of the HFS splitting of the $4d^5 5s^2 6S_{5/2}$ ground state and the first excited state $4d^5 5s 5p^6 P_{J'}^0$ in Tc

Transition $6S_{5/2} - 6P_{7/2}^0$

The transition from the ground state to the $4d^5 5s 5p^6 P_{7/2}^0$ state was the first one to be investigated. As the nuclear spin of $^{97,99}\text{Tc}$ is $I_{97,99} = 9/2$, the coupled total angular momenta of the ground state are $F = 2, \dots, 7$. For the first excited state with $J = 7/2$, the angular momenta couple to $F' = 1, \dots, 8$, as visualized in figure 5.45. This gives rise to a total number of 18 HFS transitions, which can be clearly identified in the spectra. The laser powers of the first and second step were set to 0.5 mW and 6.0 mW with a temporal delay of about 40 ns between the two corresponding laser pulses. The power of the third step laser was set to its maximum power of 2500 mW to ensure maximum ionization efficiency. The resulting spectra are shown in figure 5.46. The frequency axis was centered at $23265.388 \text{ cm}^{-1}$, which corresponds to the center of the HFS structure of ^{97}Tc .

The formation of four triplets, two doublets and two singlets clearly confirm that the upper state splitting is significantly larger than the splitting of the ground state which is in perfect agreement with the findings in [130]. The spectrum of ^{98}Tc shows the same pattern, proving that $I_{98} \geq 4$ which is in agreement with the predicted value of $I = 6$ [136]. In fact, based on the ratios of the spacing between the corresponding transitions of this as well as the following spectra, one can confirm that the total nuclear angular momentum must be $I_{99} = 6$, which is the first major finding of this experiment. This is also supported by the fit procedures converging only for $I_{99} = 6$ properly as discussed further below. The spectra of ^{97}Tc and ^{98}Tc look very similar, as expected from the identical nuclear spin. Clearly, the isotopic shifts are small compared to the complete span of the HFS splitting.

All spectra show an excellent spectral resolution and an outstanding signal-to-noise level. Each individual HFS transition is well resolved and for most multiplets background level is

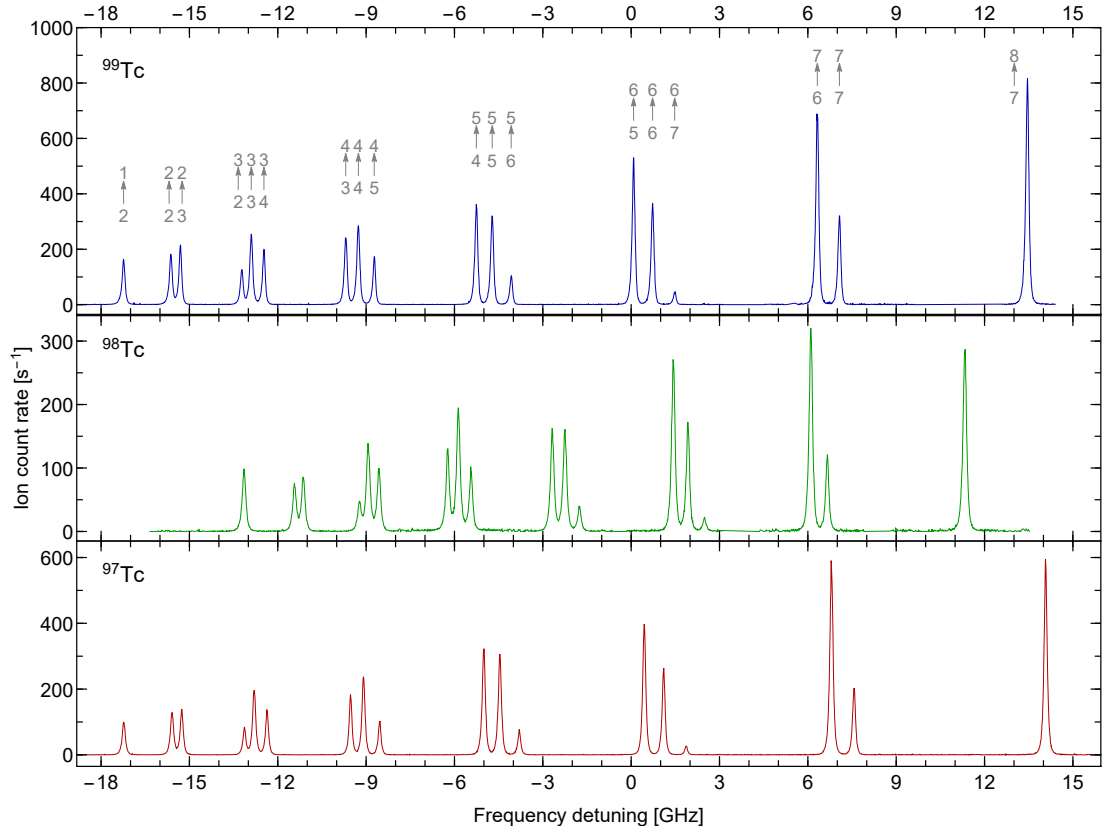


Figure 5.46: HFS structure of the $J = 5/2 - J' = 7/2$ transition at 429.8 nm in Tc. The data was binned to intervals of 10 MHz width. The associated $F - F'$ transitions in the ^{99}Tc spectrum are indicated in gray.

reached even between the individual resonances. Most resonances reach peak ion count rates of a few hundred counts per second, while the off-resonance background induced by the dark count rate of the SEM detector and its readout electronics was about 0.5 s^{-1} . The spectral resolution and signal-to-noise ratio in the ^{98}Tc spectrum are slightly inferior to those of ^{97}Tc or ^{99}Tc . This is due to the ten times smaller amount of ^{98}Tc in the sample and the resulting lower ion count rates which were partially compensated by increasing the ion source temperature, which in turn led to slightly stronger Gaussian Doppler broadening.

For this transition, a sum of 18 Voigt profiles centered at the different spacings $\Delta E_{F,F'}$ around the central frequency ν_0 , according to formula 2.18 as described in section 2.1.3, was fitted to the data. Details of the Voigt profile's special characteristics and its linewidth are discussed in section 2.3.3. The implementation increased the computing speed by several orders of magnitude, resulting in a much faster fitting procedure. As an example, the resulting fit is shown in figure 5.47 for the isotope ^{99}Tc . A compilation of the fitted spectra for all three isotopes is provided in figure D.1 in the appendix.

Each individual Voigt peak in the fit functions features a free Lorentzian and Gaussian width as well as a free parameter to adapt the total height of the profile. In principle, the relative heights of the different transitions within the HFS are given by the corresponding Racah coefficients or the Wigner $6 - j$ symbols. However, the relative heights observed in real experiments typically differ slightly from the Racah coefficients. This is caused by several effects: the signal loss over the course of the frequency scan, slightly different power saturation properties of the individual transitions which imply different power broadenings, and optical pumping effects.

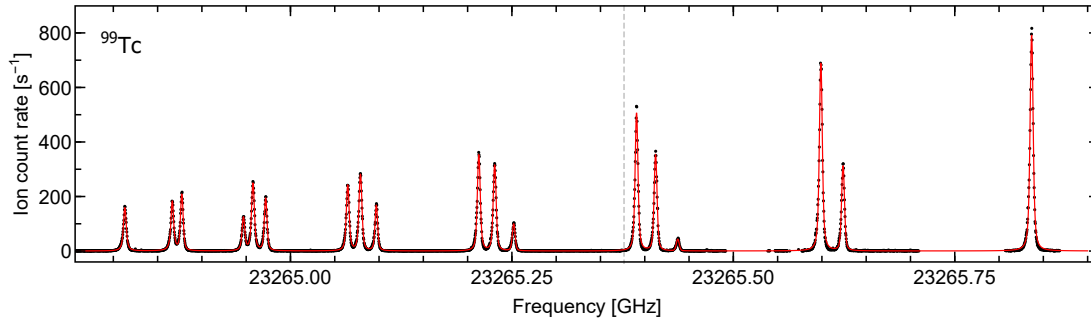


Figure 5.47: Fit to the experimental data of the $J = 5/2 - J' = 7/2$ transition at 429.8 nm in ^{99}Tc . The data was binned to intervals of 10 MHz width. A sum of Voigt profiles centered at the different $\Delta E_{F,F'}$ was fitted to the data using a least square fit algorithm. The vertical dashed line indicates the resulting center of gravity ν_0 of the HFS spectrum.

A key feature of the obtained spectra and an important property of the PI-LIST technique itself, is the achievable spectral linewidth under experimental conditions. The width of the obtained resonances define how well the hyperfine structure can be resolved and give additional information on the contributing broadening mechanisms. By applying the Voigt fit, the mean full width at half maximum of all resonances in the spectra were determined to be 121(5) MHz, 138(7) MHz, and 115(5) MHz for the spectrum of ^{97}Tc , ^{98}Tc , and ^{99}Tc respectively. Here, the corresponding standard deviations within the spectra were considered as uncertainty. These are excellent values for optical spectroscopy, allowing the precise investigation of HFS structure. It should be emphasized that the investigated transition used frequencies in the blue part of the visible spectrum, which causes additional broadening by the required frequency doubling of the laser light and an increased influence of the Doppler broadening. The PI-LIST approach would enable even more narrow linewidth if transitions in the fundamental Ti:sapphire laser spectrum are used. This will be discussed in more detail further below.

A Quantification of the Gaussian and Lorentzian contributions to the FWHM of the Voigt profiles allow to draw conclusions about the different processes participating in the ionization process and yield additional characteristic information on the PI-LIST setup. Table 5.8 summarizes the mean Gaussian and Lorentzian FWHM to the Voigt profiles.

The Gaussian contribution is composed of the thermal Doppler broadening and the spectral laser linewidth. The FWHM of the fundamental laser radiation is about 12 MHz, which includes the statistical jitter due to the ECDL laser system as well as the LaseLock cavity stabilization. This is increased by the frequency-doubling by a factor of $\sqrt{2}$. The FWHM of the residual thermal Doppler broadening in direction of the perpendicular axis can be calculated to be about 78 MHz. This corresponds to a typical temperature of 1700 °C and an estimated effective half opening angle of about 2° to access the ionization volume starting from the exit of the ionizer. Both components add up to an estimated Gaussian FWHM of about 80 MHz, which is in good agreement with the values extracted from the Voigt fit. The Gaussian contribution in the ^{98}Tc is higher than for $^{97,99}\text{Tc}$, which is due to the higher temperatures of the ion source, which were used to compensate for the ten times smaller ^{98}Tc sample size.

The Lorentzian contribution comprises the natural linewidth and the power broadening, which cannot be completely eliminated. The addressed transition starting from the ground state is the strongest documented transition to the $4d^5 5s 5p^6 P_{7/2}^o$ level. Thus, its transition strength of $4.2 \cdot 10^7 \text{ s}^{-1}$ [128] can be used to estimate the natural linewidth to about 6.7 MHz. The natural linewidth might be larger, in the case of any undocumented sufficiently strong

Table 5.8: Contributions to the full width at half maximum of the resonance peaks in figure D.1. The values were extracted by the fitting of a sum of Voigt profiles to the experimental data. All values are given in MHz.

FWHM	⁹⁷ Tc	⁹⁸ Tc	⁹⁹ Tc
Gaussian	84(10)	92(19)	80(13)
Lorentzian	58(18)	72(27)	57(17)
Total	121(5)	138(7)	115(5)

decay channels being present. However, it is expected to stay well below 15 MHz. The FWHM of the remaining power broadening is hard to calculate precisely, but it can be estimated to be about 20–60 MHz. Both contributions sum up to a Lorentzian FWHM of about 27–75 MHz, which is in good agreement with the results from the fits. The fact that the Gaussian and Lorentzian width are similar in size, originates from the initial optimization procedure, in which the laser powers were decreased to reduce the power broadening. Obviously, a further reduction of the Lorentzian linewidth far below the Gaussian linewidth would lead only to a small improvement of the spectral resolution, but would lead to a significant sacrifice in ionization efficiency.

The fit in figure 5.47 matches the experimental data quite well, but there is more information to be found in the spectrum if the shape of the resonances is examined in more detail. In this context, all spectra showed similar peculiarities indicating the presence of systematic effects. These affect the resulting fit parameters only weakly, but a more detailed investigation is mandatory in order to gain a comprehensive understanding of the PI-LIST operation and to characterize their influence on the fit. The issue will be discussed using the spectrum of the $J = 5/2 - J' = 7/2$ transition in ⁹⁹Tc since it shows the strongest appearance of the systematic effects. The upper panel in figure 5.48 shows a triplet of the ⁹⁹Tc spectrum. The red curve represents the result of the fit to the full spectrum using a standard Voigt profile for each peak. The middle panel shows the corresponding residuals to the data points. The blue curve shows the fit with an adapted model which is discussed further below. On the Voigt fit, two different systematic features can be observed. First, the peaks of experimental data show a small asymmetry, resulting in a sawtooth structure in the residual plot. Second, the curve of the fitted function lies above the experimental data on all tailings further off the resonance center and reaches background level at about 0.03 cm^{-1} apart from the peak structure. This can be seen clearly on the left and right border area of the residual plot and in the central region between the resonance peaks of the triplet.

Asymmetric features in highly resolved HFS spectra are not uncommon and can be caused by different effects. One possibility is a non-symmetrical velocity distribution of the atoms along the laser axis. In the present case, this corresponds to the exciting laser beam being not perfectly oriented in 90° to the central axis of the atomic beam. Due to the anisotropic expansion of the atomic beam from the ionizer, the resulting Doppler profile exhibits a corresponding slight asymmetry. A major influence on the effective angle between atomic beam and perpendicular laser beam results from the alignment of the longitudinal oriented laser beams for excitation step two and three, which defines the ionization volume which in turn determines the solid angle which the atoms must follow to reach ionization.

An asymmetry could also be induced by spectral properties of the exciting laser light itself. Typically, most pulsed lasers show chirp effects, which cause the laser frequency to change slightly over the duration of a single laser pulse [65, 125]. Typically, these changes are in the order of kHz to a few MHz, a size which might be observable in the present spectra of Tc. The change of the laser frequency during the laser pulse is hardly predictable and can

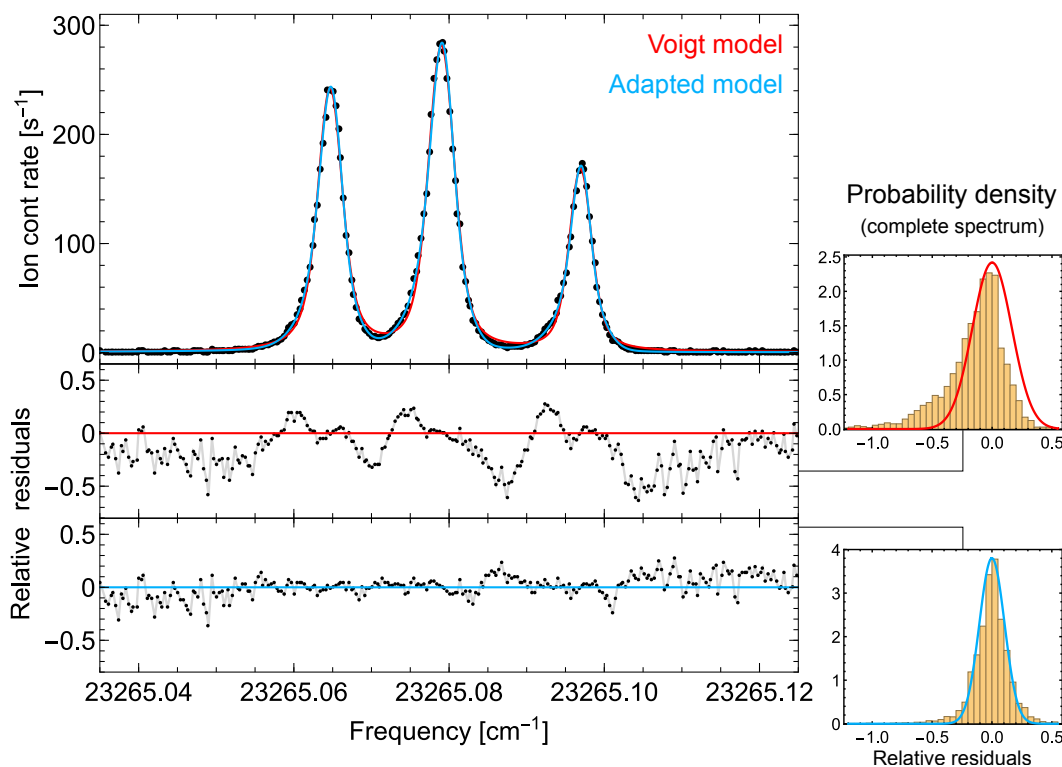


Figure 5.48: Section of the fitted ^{99}Tc spectrum showing the resulting curves for a fit using standard Voigt profiles (red) or asymmetric Bi-Voigt profiles (blue) for each resonance. The lower section shows the residuals relative to the y-value of each point. See text for further explanation.

show a trend to higher frequencies (*up-chirp*) or lower frequencies (*down-chirp*). The chirp can be caused by various effects, as for example a spatial and temporal modulation of the refractive index inside the Ti:sapphire crystal, induced by the high power pump laser pulse. Furthermore, modulations can also result from chromatic dispersion or nonlinear effects (e.g. Kerr effect) within the transmitting optical components in the beam path. Eventually, the evolution of the laser frequency, laser power, and the number of excitable Tc atoms during the course of each laser pulse can result in an asymmetry of the finally observed resonance peaks. Another side effect could be a small systematic shift of the complete spectrum, but this would not affect the determination of the HFS parameters. Unfortunately, due to the large number of interfering mechanisms responsible for the chirp effect, it is not possible to estimate its quantitative impact and shape. As spectral linewidth of about 100 MHz are now accessible with the help of the PI-LIST, it becomes relevant to systematically investigate possible chirp effects of the laser system in the near future.

The second discrepancy in the spectrum, the non-matching shape of the tailings further off and the actual peaks, indicate that the resonances cannot be completely described by Voigt profiles. This deviation can be attributed to multiple contributions with individual Lorentzian or Gaussian linewidths. This behavior is not completely unexpected as the temporal separation of the laser pulses, as mentioned earlier, induces different excitation conditions along the laser pulse. During the frequency scans, the temporal delay between the laser pulse of first and second ionization step was 40 ns, while the full width at half maximum of the laser pulses was about 45 ns. As illustrated in figure 5.49, this leads to two different phases of excitation of the first step transition: phase I, where the excitation pulse of the second step is not present; and phase II, in which photons of both excitation steps are present. This is just a simplified picture as in fact it is a smooth transition between

those two phases. However, it will be handled as two distinct phases in the following for the sake of clarity. As described in [49, 50], the two phases exhibit a different broadening in the first step transition, while the excitation rate also differs due to the varying laser powers. Therefore, the final lineshape differs from a single Voigt profile and is better described by a sum of Voigt profiles with different width and height.

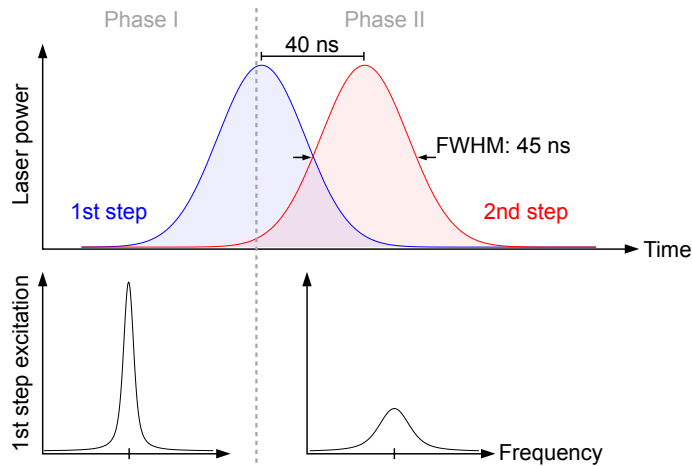


Figure 5.49: Schematic illustration of the different excitation phases for typical experimental laser pulse timing. The excitation of the first transition during a laser pulse can be divided in two phases (upper section) in which a different power broadening is observed in the first step transition (lower section). As a result, the observed shape of the resonance differs from a simple Voigt profile, but can be described as a sum of Voigt profiles with different widths and heights.

Another cause might be a nonuniform power broadening within the ionization volume. This can result from the Gaussian-shaped spatial intensity profile of the laser beams. Here, the influence of the second step laser beam is reduced by the temporal separation but cannot be completely neglected. In contrast, it is expected that the first step laser has only a weak impact, as the laser beam was strongly enlarged to a spot size of several cm^2 , which minimized the change of its intensity within the much smaller ionization volume with a cross-sectional area of only a few mm^2 .

In order to compensate any negative effects on the parameters derived by the fitting procedure, the underlying theoretical model, represented by the fit function, had to be adapted to account for the peak shapes observed in the experimental spectra. First, the basic Voigt profile was modified to allow a simple asymmetry as described in [137]. This introduced a new parameter, which defined strength and direction of the peak asymmetry. For the fitting procedure, this asymmetry parameter was kept identical for all peaks in a single spectrum.

Second, an additional, Voigt profile with lower peak height and broader width was added to each resonance peak, to account for the discrepancy of the tails further off caused by the different ionization regimes with different spectral width of the excitation. The center of each additional Voigt profile and the associated main Voigt profile were set identical. One fixed ratio of the maximum height of the main and the small Voigt profile was used for the whole spectrum. Several tests on different spectra revealed that the best fits were obtained when setting the Lorentzian width of the smaller Voigt profiles to the same width as the associated main Voigt Profile, while a single free Gaussian width was used for all additional Voigts in the entire spectrum. Each Bi-Voigt profile, the sum of the two Voigt profiles, was normalized, giving it the same maximum height as the standard Voigt profile. Typical height ratios of secondary to main Voigt profile resulting from the fit were about

30 %. The Gaussian width of the broader secondary peaks was on average a factor of 2.3 larger than the Gaussian widths of the primary peaks or the Gaussian widths from the fit using single Voigt profiles, as the latter two were very similar. It is important to note that both fit model modifications did not affect the position of the profile's maximum on the frequency axis. In the end, only three additional free fit parameters, asymmetry parameter, Bi-Voigt height ratio, and Gaussian width of the secondary peaks, were required to account for the observed peak shape in the spectra. Considering the good signal-to-noise ratio and the large number of data points in the spectra, these few additional parameters do not introduce the risk of obscuring the fitting procedure by applying to many free parameters.

Figure 5.48 gives an example of the fit with the improved model using the asymmetric Bi-Voigt profiles (blue curve). The use of the asymmetric Bi-Voigt profiles results in a much higher overall quality of the fit, as the resulting curve matches the experimental data very well across the complete multiplet and the entire spectrum. This becomes very clear when comparing both residual plots and the corresponding residual histograms for the complete spectrum. The position of the fitted peak maxima of the red curve tend to slightly lower frequencies compared to the data points, which is caused by the asymmetry of the peaks. In contrast, the fit using the asymmetric Bi-Voigt profiles yields a slightly more accurate reproduction of the peak maximum. This is observed consistently in all recorded spectra in Tc.

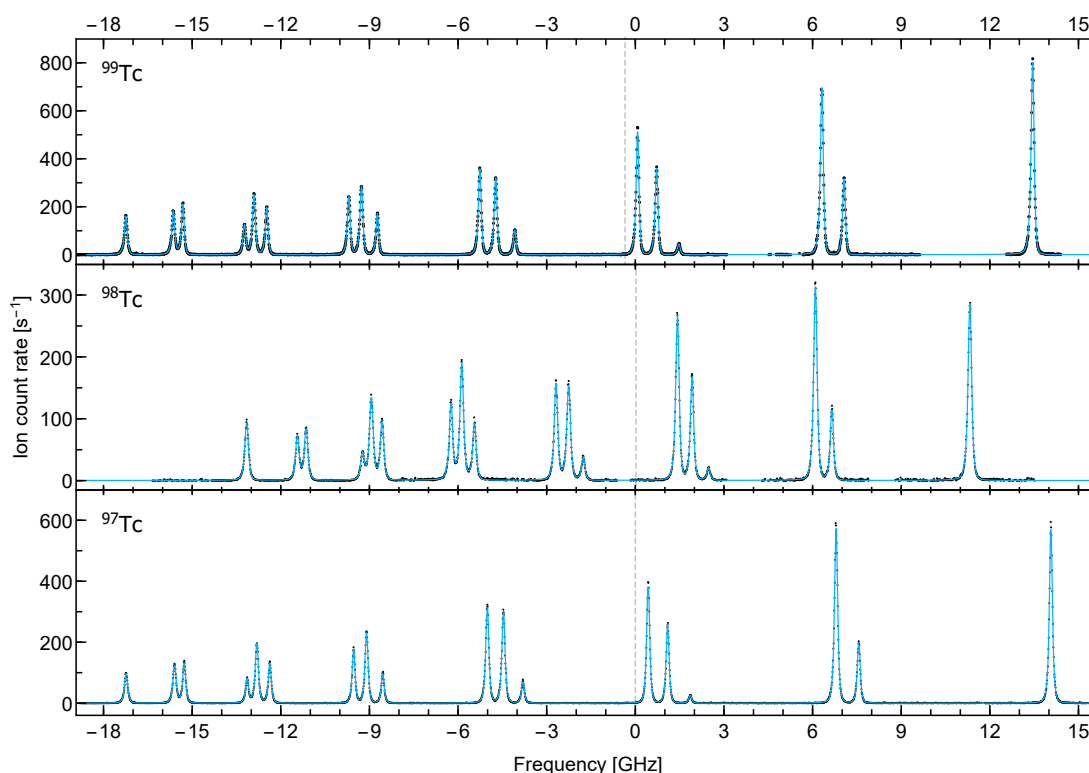


Figure 5.50: Fit to the experimental data of the ${}^6S_{5/2} - {}^6P_{7/2}^o$ transition at 429.8 nm in Tc. The data (black) was binned to intervals of 10 MHz width. A sum of asymmetric Bi-Voigt profiles centered at the $\Delta E_{F,F'}$ was fitted to the data using a least square algorithm. The frequency axis is centered around the center frequency of the ^{97}Tc transition at $23265.388 \text{ cm}^{-1}$.

Other RIS-based experiments conducting high-resolution spectroscopy with pulsed laser systems observed similar asymmetries and deviating tailings. In these cases, modifications of the fit model, similar as those presented here, proved to be reasonable and resulted in consistent data [138, 139]. The resulting fits of the full spectra using the asymmetric Bi-Voigt

profiles are shown in figure 5.50 for all three Tc isotopes. The final HFS parameter and isotope shifts extracted by the best fits are listed further below in table 5.11 together with the results of the other transitions investigated.

Transition ${}^6S_{5/2} - {}^6P_{5/2}^o$

The transition from the $4d^5 5s^2 {}^6S_{5/2}$ ground state to the $4d^5 5s 5p {}^6P_{5/2}^o$ at 23455.25 cm^{-1} splits into a total number of 16 HFS transitions as illustrated in 5.45, forming four triplets and two doublets. The obtained data is presented in figure 5.51. This transition was the last one to be investigated during the measurement campaign. Due to a restricted time schedule, it was necessary to reduce the number of fine scans across the multiplets, resulting in a slightly worse signal-to-noise ratio compared to the spectra of the other two transitions. Despite that fact, the spectral resolution is similar to those of the other transitions.

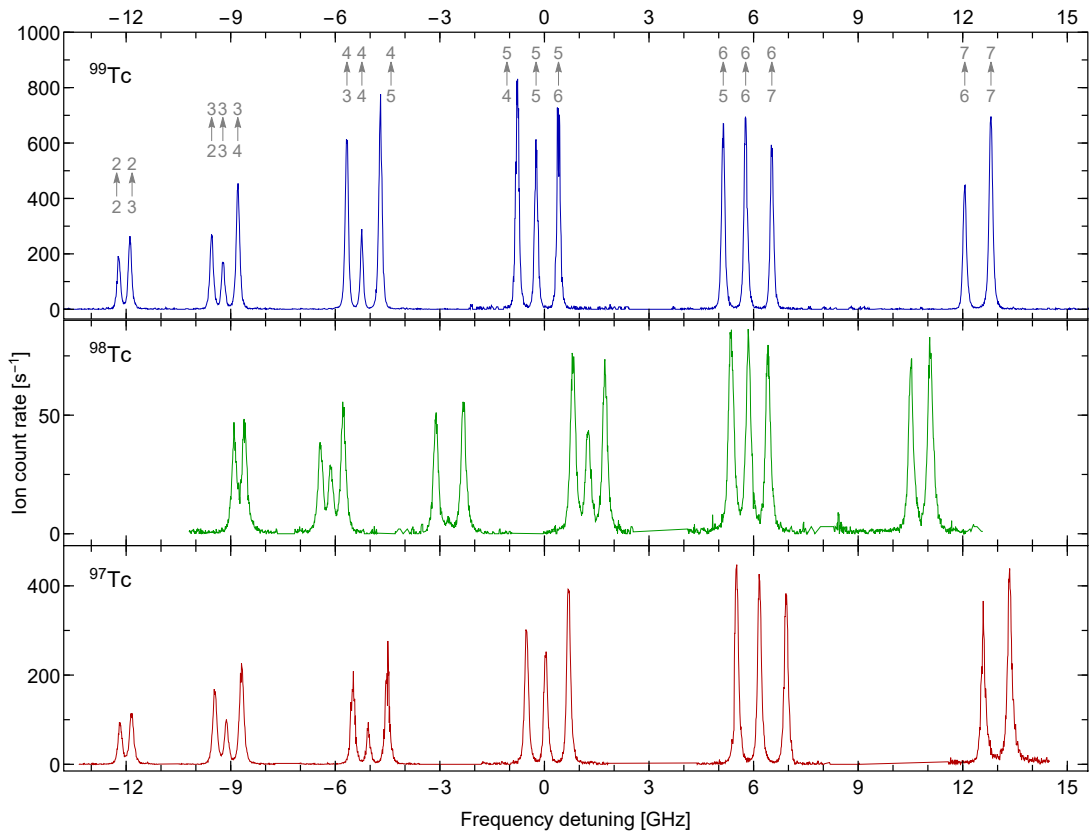


Figure 5.51: Experimental data of the HFS structure of the $J = 5/2 - J' = 5/2$ transition at 429.8 nm in Tc. The data was binned to intervals of 10 MHz width. The associated $F - F'$ transitions in the ${}^{99}\text{Tc}$ spectrum are indicated in gray.

As in the previous section, a fit function using standard Voigt profiles was fitted to the data to derive the spectral width of the observed resonance peaks. The compilation of the derived linewidths is given in table 5.9. The determined FWHM are similar to those of the HFS spectra from the $J = 5/2 - J' = 7/2$ transition. As before, the measurement on ${}^{98}\text{Tc}$ required operating the ion source at higher temperatures to compensate for the smaller sample size, which correspondingly increased the Gaussian FWHM.

Table 5.9: Contributions to the full width at half maximum of the resonance peaks in the $J = 5/2 - J' = 5/2$ spectrum as shown in figure 5.51. The values were extracted by the fitting of a sum of Voigt profiles to the experimental data. All values are given in MHz.

FWHM	^{97}Tc	^{98}Tc	^{99}Tc
Gaussian	85(35)	112(16)	87(8)
Lorentzian	67(27)	83(28)	41(10)
Total	131(12)	164(11)	111(6)

A fit function with asymmetric Bi-Voigts was fitted to determine the HFS parameter. The resulting fit is shown in the appendix in figure D.2. The fits show similar quality compared to the fits in the $J = 5/2 - J' = 7/2$ transition. The determined HFS parameter are given in table 5.11 together with the parameters of the other two transitions.

Transition ${}^6S_{5/2} - {}^6P_{3/2}^o$

The splitting of the ground state and the $4d^5 5s 5p {}^6P_{3/2}^o$ level at 23588.40 cm^{-1} is illustrated in figure 5.45. The result is a total number of 12 HFS transitions, which group in four triplets. The binned raw data for all three isotopes is shown in figure 5.52. The average count rate and the signal-to-noise ratio is very good and comparable to the data from the ${}^6S_{5/2} - {}^6P_{7/2}^o$ transition.

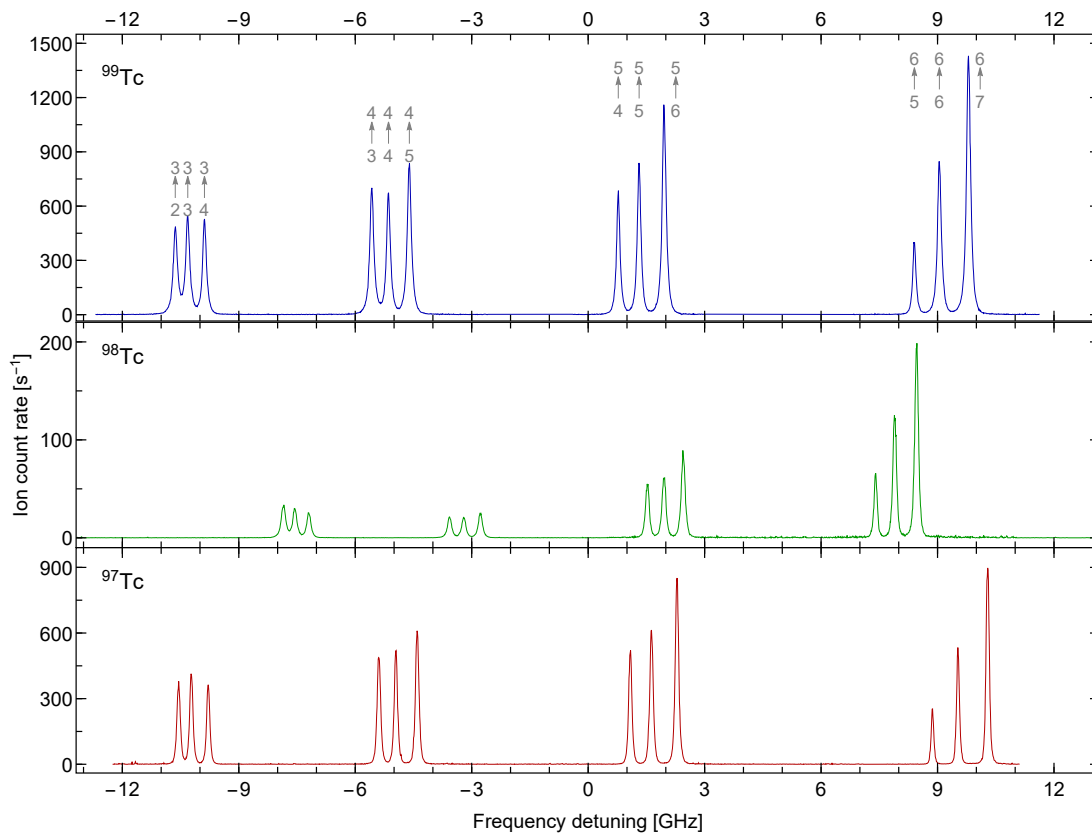


Figure 5.52: HFS structure of the $J = 5/2 - J' = 5/2$ transition at 423.9 nm in Tc. The data was binned to intervals of 10 MHz width. The associated $F - F'$ transitions in the ^{99}Tc spectrum are indicated in gray.

As in section 5.4.3, a fit function using standard Voigt profiles was fitted to the data to derive the spectral FWHM of the observed resonance peaks, which are summarized in table 5.10. Thanks to the installation of a new Tc sample, the ion source could be operated at lower temperatures, which resulted in about 20 MHz lower Gaussian FWHM compared to the measurement in the transition to the $4d^5 5s 5p^6 P_{7/2}^o$ state. As for the study of the other transitions, the temperature of the ion source was increased for the scan in ^{98}Tc , which is why the corresponding spectrum shows the largest Gaussian widths.

Table 5.10: Contributions to the full width at half maximum of the resonance peaks in the $J = 5/2 - J' = 3/2$ spectrum as shown in figure 5.52. The values were extracted by the fitting of a sum of Voigt profiles to the experimental data. All values are given in MHz.

FWHM	^{97}Tc	^{98}Tc	^{99}Tc
Gaussian	78(7)	86(12)	62(9)
Lorentzian	34(5)	54(16)	79(13)
Total	98(8)	119(10)	115(8)

Similar as for the other two transitions, a fit function with asymmetric Bi-Voigts was fitted to the experimental data to derive the HFS parameter. The resulting profiles for all three isotopes are shown in figure D.3. The quality of the fit is equal to the result from the $^6S_{5/2} - ^6P_{7/2}^o$ transition. The HFS parameter extracted by the fit are summarized in table 5.11.

Fit Results of the HFS parameters

The excellent quality of the data and the use of the asymmetric Bi-Voigt profiles allowed a very accurate fit of the theoretical model. All resulting parameters of the HFS for the ground state and the first excited states are summarized in table 5.11. The corresponding values for the fit using simple Voigt profiles are listed for comparison in table D.1 in the appendix.

As the shape of the fits using the asymmetric Bi-Voigt profiles consider the additional effects discussed above, the slope of the experimental data is significantly better reproduced compared to the simple Voigt profiles. Correspondingly, the resulting fit parameters show less scatter and yield a higher accuracy as discussed in the following. A comparison of the results in table 5.11 and table D.1, shows that the standard errors of the fit parameters are about 10-20 % smaller than for the fitting of standard Voigt profiles. When comparing the results in table 5.11 and table D.1, the first detail which can be found is that the standard errors of the fit parameters about 10-20 % smaller than for the use of standard Voigt profiles. This is confirmed by the fact that the extracted HFS parameters show less scatter across multiple measurement, as observed for example, when comparing the ground state parameters $A(^6S_{5/2})$ and $B(^6S_{5/2})$ for a certain isotope, derived independently from all three transitions measured. Furthermore, it is possible to compare the deviation of the HFS coupling constants for each individual transition, as the ratio $A_{\text{up}}/A_{\text{low}}$ is expected to stay constant across all isotopes, except for the case of HFS anomalies, i.e. the Bohr-Weisskopf effect or Breit-Rosenthal effect [140, 141, 142, 143], which usually have an effect well below 1 %. In the present case, the ratios show no systematic trend, confirming the absence of a strong HFS anomaly. In both ways of comparison, using the ground state parameters of a certain isotope (vertical comparison in the table) or the $A_{\text{up}}/A_{\text{low}}$ ratios for a single transition (horizontal comparison in the table), the corresponding standard deviations are about 20 % smaller compared to the results derived from the fits using conventional Voigt profiles. This is in good agreement with the smaller standard errors from the fit and confirms the higher accuracy obtained by using the asymmetric Bi-Voigt profiles

Table 5.11: Compilation of the HFS coupling constants of the first excitation step derived by the fits using asymmetric Bi-Voigt profiles as explained in section 5.4.3. The listed errors are standard errors from the fit routine. For comparison, table 5.11 summarizes the results using conventional Voigt profiles for the fit. The literature values for ^{99}Tc are taken from [130]. It should be noted that the ground state splitting in [130] could not be resolved and a value for B was not given. See text for detailed discussion. All values are given in units of MHz.

Parameter	^{97}Tc	^{98}Tc	^{99}Tc	$^{99}\text{Tc}_{\text{lit}}$
Transition ${}^6S_{5/2} - {}^6P_{7/2}^o$				
A_{low}	-109.582(22)	-65.908(24)	-107.347(21)	-109.12(90)
A_{up}	815.769(17)	490.961(18)	799.987(15)	798.6(36)
B_{low}	-1.42(46)	4.34(71)	1.52(41)	-
B_{up}	-59.20(53)	17.04(83)	-43.86(46)	-57(18)
$A_{\text{up}}/A_{\text{low}}$	-7.444(2)	-7.449(3)	-7.452(1)	-7.32
Transition ${}^6S_{5/2} - {}^6P_{5/2}^o$				
A_{low}	-109.530(45)	-65.839(43)	-107.306(32)	-109.12(90)
A_{up}	911.832(48)	548.602(43)	894.080(35)	892.2(39)
B_{low}	7.69(105)	-1.78(130)	-0.50(76)	-
B_{up}	71.32(107)	-9.42(123)	57.35(81)	93(18)
$A_{\text{up}}/A_{\text{low}}$	-8.325(3)	-8.333(5)	-8.332(3)	-8.18
Transition ${}^6S_{5/2} - {}^6P_{3/2}^o$				
A_{low}	-109.380(12)	-65.833(23)	-107.369(18)	-109.12(90)
A_{up}	1207.188(18)	726.847(36)	1183.268(27)	1182.1(36)
B_{low}	1.87(27)	-9.63(62)	1.14(28)	-
B_{up}	-6.52(19)	-3.09(46)	-12.64(40)	-12(12)
$A_{\text{up}}/A_{\text{low}}$	-11.037(1)	-11.041(4)	-11.021(2)	-10.83

So far, the HFS was precisely studied only on the isotope ^{99}Tc . Data on a variety of transitions was published by Wendlandt et al. in 1977 [130]. The present work is the first study of the HFS for the other two isotopes ^{97}Tc and ^{98}Tc to date. The literature values are also listed in table 5.11 for comparison. It is important to note that in the work of Wendlandt et al., "the ground-level splitting could not be completely resolved" [130]. A not further described "numerical profile analysis" was performed to derive the corresponding A coupling constants, while values for B were not given. In this context, the stated errors for A seem to be slightly underestimated, which explains the systematic difference in $A({}^6S_{5/2})$ of about 1.9σ between the present work and the less accurate literature values. The measured values for the upper states, A' and B' , agree well with literature. In contrast to [130], in the present work the ground state splitting could be perfectly resolved (see figures 5.46, 5.51, and 5.52) and the resulting values for A agree well across the three independently investigated transitions. Due to the significant enhancement in resolution, the present work allows a more precise and conclusive determination of the HFS A parameters.

Error budget and Final Results

All accuracies in the following are discussed in terms of 1σ accuracies. The examination of the scatter in the ground state parameters for each isotope across the three transitions allows a reasonable evaluation of the accuracy of the experiment. It is clear that the standard deviation derived from only three values somewhat lacks statistical significance, but it is

still a good parameter to quantify the scatter. Across the three measurements, the standard deviations are $\Delta A_{97}(^6S_{5/2}) = 105$ kHz, $\Delta A_{98}(^6S_{5/2}) = 42$ kHz, and $\Delta A_{99}(^6S_{5/2}) = 32$ kHz, which is slightly higher than the error estimated by the fitting procedure. It is not unusual that standard errors from fitting procedures are smaller than the observed scatter, as their calculation do not account for systematic effects and are calculated assuming that the mathematical fit model is the exact representation for the experimental data. The observed standard deviation is only 0.03-0.1 % of the corresponding mean values, which clearly shows the high level of accuracy of the experimental data. Yet, the scatter of B for the ground state is significantly larger, which is partially due to the much smaller sensitivity (see formula 2.15) and the small size of B of only a few MHz. The resulting standard deviations are $\Delta B_{97}(^6S_{5/2}) = 4.6$ MHz, $\Delta B_{98}(^6S_{5/2}) = 7.0$ MHz, and $\Delta B_{99}(^6S_{5/2}) = 1.1$ MHz.

The sources of errors will be discussed in the following. The slight asymmetry of the peaks and their lower slope, which deviate from a single Voigt profile were already discussed earlier. The adapted fit model is only approximating the underlying effects in an empirical way, as the origin could not be precisely determined. As mentioned earlier, this adaption of the fit model resulted in an improved overall consistency of the resulting fit parameters. However, for a conservative error estimation, it should be kept in mind that these corrections also lead to a slight change of the extracted fit parameter in comparison to the use of the standard Voigt profiles. They differ by about 30 kHz for A and about 150 kHz for B . The values of the center frequency of the structure, which will be discussed in the context of the isotope shift, differ by about 1 MHz.

The statistical inaccuracy of the HighFinesse WSU2 wavemeter on each data point can be neglected, since it is well compensated by the high number of data points recorded, in the order of 50000 per spectrum, and the fitting procedure. The remaining inaccuracy of the wavemeter is due to thermal drifts over time and systematic deviations depending on the input frequency and the calibration of the wavemeter. This effect is estimated to contribute an inaccuracy of less than 10 kHz for A , 50 kHz for B . The absolute shift of the whole HFS structure is conservatively estimated with 1 MHz, which is taken into account when calculating the error of the isotope shifts. These inaccuracy are interpreted as statistical errors of each measurement, as thermal drifts of the wavemeter and systematic effects depending on the calibration will differ for each measurement. Furthermore, the HFS structure can also be shifted by small deviations in the laser beam alignment, causing an inaccuracy of the angle between perpendicular laser beam and the direction of motion of the Tc atoms in the laser interaction volume. Based on recent results, this statistic error on the central frequency of a spectrum is estimated to be about 10 MHz.

An additional error can be caused by the chirp of the injection-locked laser system, as mentioned above. In general it can be approximated by a constant offset of the frequency and small linear variation over the duration of a laser pulse with respect to the initial frequency of the CW seed light. The latter is most likely one of the effects contributing to the slight asymmetry of the observed resonance peaks. The frequency offset will shift the entire HFS structure systematically. The chirp of the present laser setup was not characterized in earlier works and could also not be characterized in framework of the present work, due to the lag of the required technical instruments. A few studies of the chirp of comparable injection-locked Ti:sapphire laser systems can be found in literature [144, 125, 145], but the results cannot be transferred directly to the laser system used here. As a rough estimation, the frequency offset can be assumed to be smaller than ± 10 MHz for the present laser setup. However, the systematic offset is estimated to be equal for all investigated transitions, as a constant pump power was used for the injection-locked laser and the frequency range was similar for all three transitions and isotopes. Therefore, the resulting systematic effect on the isotope shifts can be neglected.

Considering the error sources discussed above and the observed scatter of the ground state parameters, a conservative error assumptions were determined which were added to the statistical errors from the fit routine of each individual measurement. The additionally assumed errors for $A(^6S_{5/2})$ are: $\Delta A_{97} = 200$ kHz, $\Delta A_{98} = 150$ kHz, and $\Delta A_{99} = 120$ kHz. For the upper states $^6P_{7/2,5/2,3/2}^o$ the corresponding error was assumed to be larger as the splitting stretched across a wider spectral region due to the larger values of A . As a consequence the doubled error values of $A(^6S_{5/2})$ were taken into account. For the B coupling constant the additional errors were assumed to be $\Delta B_{97} = 7$ MHz, $\Delta B_{98} = 10$ MHz, and $\Delta B_{99} = 3$ MHz. Table 5.12 summarizes the resulting values with final errors. The values of the $4d^5 5s^2 ^6S_{5/2}$ ground state determined in each transition were averaged, resulting in a higher accuracy. Table 5.13 lists the isotope shifts $\delta \nu$ of the transitions relative to the most common isotope ^{99}Tc . The isotope shifts are about 330 MHz, which is relatively small when compared to the total width of up to 30 GHz of the full HFS structure. They consistently show the same trend, with the shift of ^{98}Tc being 14-22 MHz larger than for ^{97}Tc . All values of the HFS and the isotope shifts agree well with the less precise results obtained at the MABU spectrometer (see section 5.2).

Table 5.12: Compilation of the final HFS coupling constants derived from the HFS spectra in the first excitation step using fits with using asymmetric Bi-Voigt profiles as explained in section 5.4.3. The literature values for ^{99}Tc were taken from [130]. It should be noted that the ground state splitting in [130] could not be resolved and a value for B was not given. See text for more details. All values are given in units of MHz.

Parameter	^{97}Tc	^{98}Tc	^{99}Tc	$^{99}\text{Tc}_{\text{lit}}$
$4d^5 5s^2 ^6S_{5/2}$				
A	-109.50(13)	-65.86(10)	-107.34(8)	-109.12(90)
B	1.9(44)	1.5(63)	0.3(20)	-
$4d^5 5s 5p ^6P_{7/2}^o$				
A	815.77(42)	490.96(32)	799.99(26)	798.6(36)
B	-59.2(75)	17.0(108)	-43.9(35)	-57(18)
$4d^5 5s 5p ^6P_{5/2}^o$				
A	911.32(45)	548.60(34)	894.08(28)	892.2(39)
B	71.3(81)	-9.4(112)	57.4(38)	93(18)
$4d^5 5s 5p ^6P_{3/2}^o$				
A	1207.19(42)	726.85(34)	1183.27(27)	1182.1(36)
B	-6.5(72)	-3.1(105)	-12.6(34)	-12(12)

Table 5.13: Compilation of the isotope shifts relative to ^{99}Tc . All values are given in units of MHz.

Parameter	^{97}Tc	^{98}Tc	^{99}Tc
$\delta \nu(^6S_{5/2} - ^6P_{7/2}^o)$	347(14)	369(14)	0
$\delta \nu(^6S_{5/2} - ^6P_{5/2}^o)$	313(14)	327(14)	0
$\delta \nu(^6S_{5/2} - ^6P_{3/2}^o)$	308(14)	324(14)	0

5.4.4 Determination of Nuclear Moments

As the HFS is based on the interaction between atomic shell and the nucleus itself, nuclear moments can be deduced from the HFS parameters as well as from the isotope shifts. As already mentioned in section 5.4.3, the nuclear spin of the isotope ^{98}Tc was not determined to date, but suggested to be $I_{98} = 6$. In the present work, the precise evaluation of the obtained spectra consistently confirm the value $I_{98} = 6$. Further nuclear moments will be derived in the following sections.

Nuclear Magnetic Dipole Moments

The hyperfine coupling constant A describes the coupling of the atomic shell to the magnetic dipole moment μ_I of the nucleus (see formula 2.14). Theoretical calculations of the magnetic field of the electrons at the position of the nucleus $B_J(0)$ require complex numerical models and are typically relatively inaccurate. A more suitable approach to derive precise values for μ_I is the usage of a precisely known dipole moment of one isotope as reference $\mu_{I,\text{ref}}$. These are typically determined by other experimental techniques, such as *nuclear magnetic resonance* (NMR). The dipole moment of another isotope can then be calculated using the measured coupling constant A and formula

$$\frac{A}{A_{\text{ref}}} = \frac{I_{\text{ref}}}{I} \frac{\mu_I}{\mu_{I,\text{ref}}} \Rightarrow \mu_I = \mu_{I,\text{ref}} \frac{A \cdot I}{A_{\text{ref}} \cdot I_{\text{ref}}} \quad (5.4)$$

In the present work, the magnetic dipole moment of ^{99}Tc is used as reference. It was measured to be $\mu_{I,99} = 5.6847(4)$ in units of the nuclear magneton μ_N by Walchli et al. using NMR [146, 147].

Formula 5.4 neglects any form of HFS anomaly, like the Bohr-Weisskopf effect, which describes the change of the shell nucleus interaction due to the distribution of magnetization inside the nucleus. Another, weaker effect is the Breit-Rosenthal effect, which accounts for the charge distribution in the nucleus. Therefore, an additional 1% uncertainty was assumed as conservative error estimation, since these effect typically cause changes well below that value in the region of $Z = 43$. The dipole moment was calculated using the precisely determined A coupling constant of the ground state. The resulting dipole moments are listed in table 5.14. It should be highlighted, that these values represent the very first determination of the nuclear magnetic dipole moments for the isotopes ^{97}Tc and ^{98}Tc .

Table 5.14: Nuclear magnetic dipole moments of Tc. Literature values are taken from [147] and marked with *. The magnetic moment of ^{99}Tc was used as reference to calculate the experimental values for $^{97,98}\text{Tc}$.

Isotope	I	μ_I [μ_N]
99	9/2	5.6847(4)*
98	6	4.651(55)
97	9/2	5.799(66)
96	7	5.09(5)*
95	9/2	5.94(6)*
94	7	5.12(5)*
93	9/2	6.32(6)*
92m	11	8.9(3)*

The nuclear spin of other isotopes of Tc with mass number $A \leq 96$ were measured in the past, mostly by NMR experiments [147]. All known values for Tc are summarized in figure 5.53a. The experimental values for ^{97}Tc and ^{98}Tc from the present work fit well to the trend of the magnetic moments from literature. For the odd-neutron numbered isotopes, ^{98}Tc represents a change in the nuclear angular momentum from $7+$ to $6+$, which also affects the magnetic dipole moment. The corresponding evolution of the nuclear g-factor is shown in figure 5.53b.

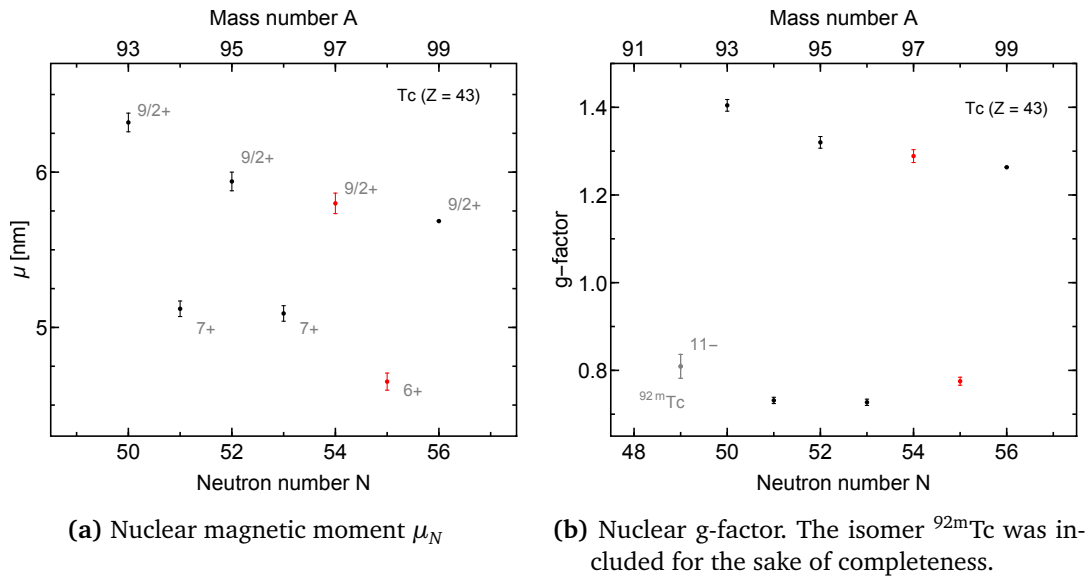


Figure 5.53: Evolution of the nuclear magnetic moment and the nuclear g-factor in the isotopic chain of Tc. The total nuclear angular momentum I is indicated in gray.

Nuclear Electric Quadrupole Moments

The hyperfine coupling constant B is linked to the spectroscopic electric quadrupole moment Q_s of the nucleus, which describes the deviation of the nucleus's shape from a simple sphere. Formula 2.16 shows the linear dependence $B \propto Q_s$. Similar to the determination of μ_I with the help of A , the electric quadrupole moments of ^{97}Tc and ^{98}Tc can be calculated using the relation

$$Q_s = Q_{s,\text{ref}} \frac{B}{B_{\text{ref}}}, \quad (5.5)$$

using the value of ^{99}Tc as reference, as the quadrupole moment is not known for any other Tc isotope. For ^{99}Tc , an spectroscopic electric quadrupole moment of $-0.129(6)$ b was determined for the nuclear ground state of ^{99}Tc [148]. This value disagrees with positive values found in [130, 149], but was confirmed by *ab initio* calculations in [150]. Due to their larger size, resulting in significantly better relative accuracy, only the B coupling constants of the upper atomic states ${}^6P_{7/2,5/2}^0$ were used to calculate Q_s . The averaged results for each isotope are listed in table 5.15. The relatively large error of the B coupling constant lead to similar large errors of the quadrupole moment, particularly for ^{98}Tc which features a low B .

The similarity of B for ^{97}Tc and ^{99}Tc , is also reflected in the corresponding values of Q_s , which indicates a similar oblate deformation of the nucleus. In contrast, the odd-neutron numbered ^{98}Tc shows a small positive value of Q_s , which corresponds to a small prolate deformation but is also in acceptable agreement with a spherical shape of the nucleus.

Table 5.15: Spectroscopic nuclear electric quadrupole moments for $^{97,98,99}\text{Tc}$. The literature value for ^{99}Tc was used as reference to calculate the values for $^{97,98}\text{Tc}$.

Isotope	I	Q_s [b]
99	9/2	-0.129(6)
98	6	+0.036(24)
97	9/2	-0.167(20)

Ratio of the Field Shift

The isotope shift $\delta \nu_{A,A'}$ is related to the difference of the mean square charge radius of two nuclei $\delta \langle r^2 \rangle_{A,A'}$, as described by formula 2.22. The normal mass shift component can be calculated using $K_{NMS} = \nu m_e$. Consequently, when the isotope shift $\delta \nu_{A,A'}$ is measured, absolute values for K_{SMS} and F_{FS} are required to extract the change in nuclear mean square charge radius $\delta \langle r^2 \rangle_{A,A'}$. Typically, this requires extensive theoretical numerical computation. Unfortunately, these values are presently not available, which hinders the extraction of $\delta \langle r^2 \rangle_{A,A'}$.

However, as the isotope shifts of three different transitions are available, relative information can be extracted by using the King plot method [151]. By multiplying equation 2.22 with the modification factor

$$\mu_{A,A'} = \frac{m_A m_{A'}}{m_A - m_{A'}} \quad , \quad (5.6)$$

a modified field shift $\mu_{A,A'} \delta \nu_{A,A'}$ is obtained. This can be plotted against the corresponding modified shift of another transition, as shown in the graphs 5.54, This is typically referred to as a *King plot*. The points resulting from transitions i and j yield a line, defined by

$$\mu_{A,A'} \delta \nu_{A,A'}^i = \frac{F^i}{F^j} \cdot \mu_{A,A'} \delta \nu_{A,A'}^j + \left(K^i - \frac{F^i}{F^j} K^j \right) \quad . \quad (5.7)$$

The ratio of the field shifts F^i/F^j is given by the slope of the line, while its y-coordinate of the y-intercept is defined by the difference in mass shifts. The field shift ratio is expected to be close to 1 as all three transitions start from the ground state and lead to different J components of the ${}^6P^o$ triplet in which the electrons experience a similar interaction with the electric field in the nucleus, relatively independent of J .

A linear function, fitted on only two points, will always cross these points perfectly, annihilating a reasonable error estimate from the fitting procedure. Therefore, additional fits were performed, using the outer borders defined by the errors of the data points. These fits give upper and lower limits for the fit parameter, which can be used to estimate conservative errors. The resulting ratios of the field shifts are $F^{426}/F^{430} = 0.87(11)$, $F^{424}/F^{430} = 0.87(11)$, and correspondingly $F^{424}/F^{426} = 0.99(12)$, which is in good agreement with the initial expectation of 1. The respective y-axis intercept are -6 GHz u, -27 GHz u, and -21 GHz u. The coarse method for the estimation of the uncertainty results in relatively large errors for the y-axis intercept of about 200 GHz u. As a consequence, all values are in agreement with zero, which matches the expectation of K being similar for all three transitions.

In order to obtain theoretical input for the mass shift and field shift, contact to the theoretical atomic physics group around Prof. Dr. Stephan Fritzsche at the Friedrich Schiller University Jena has been established. The very first results from the calculations look promising and allow a preliminary determination of the change in the mean square charge radii $\delta \langle r^2 \rangle$ of the studied Tc isotopes as depicted in figure 5.55 [152]. The data of Tc shows kink at ^{98}Tc at neutron number $N = 55$, a trend which is also observed in molybdenum ($Z =$

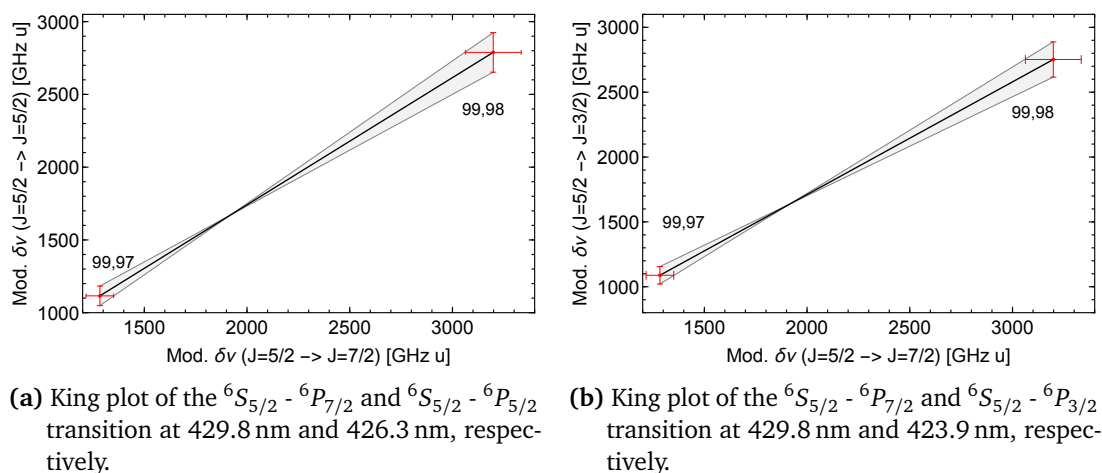


Figure 5.54: King plots for the investigated ground state transitions in Tc

42), but is significantly less pronounced in ruthetium ($Z = 44$). This localized phenomenon hints at a potential change of the neutron configuration, which would be in agreement with the different nuclear spin of ${}^{98}\text{Tc}$ compared to other odd neutron number isotopes and the observed nuclear g -factor. A detailed evaluation of experimental and theoretical data is currently in preparation and will be presented in a forthcoming publication.

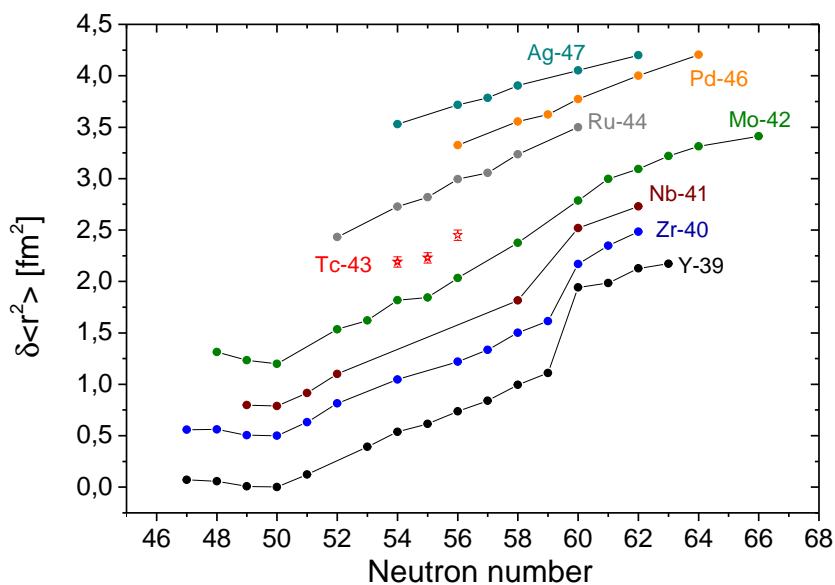


Figure 5.55: Evolution of the change in nuclear mean square charge radii in the Tc region. Reference data was taken from [153]. Theoretical calculations for mass shift and field shift were performed by [152].

CONCLUSION AND OUTLOOK

This work addressed a number of optimizations, refinements and developments which improved the performance of resonance ionization mass spectrometry experiments significantly. More precisely, two of the most important experimental aspects, the efficiency and the spectral resolution, were increased. These enhancements pave the way for future experiments, contributing to a better understanding of the structure of atoms and nuclei. Developments presented here include the identification of new ionization schemes via extensive studies of atomic level structures as well as the design of new instruments to provide narrow linewidth laser radiation and to reduce the limiting Doppler broadening significantly. The performance was demonstrated in various experiments, yielding outstanding efficiencies on palladium and excellent spectral resolution in the hyperfine spectra of technetium.

The first part of this thesis described the development of new highly efficient resonance ionization schemes in Pd. Various 2-, 3-, and 4-step excitation ladders suitable for Ti:sapphire laser systems were identified and compared with regard to maximum ionization efficiency. In order to identify the most efficient ionization step, the energetically high-lying region between the ionic ground state Pd II ($4d^9 2D_{5/2}$), representing the first ionization potential, and the higher lying ionic fine structure level Pd II ($4d^9 2D_{3/2}$) was systematically studied. Here, several autoionizing Rydberg series converging towards the $4d^9 2D_{3/2}$ state were observed. Applying an advanced graphical analysis method to the spectra obtained, the series limit as well as the ionization potential were precisely determined. The resulting value of $E_{IP} = 67241.23(9)_{\text{sys}}(5)_{\text{stat}} \text{ cm}^{-1}$ is in very good agreement with the literature value of $67241.3(8) \text{ cm}^{-1}$ but significantly more accurate [98]. The overall efficiency was carefully quantified for different ionization schemes using two independent mass separators and laser setups at Mainz University and Oak Ridge National Laboratory. Excellent values of 54.3(14)% and 59.7(21)% were obtained using the 3-step ionization scheme of choice. These values clearly exceed the typical efficiencies of 10-40% and are presently the highest efficiencies reported for laser ion sources. A summary of the efficiency study was published in J. Phys. B [4].

The developed highly efficient 3-step ionization scheme, which is suitable for Ti:sapphire laser systems as presently used at the majority of on-line RIB facilities worldwide, will enable the pure and selective production of exotic Pd ion beams as requested by the nuclear physics community. In the future, high-precision experiment on the neutron-rich isotopes far off stability will provide valuable information for nuclear physics, yielding a more conclusive picture of the formation of the heavy elements of the periodic table in the most extreme environments of the universe.

The enhancement of the spectral resolution was addressed in the second part of the present thesis. The spectral linewidth of the resonances observed in the atomic spectra

is defined by two aspects, the spectral laser linewidth and the absorption linewidth of the probed atoms. A new laser design was developed in order to address the first aspect, providing pulsed high power laser radiation with smallest linewidth. To achieve the essential laser operation on a single longitudinal cavity mode, a ring cavity was equipped with a Lyot filter, a thin etalon, and a air-spaced etalon to obtain the required frequency selection. The design of the laser cavity was systematically optimized using the ray transfer matrix formalism. An effective laser linewidth of about 45 MHz FWHM was measured using a scanning FPI. This was confirmed by spectroscopy of the hyperfine structure in Cu at the MABU spectrometer with experimental linewidths of 150(3) MHz FWHM, as published in Phys. Rev. A [127]. In a next step, the laser was used for high-resolution spectroscopy in technetium, yielding experimental linewidths of 230 MHz. The well resolved HFS spectra allowed determination of the HFS coupling constants for various atomic states as well as the isotope shift. The information obtained confirmed the excellent suitability of the ionization scheme for the ultra trace analysis project performed at the institute of nuclear chemistry. A summary of the findings will be published in a recently submitted article.

Next development steps will focus on the design of an automated electronic stabilization system for the single mode operation and laser frequency. Furthermore, several concepts will be tested in order to reduce the losses in the laser cavity caused by the air-spaced etalon. This will improve the overall laser stability and performance while allowing access to a broader wavelength region of about 700-950 nm. The final step will be the design and construction of a dedicated laser cavity, incorporating all the upgrades.

The second technical development presented in this work addressed the reduction of the absorption linewidth by a nearly complete suppression of the dominant Doppler broadening. This was achieved by adapting the existing LIST laser ion source unit in order to enable a perpendicular orientation of the probing laser beam and the directed atomic beam effusing from the heated ion source. As a result, the new device, named PI-LIST, enables access to smallest linewidths while providing the benefits of the standard LIST, a quadrupole ion guide for transversal confinement and proper shielding from the strong electric extraction field, thus offering a perfect environment for high-resolution laser spectroscopy and the production of highly pure ion beams. The commissioning and first tests proved the easy and seamless integration in the existing RISIKO setup and confirmed a low loss of ionization efficiency in comparison to conventional LIST operation. Systematic characterizations were carried out to find the optimum operation settings and provide essential information on the shape of the atomic beam, which agree with earlier observations [44].

Outstanding experimental linewidths of less than 100 MHz FWHM with exceptional signal-to-noise ratio were demonstrated at smallest radioactive samples down to 10^{11} atoms. The implementation of a second repeller electrode allowed the complete suppression of negative species from the hot ion source, resulting in a very low background of well below 1 s^{-1} , while peak count rates above 1000 s^{-1} were obtained on resonance. These specifications pose a huge step towards highly resolved resonance ionization spectroscopy on rarest samples. An additional important aspect in this context is the associated efficiency which could be estimated to be about 0.001 % during high-resolution operation. As a result of this performance, precise high-resolution HFS spectroscopy on sample sizes down to 10^9 atoms are feasible. This extends the field of RIS applications significantly and facilitates sensitive spectroscopy on rarest species, like trace elements or radioactive isotopes with lifetimes in the order of days or longer, which can be handled in the off-line laboratory of the LARISSA working group. The technical aspects of the current status of the PI-LIST as well as a summary of its performance will be published in a recently submitted article.

Using the newly developed PI-LIST, the HFS in technetium was successfully studied for three different isotopes, $^{97,98,99}\text{Tc}$, using a single mode injection-locked Ti:sapphire laser

system in perpendicular ionization geometry and samples of 10^{11} - 10^{13} atoms. This marks a new level of resolution in the element Tc and represents the very first investigation of the HFS in the isotopes ^{97}Tc and ^{98}Tc . The HFS spectra obtained were well resolved and exhibited an excellent signal-to-noise ratio, allowing the precise measurement of the HFS coupling constants and isotope shifts. Using the HFS coupling constants A and B , the nuclear magnetic dipole moments μ_I and the nuclear electric quadrupole moments Q_s were determined for the first time for ^{97}Tc and ^{98}Tc . In addition, the formerly unconfirmed nuclear spin of ^{98}Tc was determined to be $I_{98} = 6$. Contact to the theoretical atomic physics group around Prof. Dr. Stephan Fritzsche at the Friedrich Schiller University Jena has been established in order to obtain theoretical values for nuclear parameters, thus enabling the evaluation of theoretical models and the extraction of additional nuclear information from the atomic spectra. Very first results from the calculations look promising. The experimental results and the theoretical findings will be presented in a forthcoming publication.

The outstanding performance of the PI-LIST facilitated the realization of various high-resolution spectroscopy experiments within the last year. One highlight is the extensive study of the HFS in the rare radioactive ^{227}Ac . The hyperfine splitting in six transitions were investigated, demonstrating experimental linewidths of about 120 MHz FWHM. The well resolved spectra allowed the precise determination of the A and B coupling constants and the correct identification of the angular momenta J which were incorrectly documented for some states in literature. With small sample sizes of only $2 \cdot 10^{11}$ atoms per sample, sufficient signal rates were achieved, even if the ionization scheme involved weak transitions or started from a weakly thermally populated state. Further experiments were conducted on stable as well as radioactive Ho and several more spectroscopic measurements are scheduled in the near future. One key experiment is the study of an atomic transition in the fundamental frequency range of the Ti:sapphire laser. This avoids spectral broadening by frequency-doubling of the laser radiation and reduces the absolute Doppler broadening of the probed transition significantly. Based on the information about the linewidth contributions gathered in the present work, the final experimental linewidth for a suitable transition (e.g. 814 nm in uranium) can be estimated to reach down to about 55 MHz. This is comparable to well-known high-resolution collinear spectroscopy setups like COLLAPS or CRIS at ISOLDE. In addition to atomic spectroscopy, the PI-LIST seems also well suited for resonance ionization based ultra trace analysis applications, as it allows precise excitation of specific isotopes or isomers and offers an excellent low background.

Future and ongoing developments focus on improvements of the efficiency and further modifications of the PI-LIST. A higher ionization efficiency could be achieved by improving the angular distribution in the atomic beam via optimization of the shape and exit of the ionizer tube. Some improvements of the PI-LIST itself were already tested, like the reduction of the length to about 5 cm, which was successfully used in an experiment on ^{227}Ac and showed no drawbacks. A currently ongoing development, aims for the future implementation at the on-line ion source at ISOLDE to access a vast range of short-lived isotopes. Due to technical constraints at the ISOLDE ion source and the heavy radiation at the target area preventing the use of a laser entrance window, a longitudinal incoupling of the spectroscopy laser beam with subsequent deflection into perpendicular orientation inside the PI-LIST was implemented. A 3D computer model of the device is shown in figure C.1. The concept was investigated and tested at the RISIKO separator in the framework of a diploma thesis [154]. The findings showed comparable spectral resolution and confirmed an easy alignment of the laser beams through the PI-LIST. The implementation directly at the ISOLDE ion source will enable high-resolution spectroscopy on the most exotic nuclei and in addition will allow the production of isotopically and isomerically purest ion beams, essentially contributing towards a more comprehensive knowledge in atomic and nuclear physics.

IONIZATION SCHEME DEVELOPMENT IN Pd

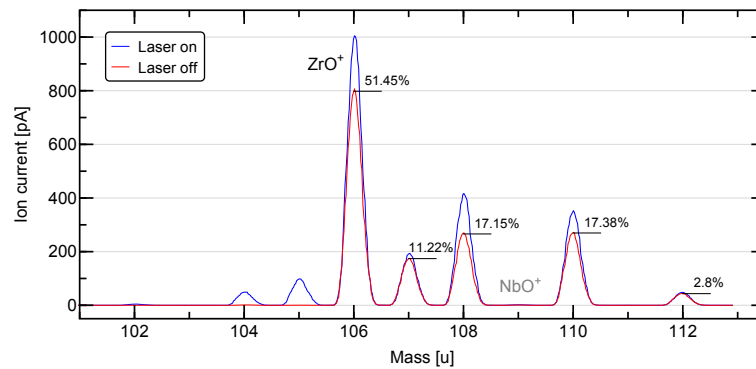


Figure A.1: Linearly plotted mass spectrum of the Pd region at the RISIKO mass separator when using Zr foil in the sample. A strong background due to surface ionized (red) ZrO is clearly visible. The black markers indicate the isotopic abundance of natural ZrO, taking into account the dominant presence of the ^{16}O isotope which has a natural abundance of 99.8% [95]. These expected ratios are in excellent agreement with the experimentally observed ratios.

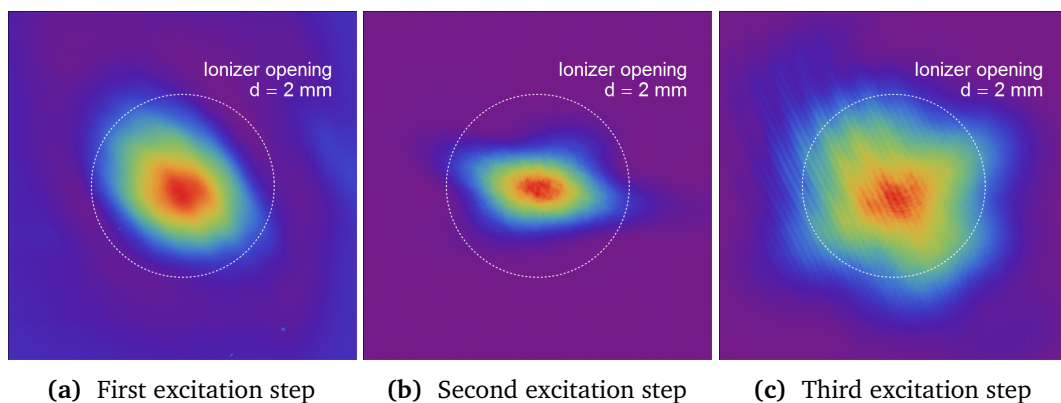
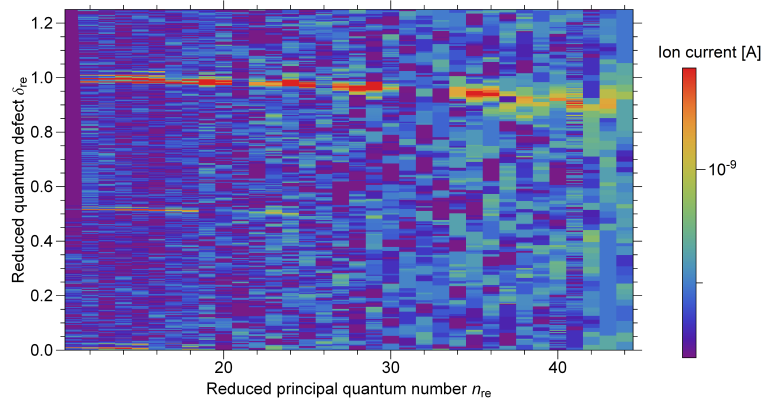
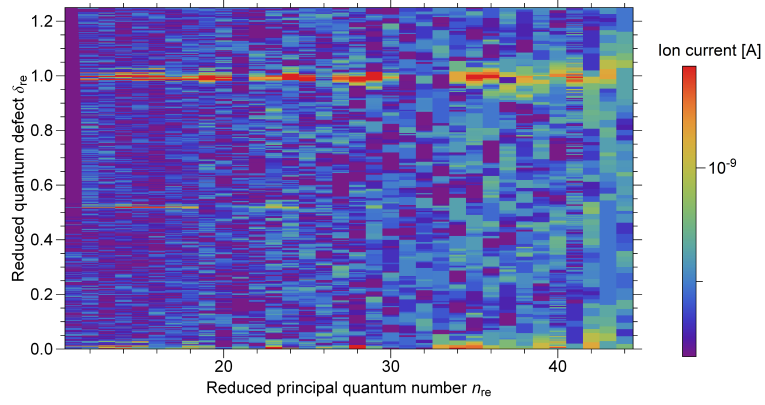


Figure A.2: Spatial profiles of the laser beams in the ion source as used during the Pd efficiency measurements with the 3-step ionization scheme. The profiles were taken in the reference beam path and show the shape of the laser beam when entering the ionizer tube, whose size is illustrated as reference in the graphs. Each graphs represents an area of $3.8 \times 3.8 \text{ cm}^2$.

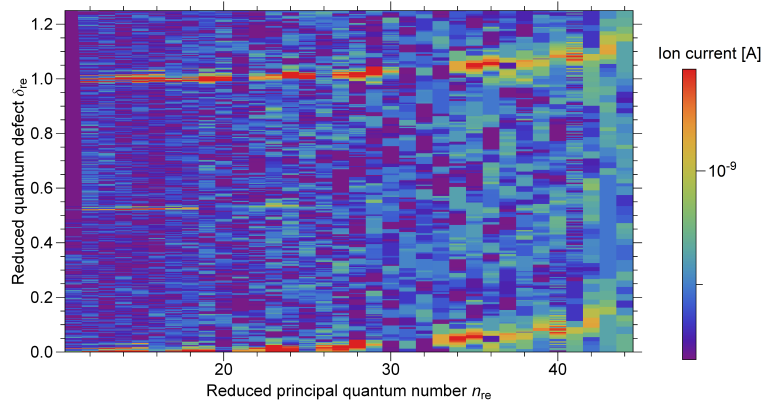
Rydberg Series Analysis in Pd



(a) $E_{\text{lim}} = 70780.20 \text{ cm}^{-1}$

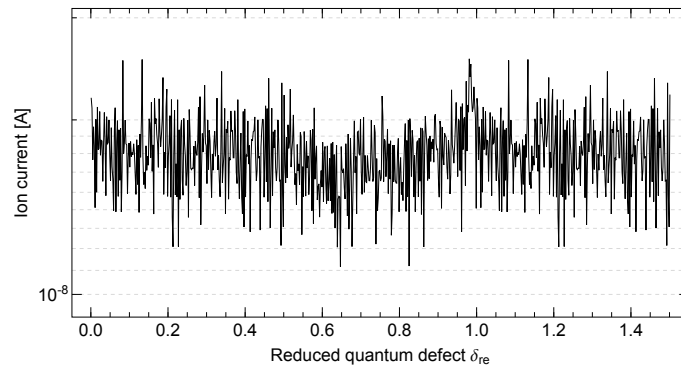


(b) $E_{\text{lim}} = 70780.50 \text{ cm}^{-1}$

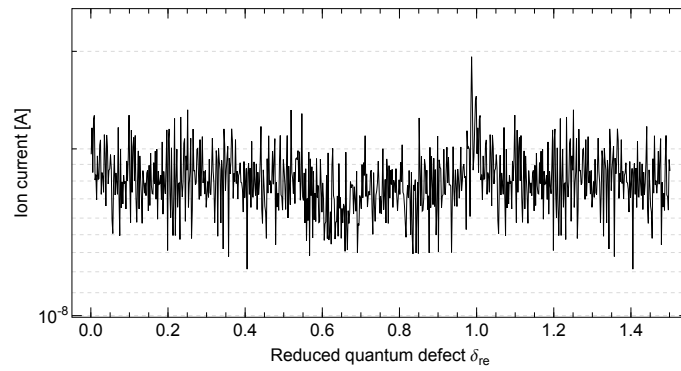


(c) $E_{\text{lim}} = 70780.80 \text{ cm}^{-1}$

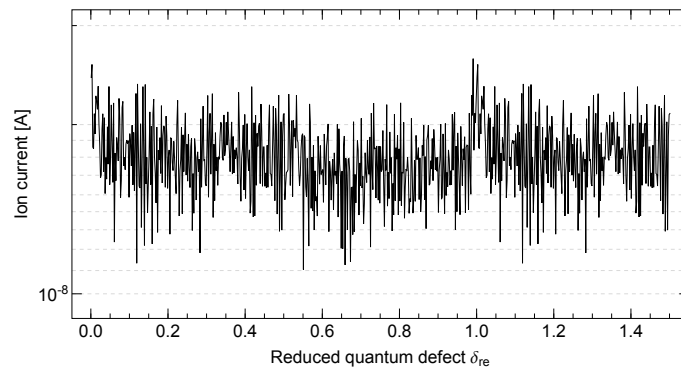
Figure A.3: Color-coded 2-dimensional visualization of the spectra obtained with frequency scans starting from the state $4d^9(^2D_{3/2})6p^2[3/2]_2$ at $58415.541 \text{ cm}^{-1}$. The three graphs show different settings for E_{lim} . See text for more details.



(a) $E_{\text{lim}} = 70780.20 \text{ cm}^{-1}$



(b) $E_{\text{lim}} = 70780.50 \text{ cm}^{-1}$



(c) $E_{\text{lim}} = 70780.80 \text{ cm}^{-1}$

Figure A.4: Projection of the data shown in the 2D-plots in figure A.3 onto the δ^* -axis. The three graphs show different settings for E_{lim} . The asymmetry of the peak from the Rydberg series can be used to evaluate the straightness of the series in the corresponding 2D-plots. See text for more details.

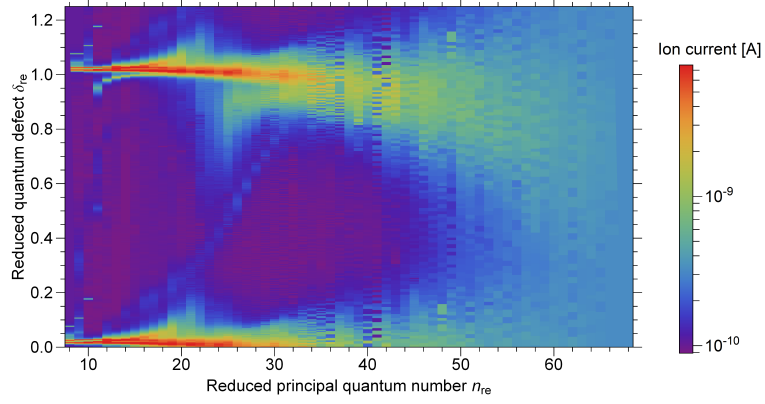
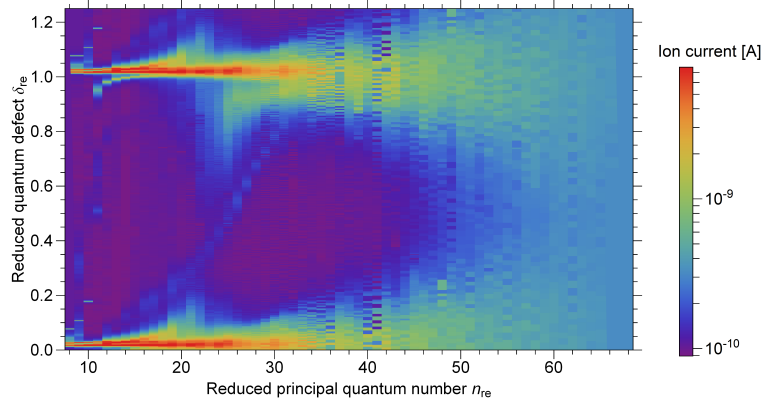
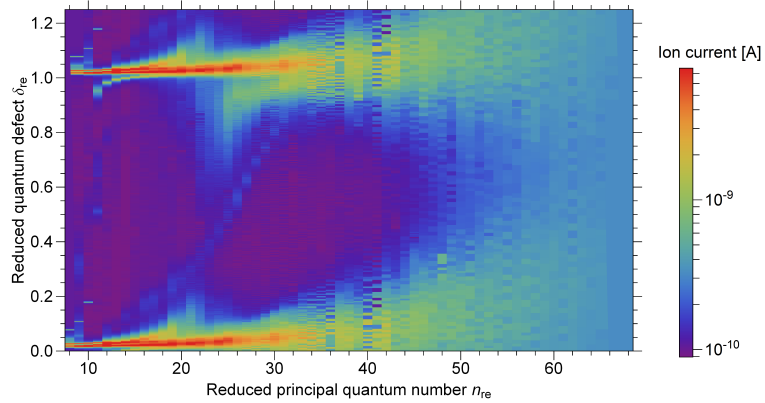
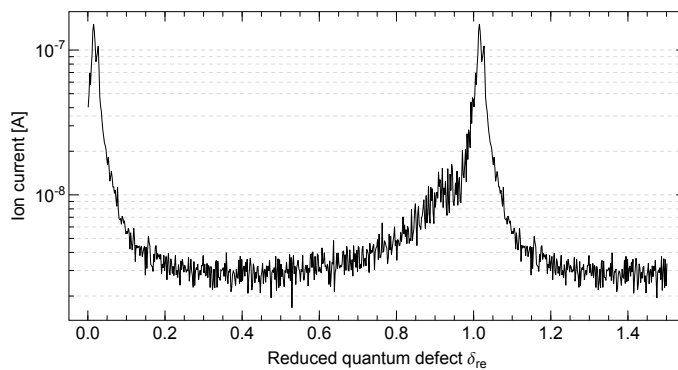
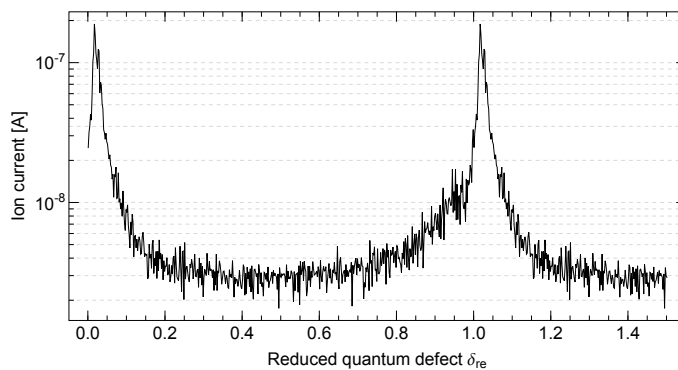
(a) $E_{lim} = 70780.28 \text{ cm}^{-1}$ (b) $E_{lim} = 70780.48 \text{ cm}^{-1}$ (c) $E_{lim} = 70780.68 \text{ cm}^{-1}$

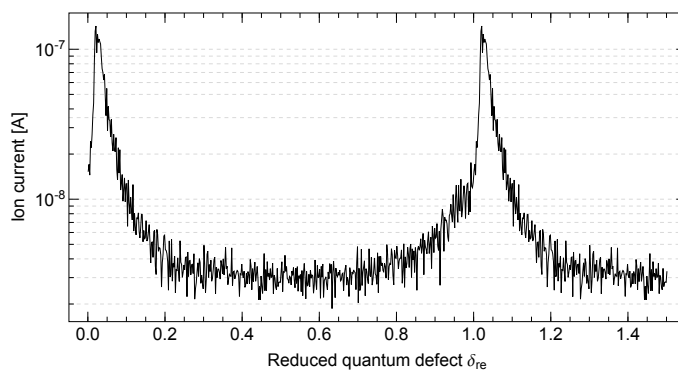
Figure A.5: Color-coded 2-dimensional visualization of the spectra obtained with frequency scans starting from the state $4d^9(^2D_{3/2})5d^2[5/2]_2$ at $58448.705 \text{ cm}^{-1}$. The three graphs show different settings for E_{lim} . See text for more details.



(a) $E_{\text{lim}} = 70780.28 \text{ cm}^{-1}$



(b) $E_{\text{lim}} = 70780.48 \text{ cm}^{-1}$



(c) $E_{\text{lim}} = 70780.68 \text{ cm}^{-1}$

Figure A.6: Projection of the data shown in the 2D-plots in figure A.5 onto the δ^* -axis. The three graphs show different settings for E_{lim} . The asymmetry of the peak from the Rydberg series can be used to evaluate the straightness of the series in the corresponding 2D-plots. See text for more details.

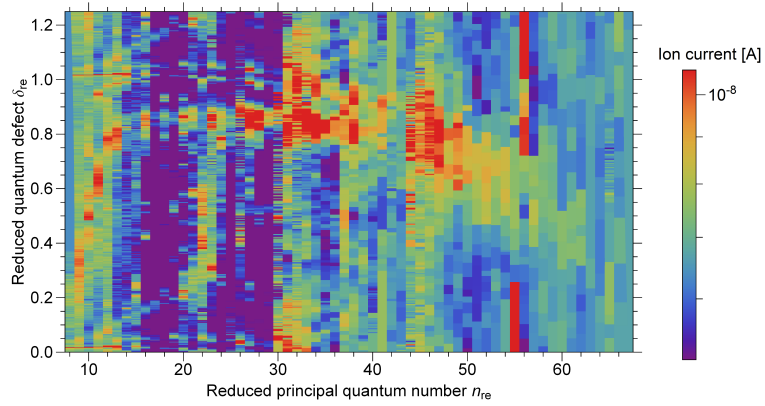
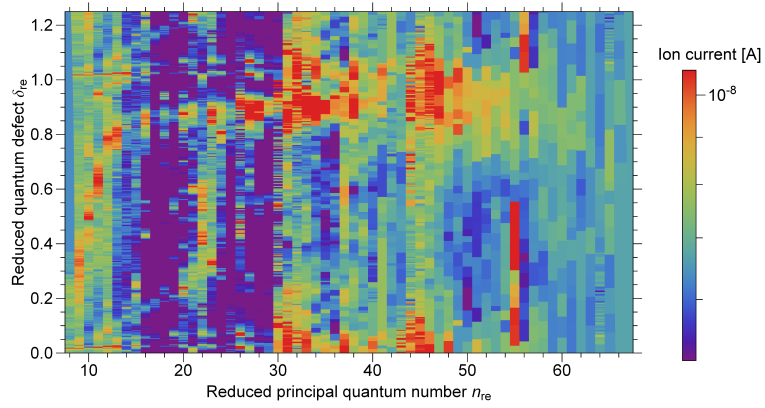
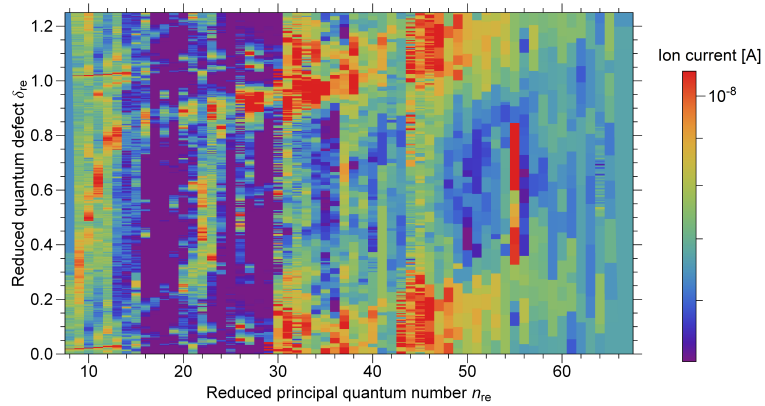
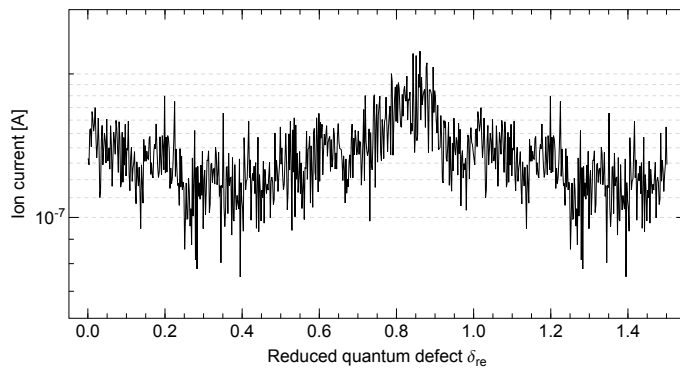
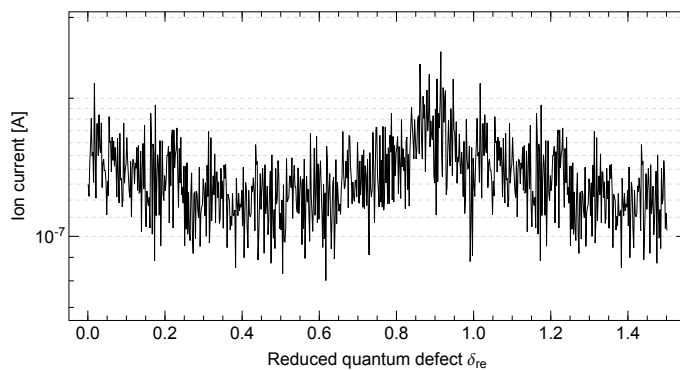
(a) $E_{\text{lim}} = 70780.00 \text{ cm}^{-1}$ (b) $E_{\text{lim}} = 70780.40 \text{ cm}^{-1}$ (c) $E_{\text{lim}} = 70780.80 \text{ cm}^{-1}$

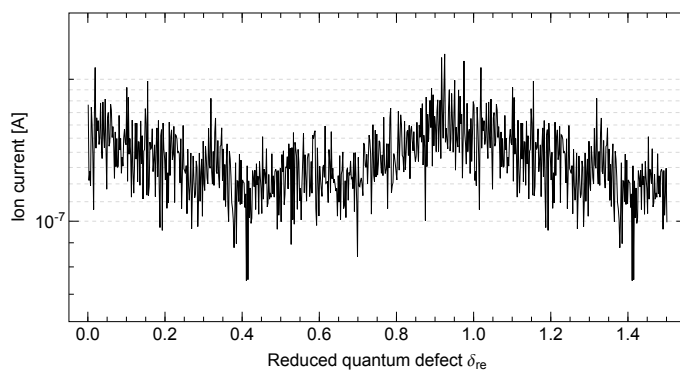
Figure A.7: Color-coded 2-dimensional visualization of the spectra obtained with frequency scans starting from the state $4d^9(^2D_{5/2})7s^2[5/2]_2$ at $58138.648 \text{ cm}^{-1}$. The three graphs show different settings for E_{lim} . See text for more details.



(a) $E_{\text{lim}} = 70780.00 \text{ cm}^{-1}$



(b) $E_{\text{lim}} = 70780.40 \text{ cm}^{-1}$



(c) $E_{\text{lim}} = 70780.80 \text{ cm}^{-1}$

Figure A.8: Projection of the data shown in the 2D-plots in figure A.7 onto the δ^* -axis. The three graphs show different settings for E_{lim} . The asymmetry of the peak from the Rydberg series can be used to evaluate the straightness of the series in the corresponding 2D-plots. See text for more details.

Efficiency Measurements in Pd

The graphs visualize the courses of efficiency measurements on Pd. The upper graphs show the ion current in green and the underlying laser-independent background in red. Gray sections indicate ion current which was not taken into account for the determination of the overall efficiency.

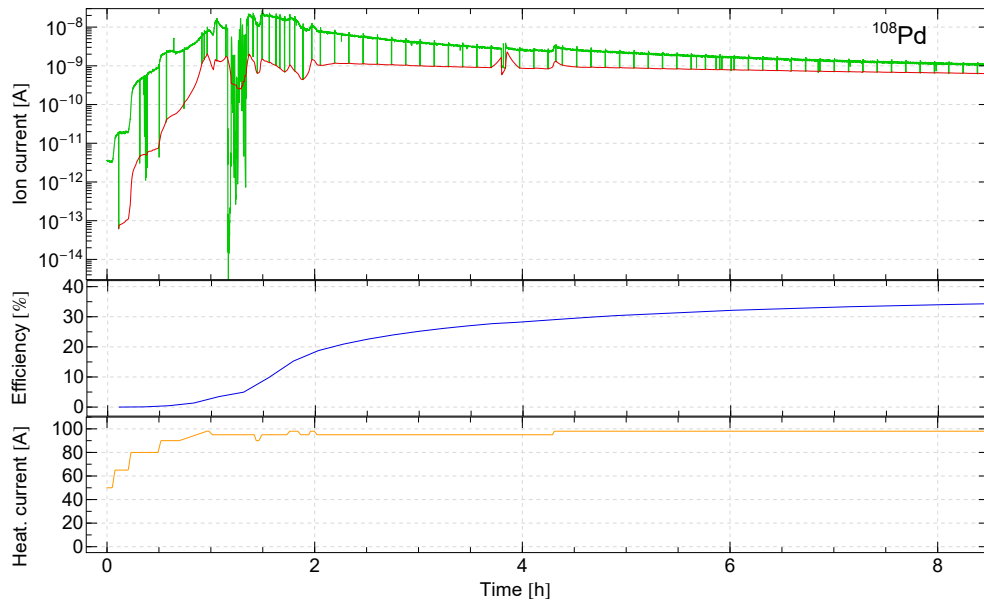


Figure A.9: Measurement # 7 RISIKO separator, 3-step ionization scheme, Efficiency: 36.1(18)%. A strong laser-independent background is caused by surface ionized ZrO.

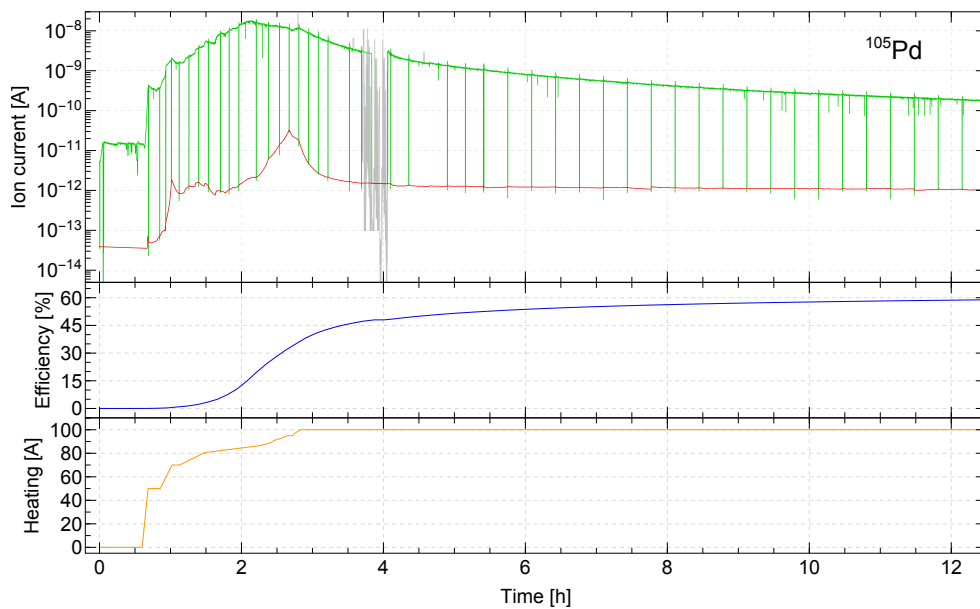


Figure A.10: Pd efficiency measurement # 14 at the RISIKO separator, 3-step ionization scheme, Efficiency: 60.1(30)%.

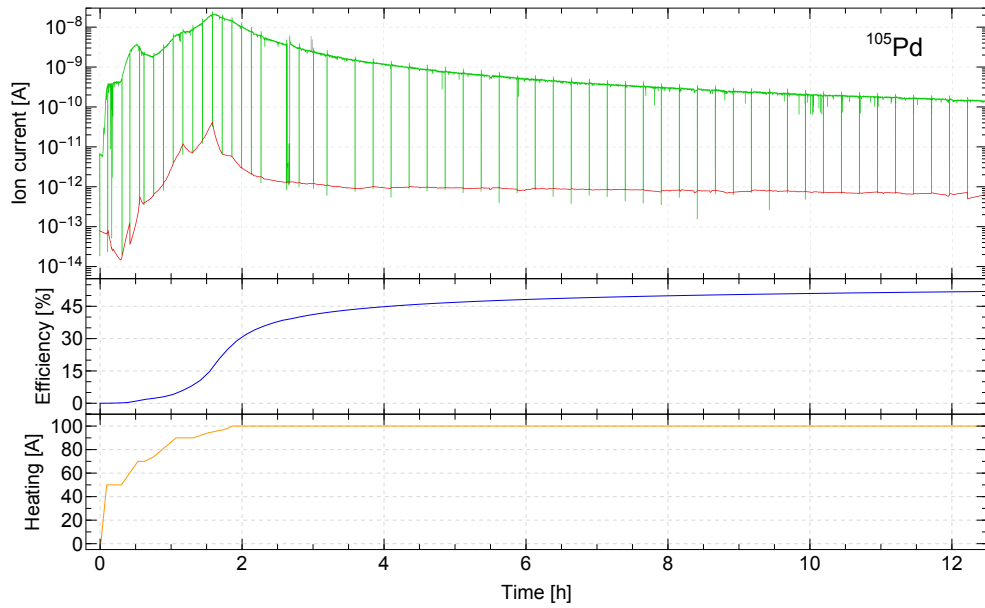


Figure A.11: Pd efficiency measurement # 15 at the RISIKO separator, 3-step ionization scheme, Efficiency: 52.6(26) %.

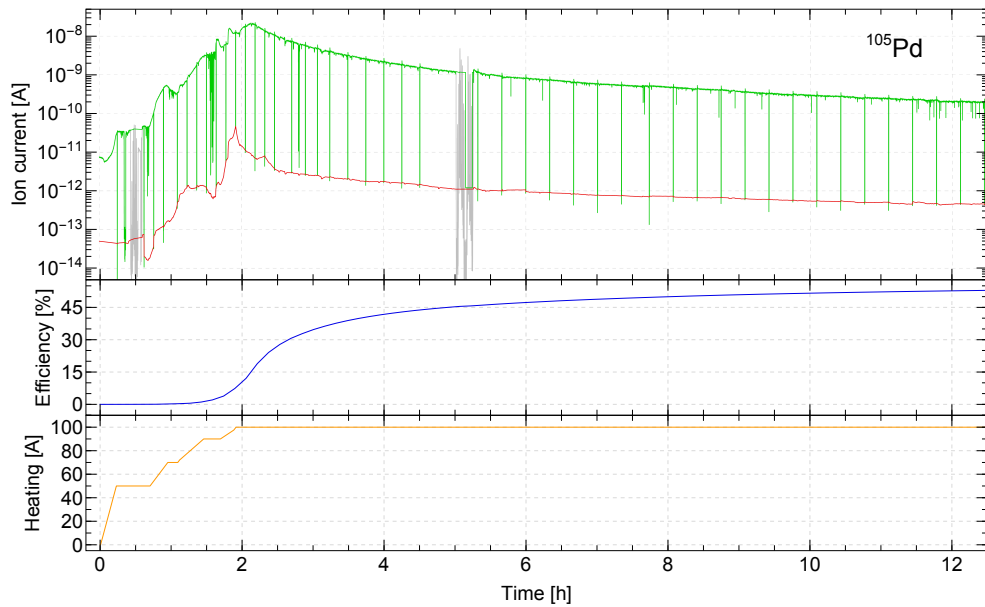


Figure A.12: Pd efficiency measurement # 16 at the RISIKO separator, 3-step ionization scheme, Efficiency: 54.8(27) %.

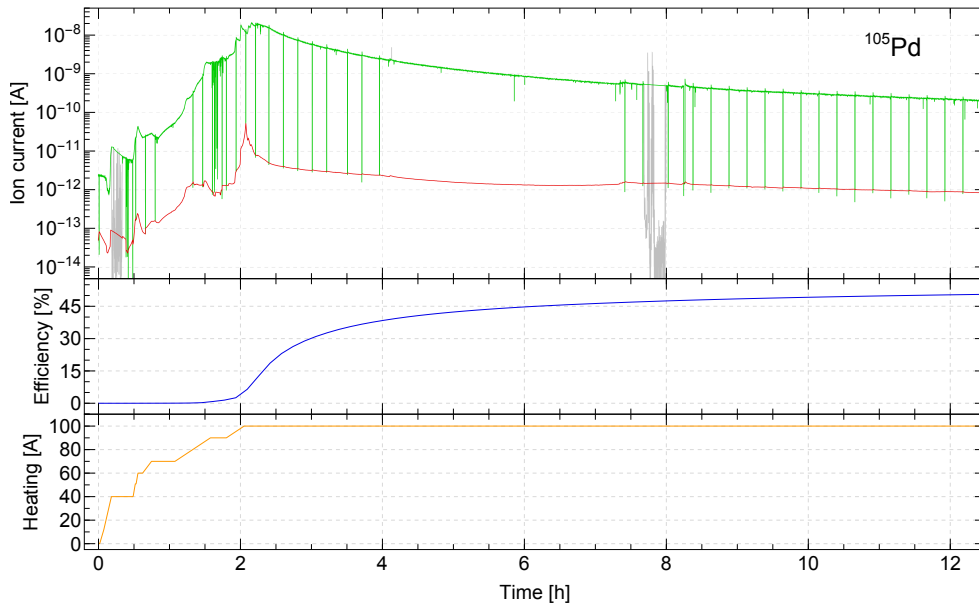


Figure A.13: Pd efficiency measurement # 17 at the RISIKO separator, 3-step ionization scheme, Efficiency: 52.6(26) %.

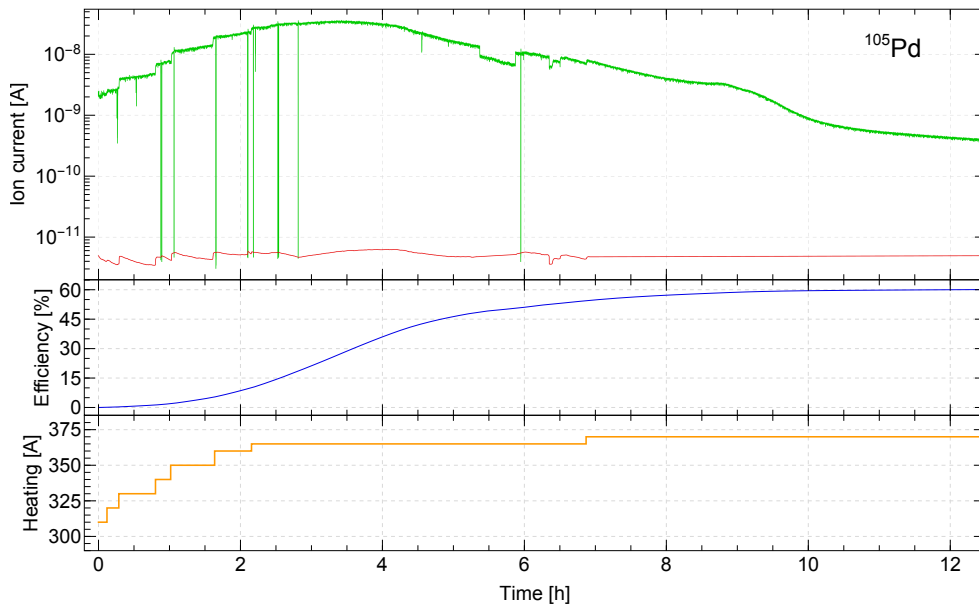


Figure A.14: Pd efficiency measurement # 4 at the IRIS2 separator: 3-step ionization scheme, Efficiency: 59.3(30) %.

HFS SPECTROSCOPY IN Tc AT THE MABU SPECTROMETER

First Excitation Steps

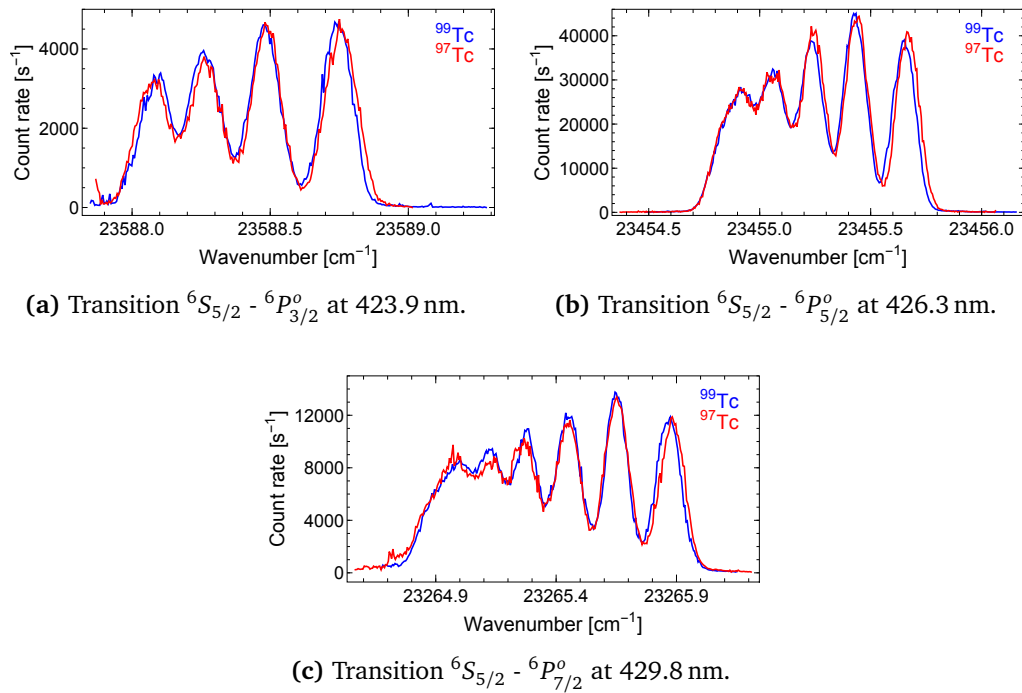
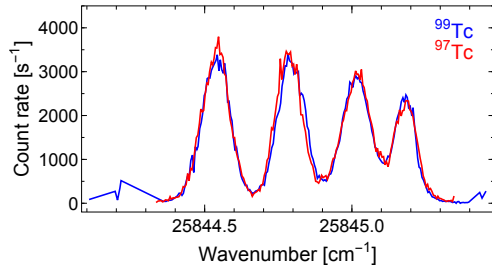
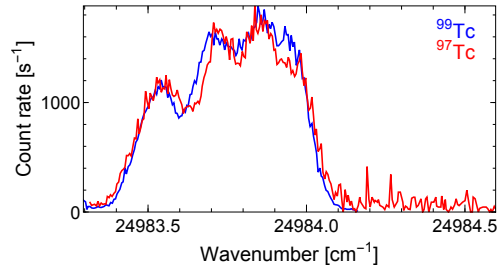


Figure B.1: Frequency scans of the first step transitions in both isotopes, ${}^{97}\text{Tc}$ and ${}^{98}\text{Tc}$.

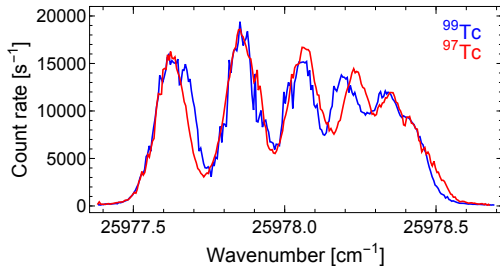
Second Excitation Steps



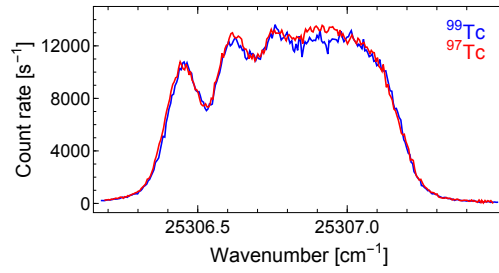
(a) Transition ${}^6P_{3/2}^o - {}^6P_{5/2}$ at 400.3 nm.



(b) Transition ${}^6P_{3/2}^o - {}^6P_{3/2}$ at 386.9 nm.



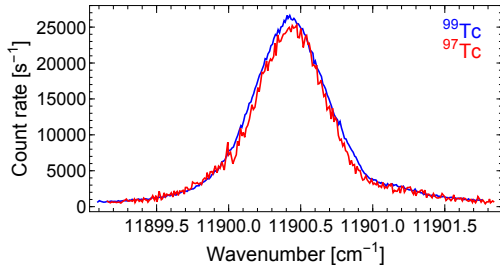
(c) Transition ${}^6P_{5/2}^o - {}^6P_{3/2}$ at 384.9 nm.



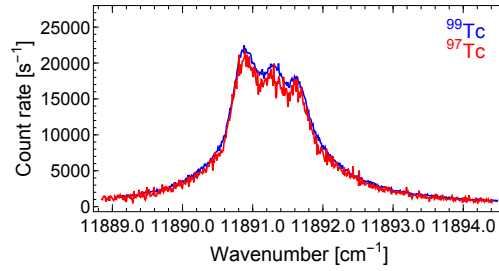
(d) Transition ${}^6P_{7/2}^o - {}^6P_{5/2}$ at 395.2 nm.

Figure B.2: Frequency scans of the second step transitions in both isotopes, ${}^{97}\text{Tc}$ and ${}^{98}\text{Tc}$.

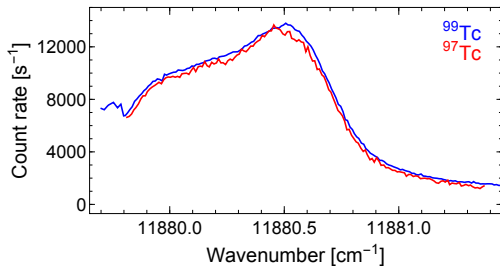
Third Excitation Steps



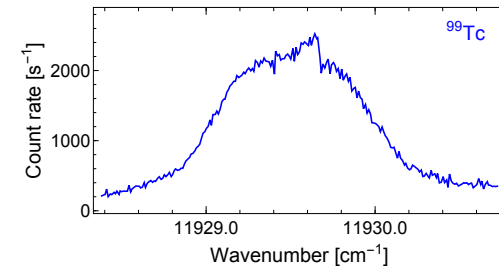
(a) Transition from the ${}^6P_{3/2}$ state to an AI state at 840.3 nm.



(b) Transition from the ${}^6P_{3/2}$ state to an AI state at 841.0 nm.



(c) Transition from the ${}^6P_{5/2}$ state to an AI state at 841.7 nm.



(d) Transition from the ${}^6P_{5/2}$ state to an AI state at 833.2 nm.

Figure B.3: Frequency scans of the third step transitions in both isotopes, ${}^{97}\text{Tc}$ and ${}^{98}\text{Tc}$.

ADDITIONAL INFORMATION ON THE PI-LIST DEVELOPMENT

Mode Suppression in the Frequency-Tripling Process of Narrow-band Laser Light

As mentioned in section 5.3.2, interaction of individual (cavity) modes in laser radiation causes additional modes in frequency mixing processes in NLO material. This leads to the output light having the same mode spacing as the initial laser radiation. However, the appearance of additional modes is suppressed when using narrowband laser light with only few oscillating cavity modes as provided by the dual etalon Ti:sapphire laser (see figure 5.28).

The theoretical spectral structure of the typical fundamental laser radiation with the present Ti:sapphire laser in narrowband configuration is visualized in figure 5.28. The full linewidth at half maximum of the whole structure is about 1 GHz and about only five to seven cavity modes can oscillate. Due to the free spectral range of the cavity modes being relatively close to the linewidth of the whole structure, the intensity of the individual modes differ significantly. For sum frequency of two modes with intensities $I_1(\nu_1)$ and $I_2(\nu_2)$, the intensity of the resulting mode is

$$I_{1+2}(\nu_1 + \nu_2) \propto I_1(\nu_1) \cdot I_2(\nu_2) \quad . \quad (C.1)$$

As a consequence, only the center cavity mode and its directly neighboring modes could generate a notable contribution to additional modes via sum frequency generation, as all other combinations result in very low intensities. The neighboring cavity modes 320 MHz away from the center frequency are already about 25 % weaker than the cavity mode at the center frequency. Even when the laser frequency is scanned, the intensity of the sum frequency mode of these two neighboring modes will stay between 75 % and 87 % relative to the 100 % of the frequency-doubled center mode. This is an important difference to the radiation of a standard laser, where the full spectral linewidth of 3 - 5 GHz comprises a large set of cavity modes at close to maximum intensity, which provide many combinations to generate additional modes by sum frequency mixing. This effect of suppression is amplified when using frequency-tripling or frequency-quadrupling with three or four subsequent NLO stages.

In addition, it has to be mentioned that figure 5.28 shows only a picture averaged over time. Earlier studies of the spectral mode structure of the fundamental laser radiation showed evidence of a strong temporal fluctuation of the intensities of the individual modes, which is

caused by thermal fluctuations, microscopic vibrations, and strong mode competition inside the laser cavity. In fact, the majority of the laser pulses show the absence of some modes except the major mode at the center. This can be interpreted as a *pulse-to-pulse flickering* of the individual cavity modes. Averaged over time, this flickering does not affect the frequency doubling of the individual modes, but it clearly reduces the probability of the sum frequency generation of two different cavity modes, as both must be present at sufficient intensity for a significant contribution to additional side modes.

In total, the suppression of sum frequency generation of two modes due to strong intensity differences and the pulse-to-pulse flickering multiply, which leads to a strong suppression of additional modes. The spectral profile of the resulting frequency tripled radiation could not be investigated, but it can be estimated that the additional modes due to sum frequency generation is suppressed by well more than 50% relative to the individually frequency-doubled modes. As a result, the observed frequency shift in figure 5.27 equals three times the fundamental free spectral range of about 947 MHz.

PI-LIST with Internal Reflection

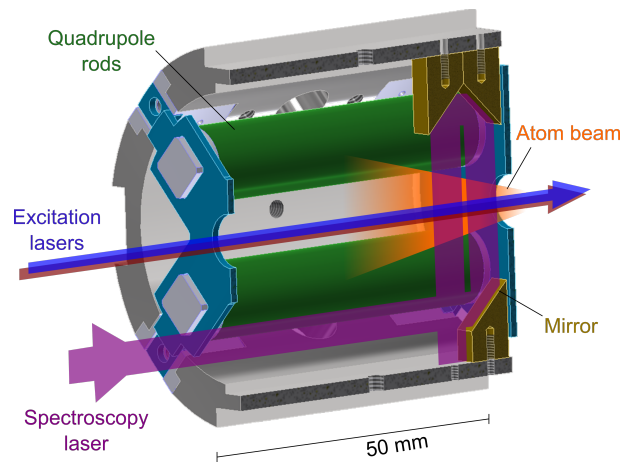


Figure C.1: 3D-model of the PI-LIST (short version) with internal reflection into perpendicular laser alignment. Courtesy of R. Heinke.

HFS SPECTROSCOPY IN Tc USING THE PI-LIST

Additional Fitted Spectra

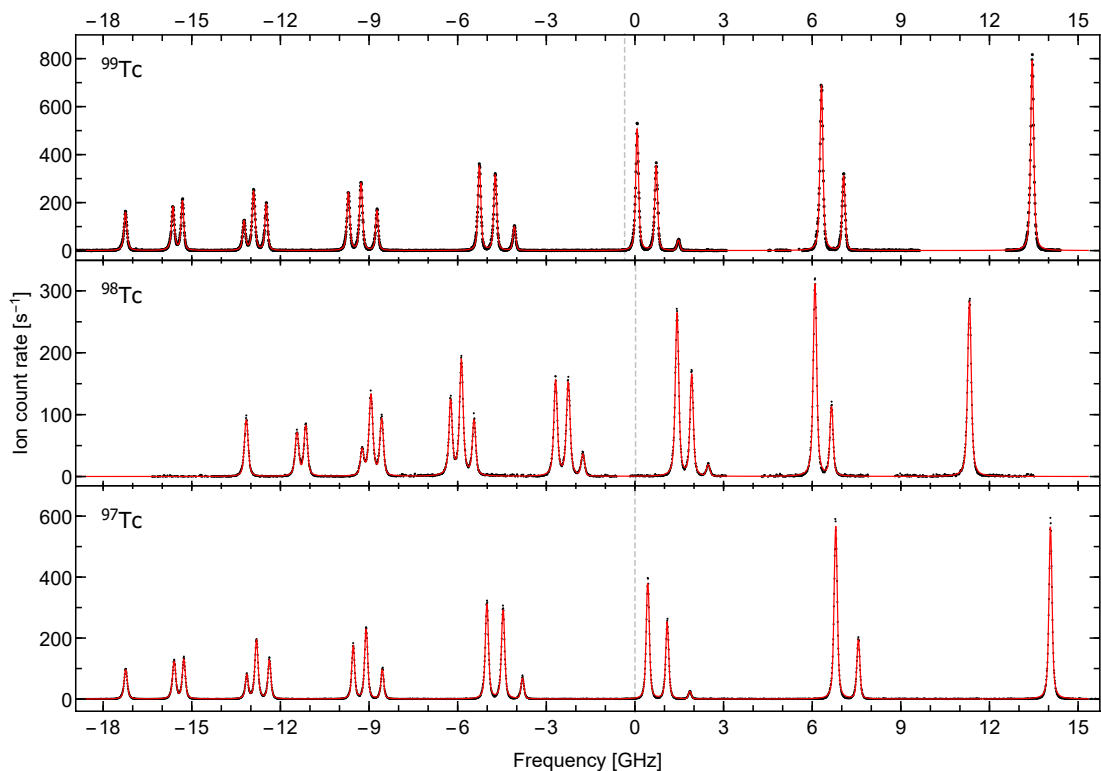


Figure D.1: Fit to the experimental data of the $J = 5/2 - J' = 7/2$ transition at 429.8 nm in Tc. The data was binned to intervals of 10 MHz width. A sum of Voigt profiles centered at the different $\Delta E_{F,F'}$ was fitted to the data using a least square fit algorithm. The frequency axis was centered around the center frequency of the ^{97}Tc transition at $23265.388 \text{ cm}^{-1}$. The vertical dashed lines indicate the resulting central frequency ν_0 of the HFS spectra.

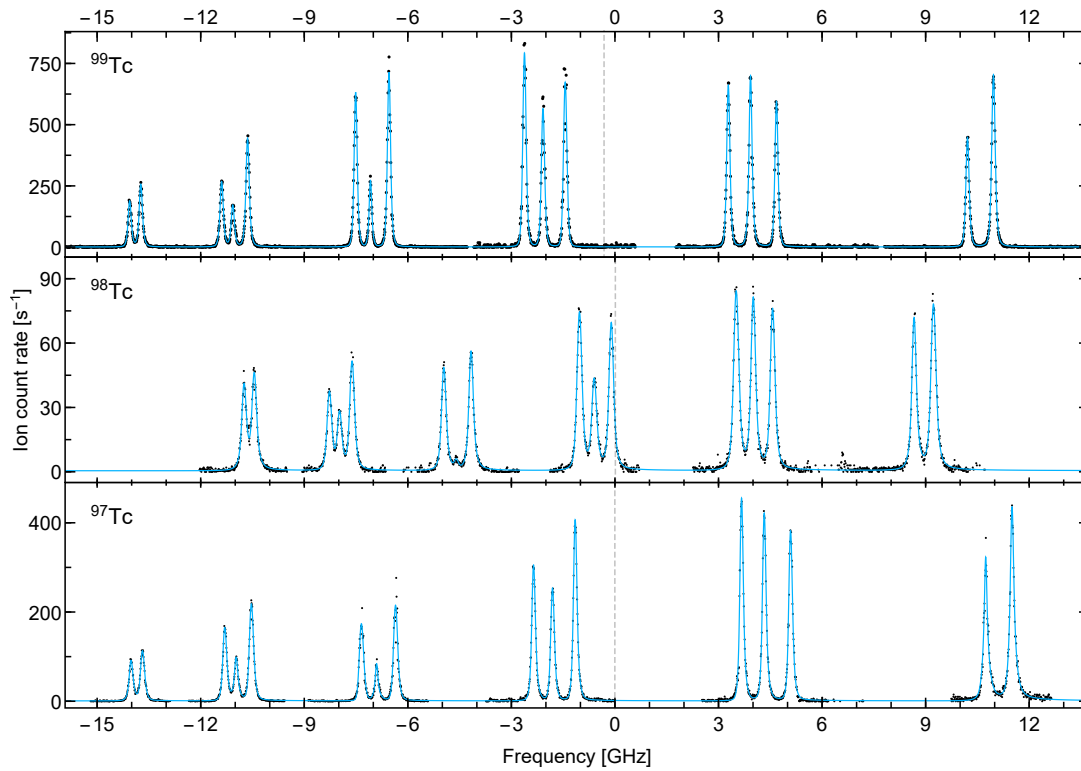


Figure D.2: Fit to the experimental data of the $J=5/2$ to $J'=5/2$ transition in Tc using asymmetric Bi-Voigt profiles.

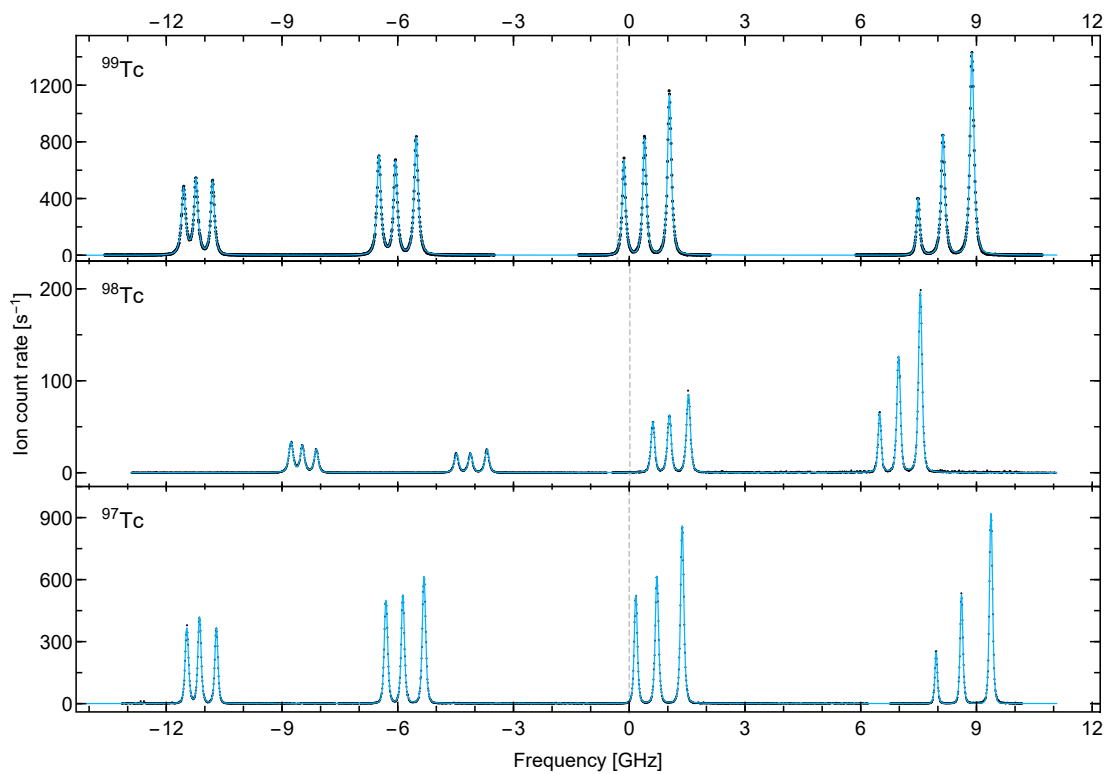


Figure D.3: Fit to the experimental data of the $J=5/2$ to $J'=3/2$ transition in Tc using asymmetric Bi-Voigt profiles.

Result of the Voigt Fits

Table D.1: Compilation of the HFS coupling constants of the first excitation step derived by the fits using Voigt profiles. The listed errors are standard errors from the fit routine. The literature values for ^{99}Tc are taken from [130]. It should be noted that the ground state splitting in [130] could not be resolved and a value for B was not given. See text for detailed discussion. All values are given in units of MHz.

Parameter	^{97}Tc	^{98}Tc	^{99}Tc	$^{99}\text{Tc}_{\text{lit}}$
Transition ${}^6S_{5/2} - {}^6P_{7/2}^o$				
A_{low}	-109.616(31)	-65.976(32)	-107.375(37)	-109.12(90)
A_{up}	815.740(23)	490.894(24)	799.943(28)	798.6(36)
B_{low}	-1.21(63)	3.40(93)	1.69(73)	-
B_{up}	-58.83(73)	15.7(11)	-43.68(83)	-57(18)
$A_{\text{up}}/A_{\text{low}}$	-7.442	-7.441	-7.450	-7.32
Transition ${}^6S_{5/2} - {}^6P_{5/2}^o$				
A_{low}	-109.557(49)	-65.830(45)	-107.325(33)	-109.12(90)
A_{up}	911.783(52)	548.640(45)	894.070(36)	892.2(39)
B_{low}	7.3(11)	-2.5(13)	-0.37(76)	-
B_{up}	71.4(12)	-10.9(13)	57.43(84)	93(18)
$A_{\text{up}}/A_{\text{low}}$	-8.322	-8.334	-8.3331	-8.18
Transition ${}^6S_{5/2} - {}^6P_{3/2}^o$				
A_{low}	-109.392(14)	-65.833(23)	-107.394(21)	-109.12(90)
A_{up}	1207.170(20)	726.849(37)	1183.253(31)	1182.1(36)
B_{low}	1.85(31)	-9.43(64)	0.98(46)	-
B_{up}	-6.59(22)	-2.91(47)	-12.83(33)	-12(12)
$A_{\text{up}}/A_{\text{low}}$	-11.035	-11.041	-11.018	-10.83

ABBREVIATIONS AND SYMBOLS

Abbreviations

List of frequently used abbreviations in alphabetical order.

AI	A autoIonizing state
AR	A nti R eflective
BB	B road B and
FPI	F abry- P érot I nterferometer
FSR	F ree S pectral R ange
FWHM	F ull W idth at H alf M aximum
HHG	H igher H armonic G eneration
HFS	H yper F ine S tructure/ S plitting
HR	H igh R eflection/ R esolution
IC-SHG	I ntra C avity - S econd H armonic G eneration
IGISOL	I on G uide I sotope S eparator O n L ine
IP	I onization P otential
LISOL	L euven I sotope S eparator O n L ine
LIST	L aser I on S ource and T rap
MABU	M ainz A tomic B eam U nit
NMR	N uclear M agnetic R esonance
OC	O utput C oupler
ORNL	O ak R idge N ational L aboratory
PI-LIST	P erpendicularly I lluminated - L aser I on S ource and T rap
RIB	R adioactive I on B eam
RIBF	R adioactive I on B eam F acility
RILIS	R esonance I onization L aser I on S ource
RIMS	R esonance I onization M ass S pectrometry
RIS	R esonance I onization S pectroscopy
RISIKO	R esonanzionisations S pektroskopie in k ollinearer G eometrie
S/DFG	S um/ D ifference F requency G eneration
S/T/FHG	S econd/ T hird/ F ourth H armonic G eneration
SM	longitudinal S ingle M ode
SPIG	S extu P ole I on G uide
TOF	T ime O f F light

Symbols

Symbols for important parameters and constants.

A, B	Hyperfine coupling constants
c	Speed of light
C	Casimir factor
μ	Reduced mass
I	Total nuclear angular momentum, nuclear spin
μ_I	Nuclear magnetic dipole moment
μ_N	Nuclear magneton
g_I	Nuclear g-factor
Q_s	Spectroscopic nuclear electric quadrupole moment
Q_0	Intrinsic nuclear electric quadrupole moment
$\delta \nu_{A,A'}$	Isotope shift between isotopes with nucleon number A and A'
K_{NMS}, K_{SMS}	Normal and specific mass shift
F	Field shift
m_e	Electron mass
m_p	Proton mass
m_n	Neutron mass
h	Planck constant
\hbar	Reduced Planck constant
k_B	Boltzmann constant
R_y	Rydberg unit of energy
R_∞	Rydberg constant

BIBLIOGRAPHY

- [1] www.nobelprize.org. Nobel Media AB 2014. Web. *The Nobel Prize in Physics 1922*. Sept. 2016. URL: http://www.nobelprize.org/nobel_prizes/physics/laureates/1922/index.html.
- [2] E.A. McCutchan. *Evaluated Nuclear Structure Data Files*. National Nuclear Data Center (NNDC), Brookhaven National Laboratory. June 2015. URL: <http://www.nndc.bnl.gov/>.
- [3] Y Blumenfeld, T Nilsson, and P Van Duppen. “Facilities and methods for radioactive ion beam production”. In: *Physica Scripta* 2013.T152 (2013), p. 014023.
- [4] T Kron et al. “High efficiency resonance ionization of palladium with Ti:sapphire lasers”. In: *Journal of Physics B: Atomic, Molecular and Optical Physics* 49.18 (2016), p. 185003. DOI: 10.1088/0953-4075/49/18/185003.
- [5] V N Fedosseev, Yu Kudryavtsev, and V I Mishin. “Resonance laser ionization of atoms for nuclear physics”. In: *Physica Scripta* 85.5 (2012), p. 058104.
- [6] A.C. Mueller et al. “Spins, moments and charge radii of barium isotopes in the range 122–146Ba determined by collinear fast-beam laser spectroscopy”. In: *Nuclear Physics A* 403.2 (1983), pp. 234–262. DOI: [http://dx.doi.org/10.1016/0375-9474\(83\)90226-9](http://dx.doi.org/10.1016/0375-9474(83)90226-9).
- [7] S. Kreim et al. “Recent exploits of the ISOLTRAP mass spectrometer”. In: *Nuclear Instruments and Methods in Physics Research Section B: Beam Interactions with Materials and Atoms* 317, Part B (2013). XVIth International Conference on ElectroMagnetic Isotope Separators and Techniques Related to their Applications, December 2–7, 2012 at Matsue, Japan, pp. 492–500. DOI: <http://dx.doi.org/10.1016/j.nimb.2013.07.072>.
- [8] T.E. Cocolios et al. “The Collinear Resonance Ionization Spectroscopy (CRIS) experimental setup at CERN-ISOLDE”. In: *Nuclear Instruments and Methods in Physics Research Section B: Beam Interactions with Materials and Atoms* 317, Part B (2013). XVIth International Conference on ElectroMagnetic Isotope Separators and Techniques Related to their Applications, December 2–7, 2012 at Matsue, Japan, pp. 565–569. DOI: <http://dx.doi.org/10.1016/j.nimb.2013.05.088>.
- [9] Y.-Z. Qian. “Nuclear physics and astrophysics of the r-process”. In: *Nuclear Physics A* 752 (2005), pp. 550–559. DOI: <http://dx.doi.org/10.1016/j.nuclphysa.2005.02.118>.
- [10] M. Arnould, S. Goriely, and K. Takahashi. “The r-process of stellar nucleosynthesis: Astrophysics and nuclear physics achievements and mysteries”. In: *Physics Reports* 450.4–6 (2007), pp. 97–213. DOI: <http://dx.doi.org/10.1016/j.physrep.2007.06.002>.
- [11] S. Kreim et al. “Nuclear masses and neutron stars”. In: *International Journal of Mass Spectrometry* 349–350 (2013). 100 years of Mass Spectrometry, pp. 63–68. DOI: <http://dx.doi.org/10.1016/j.ijms.2013.02.015>.
- [12] H. Schatz. “Nuclear masses in astrophysics”. In: *International Journal of Mass Spectrometry* 349–350 (2013). 100 years of Mass Spectrometry, pp. 181–186. DOI: <http://dx.doi.org/10.1016/j.ijms.2013.03.016>.
- [13] Marek Kanikowski et al. “Permanent implants in treatment of prostate cancer”. In: *Reports of Practical Oncology and Radiotherapy* 13.3 (2008), pp. 150–167. DOI: [http://dx.doi.org/10.1016/S1507-1367\(10\)60006-5](http://dx.doi.org/10.1016/S1507-1367(10)60006-5).

- [14] Paul T. Finger, Kimberly J. Chin, and Greg Duvall. "Palladium-103 Ophthalmic Plaque Radiation Therapy for Choroidal Melanoma: 400 Treated Patients". In: *Ophthalmology* 116.4 (2009), 790–796.e1. DOI: <http://dx.doi.org/10.1016/j.ophtha.2008.12.027>.
- [15] N. Trautmann, G. Passler, and K.D.A. Wendt. "Ultratrace analysis and isotope ratio measurements of long-lived radioisotopes by resonance ionization mass spectrometry (RIMS)". In: *Analytical and Bioanalytical Chemistry* 378 (2 2004).
- [16] Nils Stöbener. "Elementspeziation von Neptunium im Ultrapurenbereich". PhD thesis. Johannes Gutenberg-Universität Mainz, 2013.
- [17] K. Wendt et al. "Progress of ultra trace determination of technetium using laser resonance ionization mass spectrometry". In: *Analytical and Bioanalytical Chemistry* 404.8 (2012), pp. 2173–2176. DOI: 10.1007/s00216-012-6309-8.
- [18] Kenji Yoshihara. *Technetium in the environment*. Berlin, Heidelberg: Springer Berlin Heidelberg, 1996. ISBN: 978-3-540-49273-3. DOI: 10.1007/3-540-59469-8_2.
- [19] Wolfgang Demtröder. *Experimentalphysik 3 : Atome, Moleküle und Festkörper*. Springer-Lehrbuch. Springer-Verlag, 2011.
- [20] Ingolf V. Hertel nad Claus-Peter Schulz. *Atome, Moleküle und optische Physik 1*. Springer, 2008.
- [21] Gordon W F Drake. *Springer Handbook of Atomic, Molecular, and Optical Physics*. Springer, 2006.
- [22] Wolfgang Demtröder. *Laserspektroskopie 1: Grundlagen 6. Aufl.* Springer, 2011.
- [23] Vladislav Gerginov, Andrei Derevianko, and Carol E. Tanner. "Observation of the Nuclear Magnetic Octupole Moment of ^{133}Cs ". In: *Phys. Rev. Lett.* 91 (7 Aug. 2003), p. 072501. DOI: 10.1103/PhysRevLett.91.072501.
- [24] H. B. G. Casimir. "On the Interaction between Atomic Nuclei and Electrons". In: *On the Interaction between Atomic Nuclei and Electrons*. Dordrecht: Springer Netherlands, 1936, pp. 201–283. ISBN: 978-94-017-6067-6. DOI: 10.1007/978-94-017-6067-6_1.
- [25] Charles Schwartz. "Theory of Hyperfine Structure". In: *Phys. Rev.* 97 (2 Jan. 1955), pp. 380–395. DOI: 10.1103/PhysRev.97.380.
- [26] H N Russell and F A Saunders. "New Regularities in the Spectra of the Alkaline Earths". In: *Astrophysical Journal* 61 (1925), p. 38.
- [27] U. Fano, C. E. Theodosiou, and J. L. Dehmer. "Electron-optical properties of atomic fields". In: *Rev. Mod. Phys.* 48 (1 Jan. 1976), pp. 49–68. DOI: 10.1103/RevModPhys.48.49.
- [28] Christoph Mattolat. "Spektroskopische Untersuchungen an Technetium und Silizium - Ein Festkörperlasersystem für die Resonanzionisationsspektroskopie". PhD thesis. Johannes Gutenberg-Universität Mainz, 2010.
- [29] Volker Sonnenschein. "Laser developments and high resolution resonance ionization spectroscopy of actinide elements". PhD thesis. University of Jyväskylä, 2014.
- [30] P. F. Moulton. "Spectroscopic and laser characteristics of Ti:Al₂O₃". In: *J. Opt. Soc. Am. B* 3.1 (Jan. 1986), pp. 125–133. DOI: 10.1364/JOSAB.3.000125.
- [31] W. R. Rapoport and Chandra P Khattak. "Titanium sapphire laser characteristics". In: *Appl. Opt.* 27.13 (July 1988), pp. 2677–2684. DOI: 10.1364/AO.27.002677.
- [32] J. M. Eggleston, L. G. DeShazer, and K. W. Kangas. "Characteristics and kinetics of laser-pumped Ti:sapphire oscillators". In: *IEEE Journal of Quantum Electronics* 24.6 (Jan. 1988), pp. 1009–1015. DOI: 10.1109/3.222.
- [33] Kalinin V. N. Ambartsumyan R. V. and Letokhov V. S. "Two-step Selective Photoionization of Rubidium Atoms by Laser Radiation (Engl. Transl.)" In: *Appl. Opt.* 13 (1971), pp. 354–358.
- [34] R. V. Ambartsumian and V. S. Letokhov. "Selective Two-Step (STS) Photoionization of Atoms and Photodissociation of Molecules by Laser Radiation". In: *Appl. Opt.* 11 (1972), pp. 354–358. DOI: 10.1364/AO.11.000354.

- [35] F. Scheerer et al. “A chemically selective laser ion source for online mass separation”. In: *Review of Scientific Instruments* 63.4 (1992). DOI: DOI : 10 . 1063/1 . 1142820.
- [36] Y. Iwata, H. Sekiya, and C. Ito. “Ultrasensitive resonance ionization mass spectrometer for evaluating krypton contamination in xenon dark matter detectors”. In: *Nuclear Instruments and Methods in Physics Research Section A: Accelerators, Spectrometers, Detectors and Associated Equipment* 797 (2015), pp. 64–69. DOI: <http://dx.doi.org/10.1016/j.nima.2015.06.037>.
- [37] Klaus Wendt et al. “Laser Based Techniques for Ultra Trace Isotope Production, Spectroscopy and Detection”. In: *Hyperfine Interactions* 162 (1 2005), pp. 147–157.
- [38] N. Erdmann et al. “Resonance ionization mass spectroscopy for trace determination of plutonium in environmental samples”. In: *Fresenius’ Journal of Analytical Chemistry* 359 (4 1997).
- [39] S. et al. Rothe. “Measurement of the first ionization potential of astatine by laser ionization spectroscopy”. In: *Nat. Commun.* 4.1835 (2013). DOI: <http://dx.doi.org/10.1038/ncomms2819>.
- [40] K. T. Flanagan et al. “Collinear Resonance Ionization Spectroscopy of Neutron-Deficient Francium Isotopes”. In: *Phys. Rev. Lett.* 111 (21 Nov. 2013), p. 212501. DOI: 10 . 1103/PhysRevLett . 111 . 212501.
- [41] F. Schneider et al. “Resonance ionization of holmium for ion implantation in microcalorimeters”. In: *Nuclear Instruments and Methods in Physics Research Section B: Beam Interactions with Materials and Atoms* 376 (2016). Proceedings of the XVIIth International Conference on Electromagnetic Isotope Separators and Related Topics (EMIS2015), Grand Rapids, MI, U.S.A., 11-15 May 2015, pp. 388–392. DOI: <http://dx.doi.org/10.1016/j.nimb.2015.12.012>.
- [42] P. Müller et al. “⁴¹Ca ultratrace determination with isotopic selectivity > 10¹² by diode-laser-based RIMS”. In: *Fresenius’ Journal of Analytical Chemistry* 370 (5 2001).
- [43] Amin Hakimi. “Diodenlaserbasierte Resonanzionisations-Massenspektrometrie zur Spektroskopie und Ultrapurenanalyse an Uranisotopen”. PhD thesis. Johannes Gutenberg-Universität Mainz, 2013.
- [44] Sven Richter. “Implementierung der Laserionenquellenfalle LIST bei ISOLDE und Validierung der Spezifikationen Effizienz und Selektivität”. PhD thesis. Johannes Gutenberg-Universität Mainz, 2015.
- [45] U. Fano. “Effects of Configuration Interaction on Intensities and Phase Shifts”. In: *Phys. Rev.* 124 (6 Dec. 1961), pp. 1866–1878. DOI: 10 . 1103/PhysRev . 124 . 1866.
- [46] Tina Gottwald. “Studium hochkomplexer atomarer Spektren mittels Methoden der Laserresonanzionisation”. PhD thesis. Johannes Gutenberg-Universität Mainz, 2010.
- [47] Sebastian Raeder. “Spurenanalyse von Aktiniden in der Umwelt mittels Resonanzionisations-Massenspektrometrie”. PhD thesis. Johannes Gutenberg-Universität Mainz, 2010.
- [48] Dominik Studer. “Resonanzionisationsspektroskopie hochliegender Zustände in Dysprosium und Erbium zur Entwicklung effizienter Anregungsschemata und Bestimmung des ersten Ionisationspotentials”. Diploma thesis. Johannes Gutenberg-Universität Mainz, 2015.
- [49] Ruben de Groote. “Modeling and Simulations of Two-Step Resonance Ionization Processes using CW and Pulsed Lasers”. M.Sc. thesis. Katholieke Universiteit Leuven, 2013.
- [50] N.V. Vitanov et al. “Power broadening revisited: theory and experiment”. In: *Optics Communications* 199.1–4 (2001), pp. 117–126. DOI: [http://dx.doi.org/10.1016/S0030-4018\(01\)01495-X](http://dx.doi.org/10.1016/S0030-4018(01)01495-X).
- [51] M. L. Citron et al. “Experimental study of power broadening in a two-level atom”. In: *Phys. Rev. A* 16 (4 Oct. 1977), pp. 1507–1512. DOI: 10 . 1103/PhysRevA . 16 . 1507.
- [52] S.M. Abrarov and B.M. Quine. “Efficient algorithmic implementation of the Voigt/complex error function based on exponential series approximation”. In: *Applied Mathematics and Computation* 218.5 (2011), pp. 1894–1902. DOI: <http://dx.doi.org/10.1016/j.amc.2011.06.072>.

- [53] S.M. Abrarov and B.M. Quine. “On the Fourier expansion method for highly accurate computation of the Voigt/complex error function in a rapid algorithm”. In: *ArXiv e-prints* (May 2012). arXiv: 1205.1768 [math.NA].
- [54] J.J. Olivero and R.L. Longbothum. “Empirical fits to the Voigt line width: A brief review”. In: *Journal of Quantitative Spectroscopy and Radiative Transfer* 17.2 (1977), pp. 233–236. DOI: [http://dx.doi.org/10.1016/0022-4073\(77\)90161-3](http://dx.doi.org/10.1016/0022-4073(77)90161-3).
- [55] Roland Horn. “Aufbau eines Systems gepulster, abstimmbarer Festkörperlaser zum Einsatz in der Resonanzionisations-Massenspektrometrie”. PhD thesis. Johannes Gutenberg-Universität Mainz, 2003.
- [56] HighFinesse GmbH. *HighFinesse Website*. HighFinesse GmbH. Dec. 2016. URL: <http://www.highfinesse.com/>.
- [57] S. Rothe et al. “Narrow linewidth operation of the RILIS titanium: Sapphire laser at ISOLDE/CERN”. In: *Nuclear Instruments and Methods in Physics Research Section B: Beam Interactions with Materials and Atoms* 317, Part B (2013). XVIth International Conference on ElectroMagnetic Isotope Separators and Techniques Related to their Applications, December 2–7, 2012 at Matsue, Japan, pp. 561–564. DOI: <http://dx.doi.org/10.1016/j.nimb.2013.08.058>.
- [58] V. Sonnenschein et al. “Characterization of a dual-etalon Ti:sapphire laser via resonance ionization spectroscopy of stable copper isotopes”. In: *Hyperfine Interactions* 227.1 (2014), pp. 113–123. DOI: 10.1007/s10751-013-1000-9.
- [59] Pascal Naubereit. “Weiterentwicklung eines weitabstimmbaren Titan:Saphir-Lasers und sein Einsatz zur Spektroskopie hochliegender Resonanzen in Holmium”. M.Sc. thesis. Johannes Gutenberg-Universität Mainz, 2014.
- [60] C. L. Tang, H. Stutz, and G. deMars. “Spectral Output and Spiking Behavior of Solid-State Lasers”. In: *Journal of Applied Physics* 34.8 (1963), pp. 2289–2295. DOI: <http://dx.doi.org/10.1063/1.1702732>.
- [61] Tatsuya Kimura, K. Otsuka, and M. Saruwatari. “Spatial hole-burning effects in a Nd³⁺:YAG laser”. In: *Quantum Electronics, IEEE Journal of* 7.6 (June 1971), pp. 225–230. DOI: 10.1109/JQE.1971.1076746.
- [62] J. J. Zayhowski. “Limits imposed by spatial hole burning on the single-mode operation of standing-wave laser cavities”. In: *Opt. Lett.* 15.8 (Apr. 1990), pp. 431–433. DOI: 10.1364/OL.15.000431.
- [63] Christoph Mattolat. “Entwicklung der Resonanzionisations-Massenspektrometrie an 26 Aluminium mit einem geseedeten Titan:Saphir-Lasersystem”. Diploma thesis. Johannes Gutenberg-Universität Mainz, 2006.
- [64] Thomas Fischbach. “Aufbau und Charakterisierung einer interferometrischen Frequenzstabilisierung für Diodenlaser”. Diploma thesis. Johannes Gutenberg-Universität Mainz, 2012.
- [65] Bahaa E. A. Saleh and Malvin Carl Teich. *Grundlagen der Photonik*. 2. Auflage. Wiley-VCH Verlag GmbH & Co. KGaA, Mar. 2008. ISBN: 9783527406777.
- [66] P. Naubereit et al. “Resonance ionization spectroscopy of sodium Rydberg levels using difference frequency generation of high-repetition-rate pulsed Ti:sapphire lasers”. In: *Phys. Rev. A* 93 (5 May 2016), p. 052518. DOI: 10.1103/PhysRevA.93.052518.
- [67] Volker Sonnenschein et al. “Intracavity Frequency Doubling and Difference Frequency Mixing for Pulsed ns Ti:Sapphire Laser Systems at On-Line Radioactive Ion Beam Facilities”. In: *Proceedings of the Conference on Advances in Radioactive Isotope Science (ARIS2014)*. Sept. 2014. DOI: 10.7566/JPSCP.6.030126. eprint: <http://journals.jps.jp/doi/pdf/10.7566/JPSCP.6.030126>.
- [68] Pascal Naubereit. “Resonatorinterne Frequenzverdopplung eines gepulsten Titan:Saphir-Lasers”. B.Sc. thesis. Johannes Gutenberg-Universität Mainz, 2012.
- [69] Klaus Zimmer. “Konzeption, Aufbau und Test der Ionenoptik des RISIKO-Massenseparators”. Diploma thesis. Johannes Gutenberg-Universität Mainz, 1990.

- [70] Alexander Herlert. “The ISOLDE Facility”. In: *Nuclear Physics News* 20.4 (2010), pp. 5–12. DOI: 10.1080/10619127.2010.529735. eprint: <http://dx.doi.org/10.1080/10619127.2010.529735>.
- [71] ISOLDE CERN. *ISOLDE web page*. Dec. 2016. URL: <http://http://isolde.web.cern.ch/>.
- [72] Fabian Schneider. “First Steps of the ECHo Experiment: Penning-Trap Mass Measurements of the ^{163}Ho Electron Capture Process and Implantation of ultrapure Ho into Microcalorimeter Arrays”. PhD thesis. Johannes Gutenberg-Universität Mainz, 2016.
- [73] Fabio Schweltnus. “Entwicklung von Ionenquellen zur Optimierung von Selektivität und Effizienz bei der resonanten Laserionisation”. PhD thesis. Johannes Gutenberg-Universität Mainz, 2010.
- [74] S. Rothe et al. “Advances in surface ion suppression from RILIS: Towards the Time-of-Flight Laser Ion Source (ToF-LIS)”. In: *Nuclear Instruments and Methods in Physics Research Section B: Beam Interactions with Materials and Atoms* 376 (2016). Proceedings of the XVIIth International Conference on Electromagnetic Isotope Separators and Related Topics (EMIS2015), Grand Rapids, MI, U.S.A., 11-15 May 2015, pp. 86–90. DOI: <http://dx.doi.org/10.1016/j.nimb.2016.02.060>.
- [75] J.L. Henares et al. “Hot-cavity studies for the Resonance Ionization Laser Ion Source”. In: *Nuclear Instruments and Methods in Physics Research Section A: Accelerators, Spectrometers, Detectors and Associated Equipment* 830 (2016), pp. 520–525. DOI: <http://dx.doi.org/10.1016/j.nima.2015.10.061>.
- [76] Sebastian Schmidt. “Optimierung der Temperaturverteilung in der Ionenquelle des RISIKO-Massenseparators”. Staatsexamensarbeit. Johannes Gutenberg-Universität Mainz, 2015.
- [77] Pierce John Robinson. *Theory and design of electron beams*. van Nostrand Company, 1954.
- [78] K. Blaum et al. “A novel scheme for a highly selective laser ion source”. In: *Nuclear Instruments and Methods in Physics Research Section B: Beam Interactions with Materials and Atoms* 204 (2003). 14th International Conference on Electromagnetic Isotope Separators and Techniques Related to their Applications, pp. 331–335. DOI: [http://dx.doi.org/10.1016/S0168-583X\(02\)01942-0](http://dx.doi.org/10.1016/S0168-583X(02)01942-0).
- [79] Daniel Andreas Fink. “Improving the Selectivity of the ISOLDE Resonance Ionization Laser Ion Source and In-Source Laser Spectroscopy of Polonium”. PhD thesis. Ruprecht-Karls-Universität Heidelberg, 2014.
- [80] Katja Wiest. “Entwicklung des Laserionenquellen- und fallenprojekts LIST für Ultraspurendetektion und Grundlagenforschung”. PhD thesis. Johannes Gutenberg-Universität Mainz, 2006.
- [81] D.A. Fink et al. “First application of the Laser Ion Source and Trap (LIST) for on-line experiments at ISOLDE”. In: *Nuclear Instruments and Methods in Physics Research Section B: Beam Interactions with Materials and Atoms* 317, Part B (2013). XVIth International Conference on ElectroMagnetic Isotope Separators and Techniques Related to their Applications, December 2–7, 2012 at Matsue, Japan, pp. 417–421. DOI: <http://dx.doi.org/10.1016/j.nimb.2013.06.039>.
- [82] D.A. Fink et al. “On-line implementation and first operation of the Laser Ion Source and Trap at ISOLDE/CERN”. In: *Nuclear Instruments and Methods in Physics Research Section B: Beam Interactions with Materials and Atoms* 344 (2015), pp. 83–95. DOI: <http://dx.doi.org/10.1016/j.nimb.2014.12.007>.
- [83] D. A. Fink et al. “In-Source Laser Spectroscopy with the Laser Ion Source and Trap: First Direct Study of the Ground-State Properties of $^{217,219}\text{Po}$ ”. In: *Phys. Rev. X* 5 (1 Feb. 2015), p. 011018. DOI: 10.1103/PhysRevX.5.011018.
- [84] Wolfgang Paul und Helmut Steinwedel. “Ein neues Massenspektrometer ohne Magnetfeld”. In: *Zeitschrift für Physik* 8a (1953), pp. 448–450.
- [85] Wolfgang Paul. “Electromagnetic traps for charged and neutral particles”. In: *Rev. Mod. Phys.* 62 (3 July 1990), pp. 531–540. DOI: 10.1103/RevModPhys.62.531.

- [86] Christoph Mattolat. “Theoretische Beschreibung und Realisation der mehrstufigen Resonanzionisation von Calcium für die hochselektive Spurenanalyse”. PhD thesis. Johannes Gutenberg-Universität Mainz, 1999.
- [87] Christopher Geppert. “Optimierung der Atomstrahlquelle und der Laser-Ionisationsregion für die resonante Laserionisations-Massenspektrometrie”. Diploma thesis. Johannes Gutenberg-Universität Mainz, 2000.
- [88] Peter Müllert. “Ultrapurennachweis von Ca-41 mittels hochauflösender Resonanzionisations-Massenspektrometrie”. PhD thesis. Johannes Gutenberg-Universität Mainz, 2003.
- [89] Christopher Geppert. “Resonanzionisation zum Nachweis und zur Erzeugung radioaktiver Ionenstrahlen: Vom hochselektiven Ultrapurennachweis zur selektiven on-line Laserionenquelle”. PhD thesis. Johannes Gutenberg-Universität Mainz, 2005.
- [90] Johannes Rossnagel. “Aufbau einer Atomstrahl-Massenspektrometer-Apparatur zur resonanten Laserionisation”. Diploma thesis. Johannes Gutenberg-Universität Mainz, 2011.
- [91] Michael Franzmann. “Resonanzionisations-Massenspektrometrie an Aktiniden mit der Mainzer Atomstrahlquelle MABU”. Diploma thesis. Johannes Gutenberg-Universität Mainz, 2013.
- [92] K. Blaum et al. “Properties and performance of a quadrupole mass filter used for resonance ionization mass spectrometry”. In: *International Journal of Mass Spectrometry* 181.1–3 (1998), pp. 67–87. DOI: [http://dx.doi.org/10.1016/S1387-3806\(98\)14174-X](http://dx.doi.org/10.1016/S1387-3806(98)14174-X).
- [93] K. Blaum et al. “Peak shape for a quadrupole mass spectrometer: comparison of computer simulation and experiment”. In: *International Journal of Mass Spectrometry* 202.1–3 (2000), pp. 81–89. DOI: [http://dx.doi.org/10.1016/S1387-3806\(00\)00237-2](http://dx.doi.org/10.1016/S1387-3806(00)00237-2).
- [94] Klaus Blaum. “Resonante Laserionisations-Massenspektrometrie an Gadolinium zur Isotopenhäufigkeitsanalyse mit geringsten Mengen”. PhD thesis. Johannes Gutenberg-Universität Mainz, 2000.
- [95] M. Berglund and M. E. Wieser. “Isotopic compositions of the elements 2009 (IUPAC Technical Report)”. In: *Pure Appl. Chem* 83.2 (2011), pp. 397–410. DOI: <http://dx.doi.org/10.1351/PAC-REP-10-06-02>.
- [96] N. Karamatskos et al. “Rydberg series in the photoionization spectrum of Pd I”. In: *Physics Letters A* 102.9 (1984), pp. 409–411. DOI: [http://dx.doi.org/10.1016/0375-9601\(84\)91066-1](http://dx.doi.org/10.1016/0375-9601(84)91066-1).
- [97] Toshiaki Ishikawa. “Photoionization Spectra of Pd in High Rydberg States”. In: *Japanese Journal of Applied Physics* 32.10R (1993), p. 4779.
- [98] M A Baig et al. “High resolution absorption spectrum of palladium in the 4d subshell excitation region”. In: *Journal of Physics B: Atomic, Molecular and Optical Physics* 24.9 (1991), p. 2295.
- [99] T. Ishikawa, H. Kawakami, and H. Mori. “Laser purification of metals (I); high Rydberg states of Ni, Ag, and Pd”. In: *Nuclear Instruments and Methods in Physics Research Section B: Beam Interactions with Materials and Atoms* 121.1–4 (1997). Materials Synthesis and Modification by Ion and/or Laser Beams, pp. 437–441. DOI: [http://dx.doi.org/10.1016/S0168-583X\(96\)00552-6](http://dx.doi.org/10.1016/S0168-583X(96)00552-6).
- [100] M Mazzoni, Y N Joshi, and J-F Wyart. “Photoabsorption Spectrum of Atomic Palladium (Pd I) Between 1400 and 2100Å”. In: *Physica Scripta* 57.3 (1998), p. 376.
- [101] Rolf Engleman et al. “The Pd I Spectrum, Term System, Isotope Shift and Hyperfine Structure – Revised and Extended Analysis Based on FTS Emission Spectroscopy”. In: *Physica Scripta* 57.3 (1998), p. 345.
- [102] E. J. van Duijn, S. Witte, and W. Zinkstok R. and Hogervorst. “Hyperfine structure and isotope shift measurements on $4d^{10} \ ^1S_0 \rightarrow 4d^9 \ 5p \ J=1$ transitions in Pd I using deep-UV cw laser spectroscopy”. In: *The European Physical Journal D - Atomic, Molecular, Optical and Plasma Physics* 19.1 (2002), pp. 25–29. DOI: [10.1140/epjd/e20020051](https://doi.org/10.1140/epjd/e20020051).
- [103] A. Kramida et al. *NIST Atomic Spectra Database (ver. 5.3)*. National Institute of Standards and Technology, Gaithersburg, MD. Sept. 2015. URL: <http://physics.nist.gov/asd>.

- [104] Joachim Barth. “Entwicklung einer Testapparatur zur Laserionisation von Pd, Cu und Zn”. Diploma thesis. Johannes Gutenberg-Universität Mainz, 2005.
- [105] Aleksei N Tkachev and Sergei I Yakovlenko. “On laser rare-isotope separation”. In: *Quantum Electronics* 33.7 (2003), p. 581.
- [106] J. E. Sansonetti and W. C. Martin. “Handbook of Basic Atomic Spectroscopic Data”. In: *Journal of Physical and Chemical Reference Data* 34.4 (2005), pp. 1559–2259. DOI: <http://dx.doi.org/10.1063/1.1800011>.
- [107] Sebastian Rothe. “Aufbau eines Chrom:Forsterit-Lasers und Resonanzionisationsspektroskopie an Strontium, Titan, Nickel, Scandium und Silicium”. Diploma thesis. Johannes Gutenberg-Universität Mainz, 2009.
- [108] Sebastian Rothe. “An all-solid state laser system for the laser ion source RILIS and in-source laser spectroscopy of astatine at ISOLDE/CERN”. PhD thesis. Johannes Gutenberg-Universität Mainz, 2012.
- [109] K. T. Lu and U. Fano. “Graphic Analysis of Perturbed Rydberg Series”. In: *Phys. Rev. A* 2 (1 July 1970), pp. 81–86. DOI: [10.1103/PhysRevA.2.81](https://doi.org/10.1103/PhysRevA.2.81).
- [110] Patrick Dyrauf. “Resonanzionisation und Rydbergspektroskopie an Dysprosium”. Diploma thesis. Johannes Gutenberg-Universität Mainz, 2015.
- [111] C. L. Callender, P. A. Hackett, and D. M. Rayner. “First-ionizationpotential of ruthenium, rhodium, and palladium by double-resonance ionization spectroscopy”. In: *J. Opt. Soc. Am. B* 5.3 (Mar. 1988), pp. 614–618. DOI: [10.1364/JOSAB.5.000614](https://doi.org/10.1364/JOSAB.5.000614).
- [112] Ulf Litzén et al. “Analysis of the Pd II Spectrum in the Ultraviolet and Infrared Regions”. In: *Physica Scripta* 64.1 (2001), p. 63.
- [113] Tom Henning Kieck. “Adaption des RISIKO Massenseparators zur Anreicherung und Implantation von ^{163}Ho für das ECHO Projekt”. Staatsexamensarbeit. Johannes Gutenberg-Universität Mainz, 2015.
- [114] Katerina Chrysalidis. “Probenpräparation für das ECHO-Projekt-Effizienzmessungen an stabilem Holmium ^{165}Ho am RISIKO-Massenseparator”. B.Sc. thesis. Johannes Gutenberg-Universität Mainz, 2014.
- [115] Lambropoulos P and Lyras A. “Theory of resonant ionization by broad-band radiation in the determination of isotopic abundances”. In: *Phys. Rev. A* 40 (4 Aug. 1989), pp. 2199–2202. DOI: [10.1103/PhysRevA.40.2199](https://doi.org/10.1103/PhysRevA.40.2199).
- [116] A. Lyras, B. Zorman, and P Lambropoulos. “Theory of doubly resonant ionization by broad-band radiation applied to the determination of isotopic abundances”. In: *Phys. Rev. A* 42 (1 July 1990), pp. 543–549. DOI: [10.1103/PhysRevA.42.543](https://doi.org/10.1103/PhysRevA.42.543).
- [117] Raphael Haas. “Radiochemische Holmium-Probenpräparation für den RISIKO-Massenseparator für das ECHO-Projekt”. B.Sc. thesis. Johannes Gutenberg-Universität Mainz, 2014.
- [118] K Eberhardt and N Trautmann. “Neutron activation analysis at the Triga MARK II research reactor of the University of Mainz”. In: *Utilization related design features of research reactors: A compendium*. IAEA TECHNICAL REPORTS SERIES No. 455, 2007, pp. 537–545.
- [119] J R Beene et al. “ISOL science at the Holifield Radioactive Ion Beam Facility”. In: *Journal of Physics G: Nuclear and Particle Physics* 38.2 (2011), p. 024002.
- [120] Yuan Liu. “ORNL developments in laser ion sources for radioactive ion beam production”. In: *Hyperfine Interactions* 227.1 (2013), pp. 85–99. DOI: [10.1007/s10751-013-0965-8](https://doi.org/10.1007/s10751-013-0965-8).
- [121] V Sonnenschein et al. “Determination of the ground-state hyperfine structure in neutral ^{229}Th ”. In: *Journal of Physics B: Atomic, Molecular and Optical Physics* 45.16 (2012), p. 165005.
- [122] K. Wendt et al. “Hyperfine structure and isotope shift in the $3s^2 3p^2 \ ^3P_{0,1,2} \rightarrow 3s^2 3p4p \ ^3P_{0,1,2}$ transitions in silicon by Doppler-free in-source two-photon resonance-ionization spectroscopy”. In: *Phys. Rev. A* 88 (5 Nov. 2013), p. 052510. DOI: [10.1103/PhysRevA.88.052510](https://doi.org/10.1103/PhysRevA.88.052510).

- [123] Takahide Takamatsu et al. “Development of High Resolution Resonance Ionization Spectroscopy on Titanium Using Injection-Locked Ti:Sapphire Laser System”. In: *JPS Conf. Proc.* 6 (2015). Proceedings of the Conference on Advances in Radioactive Isotope Science (ARIS2014). DOI: 10.7566/JPSCP.6.030142. eprint: <http://journals.jps.jp/doi/pdf/10.7566/JPSCP.6.030142>.
- [124] Walter R. Leeb. “Losses introduced by tilting intracavity etalons”. In: *Applied physics* 6.2 (1975), pp. 267–272. DOI: 10.1007/BF00883762.
- [125] S. Hannemann, E.-J. van Duijn, and W. Ubachs. “A narrow-band injection-seeded pulsed titanium:sapphire oscillator-amplifier system with on-line chirp analysis for high-resolution spectroscopy”. In: *Review of Scientific Instruments* 78.10, 103102 (2007). DOI: <http://dx.doi.org/10.1063/1.2789690>.
- [126] A.E. Siegman. *Lasers*. University Science Books, 1986. ISBN: 9780935702118.
- [127] R. P. de Groote et al. “Double-resonance-ionization mapping of the hyperfine structure of the stable Cu isotopes using pulsed narrowband Ti:sapphire lasers”. In: *Phys. Rev. A* 92 (2 Aug. 2015), p. 022506. DOI: 10.1103/PhysRevA.92.022506.
- [128] PATRICK PALMERI and JEAN-FRANÇOIS WYART. “INTERPRETATION OF ENERGY LEVELS AND PREDICTED TRANSITION PROBABILITIES IN NEUTRAL TECHNETIUM (TcI).” In: *Journal of Quantitative Spectroscopy and Radiative Transfer* 61.5 (1999), pp. 603–616. DOI: [http://dx.doi.org/10.1016/S0022-4073\(98\)00048-X](http://dx.doi.org/10.1016/S0022-4073(98)00048-X).
- [129] C. Mattolat et al. “Determination of the first ionization potential of technetium”. In: *Phys. Rev. A* 81 (5 May 2010), p. 052513. DOI: 10.1103/PhysRevA.81.052513.
- [130] D Wendlandt, J Bauche, and P Luc. “Hyperfine structure in Tc I: experiment and theory”. In: *Journal of Physics B: Atomic and Molecular Physics* 10.10 (1977), p. 1989.
- [131] K Wendt et al. “Determination of term energy, hyperfine structure and life time of strontium Rydberg levels by resonance ionization spectroscopy in collinear geometry”. In: *Institute of Physics Conference Series*. Vol. 128. IOP PUBLISHING LTD. 1992, pp. 87–87.
- [132] L. Monz et al. “Fast, low-level detection of strontium-90 and strontium-89 in environmental samples by collinear resonance ionization spectroscopy”. In: *Spectrochimica Acta Part B: Atomic Spectroscopy* 48.14 (1993), pp. 1655–1671. DOI: [http://dx.doi.org/10.1016/0584-8547\(93\)80154-M](http://dx.doi.org/10.1016/0584-8547(93)80154-M).
- [133] K. Zimmer et al. “Determination of ^{90}Sr in environmental samples with resonance ionization spectroscopy in collinear geometry”. In: *Applied Physics B* 59.2 (1994), pp. 117–121. DOI: 10.1007/BF01081161.
- [134] K Wendt et al. “Rapid Trace Analysis of $^{89,90}\text{Sr}$ in Environmental Samples by Collinear Laser Resonance Ionization Mass Spectrometry”. In: *Radiochimica Acta* 79.3 (1997), pp. 183–190.
- [135] Marcel Trümper. “Weiterentwicklung der Laserionenquellenfalle LIST zur Untergrundunterdrückung bei Resonanzionisation in kollinearer und transversaler Geometrie”. B.Sc. thesis. Johannes Gutenberg-Universität Mainz, 2015.
- [136] Balraj Singh and Zhiqiang Hu. “Nuclear Data Sheets for $A = 98$ ”. In: *Nuclear Data Sheets* 98.2 (2003), pp. 335–513. DOI: <http://dx.doi.org/10.1006/ndsh.2003.0003>.
- [137] Aaron L. Stancik and Eric B. Brauns. “A simple asymmetric lineshape for fitting infrared absorption spectra”. In: *Vibrational Spectroscopy* 47.1 (2008), pp. 66–69. DOI: <http://dx.doi.org/10.1016/j.vibspec.2008.02.009>.
- [138] V. Sonnenschein. personal communication. 2015.
- [139] R. P. de Grootes. personal communication. 2015.
- [140] Jenny E. Rosenthal and G. Breit. “The Isotope Shift in Hyperfine Structure”. In: *Phys. Rev.* 41 (4 Aug. 1932), pp. 459–470. DOI: 10.1103/PhysRev.41.459.
- [141] M. F. Crawford and A. L. Schawlow. “Electron-Nuclear Potential Fields from Hyperfine Structure”. In: *Phys. Rev.* 76 (9 Nov. 1949), pp. 1310–1317. DOI: 10.1103/PhysRev.76.1310.

- [142] Aage Bohr and V. F. Weisskopf. “The Influence of Nuclear Structure on the Hyperfine Structure of Heavy Elements”. In: *Phys. Rev.* 77 (1 Jan. 1950), pp. 94–98. DOI: 10.1103/PhysRev.77.94.
- [143] H. J. Rosenberg and H. H. Stroke. “Effect of a Diffuse Nuclear Charge Distribution on the Hyperfine-Structure Interaction”. In: *Phys. Rev. A* 5 (5 May 1972), pp. 1992–2000. DOI: 10.1103/PhysRevA.5.1992.
- [144] T. D. Raymond and A. V. Smith. “Injection-seeded titanium-doped-sapphire laser”. In: *Opt. Lett.* 16.1 (Jan. 1991), pp. 33–35. DOI: 10.1364/OL.16.000033.
- [145] Masaki Hori and Andreas Dax. “Chirp-corrected, nanosecond Ti:sapphire laser with 6 MHz linewidth for spectroscopy of antiprotonic helium”. In: *Opt. Lett.* 34.8 (Apr. 2009), pp. 1273–1275. DOI: 10.1364/OL.34.001273.
- [146] Harold Walchli, Ralph Livingston, and William J. Martin. “The Nuclear Magnetic Moment of Tc^{99} ”. In: *Phys. Rev.* 85 (3 Feb. 1952), pp. 479–479. DOI: 10.1103/PhysRev.85.479.
- [147] N J Stone. “TABLE OF NUCLEAR MAGNETIC DIPOLE AND ELECTRIC QUADRUPOLE MOMENTS”. In: *Nuclear Data Section of the IAEA* (2014).
- [148] S Büttgenbach. “Hyperfine structure in 4d-and 5d-shell atoms”. In: 96 (1982).
- [149] RG Kidd. “Technetium-99 NMR and rationalized quadrupole moment values for transition metal nuclei”. In: *Journal of Magnetic Resonance (1969)* 45.1 (1981), pp. 88–93.
- [150] Leonardo Errico et al. “Nuclear quadrupole moment of the ^{99}Tc ground state”. In: *Phys. Rev. B* 77 (19 May 2008), p. 195118. DOI: 10.1103/PhysRevB.77.195118.
- [151] W H King. *Isotope Shifts in Atomic Spectra*. Springer New York, 1984.
- [152] R. Beerwerth. personal communication. 2016.
- [153] I. Angeli and K.P. Marinova. “Table of experimental nuclear ground state charge radii: An update”. In: *Atomic Data and Nuclear Data Tables* 99.1 (2013), pp. 69–95. DOI: <http://dx.doi.org/10.1016/j.adt.2011.12.006>.
- [154] Carsten Weichhold. “Entwicklung, Charakterisierung und Anwendung eines Aufbaus zur dopplerfreien Laserresonanzionisationsspektroskopie in einer hochselektiven Ionenquelle”. Diploma thesis. Johannes Gutenberg-Universität Mainz, 2016.

CURRICULUM VITAE

TOBIAS KRON

Rhabanusstr. 16
55118 Mainz
kron@uni-mainz.de

PERSÖNLICHE ANGABEN

Geburtstag/-ort	26.01.1987, Worms
Staatsangehörigkeit	Deutsch
Familienstand	ledig

BILDUNGSWEG

03/2012 - 12/2016	Promotion, Fachrichtung: Physik Johannes Gutenberg-Universität Mainz Titel der Abschlussarbeit: „ <i>Pushing the Limits of Resonance Ionization Mass Spectrometry – Ionization Efficiency in Palladium and Spectral Resolution in Technetium</i> “ Gutachter: Prof. Dr. K. Wendt
10/2006 - 12/2011	Diplom-Studium Physik Johannes Gutenberg-Universität Mainz Titel der Abschlussarbeit: „ <i>Konzeption, Aufbau und Test einer Referenzzelle für die resonante Laserionisation</i> “ Gutachter: Prof. Dr. K. Wendt
09/1997 - 03/2006	Abitur Gauß-Gymnasium Worms